Structural Engineering and Surface Modulation of Monoclinic $BiVO_4$ for Efficient Visible-Light-Driven Photocatalysis

（単斜晶 $BiVO_4$ の構造制御および表面修飾による効率的な可視光応答光触媒反応に関する研究）

Davin PHILO

Graduate School of Chemical Sciences and Engineering

Hokkaido University

2023

Contents

Contents

Contents

Abstract

The production of renewable green energy stocks by harnessing unlimited solar energy via artificial photosynthesis (APS) technology has been recognized as one of the best and most adaptable solutions for addressing the global energy crisis and environmental problems. Among many photocatalyst candidates, monoclinic bismuth vanadate ($BiVO_4$) semiconductor has attracted growing interest as one of the most promising and advanced materials for various APS applications. Nonetheless, the traditional monoclinic $BiVO_4$ photocatalyst still manifests some downsides, such as poor charge carrier dynamics, relatively low surface area, and the absence of innate reactive sites, yielding monoclinic $BiVO_4$ with unsatisfactory photocatalytic conversion efficiencies. With that being the case, this thesis aims to rationally design some superior monoclinic $BiVO_4$ photocatalysts via structural engineering and surface modulation for highly efficient visible-light-driven photocatalysis. Accordingly, some facile and smart methods were effectively employed during the fabrication process, paving the way for manipulating and modulating the unique properties of the as-synthesized monoclinic $BiVO_4$ photocatalyst. Furthermore, some in-depth investigations to probe the origin of the properties variations and enhanced photocatalytic performance are also presented and discussed comprehensively.

In chapter 1, a general background about heterogenous photocatalysis and a brief overview about monoclinic $BiVO_4$ photocatalyst are introduced. Furthermore, an extensive discussion regarding some prospective photocatalytic applications and the unique properties of monoclinic $BiVO_4$ photocatalyst along with some strategies to control and modulate those properties are presented.

In chapter 2, a cooperative strategy is represented that enables 2D structure tailoring and lattice distortion engineering simultaneously over a $BiVO_4$ photocatalyst for efficient visible-light-driven OER. Specifically, the lattice distortion engineering was achieved through the introduction of sodium (Na^+) additive during the ion exchange process. Structural characterizations suggest the formation of ultrathin 2D monoclinic $BiVO_4$ nanoflakes (BVO NFs) with shrank V–O and elongated Bi–O bonds. Mechanistic investigations reveal the advantages of ultrathin 2D features for exposing more active (010) facets and shortening the required migration distance for charge carriers to reach the catalytic surface. More importantly, the lattice distortion effect is found to crucially govern the charge carrier dynamics and surface behavior of $BiVO_4$ photocatalyst,

endowing the optimized sample with an outstanding photocatalytic OER performance triggering up to 69.4% apparent quantum efficiency (AQE) over Fe^{3+} sacrificial solution. These findings highlight the functional application of morphology and dimensional modification, as well as lattice distortion engineering in synthesizing superior monoclinic $BiVO_4$ photocatalyst for efficient visible-light-driven water oxidation.

In chapter 3, following the previous chapter, an in-depth investigation to probe the effect of lattice distortion peculiarly to the catalytic OER over the (010) surface of monoclinic $BiVO_4$ crystals is represented. By initially engaging the ATR-IR spectroscopy to analyze the interaction between the as-prepared monoclinic $BiVO_4$ sample and water suspension under light irradiation, some reaction intermediates structures were identified, by which a surface OER mechanism could be reasonably deduced. Correspondingly, the first principal calculations for Gibbs free energy of the intermediate structures on the (010) facet of monoclinic $BiVO_4$ slabs unravel the decrease in the reaction energy barrier as the degree of lattice distortion increases, thus affirming the benefit of lattice distortion effect over the catalytic surface reaction of the water oxidation process. Furthermore, by employing the first-principal molecular dynamic simulations, the oxidazibility of some key OER intermediates and the spontaneous water dissociative adsorption process over the (010) surface of the monoclinic $BiVO_4$ slab model are inspected and discussed in detail.

In chapter 4, an effective oxygen vacancy-mediated size engineering strategy over the well-dispersed palladium (Pd) metal photodeposited on the surface of monoclinic $BiVO_4$ photocatalyst for efficient visible-light-driven ORR is demonstrated. By simply adjusting the pH during the fabrication process, various monoclinic $BiVO_4$ photocatalyst with different degrees of oxygen vacancy were successfully synthesized, as confirmed by the spectroscopy characterizations. Upon the selective photodeposition of Pd metal over the (010) surface of the monoclinic $BiVO_4$ samples, it was discovered that the higher the amount of oxygen vacancy the smaller the size of Pd, which would be beneficial for increasing the number of active sites and thus triggering more swift catalytic surface reaction. Therein, the optimized Pd/$BiVO_4$ sample was able to realize an excellent photocatalytic H_2O_2 production up to 2.35 mM/h, accomplishing the state-of-the-art AQE of 19.2% at 420 nm in photocatalytic H_2O_2 production over $BiVO_4$-based materials. This study sets a milestone and also provides some insights into the delicate design of Pd metal-monoclinic $BiVO_4$ composites for more efficient H_2O_2 photosynthesis.

Abstract

In chapter 5, an overall summary of this dissertation work is presented. This thesis carries out some systematic study on structural engineering and surface modulation of monoclinic $BiVO_4$ for efficient visible-light-driven photocatalysis. More importantly, this thesis emphasizes the great importance and significance of controlling and exploiting the unique properties of monoclinic $BiVO_4$. It is unraveled that, by doing so, it would greatly enhance the charge carrier dynamics and/or provide some necessary reactive sites, thus effectively satisfying the fundamental requirements for promoting more efficient artificial photosynthesis. The findings in this study sheds new light on the design and fabrication of high-performance monoclinic $BiVO_4$-based materials for various photocatalytic applications.

Chapter 1. Introduction

1.1. Fundamentals of Artificial Photosynthesis (APS)

Natural photosynthesis (NPS) is a chemical process conducted by green plants, photosynthetic bacteria, and all other photosynthetic organisms, where CO_2 and water are transformed into carbohydrates and molecular oxygen, respectively.[1,2] This process can be considered as the most efficient and effective method of converting light energy into chemical energy. Over billions of years, NPS has provided an overwhelming amount of energy stock, mostly in the form of fossil fuel, for the world.[3] However, as is widely known, the depletion rate of this energy stock is much higher than the rate at which nature can replenish it.[1,4] Consequently, it is only a matter of time before fossil fuels finally run out. Furthermore, the continuous usage of fossil fuels has taken a heavy toll on our nature, leading to severe environmental problems, such as global warming, melting of the polar ice caps, sea level rises, and worsening droughts.[5,6] With this looming energy crisis and environmental concern, many approaches have been made to imitate NPS by artificially utilizing light energy to drive the thermodynamically uphill reactions of abundant substances to produce clean energy-containing chemicals, e.g. hydrogen (H_2), hydrogen peroxide (H_2O_2), hydrocarbons (C_xH_y), and ammonia (NH_3).[3,7-9] At present, this method is generally known as artificial photosynthesis (APS) or the so-called photocatalysis process.[10] Considering the great amount of free solar energy reaching the earth (> 1.465×10^{14} J/s) which can be readily accessed, the APS is believed to be the most feasible and adaptable solution to the aforementioned problems.[9,11]

As is widely known, the green chlorophyll pigment plays a major role in carrying out the NPS reaction. Generally, light energy or photons are absorbed by chlorophyll and used to remove electrons from water molecules to produce oxygen gas as follows:

$$2H_2O \longrightarrow O_2 + 4H^+ + 4e^- \qquad (1\text{-}1)$$

This oxidation reaction occurs in the reaction center of photosystem II. Afterward, the freed hydrogen and electrons are transferred to photosystem I and trigger the reduction of carbon dioxide (CO_2) to produce sugar ($C_6H_{12}O_6$) through the Calvin cycle:

$$CO_2 + 4H^+ + 4e^- \longrightarrow \frac{1}{6} C_6H_{12}O_6 + H_2O \qquad (1\text{-}2)$$

The overall reaction of NPS is written as:

$$CO_2 + H_2O \longrightarrow \frac{1}{6} C_6H_{12}O_6 + O_2 \quad (1\text{-}3)$$

Meanwhile, in APS, a material called a photocatalyst (mostly a semiconductor) is usually employed to harvest light energy.[10] Similar to NPS, this photon energy is used by the photocatalyst to generate charge carriers or excitons, i.e., electrons (e^-) and holes (h^+). In detail, upon light illumination, the excitation of e^- from the valence band (VB) to the conduction band (CB) of the photocatalyst occurs, leaving behind the h^+ in the valence band region.[12] These charge carriers are transferred separately to different reaction centers, where they trigger some endothermic redox reactions; electrons drive the reduction reaction, while holes drive the oxidation reaction as follows:

$$A + e^- \longrightarrow A^- \quad (1\text{-}4)$$

$$D + h^+ \longrightarrow D^+ \quad (1\text{-}5)$$

A and D represent an electron acceptor and electron donor, respectively. In summary, there are three pivotal steps in APS: light absorption (generation of charge carriers), charge transfer, and surface catalytic reactions. **Figure 1.1** illustrates a comparison between NPS and APS.

In relation to the above-explained APS process, there are some principal conditions that must be fulfilled so that the target reaction may occur efficiently. These requirements are valid and prevalent for all APS reactions, and therefore, it is important to identify them as the very first stepping stones toward designing an effective photocatalytic system.

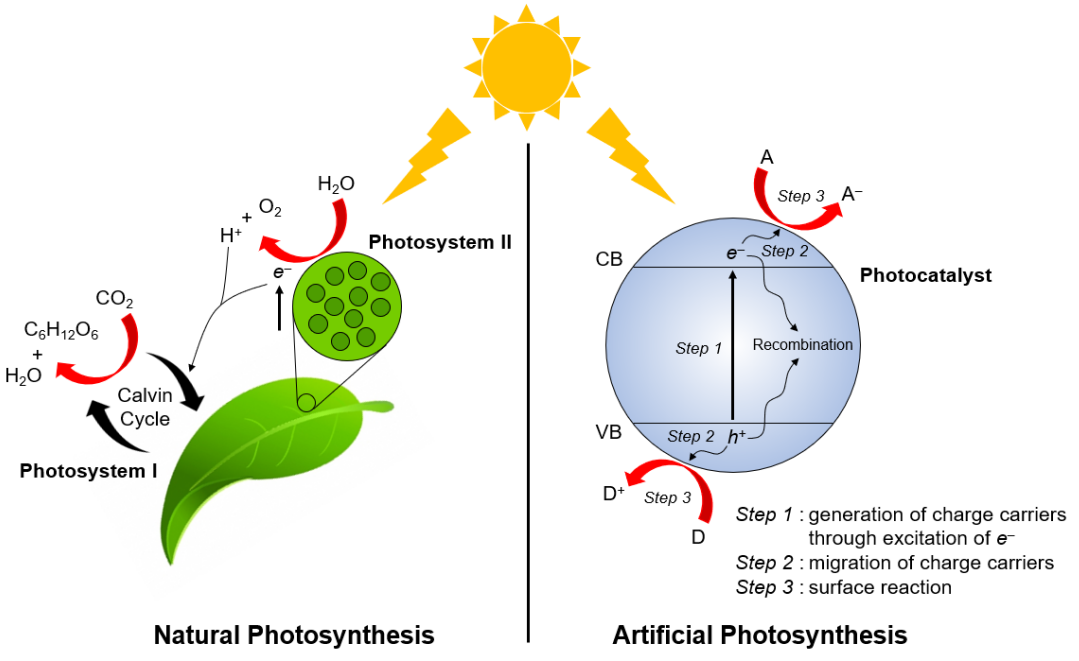

Figure 1.1. Comparison between natural and artificial photosynthesis.[13]

1.1.1. Photon Absorption and Thermodynamic Boundaries

Since the ultimate aim of APS is to utilize solar energy, it is necessary to consider the characteristics of sunlight itself. As depicted in **Figure 1.2**, the sun emits a spectrum of electromagnetic waves with a relatively broad wavelength, which comprises 3 – 5% UV (< 400 nm), 42 – 43% visible light (400 – 700 nm), and 52 – 55% infrared (> 700 nm).[14] On the basis of this fact, the utilization of visible light, near-infrared (NIR), and infrared is more favorable and essential to achieving substantial solar energy conversion, although this is more challenging. In this case, we often use the term band gap (E_g) to evaluate the light-harvesting ability of a semiconductor photocatalytic material. In the electronic structure of solid materials, including semiconductors, the band gap is usually defined as the energy difference between the top of the valence band (valence band maximum, VBM) and the bottom of the conduction band (conduction band minimum, CBM). The value of E_g is usually obtained by applying the Kubelka–Munk transformation and can be used to determine the maximum wavelength of light (λ_{max}) that the photocatalyst can absorb using the following equation:

$$\lambda_{max} = hc/E_g \tag{1-6}$$

where h is Planck's constant (6.626×10^{-34} m^2 kg/s) and c is the speed of light (3×10^8 m/s). Generally, a photocatalyst can absorb light with a higher energy than its band gap, or in other words, a wavelength less than the value of λ_{max} calculated as above. Hence, to enable the absorption of a larger proportion of the solar spectrum, a semiconductor with a relatively small band gap is preferred.

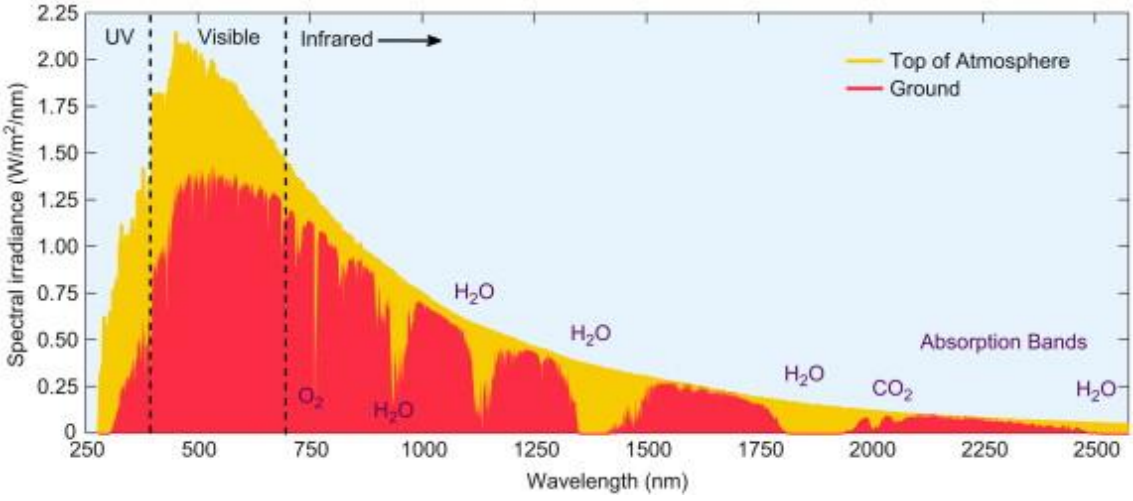

Figure 1.2. Standard spectral properties of sunlight.[15]

Furthermore, in order to successfully perform any redox reaction, one needs to pay careful attention to the thermodynamic constraints of the corresponding reaction. In this case, we mostly use the term standard reduction potential (E^0) to quantify the thermodynamic state of a certain reaction. The reduction potential or electrode potential is usually defined as a value for measuring the tendency of some substances to receive electrons and thus be reduced. It is measured as the energy level, with volt (V) as the unit, with respect to a certain standard potential, such as the standard hydrogen electrode (SHE). The higher (more positive) the value of this potential, the greater the likelihood of the species acquiring electrons and being reduced. In contrast, the lower (more negative) this value, the greater the tendency for the backward reaction (oxidation) of the species to occur. For a redox photon-induced reaction to successfully occur, the CB energy level of the photocatalyst must be higher than the potential of the reduction reaction, while the VB must be located at a more positive potential than the oxidation reaction. Since different reactions require different thermodynamic boundaries, some photocatalysts will be suitable for a certain reaction but might not be suitable for other purposes. However, it is also possible to shift the position of the energy band by introducing some impurities, known as dopants, to meet different thermodynamic requirements.[16]

1.1.2. Photogenerated Charge Carriers Separation and Transfer

Following the generation of charge carriers as a result of the photon absorption, the electron–hole pairs need to be separated immediately and transported into different zones; otherwise, they will recombine with each other within the photocatalyst, generating either heat or photoluminescence.[17,18] In general, the wide bandgap semiconductors are benefitted with better charge carrier separation efficiency compared to narrow bandgap semiconductors, because the smaller the band gap, the easier the excited electrons come back to their original state and thus recombine with the holes. In addition, the recombination process is also strongly affected by the presence of defects within the body/bulk of a photocatalyst, since they can operate as trapping and recombination centers for the photogenerated electrons and holes.[17] This electron–hole recombination usually results in a significant loss of energy, thus limitting the quantum efficiency of the photocatalytic system.[10] Up until now, modulating the charge carrier dynamic properties of photocatalyst by suppressing the charge recombination has been a challenging and long-standing issue in APS.[19] Hence, extensive effort and strategies have been employed in order to tackle this challenge, i.e., (1) increasing the crystallinity of the photocatalyst

in order to decrease the amount of defect; (2) controlling the shape, structure, and size of the photocatalysts in order to reduce the distance that the charge carriers must travel before reaching the surface of the photocatalyst; (3) formation of a homojunction and heterojunction to promote the spatial separation of electrons and holes; (4) utilization of a sacrificial agent as a scavenger of particular charge carriers, thus increasing the proportion of opposite charge carriers in the photocatalyst; and (5) introduction of a cocatalyst on the surface of a photocatalyst, which can provide charge accumulation centers and also accelerate interfacial reaction kinetics.[10,17,20]

1.1.3. Existence of Surface Reactive Sites

From the time scale perspective, i.e. picosecond to nanosecond for light harvesting; microsecond to millisecond for charge transfer; millisecond to second for surface reaction, it can be concluded that surface reaction is the crucial step in APS.[21,22] Therefore, a photocatalyst material should possess active catalytic sites on its surface for the photocatalytic reaction to occur. However, most photocatalyst surfaces are not typically designed to catalyze redox reactions.[18] To address this problem, a cocatalyst that can provide the reactive sites for a certain APS reaction is frequently loaded and dispersed on the surface of the photocatalyst.[23] For this purpose, cocatalyst components are often adapted from the components of electrocatalysts applied for the same reactions.[7] In other cases, some surface defects are introduced on the surface of the photocatalyst, which can unexpectedly provide the reactive sites for APS reactions.[24,25]

To establish effective surface reactions, the reactive sites must be designed according to the Sabatier principle, which states that the catalytic surface must have a trade-off between being reactive and not being poisoned by the reaction intermediates.[26] Hence, the interactions between the sites and the substances (either reactant or product) should be modest: neither too weak so that the sites can adequately bind the reactant and the surface reaction (through the electron transfer process) may take place, nor too strong so that the product can easily desorb from the catalytic surface.[27-29] Secondly, if a cocatalyst is employed, the cocatalyst should form a good coordination with the semiconductor to ensure smooth charge migration into/from the reactive sites [7,30]. This is because, for any catalytic reaction, a sustained charge carrier supply is the key to a continuous and effective surface reaction.[31] In this case, a suitable loading method and a precursor of the cocatalyst are accordingly crucial. Finally, increasing the number of reactive sites by either altering the morphology of the material into low-dimensional structure,[32,33]

exposing more active edges of the cocatalyst,[34,35] or reducing the size of the cocatalyst into cluster[36-38] or single-atom[39-41] is also an effective way of enhancing the photocatalytic activity.

1.1.4. Quantum Efficiency

Especially in the particulate photocatalysis (where some light-driven photocatalytic reaction is carried out by dispersing some powder or solid photocatalyst in the reactant solution), the performance of a photocatalytic system is often reported as the evolution rates of the target product(s). However, it is extremely difficult and sometimes becomes unfair to compare the measured activities in different experimental conditions, including reactor geometry, reaction temperature, light source, illumination condition, etc.[12,19] Therefore, the concept of quantum efficiency (QE) is developed and employed in order to make valid comparisons between different experimental and illumination conditions. QE can be defined as the number of reacted electrons relative to the total number of photons adsorbed by the photocatalyst.[19] Unfortunately, it is difficult to accurately quantify the real amount of adsorbed photons in a particulate photocatalysis system due to the light scattering effect. [17] Hence, in the case of heteregenous photocatalysis, QE is usually represented as apparent quantum efficiency (AQE), by which the total number of incident photons in reaction system is utilized instead as the denominator. The AQE is estimated to be smaller than the real QE because the number of absorbed photons is usually smaller than that of incident light.[17] AQE is usually evaluated for a certain photon wavelength (monochromatic) and calculated using the following equation:

$$\mathrm{AQE} = nr/I \tag{1-7}$$

where n, r, and I represent the number of e^- involved in the photocatalytic reaction, the corresponding production rate, and the rate of incident photons, respectively. Typically, the wavelength-dependent AQE follows the optical absorbance pattern of the semiconductor, which decreases as the irradiation wavelength approaches the absorption edge because of the lower absorption coefficients and larger migration distances for photogenerated carriers.[12]

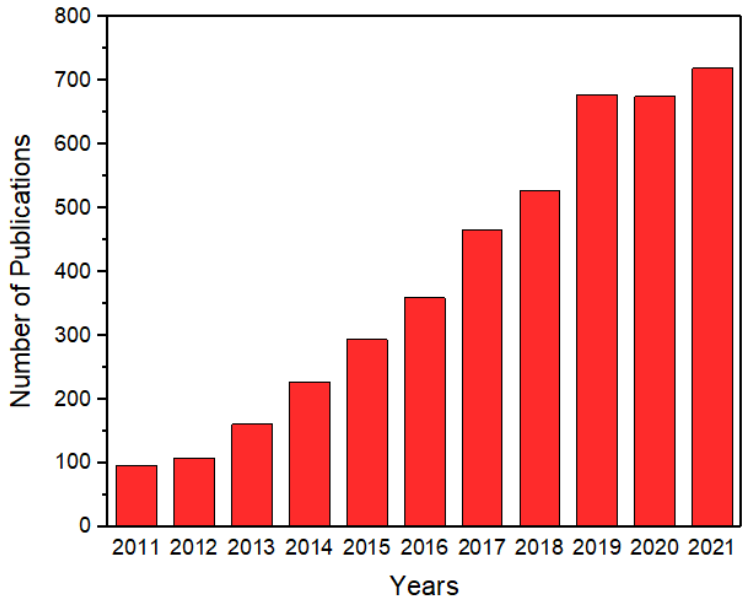

Figure 1.3. Number of scientific publications on $BiVO_4$-based photocatalytic materials over the past decades (source: Web of Science Core Collection on October 21st, 2022; search terms: "$BiVO_4$" or "Bismuth Vanadate" and "Photocatalysts").

1.2. Monoclinic Bismuth Vanadate, a Promising Photocatalyst

Bismuth vanadate ($BiVO_4$) is direct band gap semiconductor with unique physical and chemical properties, which belongs to the group of Aurivillius bismuth metal oxide compounds, i.e. $Bi_xM_yO_z$ (M: Mo, W, V, Nb, and Ta).[42-44] Since decades ago, $BiVO_4$ has been known for its great potential as ferroelastic, pigmentary (bright yellow), and ion conductive materials.[42,45,46] More importantly, it also attracts intensive interest as one of the most promising and advanced materials for various photocatalytic applications, due to its visible light absorption ability, non-toxicity, plentiful abundance, low cost, good photostability, and also deep valence band energy, which is very favorable for driving any oxidation reactions.[21,47-49] **Figure 1.3** indicates the total number of publications regarding $BiVO_4$-based photocatalytic materials during 2011–2021, which clearly shows an increasing trend as an emerging topic in the field of APS.

Concerning the structural characteristics, it has been widely known that $BiVO_4$ exists in three types of crystal polymorphs: tetragonal zircon, tetragonal scheelite, and monoclinic scheelite, with E_g of 2.90, 2.34, and 2.40 eV, respectively.[43,50-52] The crystal structures of $BiVO_4$ are generally composed of (VO_4) tetrahedral and (BiO_8) polyhedral where V(V) and Bi(III) are located at the center of the units.[53] The typical crystal structures of the three polymorphs of $BiVO_4$ can be seen in **Figure 1.4 a-c**. While in

zircon structure, the (BiO_8) units are surrounded by six (VO_4), in the scheelite phases, each Bi unit is surrounded by eight (VO_4).[53] Compared to tetragonal scheelite, monoclinic scheelite $BiVO_4$ possesses a relatively more distorted local crystal structure,[45,46,54] which will be discussed in the later section. As shown in **Figure 1.4 d**, when zirgon type $BiVO_4$ is subjected to thermal treatment at about 400–500 °C, it will undergo an irreversible phase transformation to monoclinic structure.[45,55] Furthermore, the phase transition between tetragonal and monoclinic scheelite $BiVO_4$ reversibly occurs at about 255 °C.[45,56]

Of the three above-mentioned polymorphs, monoclinic $BiVO_4$ shows the highest photocatalytic performance under visible light irradiation, while the zircon-type $BiVO_4$ is only active under UV light irradiation, due to its relatively wide band gap.[55] Tokunaga et al. reported selective preparation of monoclinic and tetragonal $BiVO_4$ with schelite structure by adjusting the amount of bases (Na_2CO_3 and $NaHCO_3$), by which negligible photocatalytic OER activity over $AgNO_3$ solution was observed for tetragonal $BiVO_4$, in contrast to monoclinic $BiVO_4$ which showed high photocatalytic activity.[45] Years later, Ke et al. investigated the effects of hydrothermal temperature on the microstructures of $BiVO_4$, whereby they found that the pure monoclinic $BiVO_4$ possesses the best photoactivity for OER over $Fe(NO_3)_3$ solution compared to other samples with mixed crystal phases of tetragonal zircon and monoclinic scheelite, though it has the smallest surface area, indicating that the crystal phase is the decisive factor in the photoactivity of $BiVO_4$.[57]

The base-centered monoclinic crystal structure of $BiVO_4$ (space group 15, $C2h^6$) contains four unique lattice sites: Bi (4e), V (4e), O1 (8f), and O2 (8f).[54,58] **Figure 1.4 e** displays a $BiVO_4$ monoclinic primitive cell of two formula units, constructed by considering the crystal inversion symmetry.[58] In this kind of crystal lattice, O1 is coordinated to one Bi and V, while O2 is coordinated to two Bi and a single V. The stoichiometry of the $BiVO_4$ material indicates formal oxidation states of 3+, 5+, and 2– for Bi ($5d^{10}6s^2$), V ($3d^0$), and O ($2p^6$), respectively. Monoclinic $BiVO_4$ exhibits layered structure of Bi–V–O units stacked parallel to the *c* axis which draws features from both the Bi_2O_3 and V_2O_5 binary analogues.[59,60] As typical clinobisvanite structures, the Bi is coordinated in a distorted oxygen octahedron with four types of Bi−O bonds, while the V unit is located at the center of distorted tetrahedron with two types of V−O bonds.[46,54,58,61]

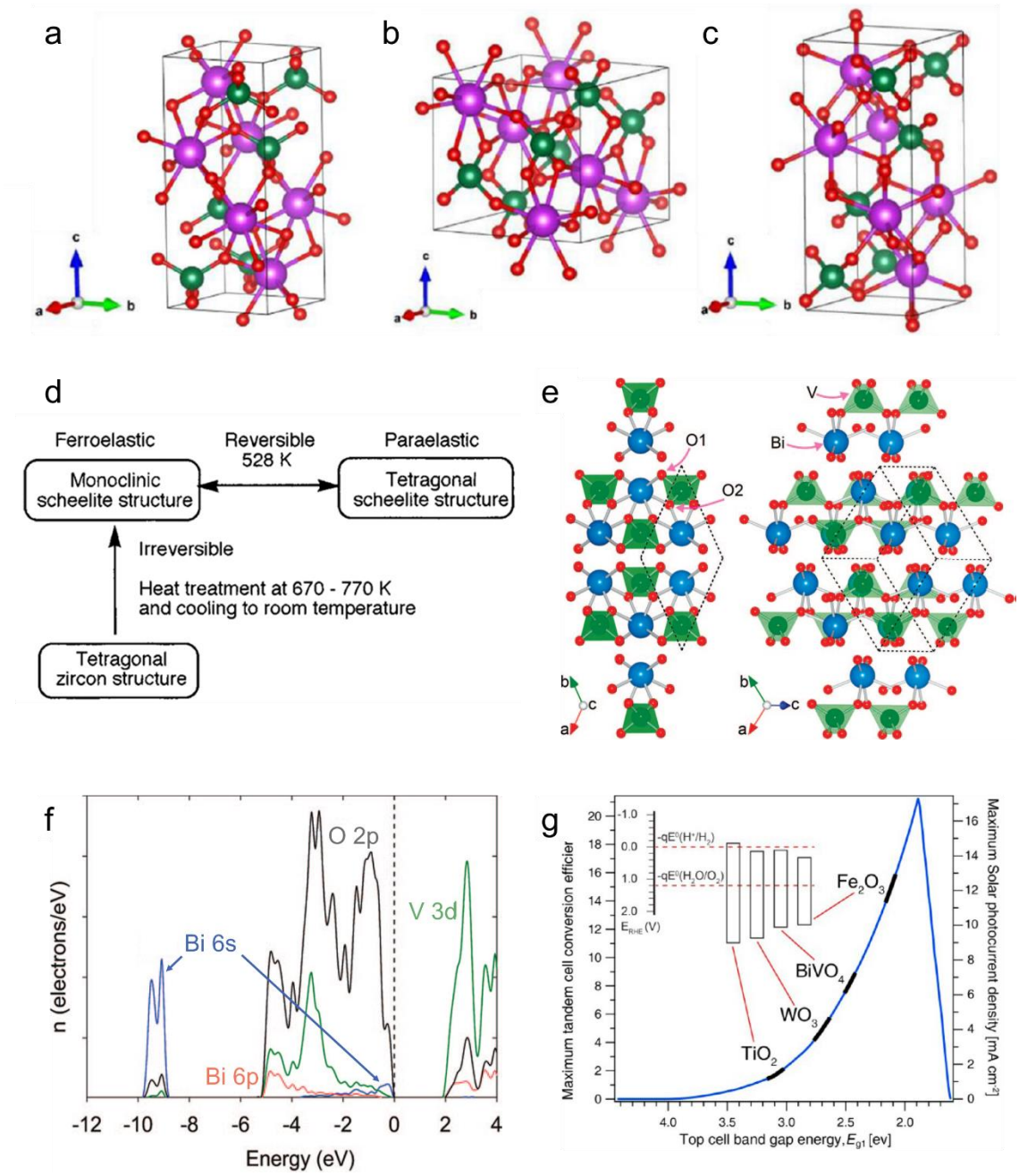

Figure 1.4. Crystal structures of $BiVO_4$ polymorphs: (a) tetragonal scheelite, (b) tetragonal zircon, and (c) monoclinic scheelite (purple: Bi, green: V, and gray: O),[62] (d) phase transitions of $BiVO_4$,[45] (e) monoclinic $BiVO_4$ primitive cell of two formula units (blue: Bi; green: V, and red: O),[58] (f) ion-projected density of states (DOS) of monoclinic $BiVO_4$,[58] and (g) maximum theoretical solar-to-hydrogen conversion efficiency and solar photocurrent as a function of the top cell band gap energy in a tandem cell.[63]

The typical electron density of states (DOS) profiles of monoclinic $BiVO_4$ orbitals is presented in **Figure 1.4 f**.[58] It discloses that the unoccupied V 3d orbitals act as the major character within the CB of monoclinic $BiVO_4$, with minor contributions from the

unoccupied Bi 6p and O 2p states. According to a comprehensive theoretical study by Copper et al., the poor overlap between the V 3d and Bi 6p orbitals around the CBM might be responsible for the poor electron mobility in the material.[61] Furthermore, it also reveals that the VBM is mainly composed of O 2p occupied states, which overlap with a small amount of Bi 6s orbitals, while the dominant components of Bi 6s are located at a much lower energy range (roughly 9 eV below VBM). Those orbitals act as bonding states below the Fermi level, rendering the monoclinic phase of $BiVO_4$ energetically more favorable.[64] In addition, the hybridization of Bi 6s and O 2p orbitals will create new preferable hybridized states, which will lead to a narrow band gap to harvest visible light and highly dispersive band structures.[43,65] As shown in **Figure 1.4 g**, originating from the photoelectrochemical (PEC) field, it is predicted that under standard AM 1.5 solar light irradiation, monoclinic $BiVO_4$ would be able to achieve a high theoretical solar-to-hydrogen conversion efficiency (η_{STH}) of 9.2% with a maximum photocurrent of 7.5 mA cm^{-2}, thus rendering it an excellent photocatalyst candidate for further research and development.[49,63]

1.3. Potential Photocatalytic Applications of Monoclinic $BiVO_4$ Photocatalyst

In this section, we are going to discuss about the prospective particulate photocatalytic applications over monoclinic $BiVO_4$-based materials which have been studied and reported in the literatures thus far. **Figure 1.5** displays the reduction potentials of various photocatalytic reactions relative to the band positions of monoclinic $BiVO_4$. As mentioned earlier, considering the deep energy level of its VB, monoclinic $BiVO_4$ can be regarded as an ideal oxidation photocatalyst, especially to drive the water oxidation reaction.[21,47] Regardless, only the four electron water oxidation to produce O_2 has been scientifically and experimentally demonstrated over the particulate photocatalysis of monoclinic $BiVO_4$-based materials.[55,66-69] In contrast, the two electron water oxidation to produce hydrogen peroxide (H_2O_2) by the heterogeneous $BiVO_4$-based photocatalysis, even though with thermodynamic feasibility, indicates no scientific report yet, due to the difficulty to realize this reaction,[11,70] probably related to the absence of reactive sites and poor selectivity compared to the former water oxidation. Intriguingly, recent reports have disclosed that the modification of monoclinic $BiVO_4$ might enable the reductive photocatalytic H_2O_2 synthesis through the two electron oxygen reduction scheme.[8,71-75] Surprisingly, solar driven CO_2 and N_2 reduction reactions over $BiVO_4$-based materials, although being thermodynamically difficult considering that their reduction potentials are

mainly located on top of the CB of pristine monoclinic $BiVO_4$, have, in fact, been reported a few times already.[76-84] In those works, some modulation strategies, such as surface defects, band changing morphology modification, and plasmonic photocatalysis were employed in order to modify the properties of monoclinic $BiVO_4$, thus paving the way for circumventing the thermodynamic obstacles of the corresponding reactions.

1.3.1. Oxygen Evolution Reaction

The most popular photocatalytic reaction which has been extensively applied and studied over monoclinic $BiVO_4$ material is the water oxidation reaction to produce O_2, which can be also called as oxygen evolution reaction (OER). As previously mentioned, the APS technology is designed and developed with the ultimate aim to promote the conversion of abundantly available sources into energy-containing chemicals, which mostly take the form of reduction reactions. Similar to NPS, in the ideal situation for the industrial application, these fuel-forming reduction reactions will be paired with the OER as the other half-reaction.[85] However, due to its complex four-electron transfer process, unclear reaction mechanism, high energy barrier, and sluggish reaction kinetics, OER has been regarded as the bottleneck for the realization of APS technology.[67,86,87]

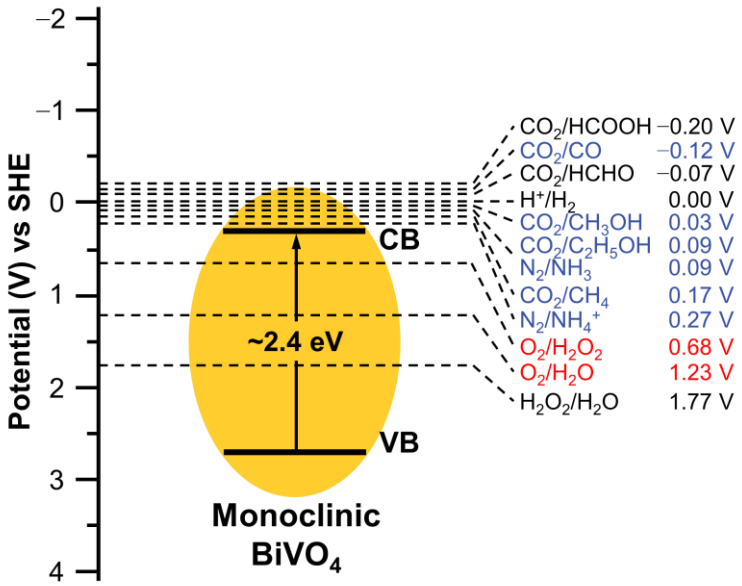

Figure 1.5. Band position of monoclinic $BiVO_4$ semiconductor and reduction potentials of various heterogeneous APS reactions. The colors of the reactions can be regarded as follows, black: no related scientific report yet and/or thermodynamically not feasible; blue: have been reported but actually thermodynamically difficult; red: thermodynamically feasible with some valid scientific literatures.

As aforementioned, the OER process can be written as below:

$$2H_2O \longrightarrow O_2 + 4H^+ + 4e^- \quad (1\text{-}1)$$

Thermodynamically, the standard redox potential for the above reaction is +1.23 V *vs*. SHE. Accordingly, in order to drive the OER, the VBM of a photocatalyst should be more positive than 1.23 V, which actually is commonly found in many semiconductors, including monoclinic $BiVO_4$, thus rendering it relatively easy to fulfill this requirement.[49] Nevertheless, only a few semiconductors are found to be effective photocatalysts for OER. This can happen due to the requirement of multiple (four) electron transfer, complicated reaction processes, and high kinetic barrier, which make the kinetic of catalytic OER become really challenging.[67,85-87] Hence, the presence of suitable surface reactive sites which can satisfy the above issues is indispensable for triggering an efficient OER.

The process of oxygen evolution from water usually starts with the binding of OH^- anion to the active catalytic site.[88] Regarding this first step, there are actually different opinions on where and how the OH^- adsorption process occurs. According to the early literatures, it is believed that the OH^- ion is attracted and bind by the metal active center.[89] Interestingly, some recent studies on La_2LiIrO_6 and $SrCoO_3$ perovskites as OER catalysts suggest that the oxygen radical on the catalytic surface can also act as an electrophilic active site to bind the hydroxyl ion through nucleophilic attack (by the water oxygen lone pairs), resulting in the formation of –O–O–H species.[90,91] Following the OH^- adsorption, a series of proton-coupled electrons transfer (PCET) occurs by which some reaction intermediates, such as adsorbed atomic O (either metal=O or radical O· species),[92-96] superoxide O_2^-,[90,91,97] bridged peroxo species (μ-peroxo),[90,98] surface hydro peroxo,[90-93,96-98] and surface peroxo,[94,97] are formed one after another. A consensus regarding the final step of the oxygen evolution process is settled, whereby either the surface hydroperoxo M–O–O–H species or superoxide $M–O_2^-$ complex act as the final adsorbate intermediate before it finally releases the O_2 molecule.[90,91,94,96,98]

Practically, in order to perform the heterogeneous photocatalytic OER, there are two strategies which are commonly used over monoclinic $BiVO_4$ photocatalyst. First, it is possible to use the sacrificial agent which will act as electron scavenger for capturing the photogenerated electron, enabling the remaining holes to oxidize water and produce oxygen. In this case, $AgNO_3$ is the most popular sacrificial agent for photocataytic OER.[57,86,99-101] Nevertheless, the usage of Ag^+ will lead to photodeposition of Ag metal over the surface of $BiVO_4$ which might significantly obstruct the light absorption (since

it tends to have relatively low specific surface area) and thus reduce the photocatalytic efficiency over the time, as more and more Ag metal is deposited.[55,67] The other sacrificial agents which have been reported to be effective for photocatalytic OER over $BiVO_4$ are $NaIO_3$,[69,102-104], $NaIO_4$,[105] $Fe(NO_3)_3$,[57,67,68] $FeCl_3$,[68,106] and K_3FeCN_6.[68]

The second strategy is by applying the advance Z-scheme concept. This method is basically inspired by the natural photosynthesis, which involves two photosystems where the reduction and oxidation reactions occur separately,[7,14] as illustrated in **Figure 1.6 a**. Similarly, in the $BiVO_4$-based Z-scheme photocatalyst system, another semiconductor acts as the reduction photocatalyst, while $BiVO_4$ takes charge as the oxidation photocatalyst (see **Figure 1.6 b**).[14,62] In this case, the photogenerated electrons in the reduction photocatalyst will perform a reduction reaction, such as hydrogen evolution reaction and CO_2 reduction reaction, whereas the holes in $BiVO_4$ will oxidize water to evolve O_2.[107-110] The remaining holes and electrons in reduction and oxidation photocatalysts, respectively recombine through a solid-state electron mediator (e.g., Au, Rh, Ni, Ag, Ir, and RGO)[111-115] or an aqueous redox mediator (e.g., Fe^{3+}/Fe^{2+}, $[Fe(CN)_6]^{3-}/[Fe(CN)_6]^{4-}$, IO_3^-/I^-, and I_3^-/I^- solutions).[108,116-118] Due to their dual absorber engineering, Z-scheme photocatalytic system benefits from the combined sunlight absorption abilities and high charge separation while preserving the original high redox strength of each photocatalyst.[14,62] By this way, semiconductors with unsuitable band positions and a relatively small band gap can be utilized, thus expanding the choices for semiconductors.[14,119] However, the major drawback of Z-scheme system is the reduced amount of products which can be achieved, since half of the charge carriers will recombine within the mediator.[20]

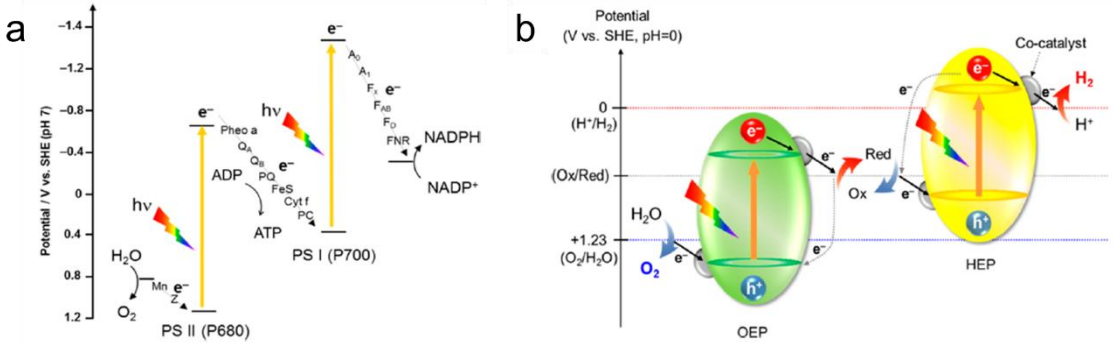

Figure 1.6. Schematic diagrams of (a) natural photosynthesis double excitation process and (b) Z-scheme photocatalysis system involving two different photocatalysts for reduction and oxidation reactions, respectively.[14]

Figure 1.7. Applications of H_2O_2 in industrial manufacturing.[11]

1.3.2. Synthesis of Hydrogen Peroxide

Since the first discovery of hydrogen peroxide (H_2O_2) through the reaction of barium oxide and nitric acid by Louis-Jacques Thenard in 1818,[120] H_2O_2 has attracted great interest from many research areas and has been listed as one of the 100 most important chemicals in the world.[121-124] H_2O_2 is the simplest peroxide compound with a high active oxygen content (47.1% w/w), which can serve as a clean oxidizing agent without any toxic byproducts generated from its reaction (only water and O_2).[70,125] Accordingly, it has been widely applied in many areas, including pulp and textile bleaching, medical disinfection, organic synthesis (advanced oxidation processes), wastewater treatment, and many other industrial fields (see **Figure 1.7**).[11,121-123] In addition, H_2O_2 has also shown a great prospect in the field of energy research as it can serve as liquid fuel (both as oxidant and reductant) for a single-compartment-fuel cell.[126-128] Considering the energy density of H_2O_2 (3.0 MJ L^{-1} or 2.1 MJ kg^{-1} for 60% aqueous H_2O_2) which is comparable to that of H_2 (2.8 MJ L^{-1} or 3.5 MJ kg^{-1} for compressed hydrogen with 35 MPa),[126] it has become an ideal alternative energy carrier, especially since it is relatively more cost-effective (it can operate in a membrane-free system) and easily transportable (fully soluble in water).[8,70,122,123] According to a comprehensive research report by Market Research Future (MRFR), the market value of H_2O_2 is estimated to grow at a 4.3% CAGR to reach USD 5.5 billion by 2027.[129]

In the current industrial situation, H_2O_2 is mainly prepared through the anthraquinone method, which accounts for more than 95% of the total production of H_2O_2.[71,121] Despite of the safety and high efficiency of this technology, it suffers a great drawback due to its high required energy input, high production cost, unsafe transportation process, and vulnerability to environmental contamination.[11,122] Other alternative methods, such as alcohol oxidation and electrochemical synthesis have also been developed and applied in industrial production of H_2O_2, however the quality of the products is not satisfactory compared to the one via antraquinone method.[121,130] Another alternative route is by employing Pd or bimetallic Au-Pd to catalyze the direct synthesis of H_2O_2 from H_2 and O_2 gaseous, according to the following reaction:[131,132]

$$H_2 + O_2 \longrightarrow H_2O_2 \tag{1-8}$$

Unfortunately this strategy is lacking of the safety aspect, since it requires the precise control of hydrogen to oxygen ratio in order to prevent the explosion of H_2/O_2 mixtures, even though it's possible to add some diluents (e.g. N_2, CO_2, and Ar) to reduce the risk of explosions. As a consequence, this process has not yet been scaled up to industrial applications.[122] In this regard, it is highly desirable to develop some new methods for the synthesis of H_2O_2, which are more straightforward and safe, less energy consuming, and environmentally friendly.[11,71,122] In the last decade, artificial photosynthesis of H_2O_2 has aroused much attention from the researchers all over the world, which might provide a meaningful breakthrough for the efficient production of H_2O_2.[133] Compared to the above-mentioned methods, photocatalytic approach offers a much safer and green route, since it only requires the usage of earth abundant and non-dangerous raw materials (water and O_2) with zero pollutant emission in the overall process.[130]

The photocatalytic synthesis of H_2O_2 can proceed through the two electron oxygen reduction reaction (ORR) and two electron water oxidation reaction (WOR), as shown in the following equations, respectively:

$$O_2 + 2H^+ + 2e^- \longrightarrow H_2O_2 \tag{1-9}$$

$$2H_2O \longrightarrow H_2O_2 + 2H^+ + 2e^- \tag{1-10}$$

The standard redox potential for the ORR is +0.68 V *vs*. SHE, while the redox potential of the WOR is +1.77 V *vs*. SHE. Up until now, only the former reaction has been successfully realized by using the particulate photocatalysis, with the latter one being scarcely discussed and studied (might be due to the very poor selectivity compared to the

four electron water oxidation). Therefore, the photocatalytic production of H_2O_2 will usually involve two major half-reactions, i.e. the two electron ORR and water oxidation to evolve O_2, with a total standard Gibbs fee energy change of 117 kJ/mol (uphill).[130] In general, the photosynthesis of H_2O_2 by the means of ORR can proceed through either a sequential two-step single-electron indirect reduction ($O_2 \rightarrow O_2{\bullet}^- \rightarrow H_2O_2$) or a one-step two-electron direct reduction ($O_2 \rightarrow H_2O_2$) route.[122] In the first case, the O_2 is firstly reduced by one electron to generate the superoxide radicals ($O_2{\bullet}^-$), which further react with H^+ to produce ($HO_2{\bullet}^-$) radicals. The ($HO_2{\bullet}^-$) will then receive another electron and thus be reduced to form the HO_2^- anion. Finally, the HO_2^- will react with another proton to generate H_2O_2. These sequential reactions can be written as follows:

$$O_2 + e^- \longrightarrow O_2{\bullet}^- \quad (1\text{-}11)$$

$$O_2{\bullet}^- + H^+ \longrightarrow HO_2{\bullet}^- \quad (1\text{-}12)$$

$$HO_2{\bullet}^- + e^- \longrightarrow HO_2^- \quad (1\text{-}13)$$

$$HO_2^- + H^+ \longrightarrow H_2O_2 \quad (1\text{-}14)$$

As for the H_2O_2 production via a one-step two-electron direct reduction of oxygen, the O_2 is directly reduced by two electrons followed by the coupling with H^+ to form H_2O_2 product. In or to achieve a high conversion efficiency and selectivity for the synthesis of H_2O_2, it is important to beware of the possible side reactions, such as four-electron reduction of O_2 to generate H_2O and H_2O_2 decomposition by either the reduction or oxidation reaction:

$$O_2 + 4H^+ + 4e^- \longrightarrow 2H_2O \quad (1\text{-}15)$$

$$H_2O_2 + 2H^+ + 2e^- \longrightarrow 2H_2O \quad (1\text{-}16)$$

$$H_2O_2 \longrightarrow O_2 + 2H^+ + 2e^- \quad (1\text{-}17)$$

For monoclinic $BiVO_4$ photocatalyst, since its CBM is located below the one-electron reduction potential of O_2 (−0.13 V *vs*. SHE), but still more negative than the two-electron reduction potential of O_2, it is be able to promote the two-electron ORR for H_2O_2 production. The first work of H_2O_2 artificial photosynthesis over monoclinic $BiVO_4$ was reported by Hirakawa et al., where the authors utilized Au loaded $BiVO_4$ to achieve 40.2 μM of H_2O_2 photocatalytic production in pure water after 10 h visible light illumination, which was larger than that of Au/TiO_2.[71] It is noteworthy that most reported literatures about photocatalytic H_2O_2 production over $BiVO_4$ involve the usage of noble metals, such as Au,[71,72] Pd,[8,73] bimetallic Au-Pd,[74] and Cu@Au core shell[75] to act as cocatalyst for

the ORR, since the unmodified monoclinic $BiVO_4$ is rather inactive with negligible H_2O_2 production activity.

1.3.3. Carbon Dioxide and Nitrogen reduction

Carbon dioxide (CO_2) and nitrogen (N_2) reduction reactions can be regarded as two of the most important and yet challenging APS applications.[28,134] Both CO_2 and N_2 are very stable compounds owing to the possession of extremely strong bonds of C=O and N≡N, with dissociation energies of 745 kJ/mol and 945 kJ/mol, respectively.[28,135] The extremely high stability of those molecules can be considered as the major disadvantage to the kinetic feasibility of the CO_2 and N_2 reduction reactions. In this regard, the activation of CO_2 and N_2 molecules, which is closely related to the adsorption of those species on the catalytic surface, would very likely become the rate-determining step for overall reactions.[136,137] Furthermore, both reactions have a great dependency to the multiple PCET processes, in order to bypass the principal energy barrier of single electron reduction reactions with very high reduction potentials.[28,138]

As can be seen in **Figure 1.5**, the CB position of monoclinic $BiVO_4$ is actually lower than the CO_2 and N_2 reduction reactions (even with multiple electron transfer already), thus making it thermodynamically difficult to realize those reactions over $BiVO_4$ photocatalyst. With that being the case, many surface modulation strategies have been developed to manipulate the adsorption and activation of CO_2 and N_2 molecules over the $BiVO_4$-based photocatalysts. Gao et al. demonstrated the utilization of vanadium metal vacancy over the atomic layers of $BiVO_4$ photocatalyst to achieve a high CO_2 photoreduction performance, with methanol formation rate up to 398.3 mmol g^{-1} h^{-1}.[76] An effective strategy to widen the band gap of $BiVO_4$ photocatalyst (from 2.41 eV to 2.72 eV), by reducing the particle size to a few nanometers quantum dots scale (~5 nm) was reported by Chen et al., where the CB of $BiVO_4$ was elevated to enable the efficient photoreduction of CO_2 to CO and CH_4.[77] Recently, Huang et al. develop a facile solvothermal method to construct some $BiVO_4$ microplates with abundant surface oxygen vacancies decorated with metallic Cu and Bi nanoparticles, which exhibited remarkably improved production rates of CH_4 and CO in comparison with Bi/$BiVO_4$ and pristine $BiVO_4$. In that study, it was discovered that the active surface oxygen vacancies were generated during the reduction procedure of partial $BiVO_4$ and/or Cu precursors.[79] By performing precise location and regulation of active sites, Zhang et al. was able to realize high photocatalytic N_2 reduction reaction of 103.4 μmol g^{-1} h^{-1}.[83] The authors proposes

a catalytic mechanism where the V^{4+} plays the role of chemisorption of N_2, while V^{5+} acts as electron transfer bridge, and the photogenerated electrons trapped in surface oxygen vacancies provide the driving force for the ammonia synthesis. In other work, Wang et al. reported a synergestic strategy by combining surface oxygen vacancy with the local surface plasmon resonance (LSPR) effect of Ag nanoparticles to enhance the photocatalytic N_2 fixation over a mulberry-like $BiVO_4$ photocatalyst.[84]

1.4. Unique Properties and Strategies to Enhance the Photocatalytic Properties of Monoclinic $BiVO_4$

Despite the enormous potential of monoclinic $BiVO_4$-based photocatalytic materials and/or systems for APS applications, as has been previously discussed, up until now, the reported conversion efficiencies are still far below the expectation because of several disadvantages. First, monoclinic $BiVO_4$ usually possesses slow charge transfer ability, especially for transporting the electrons, which can be attributed to some self-trapping phenomenon and small electron polaron formation, which would obstruct the charge separation and thus lead to severe electron-hole recombination before they can reach the surface reactive sites.[61,139] The second issue is the absence of innate reactive sites on the surface of unmodified $BiVO_4$, thus making it unable to effectively catalyze the redox reactions.[21,140] In this case, most reported $BiVO_4$ photocatalysts exhibit great dependence on metal-based cocatalysts and/or surface defects in order to efficiently trigger some specific APS reactions.[8,76,105,117,141-144] Third, in addition to the former problem, $BiVO_4$ material tends to have small surface area due to the relatively large size of its particle, which is unfavorable for the adsorption/desorption kinetics of reactants onto the catalytic surface.[42] Fourth, the position of its CBM is relatively lower than the reduction potential of hydrogen evolution reaction (HER, E^0 = 0 V), which can be regarded as one of the most important APS reactions.[49,63] Hence, it is practically difficult for $BiVO_4$ to drive the HER, particularly in the heteregenous photocatalysis. Fortunately, it is possible for $BiVO_4$ to drive some other APS reduction reactions, especially the ORR for the production of H_2O_2, which is also a very crucial chemical with a ton of applications and potential (as an alternative green fuel), as mentioned earlier. In order to effectively address the aforementioned issues, it is important to understand the unique properties and potential of monoclinic $BiVO_4$ which are liable to exploitation, so we can design a superior $BiVO_4$-based photocatalyst for any APS applications.

1.4.1. Lattice Distortion

As previously mentioned, the visible-light-driven photocatalytic performance of monoclinic scheelite $BiVO_4$ is much higher compared to that of the tetragonal scheelite $BiVO_4$, even though they possess similar composition, elements, crystal structure, and band gap (around 2.3–2.4 eV).[42] The only difference between those two polymorphs is that the lattice of monoclinic $BiVO_4$ is greatly distorted compared to the tetragonal $BiVO_4$, thus suggesting that the lattice distortion of monoclinic $BiVO_4$ plays a critical role in regulating its excellent photocatalytic properties and performances.[45] While the tetragonal scheelite $BiVO_4$ exhibit a symmetrical crystal structure with one type of V−O bond and two types of Bi−O bonds, the monoclinic scheelite $BiVO_4$ manifests an asymmetric coordination environment with two types of V−O bonds and four types of Bi−O bonds.[46,54,61] The parameters of tetragonal $BiVO_4$ are $a = c = 5.1509$ Å, b = 11.730 Å, and $\alpha = \beta = \gamma = 90°$, which also indicate balanced symmetry constraints in the corresponding crystal lattice.[145] On the other hand, the distorted structure of monoclinic $BiVO_4$ can be further testified by surveying the lattice parameters of a typical monoclinic $BiVO_4$ crystal (a = 5.1966 Å, b = 11.7044 Å, c = 5.0935 Å, $\alpha = \gamma = 90°$, and β = 90.383°),[46,145] which are slightly different than those of tetragonal scheelite. This kind of lattice distortion can be attributed to the presence of sterically active lone pair electrons derived from the Bi $6s^2$ orbital, which is commonly encountered for Bi-based complex oxide materials.[50,146-150]

The actual role of lone pair distortions in structural chemistry has been studied and addressed many times over the past seven decades, in both molecular and solid-state chemistry.[151] Specifically for monoclinic scheelite $BiVO_4$, it has been reported by Stoltzfus et al. that lone-pair distortion causes the pronounced overlap of O 2p and Bi 6s orbitals,[151] as has been mentioned earlier. Yu et al. stated that greater hybridization between Bi 6s and O 2p orbitals in monoclinic $BiVO_4$ compared to that in tetragonal $BiVO_4$ enhances the photogenerated holes mobility.[145] In agreement to the previous notion, Zhao et al. proposed the occurrence of optical anisotropy near the absorption edge due to lone-pair distortion of the Bi 6s orbital, which will influence the charge carriers transportation rate.[152] Through some hybrid density functional theory (DFT) calculations, Kweon and Hwang examined and compared the [010] surface geometries and electronic structures of tetragonal and monoclinic scheelite $BiVO_4$.[153] They stated that the relatively more favorable hole formation in bulk tetragonal $BiVO_4$ may cause

retardation in hole transport to the surface and thus suppression of the hole to a certain extent, in comparison to the case of monoclinic $BiVO_4$

Generally, in order to characterize the lattice distortion within the crystal structure of monoclinic $BiVO_4$, Raman spectroscopy can be employed, because it can serve as a sensitive method for investigating the local structure, crystallization, and electronic properties of materials since it is possible to deduce the bonding states in the coordination polyhedral of the materials directly from the corresponding Raman vibrational spectrum.[145] In particular, by observing the Raman stretching frequency around 800-820 cm, (corresponding to the stretching mode of the shorter V–O bonds), the bond length of V−O can be estimated by using an empirical equation, suggested by Brown and Wu as well as Hardcastle and Wachs,[154,155] as follows:

$$\nu\ (cm^{-1}) = 21349 \exp\ (-1.9176\ R\ (Å)) \qquad (1\text{-}18)$$

where ν is the stretching Raman frequency for V−O and R is the estimated bond length of V−O. Based on the above functional relationship, the stretching Raman shift position would have an inverse relationship with the V−O bond length, which means that the higher the stretching frequency is, the smaller the metal−oxygen bond length would be. Even though it is not possible to extract the information about the Bi−O polyhedron from the Raman characterization, by considering the coordination state of Bi units, it can be predicted that the change in the V−O bond length would be canceled by the reverse change in the Bi−O bond length in order to balance the structure.[145] Accordingly, the increase in distortion degree can be characterized by the shrinking of V−O bonds and the elongation of Bi−O bonds within the local crystal structure of monoclinic $BiVO_4$.

Since lattice distortion of monoclinic $BiVO_4$ serves as the decisive factor for its superior photocatalytic performance, several researchers have attempted to control this distortion phenomenon by using various methods. Yu and Kudo devised a hydrothermal strategy for synthesizing monoclinic $BiVO_4$ with various morphologies, surface textures, and grain shapes, by which the structural distortion degree can be altered by simply adjusting the solution pH.[145] In another study, Thalluri et al. demonstrated the effect of calcination temperatures on the structural variations of the as-prepared monoclinic $BiVO_4$, suggesting the linear correlation of calcination temperature with the distortion degree as well as the photocatalytic water oxidation activity.[156] In particular, both aforementioned studies correlate the lattice distortion effect with the hybridization of Bi 6s and O 2p orbitals near the VBM of monoclinic $BiVO_4$.[145,156] Furthermore, it is also said that the

greater the degree of distortion, the more Bi 6s and O 2p orbitals would overlap, which might enable more efficient transfer of photogenerated holes between both orbitals and reduce the hole effective mass, and as a consequence, it would elevate the photogenerated holes migration rate to the catalytic surface and suppress the charge carriers recombination.[145,148,150,156] Nonetheless, considering the substantial effect of lattice distortion on the photocatalytic activity of monoclinic $BiVO_4$, we believe that there is much more to it than that which has not been unraveled yet and thus will require further in-depth study and comprehensive investigation, especially since the research reports and literatures about this lattice distortion phenomenon on monoclinic $BiVO_4$ are relatively still limited.

1.4.2. 2D Layered Structure

$BiVO_4$ is included in the big family of bismuth-based materials, which usually possess layered crystals with either stacking van der Waals layers (e.g., BiOCl, BiOBr, and BiOI) or chemically bonded layer stacks (e.g., Bi_2WO_6, Bi_2MoO_6, and $BiVO_4$), with alternating stacks of $[Bi_2O_2]^{2+}$ slabs and some other (2−) anionic slabs.[65] Correspondingly, the crystal structure of $BiVO_4$ is constructed by alternate stacking of $[Bi_2O_2]^{2+}$ slabs and $[V_2O_6]^{2-}$slabs with oxygen atoms shared between slabs to create chemical bonds. Accordingly, monoclinic $BiVO_4$ exhibits some potential to manifest the 2D layered structure.[157] In these recent years, 2D structured materials, especially with ultrathin thickness, have aroused widespread research interest, owing to their unique structural features, photoelectric properties, and enormous potential for further innovations.[65,158,159] In general, by modifying the morphology of certain material into 2D, the corresponding specific surface area can be expected to increase dramatically, and thus, more surface reactive sites will be exposed, which are very beneficial for accelerating the catalytic reaction kinetics.[76,160] Moreover, when the thickness of a 2D semiconductor further decreases (especially to ultrathin scale), it will also reduce the required migration distance for the charge carriers to reach the active catalytic surface, thus efficiently preventing the recombination process.[144] It has also been reported that the photocatalytic water oxidation activity of $BiVO_4$ is proportionally correlated with the exposed surfaces of the (040) facet, as illustrated in **Figure 1.8 a**.[157] Profiting from these features, morphology and dimensional assembly of monoclinic $BiVO_4$ into some 2D structures would be an effective strategy to modulate its photocatalytic properties and performance.

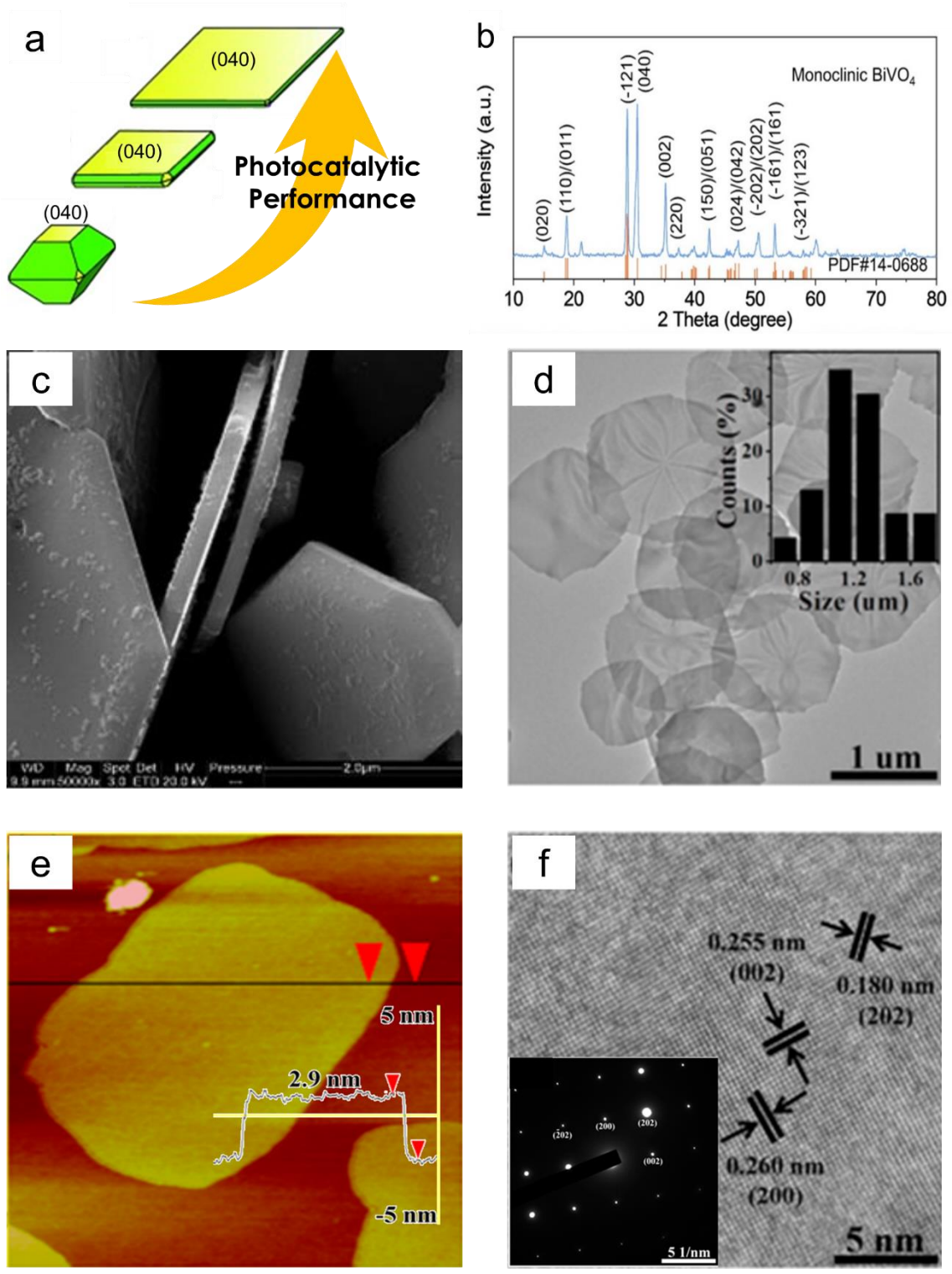

Figure 1.8. (a) Schematic illustration about the effect of exposed (040) facet on photocatalytic performance of monoclinic $BiVO_4$,[157] (b) typical XRD pattern of 2D monoclinic $BiVO_4$ with an intensive (040) peak,[159] (c) SEM image of 2D nanoplate monoclinic $BiVO_4$,[157] (d) TEM, (e) AFM and, (f) HR-TEM image of 2D nanosheet monoclinic $BiVO_4$.[144] The inset of (e) is the corresponding height profile and the inset of (f) is the corresponding SAED pattern.

In order to verify the successful formation of 2D structure over monoclinic $BiVO_4$ material, there are several analysis which can be employed. In a typical XRD spectrum of monoclinic $BiVO_4$ with a well-crystallized 2D structure, an intensive peak at $2\theta = 30.5°$ which corresponds to the (040) lattice planes of monoclinic $BiVO_4$ will be observed (see **Figure 1.8 b**), indicating the preferential crystal orientation along the [010] direction and more exposed (010) facets.[144,157,159] Some basic microscopy techniques, such as SEM, TEM, and AFM can also be utilized to inspect the morphology of the as-prepared $BiVO_4$ material, where we should be able to observe a clear 2D plate, sheet, disc, or flake-like structure, as representated in **Figure 1.8 c-e**.[44,76,144,157,159,161-163] In addition, **Figure 1.8 f** shows an example of well taken HR-TEM image of 2D monoclinic $BiVO_4$ material, whereby we will be able to discern some interplanar d-spacings of 0.255, 0.260, 0.181, and 0.182 nm which are consistent to the (002), (200), (202), and (−202) crystallographic facets of monoclinic $BiVO_4$, respectively, as also ascertained with the corresponding selected area electron diffraction (SAED).[144,159]

Unfortunately, the venture to tailor monoclinic $BiVO_4$ into 2D nanostructures is still challenging, due to the lacking of intrinsic driving force for 2D anisotropic growth.[144] In order to do that, some strategies have been developed, such as usage of directing agent, pH adjustment, template synthesis self-assembly process, anion exchange, colloidal synthesis, etc.[44,76,144,157,159,162-165] Wang et al. utilized $TiCl_3$ as directing agent and controlled the solution pH for synthesizing monoclinic $BiVO_4$ crystals with highly exposed (040) facets (**Figure 1.9 a**).[165] In similar fashion, Zhang et al. reported the morphology directing effect of halide ions (Cl^-, Br^-, I^-) to induce preferential growth along the [010] direction over monoclinic $BiVO_4$ crystal.[21] For the hydrothermal fabrication method, the pH of the reactant solution is found to be crucial for governing the resulting morphology of the synthesized monoclinic $BiVO_4$ photocatalyst.[44,163] For example, Xi and Ye demonstrates that only at pH 6.15, the as-prepared monoclinic $BiVO_4$ would manifest the 2D nanoplates structure, whereas at other pH, it would form irregular large particles, hyperbranched microcrystals, polyhedral microcrystals, rod-like microcrystals, and nanorod structure (see **Figure 1.9 b**), by which the nanoplates $BiVO_4$ exhibits the best photocatalytic properties compared to the other morphologies.[44]

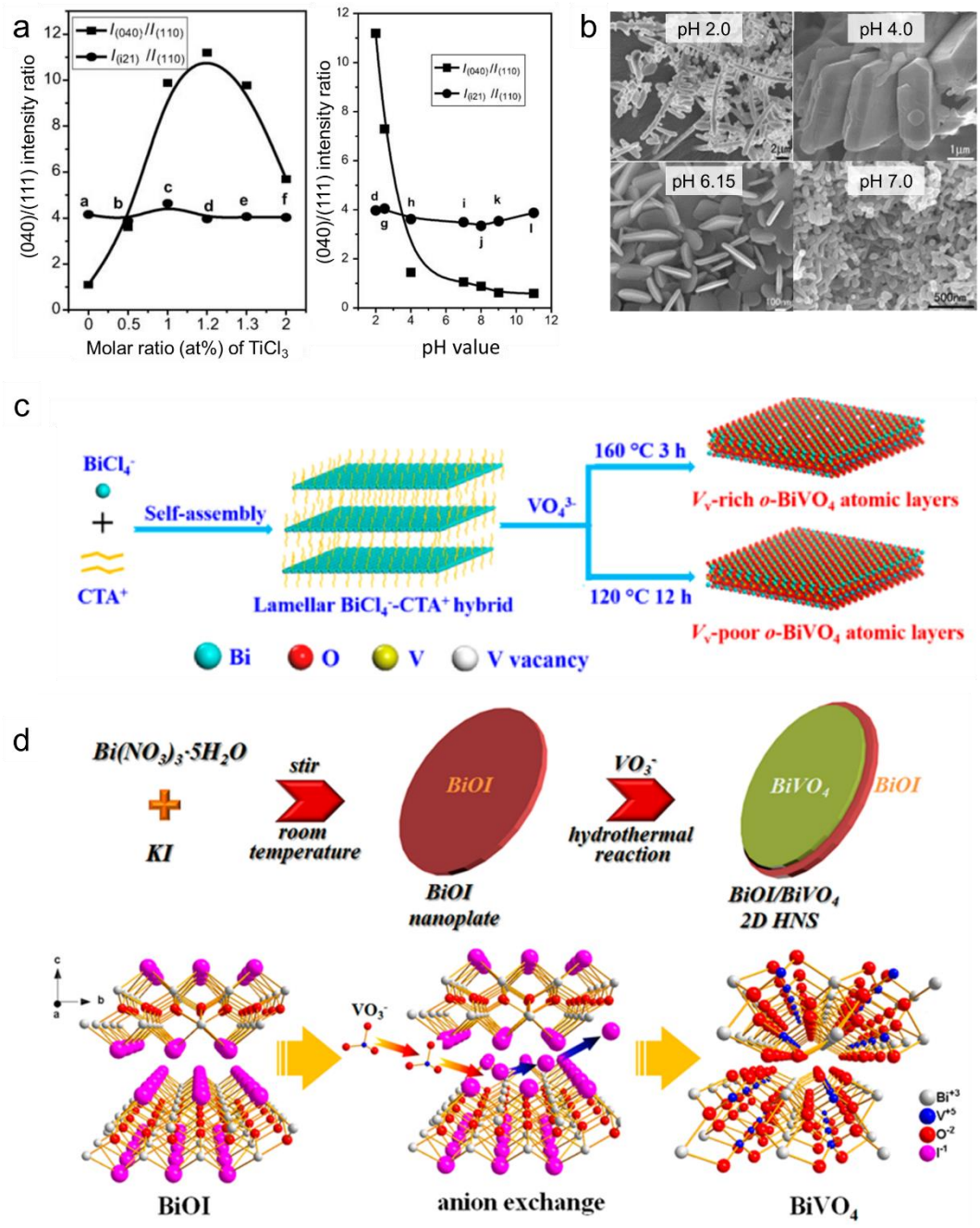

Figure 1.9. (a) Effects of the $TiCl_3$ molar ratio (to Bi) and pH value on the intensity ratios of (040)/(110) and (121)/(110) in the XRD patterns of the monoclinic $BiVO_4$ samples.[157] (b) effect of hydrothermal solution pH on the morphology of monoclinic $BiVO_4$ photocatalyst,[44] (c) schematic illustration for the $BiVO_4$ atomic layer preparation by template synthesis self-assembly strategy,[76] (d) schematic process of the hydrothermal anion exchange for synthesizing BiOI-$BiVO_4$ 2D nanocomposite.[164]

Gao et al. employed CTAB to react with $BiCl_3$ to create an artificial lamellar $BiCl_4^-$–CTA^+ hybrid precursor through the self-assembly process, which would serve as the

template for the fabrication of 2D $BiVO_4$ photocatalyst (**Figure 1.9 c**).[76] After the introduction of Na_3VO_4 followed by the hydrothermal process, $BiCl_4^-$–CTA^+ precursor would react with the VO_4^{3+} and self-exfoliate into $BiVO_4$ nanolayers with a thickness of around 1.28 nm, which displays an outstanding CO_2 photoreduction performance, with methanol formation rate of 398.3 mmol g^{-1} h^{-1}. Li et al. utilized ethanolamine which would act as a pH regulator to intrigue the exposure of [010] planes of $BiVO_4$ as well as a crosslinking agent to fabricate an aerogel 2D composite of $BiVO_4$ nanoplates and reduced graphene oxide sheets, which could exhibit enhanced photocatalytic performance and in both the O_2 evolution from water and the oxidation of phenol.[162] In another study, a colloidal synthesis route using oleic acid, oleylamine and octadecene has been successfully applied to prepare oxygen defective ultrathin monoclinic $BiVO_4$ nanosheets with an average thickness of ~2.9–3.0 nm.[144,159] The as-prepared $BiVO_4$ ultrathin nanosheets can display good photocatalytic OER performance over $AgNO_3$ solution with a high AQE of 26.1% (at 420 nm). Ni et al. has successfully prepared a smart BiOI/$BiVO_4$ 2D heteronanostructure by virtue of the facile anion-exchange technique.[164] The in-situ growth of 2D $BiVO_4$ on the scaffolds of $BiVO_4$ nanoplates can be prompted by active exchange between I^- and VO_3^- during hydrothermal treatment at 160 °C for 12 h (as illustrated in **Figure 1.9 d**), endowing the optimized sample with superior photocatalytic performances for the degradation of Rhodamine B and salicylic acid.

1.4.3. Selective Metal Photodeposition

Some early investigations on crystal facet engineering of semiconductors have unraveled the possible photogenerated charge separation into different crystal facets, in a way that certain facets favor reduction reactions, while the other facets prefer oxidation reactions.[102,103,166-168] However, for some semiconductor, such as TiO_2, contradictory conclusions regarding reduction and oxidation facets can be found from different literatures. For instance, some early reports suggested the preferred oxidation reaction on the rutile (011) and anatase (001) facets, while the rutile (110) and anatase (101) facets offered the sites for reduction reaction.[169-172] Nevertheless, some other references observed higher photocatalytic organic degradation activity on anatase nanocrystals with well-faceted (101) surfaces than that of (001) facets, indicating that the (101) facets of TiO_2 anatase might also be able to receive holes and thus catalyze the oxidation reaction.[173-175] In the case of metal deposition, while Farneth et al. observed the photoreduction of Ag metal nanoparticles on the (110) surface of TiO_2,[176] in contrast,

Hotsenpiller et al. reported that Ag particles were photodeposited at higher velocity on the (001) and (011) facets than on the (110) and (010) facets.[177] A possible explanation for the above mentioned conflicting findings is that the reaction selectivity on different facets is also influenced by the adsorption/desorption behaviors of reactant molecules and reaction intermediates on different facets.[103,178,179]

Interestingly, many reports have shown conclusive and similar findings concerning the photodeposition of various metals over monoclinic $BiVO_4$ surfaces, especially the well-faceted one.[64,102,103,117] The first complete report and study about this issue was provided by Li et al.,[103] where they observed the selective photodeposition of reduction and oxidation cocatalysts over the (010) and (011)/(110) crystal facets of monoclinic $BiVO_4$, respectively, as the result of spatial charge-carrier separation, as illustrated in **Figure 1.10 a**. Initially, the authors demonstrated that noble metals with high reduction potential, i.e. Au, Pt, and Ag metal were selectively deposited on the (010) facets of monoclinic $BiVO_4$ through photoreduction from both anionic $[AuCl_4]^-$, $[PtCl_6]^{2-}$ and cationic Ag^+ precursors. On the other hand, transition metal oxide (with relatively low reduction potential), such as MnO_x and PbO_2 were selectively formed on the (011)/(110) facets through photooxidation of Mn^{2+} and Pb^{2+} cations, respectively (see **Figure 1.10 b**). These phenomena happened not only when oxidative/reductive photodeposition was performed separately but also when they were carried out simultaneously, as can be seen in **Figure 1.10 c**, further affirming the spatial charge separation nature of monoclinic $BiVO_4$, where the photogenerated electrons and holes would be transferred and accumulated on (010) and (011)/(110) facets, respectively. Although several precursors of Mn^{2+} ($MnCl_2$, $Mn(NO_3)_2$, and $MnSO_4$) were used for MnO_x photodeposition, similar structure directed photodeposition tendency was observed. Compared to the products derived from impregnation method with uniform distribution of metals and metal oxide, the monoclinic $BiVO_4$ loaded with Pt and MnO_x via photodeposition process demonstrated a significantly higher photocatalytic water oxidation, thus emphasizing the superiority of selective photodeposition method. A year later, the same group extended the study, where they attempted to further improve the photocatalytic performance by utilizing the Co species as the oxidation cocatalyst.[102] As expected, the Co^{2+} cations (from $Co(NO_3)_2$) which belongs to the transition metal group, were oxidized and loaded as Co_3O_4 over the (011)/(110) oxidation facets upon light illumination.

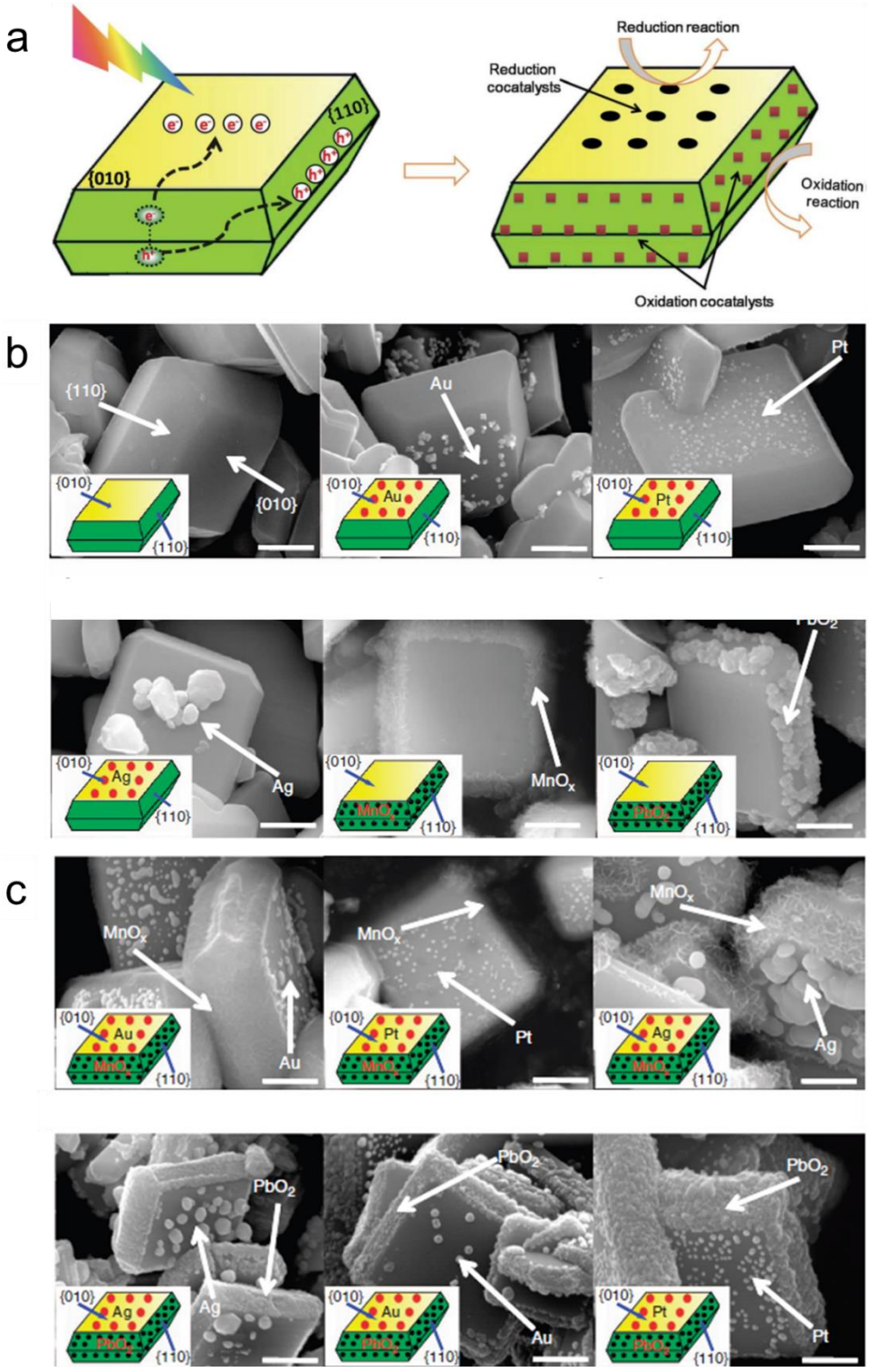

Figure 1.10. (a) Schematic illustration of spatial charge separation between different facets of monoclinic $BiVO_4$ resulting in selective photodeposition of reduction and oxidation metal cocatalysts on (010) and (110) facets, respectively,[102] (b) SEM images of single metal and (c) dual metal (simulatenously) photodeposited on the respective facets of monoclinic $BiVO_4$ (reduction cocatalysts: Au, Pt, and Ag; oxidation cocatalysts: MnO_x and PbO_2).[103]

Through a comprehensive density functional theory (DFT) study, Liu et al. proposed some explanation regarding this spatial charge separation nature of monoclinic $BiVO_4$, where they monitored the photogenerated charge migration in $BiVO_4$ by employing the formalism of DFT with Hubbard U corrections and Marcus/Holstein theory using a small polaron model.[64] It was found that for the exposed facets of (010) and (110), the mobility of electrons along [010] is five orders of magnitude larger than that of the [110] direction and the mobility of holes along [110] is two orders of magnitude larger than that of the [010] direction. Accordingly, they suggested that there is a parallel relationship between the carrier mobility along the crystal axis and the charge carrier preferred accumulation on the corresponding crystal facets of monoclinic $BiVO_4$. Following these above-mentioned pioneer works, many other authors have tried to exploit this special feature, for synthesizing superior metal/metal oxide-monoclinic $BiVO_4$ composites for various photocatalytic applications. For example, Qi et al. demonstrated significantly enhanced water oxidation on the particulate $BiVO_4$ photocatalyst via in situ facet-selective photodeposition of dual-cocatalysts that exist separately as metallic Ir nanoparticles and nanocomposite of FeOOH and CoOOH (denoted as $FeCoO_x$).[117] Very recently, a rationally designed monoclinic $BiVO_4$-based system for efficient overall photocatalytic H_2O_2 generation was reported, where the authors employed faceted Mo-doped $BiVO_4$ particles as light absorber and selectively loaded CoO_x (water oxidation cocatalyst) and Pd (oxygen reduction cocatalyst) on the (110) and (010) facets, respectively.[8]

1.5. Thesis Motivation and Organization

Artificial photosynthesis for the production of renewable energy stocks has been regarded as one of the most essential and effective strategies for tackling the global energy crisis and environmental problems. In order to design an efficient photocatalyst, several principal criteria should be considered and administered properly, i.e. light absorption (with the priority of visible light, near-infrared, and infrared), thermodynamic boundaries, charge carrier separation, and existence of surface reactive sites. Accordingly, monoclinic $BiVO_4$ has attracted growing interest as a promising photocatalyst candidate with abundant potentials, due to its visible light absorption ability, non-toxicity, plentiful abundance, low cost, good photostability, and favorable band position (especially for driving oxidation reactions). In this regard, diverse photocatalytic applications have been studied and reported over monoclinic $BiVO_4$-based materials. Despite its advantages and immense potentials, the conventional monoclinic $BiVO_4$ still exhibits some drawbacks,

i.e. poor charge carrier separation efficiency, relatively low surface area, and the absence of innate reactive sites, which are responsible for the unsatisfactory photocatalytic performance of monoclinic $BiVO_4$. Concerning these issues, significant research efforts should be devoted to probing, modulating, and exploiting the intrinsic and unique properties of monoclinic $BiVO_4$, in order to accomplish some meaningful breakthroughs for developing and fabricating superior monoclinic $BiVO_4$-based photocatalysts.

Based on above-mentioned discussions, in this thesis, I focus on the rational design of some superior monoclinic $BiVO_4$ photocatalysts for highly efficient visible-light-driven photocatalysis. Several strategies, including structural engineering and surface modulation, are considered for monoclinic $BiVO_4$ in order to enhance the corresponding photocatalytic properties and performances. Correspondingly, two important photocatalytic applications are chosen as the target reactions: oxygen evolution reaction (OER) and H_2O_2 evolution via oxygen reduction reaction (ORR). Furthermore, some in-depth studies and theoretical investigations are also prompted to further enrich our understanding of the underlying mechanism. This dissertation is divided into five chapters. A summary of the remaining four chapters is described as follows:

Chapter 2 Lattice distortion engineering over ultrathin monoclinic $BiVO_4$ nanoflakes triggering AQE up to 69.4% in visible-light-driven water oxidation

Monoclinic $BiVO_4$ is often distinguished for its superior photocatalytic performance under visible light irradiation due to its relatively more distorted crystal structure compared to the tetragonal scheelite $BiVO_4$ (the other polymorph of $BiVO_4$ with a similar bandgap, however, with an orderly crystal structure). Surprisingly, there are only few research reports about the exploration and exploitation of this prominent lattice distortion effect, even though it holds the primary key to the enhanced photocatalytic properties of monoclinic $BiVO_4$. In addition to the lattice distortion feature, monoclinic $BiVO_4$ also exhibits some potential to manifest the 2D layered structure, which are beneficial for accelerating the catalytic reaction kinetics and improving the charge carrier mobility; these advantages will be further extended in the case of ultrathin scale. Nevertheless, the venture to tailor $BiVO_4$ into ultrathin 2D nanostructures encounters some extent of difficulty, due to its lacking of the intrinsic driving force for 2D anisotropic growth. These above-mentioned notions inspired me to devise and develop a facile strategy which enabled 2D structure tailoring and lattice distortion engineering simultaneously over monoclinic $BiVO_4$. The synergistic effects of ultrathin 2D features and lattice distortion

effect were expected to significantly enhance the photocatalytic properties of monoclinic $BiVO_4$ photocatalyst, thus promoting more efficient visible-light-driven OER performance.

Chapter 3 New insights into water oxidation reaction over (010) facet of monoclinic $BiVO_4$: Unravelling the key role of lattice distortion

As previously mentioned, lattice distortion of monoclinic $BiVO_4$ serves as the distinguishing factor for its superior photocatalytic water oxidation performance compared to other polymorphs. Based on the available (not so many) literatures, lattice distortion of monoclinic $BiVO_4$ is believed to positively affect the mobility of photogenerated holes, due to the hybridization of Bi 6s and O 2p orbitals. However, considering the major effect of lattice distortion on the photocatalytic activity of monoclinic $BiVO_4$, I believe that there is much more to it than that which has not been unraveled yet and thus will require further in-depth study and comprehensive investigation, specifically whether it has the access to dictate the surface catalytic behavior of $BiVO_4$ photocatalyst for catalyzing the OER process. Meanwhile, some other reports indicate the significance of exposing more (010) facet of monoclinic $BiVO_4$ in order to trigger the photocatalytic water oxidation more efficiently. In order to fill the knowledge gap between these issues, in this chapter, I attempted to investigate the OER process over (010) facet of monoclinic $BiVO_4$, with the aim to obtain more understanding of the connection between the lattice distortion and surface catalytic behavior of the corresponding (010) facet. Accordingly, the combination of experimental and theoretical studies would be a good strategy to produce more dependable results and conclusions. The insights from this work might provide some new hints into the rational design of monoclinic $BiVO_4$-based photocatalyst for driving more efficient photocatalytic water oxidation.

Chapter 4 Oxygen Vacancy-Mediated Size Engineering of Pd Cocatalyst over Monoclinic $BiVO_4$ for Visible-Light-Driven H_2O_2 Synthesis

Hydrogen peroxide (H_2O_2) has received much attention as an alternative liquid energy carrier since it is relatively more cost-effective and easily transportable. In this case, artificial photosynthesis of H_2O_2 from earth-abundant water and O_2 as resources can be regarded as a promising and ideal strategy. Monoclinic $BiVO_4$ is a good photocatalyst candidate for this purpose, due to its suitable band structure and relatively narrow band-gap (~2.4 eV). Unfortunately, pristine surface of monoclinic $BiVO_4$ has been reported to

be inactive for catalyzing the O_2 reduction into H_2O_2. With that being the case, the surface modulation strategy to generate external reactive sites by the means of cocatalyst loading might be an ideal approach for promoting solar-driven H_2O_2 production over monoclinic $BiVO_4$ photocatalyst. In addition to that, monoclinic $BiVO_4$ exhibits the spatial charge separation nature, thus enabling selective photodeposition of metal cocatalyst into a designated facet. However, this photodeposition method also comes with some shortcomings, especially the difficulty and complexity of controlling the size of photodeposited metal cocatalyst, which actually is the decisive factor for determining whether the surface reaction can proceed efficiently. In this chapter, Pd cocatalyst was selected to modify the surface of monoclinic $BiVO_4$ photocatalyst and provide the necessary reactive sites for the H_2O_2 evolution via ORR. In order to effectively control the size of Pd cocatalyst, some surface modulation technique by the means of oxygen vacancy introduction was executed. The surface oxygen vacancies were expected to facilitate an effective interaction between the (010) reduction surfaces of monoclinic $BiVO_4$ and the $PdCl_4^{2-}$ precursor, thus establishing well dispersed and downsized Pd cocatalyst. After some optimization, the resulting Pd/$BiVO_4$ composite might be able to demonstrate highly efficient photocatalytic H_2O_2 production, due to the existence of abundant active sites and enhanced charge carrier separation efficiency.

Chapter 5 General conclusions and future prospects

This chapter presents an overall summary and conclusion of this dissertation and gives the prospects for future work.

References

1. A. C. Benniston, A. Harriman (2008) Artificial photosynthesis. Mater. Today 11 (12):26-34. doi:10.1016/S1369-7021(08)70250-5

2. A. J. Bard, M. A. Fox (1995) Artificial Photosynthesis: Solar Splitting of Water to Hydrogen and Oxygen. Acc. Chem. Res. 28 (3):141-145. doi:10.1021/ar00051a007

3. V. Balzani, A. Credi, M. Venturi (2008) Photochemical Conversion of Solar Energy. ChemSusChem 1 (1-2):26-58. doi:10.1002/cssc.200700087

4. N. S. Lewis, D. G. Nocera (2006) Powering the planet: Chemical challenges in solar energy utilization. Proceedings of the National Academy of Sciences 103 (43):15729-15735. doi:10.1073/pnas.0603395103

5. J. Ran, M. Jaroniec, S.-Z. Qiao (2018) Cocatalysts in Semiconductor-based Photocatalytic CO_2 Reduction: Achievements, Challenges, and Opportunities. Adv. Mater. 30 (7):1704649. doi:10.1002/adma.201704649

6. M. Mikkelsen, M. Jørgensen, F. C. Krebs (2010) The Teraton Challenge. A Review of Fixation and Transformation of Carbon Dioxide. Energy Environ. Sci. 3 (1):43-81. doi:10.1039/B912904A

7. S. Chen, T. Takata, K. Domen (2017) Particulate Photocatalysts for Overall Water Splitting. Nat. Rev. Mater. 2 (10):17050. doi:10.1038/natrevmats.2017.50

8. T. Liu, Z. Pan, J. J. M. Vequizo, K. Kato, B. Wu, A. Yamakata, K. Katayama, B. Chen, C. Chu, K. Domen (2022) Overall Photosynthesis of H_2O_2 by an Inorganic Semiconductor. Nat. Commun. 13 (1):1034. doi:10.1038/s41467-022-28686-x

9. Z. Wang, C. Li, K. Domen (2019) Recent Developments in Heterogeneous Photocatalysts for Solar-Driven Overall Water Splitting. Chem. Soc. Rev. 48 (7):2109-2125. doi:10.1039/C8CS00542G

10. Y. Tachibana, L. Vayssieres, J. R. Durrant (2012) Artificial Photosynthesis for Solar Water-Splitting. Nat. Photonics 6 (8):511-518. doi:10.1038/nphoton.2012.175

11. J. Liu, Y. Zou, B. Jin, K. Zhang, J. H. Park (2019) Hydrogen Peroxide Production from Solar Water Oxidation. ACS Energy Lett. 4 (12):3018-3027. doi:10.1021/acsenergylett.9b02199

12. T. Hisatomi, K. Takanabe, K. Domen (2015) Photocatalytic Water-Splitting Reaction from Catalytic and Kinetic Perspectives. Catal. Lett. 145 (1):95-108. doi:10.1007/s10562-014-1397-z

13. D. Philo, H. El-Hosainy, S. Luo, H. Huang, F. Ichihara, J. Ye (2022) Artificial Photosynthesis: Fundamentals, Challenges, and Strategies. In: Wakayama Y, Ariga K (eds) System-Materials Nanoarchitectonics. Springer Japan, Tokyo, pp 233-263. doi:10.1007/978-4-431-56912-1_14

14. Y. Wang, H. Suzuki, J. Xie, O. Tomita, D. J. Martin, M. Higashi, D. Kong, R. Abe, J. Tang (2018) Mimicking Natural Photosynthesis: Solar to Renewable H_2 Fuel Synthesis by Z-Scheme Water Splitting Systems. Chem. Rev. 118 (10):5201-5241. doi:10.1021/acs.chemrev.7b00286

15. Section 10 - Solar (2013). In: Cleveland CJ, Morris C (eds) Handbook of Energy. Elsevier, Amsterdam, pp 405-450. doi:10.1016/B978-0-08-046405-3.00010-3

16. J. Zhang, S. Hu, Y. Wang (2014) A Convenient Method to Prepare a Novel Alkali Metal Sodium Doped Carbon Nitride Photocatalyst with a Tunable Band Structure. RSC Adv. 4 (108):62912-62919. doi:10.1039/C4RA11377B

17. A. Kudo, Y. Miseki (2009) Heterogeneous Photocatalyst Materials for Water Splitting. Chem. Soc. Rev. 38 (1):253-278. doi:10.1039/B800489G

18. K. Takanabe (2017) Photocatalytic Water Splitting: Quantitative Approaches toward Photocatalyst by Design. ACS Catal. 7 (11):8006-8022. doi:10.1021/acscatal.7b02662

19. R. Li, C. Li (2017) Chapter One - Photocatalytic Water Splitting on Semiconductor-Based Photocatalysts. In: Song C (ed) Advances in Catalysis, vol 60. Academic Press, pp 1-57. doi:10.1016/bs.acat.2017.09.001

20. L. Zhang, M. Jaroniec (2018) Toward designing semiconductor-semiconductor heterojunctions for photocatalytic applications. Appl. Surf. Sci. 430:2-17. doi:10.1016/j.apsusc.2017.07.192

21. Q. Zhang, M. Liu, W. Zhou, Y. Zhang, W. Hao, Y. Kuang, H. Liu, D. Wang, L. Liu, J. Ye (2021) A Novel Cl^- Modification Approach to Develop Highly Efficient Photocatalytic Oxygen Evolution over $BiVO_4$ with AQE of 34.6%. Nano Energy 81:105651. doi:10.1016/j.nanoen.2020.105651

22. Z. Wang, L. Wang (2018) Progress in Designing Effective Photoelectrodes for Solar Water Splitting. Chinese J. Catal. 39 (3):369-378. doi:10.1016/S1872-2067(17)62998-X

23. J. Yang, D. Wang, H. Han, C. Li (2013) Roles of Cocatalysts in Photocatalysis and Photoelectrocatalysis. Acc. Chem. Res. 46 (8):1900-1909. doi:10.1021/ar300227e

24. G. Dong, W. Ho, C. Wang (2015) Selective photocatalytic N_2 fixation dependent on g-C_3N_4 induced by nitrogen vacancies. J. Mater. Chem. A 3 (46):23435-23441. doi:10.1039/C5TA06540B

25. H. Pang, X. Meng, H. Song, W. Zhou, G. Yang, H. Zhang, Y. Izumi, T. Takei, W. Jewasuwan, N. Fukata, J. Ye (2019) Probing the role of nickel dopant in aqueous colloidal ZnS nanocrystals for efficient solar-driven CO_2 reduction. Appl. Catal. B 244:1013-1020. doi:10.1016/j.apcatb.2018.12.010

26. J. Rossmeisl, W. G. Bessler (2008) Trends in Catalytic Activity for SOFC Anode Materials. Solid State Ionics 178 (31):1694-1700. doi:10.1016/j.ssi.2007.10.016

27. A. B. Laursen, A. S. Varela, F. Dionigi, H. Fanchiu, C. Miller, O. L. Trinhammer, J. Rossmeisl, S. Dahl (2012) Electrochemical Hydrogen Evolution: Sabatier's Principle and the Volcano Plot. J. Chem. Educ. 89 (12):1595-1599. doi:10.1021/ed200818t

28. H. Pang, T. Masuda, J. Ye (2018) Semiconductor-Based Photoelectrochemical Conversion of Carbon Dioxide: Stepping Towards Artificial Photosynthesis. Chem. Asian J. 13 (2):127-142. doi:10.1002/asia.201701596

29. A. J. Medford, A. Vojvodic, J. S. Hummelshøj, J. Voss, F. Abild-Pedersen, F. Studt, T. Bligaard, A. Nilsson, J. K. Nørskov (2015) From The Sabatier Principle to A Predictive Theory of Transition-Metal Heterogeneous Catalysis. J. Catal. 328:36-42. doi:10.1016/j.jcat.2014.12.033

30. G. Zhao, Y. Sun, W. Zhou, X. Wang, K. Chang, G. Liu, H. Liu, T. Kako, J. Ye (2017) Superior Photocatalytic H_2 Production with Cocatalytic Co/Ni Species Anchored on Sulfide Semiconductor. Adv. Mater. 29 (40):1703258. doi:10.1002/adma.201703258

31. S. Wang, F. Ichihara, H. Pang, H. Chen, J. Ye (2018) Nitrogen Fixation Reaction Derived from Nanostructured Catalytic Materials. Adv. Funct. Mater. 28 (50):1803309. doi:10.1002/adfm.201803309

32. X. Hai, K. Chang, H. Pang, M. Li, P. Li, H. Liu, L. Shi, J. Ye (2016) Engineering the Edges of MoS_2 (WS_2) Crystals for Direct Exfoliation into Monolayers in Polar Micromolecular Solvents. J. Am. Chem. Soc. 138 (45):14962-14969. doi:10.1021/jacs.6b08096

33. P. Wang, S. Zhan, H. Wang, Y. Xia, Q. Hou, Q. Zhou, Y. Li, R. R. Kumar (2018) Cobalt phosphide nanowires as efficient co-catalyst for photocatalytic hydrogen evolution over $Zn_{0.5}Cd_{0.5}S$. Appl. Catal. B: Environ. 230:210-219. doi:10.1016/j.apcatb.2018.02.043

34. K. Chang, X. Hai, H. Pang, H. Zhang, L. Shi, G. Liu, H. Liu, G. Zhao, M. Li, J. Ye (2016) Targeted Synthesis of 2H- and 1T-Phase MoS_2 Monolayers for Catalytic Hydrogen Evolution. Adv. Mater. 28 (45):10033-10041. doi:10.1002/adma.201603765

35. J. Fu, C. Bie, B. Cheng, C. Jiang, J. Yu (2018) Hollow CoS_x Polyhedrons Act as High-Efficiency Cocatalyst for Enhancing the Photocatalytic Hydrogen Generation of g-C_3N_4. ACS Sustain. Chem. Eng. 6 (2):2767-2779. doi:10.1021/acssuschemeng.7b04461

36. Y. Attia, M. Samer (2017) Metal clusters: New era of hydrogen production. Renew. Sust. Energ. Rev. 79:878-892. doi:10.1016/j.rser.2017.05.113

37. W. Zhen, H. Gao, B. Tian, J. Ma, G. Lu (2016) Fabrication of Low Adsorption Energy Ni–Mo Cluster Cocatalyst in Metal–Organic Frameworks for Visible Photocatalytic Hydrogen Evolution. ACS Appl. Mater. Interfaces 8 (17):10808-10819. doi:10.1021/acsami.5b12524

38. M. Yamamoto, T. Yoshida, N. Yamamoto, T. Nomoto, Y. Yamamoto, S. Yagi, H. Yoshida (2015) Photocatalytic reduction of CO_2 with water promoted by Ag clusters in Ag/Ga_2O_3 photocatalysts. J. Mater. Chem. A 3 (32):16810-16816. doi:10.1039/C5TA04815J

39. W. Liu, L. Cao, W. Cheng, Y. Cao, X. Liu, W. Zhang, X. Mou, L. Jin, X. Zheng, W. Che, Q. Liu, T. Yao, S. Wei (2017) Single-Site Active Cobalt-Based Photocatalyst with a Long Carrier Lifetime for Spontaneous Overall Water Splitting. Angew. Chem. Int. Ed. 56 (32):9312-9317. doi:10.1002/anie.201704358

40. Y. Cao, S. Chen, Q. Luo, H. Yan, Y. Lin, W. Liu, L. Cao, J. Lu, J. Yang, T. Yao, S. Wei (2017) Atomic-Level Insight into Optimizing the Hydrogen Evolution Pathway over a Co_1-N_4 Single-Site Photocatalyst. Angew. Chem. Int. Ed. 56 (40):12191-12196. doi:10.1002/anie.201706467

41. G. Zhao, H. Liu, J. Ye (2018) Constructing and Controlling of Highly Dispersed Metallic Sites for Catalysis. Nano Today 19:108-125. doi:10.1016/j.nantod.2018.02.013

42. J. Yu, Y. Zhang, A. Kudo (2009) Synthesis and Photocatalytic Performances of $BiVO_4$ by Ammonia Co-Precipitation Process. J. Solid State Chem. 182 (2):223-228. doi:10.1016/j.jssc.2008.10.021

43. O. Monfort, G. Plesch (2018) Bismuth Vanadate-Based Semiconductor Photocatalysts: A Short Critical Review on the Efficiency and the Mechanism of Photodegradation of Organic Pollutants. Environmental Science and Pollution Research 25 (20):19362-19379. doi:10.1007/s11356-018-2437-9

44. G. Xi, J. Ye (2010) Synthesis of Bismuth Vanadate Nanoplates with Exposed {001} Facets and Enhanced Visible-Light Photocatalytic Properties. Chem. Commun. 46 (11):1893-1895. doi:10.1039/B923435G

45. S. Tokunaga, H. Kato, A. Kudo (2001) Selective Preparation of Monoclinic and Tetragonal $BiVO_4$ with Scheelite Structure and Their Photocatalytic Properties. Chem. Mater. 13 (12):4624–4628. doi:10.1021/cm0103390

46. W. I. F. David, A. M. Glazer, A. W. Hewat (1979) The Structure and Ferroelastic Phase Transition of $BiVO_4$. Phase Transit. 1 (2):155-169. doi:10.1080/01411597908213198

47. H. L. Tan, X. Wen, R. Amal, Y. H. Ng (2016) $BiVO_4$ {010} and {110} Relative Exposure Extent: Governing Factor of Surface Charge Population and Photocatalytic Activity. J. Phy. Chem. Let. 7 (7):1400-1405. doi:10.1021/acs.jpclett.6b00428

48. M. D. Bhatt, J. Y. Lee (2021) Theoretical Insights into the Mechanism of Oxygen Evolution Reaction (OER) on Pristine $BiVO_4$ (001) and $BiVO_4$ (110) Surfaces in Acidic Medium Both in the Gas and Solution (Water) Phases. Nanotechnology 32 (33):335401. doi:10.1088/1361-6528/abfcfd

49. Z.-F. Huang, L. Pan, J.-J. Zou, X. Zhang, L. Wang (2014) Nanostructured Bismuth Vanadate-Based Materials for Solar-Energy-Driven Water Oxidation: A Review on Recent Progress. Nanoscale 6 (23):14044-14063. doi:10.1039/C4NR05245E

50. M. A. Gaikwad, U. P. Suryawanshi, U. V. Ghorpade, J. S. Jang, M. P. Suryawanshi, J. H. Kim (2022) Emerging Surface, Bulk, and Interface Engineering Strategies on $BiVO_4$ for Photoelectrochemical Water Splitting. Small 18 (10):2105084. doi:10.1002/smll.202105084

51. J. H. Kim, J. S. Lee (2019) Elaborately Modified $BiVO_4$ Photoanodes for Solar Water Splitting. Adv. Mater. 31 (20):1806938. doi:10.1002/adma.201806938

52. Z. Wang, X. Huang, X. Wang (2019) Recent Progresses in the Design of $BiVO_4$-Based Photocatalysts for Efficient Solar Water Splitting. Catal. Today 335:31-38. doi:10.1016/j.cattod.2019.01.067

53. Y. Park, K. J. McDonald, K.-S. Choi (2013) Progress in Bismuth Vanadate Photoanodes for Use in Solar Water Oxidation. Chem. Soc. Rev. 42 (6):2321-2337. doi:10.1039/C2CS35260E

54. A. W. Sleight, H. y. Chen, A. Ferretti, D. E. Cox (1979) Crystal Growth and Structure of $BiVO_4$. Mater. Res. Bull. 14 (12):1571-1581. doi:10.1016/0025-5408(72)90227-9

55. A. Kudo, K. Omori, H. Kato (1999) A Novel Aqueous Process for Preparation of Crystal Form-Controlled and Highly Crystalline BiVO4 Powder from Layered Vanadates at Room Temperature and Its Photocatalytic and Photophysical Properties. J. Am. Chem. Soc. 121 (49):11459-11467. doi:10.1021/ja992541y

56. J. D. Bierlein, A. W. Sleight (1975) Ferroelasticity in $BiVO_4$. Solid State Commun. 16 (1):69-70. doi:10.1016/0038-1098(75)90791-7

57. D. Ke, T. Peng, L. Ma, P. Cai, K. Dai (2009) Effects of Hydrothermal Temperature on the Microstructures of $BiVO_4$ and Its Photocatalytic O_2 Evolution Activity under Visible Light. Inorg. Chem. 48 (11):4685-4691. doi:10.1021/ic900064m

58. A. Walsh, Y. Yan, M. N. Huda, M. M. Al-Jassim, S.-H. Wei (2009) Band Edge Electronic Structure of $BiVO_4$: Elucidating the Role of the Bi s and V d Orbitals. Chem. Mater. 21 (3):547-551. doi:10.1021/cm802894z

59. D. O. Scanlon, A. Walsh, B. J. Morgan, G. W. Watson (2008) An *ab initio* Study of Reduction of V2O5 through the Formation of Oxygen Vacancies and Li Intercalation. J. Phy. Chem. C 112 (26):9903-9911. doi:10.1021/jp711334f

60. A. Walsh, G. W. Watson, D. J. Payne, R. G. Edgell, J. Guo, P.-A. Glans, T. Learmonth, K. E. Smith (2006) Electronic Structure of the α and δ Phases of Bi_2O_3: A Combined *ab initio* and X-Ray Spectroscopy Study. Phys. Rev. B 73 (23):235104. doi:10.1103/PhysRevB.73.235104

61. J. K. Cooper, S. Gul, F. M. Toma, L. Chen, P.-A. Glans, J. Guo, J. W. Ager, J. Yano, I. D. Sharp (2014) Electronic Structure of Monoclinic $BiVO_4$. Chem. Mater. 26 (18):5365-5373. doi:10.1021/cm5025074

62. N. Khan, F. Stelo, G. H. C. Santos, L. M. Rossi, R. V. Gonçalves, H. Wender (2022) Recent Advances on Z-Scheme Engineered $BiVO_4$-based Semiconductor Photocatalysts for CO_2 Reduction: A Review. Appl. Surf. Sci. Adv. 11:100289. doi:10.1016/j.apsadv.2022.100289

63. M. S. Prévot, K. Sivula (2013) Photoelectrochemical Tandem Cells for Solar Water Splitting. J. Phy. Chem. C 117 (35):17879-17893. doi:10.1021/jp405291g

64. T. Liu, X. Zhou, M. Dupuis, C. Li (2015) The Nature of Photogenerated Charge Separation among Different Crystal Facets of $BiVO_4$ Studied by Density Functional Theory. Phys. Chem. Chem. Phys. 17 (36):23503-23510. doi:10.1039/C5CP04299B

65. J. Xiong, P. Song, J. Di, H. Li, Z. Liu (2019) Freestanding Ultrathin Bismuth-Based Materials for Diversified Photocatalytic Applications. J. Mater. Chem. A 7 (44):25203-25226. doi:10.1039/C9TA10144F

66. J. Hu, H. He, L. Li, X. Zhou, Z. Li, Q. Shen, C. Wu, A. M. Asiri, Y. Zhou, Z. Zou (2019) Highly Symmetrical, 24-Faceted, Concave BiVO4 Polyhedron Bounded by

Multiple High-Index Facets for Prominent Photocatalytic O_2 Evolution under Visible Light. Chem. Commun. 55 (33):4777-4780. doi:10.1039/C9CC01366K

67. W. Han, H. Lin, F. Fang, Y. Zhang, K. Zhang, X. Yu, K. Chang (2021) The Effect of Fe(iii) Ions on Oxygen-Vacancy-Rich $BiVO_4$ on the Photocatalytic Oxygen Evolution Reaction. Catal. Sci. Technol. 11 (23):7598-7607. doi:10.1039/D1CY01559A

68. Y. Zhao, C. Ding, J. Zhu, W. Qin, X. Tao, F. Fan, R. Li, C. Li (2020) A Hydrogen Farm Strategy for Scalable Solar Hydrogen Production with Particulate Photocatalysts. Angew. Chem. Int. Ed. 59 (24):9653-9658. doi:10.1002/anie.202001438

69. P. Li, X. Chen, H. He, X. Zhou, Y. Zhou, Z. Zou (2018) Polyhedral 30-Faceted BiVO4 Microcrystals Predominantly Enclosed by High-Index Planes Promoting Photocatalytic Water-Splitting Activity. Adv. Mater. 30 (1):1703119. doi:10.1002/adma.201703119

70. S. Fukuzumi, Y.-M. Lee, W. Nam (2018) Solar-Driven Production of Hydrogen Peroxide from Water and Dioxygen. Chem. Eur. J. 24 (20):5016-5031. doi:10.1002/chem.201704512

71. H. Hirakawa, S. Shiota, Y. Shiraishi, H. Sakamoto, S. Ichikawa, T. Hirai (2016) Au Nanoparticles Supported on $BiVO_4$: Effective Inorganic Photocatalysts for H_2O_2 Production from Water and O_2 under Visible Light. ACS Catal. 6 (8):4976-4982. doi:10.1021/acscatal.6b01187

72. H. Shi, Y. Li, X. Wang, H. Yu, J. Yu (2021) Selective Modification of Ultra-thin g-C_3N_4 Nanosheets on the (110) Facet of Au/$BiVO_4$ for Boosting Photocatalytic H_2O_2 production. Appl. Catal. B 297:120414. doi:10.1016/j.apcatb.2021.120414

73. K. Fuku, R. Takioka, K. Iwamura, M. Todoroki, K. Sayama, N. Ikenaga (2020) Photocatalytic H_2O_2 Production from O_2 under Visible Light Irradiation over Phosphate Ion-Coated Pd Nanoparticles-Supported $BiVO_4$. Appl. Catal. B 272:119003. doi:10.1016/j.apcatb.2020.119003

74. H. Shi, Y. Li, K. Wang, S. Li, X. Wang, P. Wang, F. Chen, H. Yu (2022) Mass-Transfer Control for Selective Deposition of Well-Dispersed AuPd Cocatalysts to Boost Photocatalytic H_2O_2 Production of $BiVO_4$. Chem. Eng. J. 443:136429. doi:10.1016/j.cej.2022.136429

75. K. Wang, M. Wang, J. Yu, D. Liao, H. Shi, X. Wang, H. Yu (2021) $BiVO_4$ Microparticles Decorated with Cu@Au Core-Shell Nanostructures for Photocatalytic

H_2O_2 Production. ACS Appl. Nano Mater. 4 (12):13158-13166. doi:10.1021/acsanm.1c02688

76. S. Gao, B. Gu, X. Jiao, Y. Sun, X. Zu, F. Yang, W. Zhu, C. Wang, Z. Feng, B. Ye, Y. Xie (2017) Highly Efficient and Exceptionally Durable CO_2 Photoreduction to Methanol over Freestanding Defective Single-Unit-Cell Bismuth Vanadate Layers. J. Am. Chem. Soc. 139 (9):3438-3445. doi:10.1021/jacs.6b11263

77. L. Chen, M. Zhang, J. Yang, Y. Li, Y. Sivalingam, Q. Shi, M. Xie, W. Han (2019) Synthesis of $BiVO_4$ Quantum Dots/Reduced Graphene Oxide Composites for CO_2 Reduction. Mater. Sci. Semicond. Process. 102:104578. doi:10.1016/j.mssp.2019.06.013

78. Y. Liu, B. Huang, Y. Dai, X. Zhang, X. Qin, M. Jiang, M.-H. Whangbo (2009) Selective Ethanol Formation from Photocatalytic Reduction of Carbon Dioxide in Water with $BiVO_4$ Photocatalyst. Catal. Commun. 11 (3):210-213. doi:10.1016/j.catcom.2009.10.010

79. L. Huang, Z. Duan, Y. Song, Q. Li, L. Chen (2021) $BiVO_4$ Microplates with Oxygen Vacancies Decorated with Metallic Cu and Bi Nanoparticles for CO_2 Photoreduction. ACS Appl. Nano Mater. 4 (4):3576-3585. doi:10.1021/acsanm.1c00115

80. S. Yue, L. Chen, M. Zhang, Z. Liu, T. Chen, M. Xie, Z. Cao, W. Han (2021) Electrostatic Field Enhanced Photocatalytic CO_2 Conversion on $BiVO_4$ Nanowires. Nano-Micro Lett. 14 (1):15. doi:10.1007/s40820-021-00749-6

81. J. Mao, T. Peng, X. Zhang, K. Li, L. Zan (2012) Selective Methanol Production from Photocatalytic Reduction of CO_2 on $BiVO_4$ under Visible Light Irradiation. Catal. Commun. 28:38-41. doi:10.1016/j.catcom.2012.08.008

82. M. Sui, X. Gu (2022) Au Modified $BiVO_4$ Microparticles for Photocatalytic N_2 Fixation. Optoelectron. Lett. 18 (1):24-28. doi:10.1007/s11801-022-1023-z

83. G. Zhang, Y. Meng, B. Xie, Z. Ni, H. Lu, S. Xia (2021) Precise Location and Regulation of Active Sites for Highly Efficient Photocatalytic Synthesis of Ammonia by Facet-Dependent $BiVO_4$ Single Crystals. Appl. Catal. B 296:120379. doi:10.1016/j.apcatb.2021.120379

84. L. Wang, M. Li, S. Wang, T. Zhang, F. Li, L. Xu (2021) Enhanced Photocatalytic Nitrogen Fixation in $BiVO_4$: Constructing Oxygen Vacancies and Promoting Electron Transfer through Ohmic Contact. New J. Chem. 45 (47):22234-22242. doi:10.1039/D1NJ04580F

85. M. Kondo, H. Tatewaki, S. Masaoka (2021) Design of Molecular Water Oxidation Catalysts with Earth-Abundant Metal Ions. Chem. Soc. Rev. 50 (12):6790-6831. doi:10.1039/D0CS01442G

86. G. Ge, M. Liu, C. Liu, W. Zhou, D. Wang, L. Liu, J. Ye (2019) Ultrathin FeOOH Nanosheets as an Efficient Cocatalyst for Photocatalytic Water Oxidation. J. Mater. Chem. A 7 (15):9222-9229. doi:10.1039/C9TA01740B

87. J. Li, C. A. Triana, W. Wan, D. P. Adiyeri Saseendran, Y. Zhao, S. E. Balaghi, S. Heidari, G. R. Patzke (2021) Molecular and Heterogeneous Water Oxidation Catalysts: Recent Progress and Joint Perspectives. Chem. Soc. Rev. 50 (4):2444-2485. doi:10.1039/D0CS00978D

88. S. B. A. Hamid, S. J. Teh, C. W. Lai (2017) Photocatalytic Water Oxidation on ZnO: A Review. Catalysts 7 (3). doi:10.3390/catal7030093

89. J. K. Nørskov, J. Rossmeisl, A. Logadottir, L. Lindqvist, J. R. Kitchin, T. Bligaard, H. Jónsson (2004) Origin of the Overpotential for Oxygen Reduction at a Fuel-Cell Cathode. J. Phy. Chem. B 108 (46):17886-17892. doi:10.1021/jp047349j

90. A. Grimaud, A. Demortière, M. Saubanère, W. Dachraoui, M. Duchamp, M.-L. Doublet, J.-M. Tarascon (2016) Activation of surface oxygen sites on an iridium-based model catalyst for the oxygen evolution reaction. Nat. Energy 2 (1):16189. doi:10.1038/nenergy.2016.189

91. A. Grimaud, O. Diaz-Morales, B. Han, W. T. Hong, Y.-L. Lee, L. Giordano, K. A. Stoerzinger, M. T. M. Koper, Y. Shao-Horn (2017) Activating lattice oxygen redox reactions in metal oxides to catalyse oxygen evolution. Nat. Chem. 9 (5):457-465. doi:10.1038/nchem.2695

92. M. Zhang, M. de Respinis, H. Frei (2014) Time-Resolved Observations of Water Oxidation Intermediates on a Cobalt Oxide Nanoparticle Catalyst. Nat. Chem. 6 (4):362-367. doi:10.1038/nchem.1874

93. O. Zandi, T. W. Hamann (2016) Determination of Photoelectrochemical Water Oxidation Intermediates on Haematite Electrode Surfaces Using Operando Infrared Spectroscopy. Nat. Chem. 8 (8):778-783. doi:10.1038/nchem.2557

94. Q. Ding, Y. Liu, T. Chen, X. Wang, Z. Feng, X. Wang, M. Dupuis, C. Li (2020) Unravelling the Water Oxidation Mechanism on $NaTaO_3$-Based Photocatalysts. J. Mater. Chem. A 8 (14):6812-6821. doi:10.1039/C9TA14235E

95. J. Hu, X. Zhao, W. Chen, H. Su, Z. Chen (2017) Theoretical Insight into the Mechanism of Photoelectrochemical Oxygen Evolution Reaction on $BiVO_4$ Anode with Oxygen Vacancy. J. Phy. Chem. C 121 (34):18702-18709. doi:10.1021/acs.jpcc.7b05884

96. N. Sivasankar, W. W. Weare, H. Frei (2011) Direct Observation of a Hydroperoxide Surface Intermediate upon Visible Light-Driven Water Oxidation at an Ir Oxide Nanocluster Catalyst by Rapid-Scan FT-IR Spectroscopy. J. Am. Chem. Soc. 133 (33):12976-12979. doi:10.1021/ja205300a

97. R. Nakamura, A. Imanishi, K. Murakoshi, Y. Nakato (2003) In Situ FTIR Studies of Primary Intermediates of Photocatalytic Reactions on Nanocrystalline TiO_2 Films in Contact with Aqueous Solutions. J. Am. Chem. Soc. 125 (24):7443-7450. doi:10.1021/ja029503q

98. R. Nakamura, Y. Nakato (2004) Primary Intermediates of Oxygen Photoevolution Reaction on TiO_2 (Rutile) Particles, Revealed by in Situ FTIR Absorption and Photoluminescence Measurements. J. Am. Chem. Soc. 126 (4):1290-1298. doi:10.1021/ja0388764

99. J. Di, C. Chen, C. Zhu, M. Ji, J. Xia, C. Yan, W. Hao, S. Li, H. Li, Z. Liu (2018) Bismuth Vacancy Mediated Single Unit Cell Bi_2WO_6 Nanosheets for Boosting Photocatalytic Oxygen Evolution. Appl. Catal. B 238:119-125. doi:10.1016/j.apcatb.2018.06.066

100. S. Chen, S. Shen, G. Liu, Y. Qi, F. Zhang, C. Li (2015) Interface Engineering of a CoO_x/Ta_3N_5 Photocatalyst for Unprecedented Water Oxidation Performance under Visible-Light-Irradiation. Angew. Chem. Int. Ed. 54 (10):3047-3051. doi:10.1002/anie.201409906

101. K. Maeda, K. Ishimaki, Y. Tokunaga, D. Lu, M. Eguchi (2016) Modification of Wide-Band-Gap Oxide Semiconductors with Cobalt Hydroxide Nanoclusters for Visible-Light Water Oxidation. Angew. Chem. Int. Ed. 55 (29):8309-8313. doi:10.1002/anie.201602764

102. R. Li, H. Han, F. Zhang, D. Wang, C. Li (2014) Highly Efficient Photocatalysts Constructed by Rational Assembly of Dual-Cocatalysts Separately on Different Facets of $BiVO_4$. Energy Environ. Sci. 7 (4):1369-1376. doi:10.1039/C3EE43304H

103. R. Li, F. Zhang, D. Wang, J. Yang, M. Li, J. Zhu, X. Zhou, H. Han, C. Li (2013) Spatial Separation of Photogenerated Electrons and Holes among {010} and {110} Crystal Facets of $BiVO_4$. Nat. Commun. 4 (1):1432. doi:10.1038/ncomms2401

104. X. Liang, J. Lin, X. Cao, W. Sun, J. Yang, B. Ma, Y. Ding (2019) Enhanced Photocatalytic Activity of $BiVO_4$ Coupled with Iron-Based Complexes for Water Oxidation under Visible Light Irradiation. Chem. Commun. 55 (17):2529-2532. doi:10.1039/C8CC09807G

105. Y. Zhang, L. Shi, Z. Geng, T. Ren, Z. Yang (2019) The Improvement of Photocatalysis O_2 Production over $BiVO_4$ with Amorphous FeOOH Shell Modification. Sci. Rep. 9 (1):19090. doi:10.1038/s41598-019-54940-2

106. O. Tomita, S. Nitta, Y. Matsuta, S. Hosokawa, M. Higashi, R. Abe (2016) Improved Photocatalytic Water Oxidation with Fe^{3+}/Fe^{2+} Redox on Rectangular-shaped WO_3 Particles with Specifically Exposed Crystal Faces via Hydrothermal Synthesis. Chem. Lett. 46 (2):221-224. doi:10.1246/cl.160950

107. Q. Wang, T. Hisatomi, Q. Jia, H. Tokudome, M. Zhong, C. Wang, Z. Pan, T. Takata, M. Nakabayashi, N. Shibata, Y. Li, I. D. Sharp, A. Kudo, T. Yamada, K. Domen (2016) Scalable Water Splitting on Particulate Photocatalyst Sheets with a Solar-to-Hydrogen Energy Conversion Efficiency Exceeding 1%. Nat. Mater. 15 (6):611-615. doi:10.1038/nmat4589

108. H. Kato, Y. Sasaki, N. Shirakura, A. Kudo (2013) Synthesis of Highly Active Rhodium-Doped $SrTiO_3$ Powders in Z-Scheme Systems for Visible-Light-Driven Photocatalytic Overall Water Splitting. J. Mater. Chem. A 1 (39):12327-12333. doi:10.1039/C3TA12803B

109. S. Yoshino, K. Sato, Y. Yamaguchi, A. Iwase, A. Kudo (2020) Z-Schematic CO_2 Reduction to CO through Interparticle Electron Transfer between $SrTiO_3$:Rh of a Reducing Photocatalyst and $BiVO_4$ of a Water Oxidation Photocatalyst under Visible Light. ACS Applied Energy Materials 3 (10):10001-10007. doi:10.1021/acsaem.0c01684

110. Z.-H. Wei, Y.-F. Wang, Y.-Y. Li, L. Zhang, H.-C. Yao, Z.-J. Li (2018) Enhanced Photocatalytic CO_2 Reduction Activity of Z-Scheme CdS/$BiVO_4$ Nanocomposite with Thinner $BiVO_4$ Nanosheets. Journal of CO2 Utilization 28:15-25. doi:10.1016/j.jcou.2018.09.008

111. Q. Wang, T. Hisatomi, Q. Jia, H. Tokudome, M. Zhong, C. Wang, Z. Pan, T. Takata, M. Nakabayashi, N. Shibata, Y. Li, I. D. Sharp, A. Kudo, T. Yamada, K. Domen (2016) Scalable Water Splitting on Particulate Photocatalyst Sheets with A Solar-to-Hydrogen Energy Conversion Efficiency Exceeding 1%. Nat. Mater. 15:611. doi:10.1038/nmat4589

112. Q. Wang, Y. Li, T. Hisatomi, M. Nakabayashi, N. Shibata, J. Kubota, K. Domen (2015) Z-Scheme Water Splitting Using Particulate Semiconductors Immobilized onto Metal Layers for Efficient Electron Relay. J. Catal. 328:308-315. doi:10.1016/j.jcat.2014.12.006

113. R. Kobayashi, T. Takashima, S. Tanigawa, S. Takeuchi, B. Ohtani, H. Irie (2016) A heterojunction photocatalyst composed of zinc rhodium oxide, single crystal-derived bismuth vanadium oxide, and silver for overall pure-water splitting under visible light up to 740 nm. PCCP 18 (40):27754-27760. doi:10.1039/C6CP02903E

114. Q. Wang, T. Hisatomi, S. S. K. Ma, Y. Li, K. Domen (2014) Core/Shell Structured La- and Rh-Codoped $SrTiO_3$ as a Hydrogen Evolution Photocatalyst in Z-Scheme Overall Water Splitting under Visible Light Irradiation. Chem. Mater. 26 (14):4144-4150. doi:10.1021/cm5011983

115. A. Iwase, Y. H. Ng, Y. Ishiguro, A. Kudo, R. Amal (2011) Reduced Graphene Oxide as a Solid-State Electron Mediator in Z-Scheme Photocatalytic Water Splitting under Visible Light. J. Am. Chem. Soc. 133 (29):11054-11057. doi:10.1021/ja203296z

116. S. Chen, Y. Qi, T. Hisatomi, Q. Ding, T. Asai, Z. Li, S. S. K. Ma, F. Zhang, K. Domen, C. Li (2015) Efficient Visible-Light-Driven Z-Scheme Overall Water Splitting Using a $MgTa_2O_{6-x}N_y$ /TaON Heterostructure Photocatalyst for H_2 Evolution. Angew. Chem. Int. Ed. 54 (29):8498-8501. doi:doi:10.1002/anie.201502686

117. Y. Qi, J. Zhang, Y. Kong, Y. Zhao, S. Chen, D. Li, W. Liu, Y. Chen, T. Xie, J. Cui, C. Li, K. Domen, F. Zhang (2022) Unraveling of Cocatalysts Photodeposited Selectively on Facets of $BiVO_4$ to Boost Solar Water Splitting. Nat. Commun. 13 (1):484. doi:10.1038/s41467-022-28146-6

118. Y. Miseki, S. Fujiyoshi, T. Gunji, K. Sayama (2013) Photocatalytic Water Splitting under Visible Light Utilizing I_3^-/I^- and IO_3^-/I^- Redox Mediators by Z-Scheme System Using Surface Treated PtO_x/WO_3 as O_2 Evolution Photocatalyst. Catal. Sci. Technol. 3 (7):1750-1756. doi:10.1039/C3CY00055A

119. Y. Tachibana, L. Vayssieres, J. R. Durrant (2012) Artificial Photosynthesis for Solar Water-Splitting. Nat. Photonics 6:511. doi:10.1038/nphoton.2012.175

120. L. J. Thénard (1818) Observations sur des Nouvelles Combinaisons entre L'oxigène et Divers Acides. Ann. Phys. 8:306-312

121. J. M. Campos-Martin, G. Blanco-Brieva, J. L. G. Fierro (2006) Hydrogen Peroxide Synthesis: An Outlook beyond the Anthraquinone Process. Angew. Chem. Int. Ed. 45 (42):6962-6984. doi:10.1002/anie.200503779

122. H. Hou, X. Zeng, X. Zhang (2020) Production of Hydrogen Peroxide by Photocatalytic Processes. Angew. Chem. Int. Ed. 59 (40):17356-17376. doi:10.1002/anie.201911609

123. Y. Xue, Y. Wang, Z. Pan, K. Sayama (2021) Electrochemical and Photoelectrochemical Water Oxidation for Hydrogen Peroxide Production. Angew. Chem. Int. Ed. 60 (19):10469-10480. doi:10.1002/anie.202011215

124. R. L. Myers (2007) The 100 Most Important Chemical Compounds: A Reference Guide. ABC-CLIO,

125. S. Fukuzumi (2017) Production of Liquid Solar Fuels and Their Use in Fuel Cells. Joule 1 (4):689-738. doi:10.1016/j.joule.2017.07.007

126. K. Mase, M. Yoneda, Y. Yamada, S. Fukuzumi (2016) Seawater Usable for Production and Consumption of Hydrogen Peroxide as A Solar Fuel. Nat. Commun. 7 (1):11470. doi:10.1038/ncomms11470

127. E. Miglbauer, P. J. Wójcik, E. D. Głowacki (2018) Single-Compartment Hydrogen Peroxide Fuel Cells with Poly(3,4-ethylenedioxythiophene) Cathodes. Chem. Commun. 54 (84):11873-11876. doi:10.1039/C8CC06802J

128. Y. Yamada, M. Yoneda, S. Fukuzumi (2013) A Robust One-Compartment Fuel Cell with a Polynuclear Cyanide Complex as a Cathode for Utilizing H_2O_2 as a Sustainable Fuel at Ambient Conditions. Chem. Eur. J. 19 (35):11733-11741. doi:10.1002/chem.201300783

129. M. R. F. (MRFR) (2022) Hydrogen Peroxide Market: Information by Grade (Standard, Chemical, Aseptic, Semiconductor), Application (Bleaching, Oxidation, Environmental), End-Use Industry (Pulp & Paper, Chemicals, Textile, Food & Beverage), and Region — Forecast till 2027. MRFR/CnM/5927-HCR

130. H. Song, L. Wei, L. Chen, H. Zhang, J. Su (2020) Photocatalytic Production of Hydrogen Peroxide over Modified Semiconductor Materials: A Minireview. Top. Catal. 63 (9):895-912. doi:10.1007/s11244-020-01317-9

131. J. García-Serna, T. Moreno, P. Biasi, M. J. Cocero, J.-P. Mikkola, T. O. Salmi (2014) Engineering in Direct Synthesis of Hydrogen Peroxide: Targets, Reactors and Guidelines for Operational Conditions. Green Chemistry 16 (5):2320-2343. doi:10.1039/C3GC41600C

132. J. K. Edwards, G. J. Hutchings (2008) Palladium and Gold–Palladium Catalysts for the Direct Synthesis of Hydrogen Peroxide. Angew. Chem. Int. Ed. 47 (48):9192-9198. doi:10.1002/anie.200802818

133. Z. Haider, H.-i. Cho, G.-h. Moon, H.-i. Kim (2019) Minireview: Selective Production of Hydrogen Peroxide as a Clean Oxidant over Structurally Tailored Carbon Nitride Photocatalysts. Catal. Today 335:55-64. doi:10.1016/j.cattod.2018.11.067

134. A. J. Medford, M. C. Hatzell (2017) Photon-Driven Nitrogen Fixation: Current Progress, Thermodynamic Considerations, and Future Outlook. ACS Catal. 7 (4):2624-2643. doi:10.1021/acscatal.7b00439

135. S. Wang, F. Ichihara, H. Pang, H. Chen, J. Ye (2018) Nitrogen Fixation Reaction Derived from Nanostructured Catalytic Materials. Adv. Funct. Mater.:1803309. doi:10.1002/adfm.201803309

136. X. Chang, T. Wang, J. Gong (2016) CO_2 photo-reduction: insights into CO_2 activation and reaction on surfaces of photocatalysts. Energy Environ. Sci. 9 (7):2177-2196. doi:10.1039/C6EE00383D

137. C. J. H. Jacobsen, S. Dahl, B. S. Clausen, S. Bahn, A. Logadottir, J. K. Nørskov (2001) Catalyst Design by Interpolation in the Periodic Table: Bimetallic Ammonia Synthesis Catalysts. J. Am. Chem. Soc. 123 (34):8404-8405. doi:10.1021/ja010963d

138. B. M. Lindley, A. M. Appel, K. Krogh-Jespersen, J. M. Mayer, A. J. M. Miller (2016) Evaluating the Thermodynamics of Electrocatalytic N_2 Reduction in Acetonitrile. ACS Energy Lett. 1 (4):698-704. doi:10.1021/acsenergylett.6b00319

139. C. Feng, D. Wang, B. Jin, Z. Jiao (2015) The Enhanced Photocatalytic Properties of BiOCl/$BiVO_4$ p–n Heterojunctions via Plasmon Resonance of Metal Bi. RSC Adv. 5 (93):75947-75952. doi:10.1039/C5RA13886H

140. M. Oshikiri, M. Boero (2006) Water Molecule Adsorption Properties on the $BiVO_4$ (100) Surface. J. Phy. Chem. B 110 (18):9188-9194. doi:10.1021/jp0555100

141. M. Kaur, M. Chhetri, C. N. R. Rao (2020) Photoelectrochemical OER Activity by Employing $BiVO_4$ with Manganese Oxide Co-Catalysts. Phys. Chem. Chem. Phys. 22 (2):811-817. doi:10.1039/C9CP05293C

142. X. Meng, S. Xu, C. Zhang, P. Feng, R. Li, H. Guan, Y. Ding (2022) Prussian Blue Type Cocatalysts for Enhancing the Photocatalytic Water Oxidation Performance of $BiVO_4$. Chem. Eur. J. 28 (51):e202201407. doi:10.1002/chem.202201407

143. T. Palaniselvam, L. Shi, G. Mettela, D. H. Anjum, R. Li, K. P. Katuri, P. E. Saikaly, P. Wang (2017) Vastly Enhanced $BiVO_4$ Photocatalytic OER Performance by $NiCoO_2$ as Cocatalyst. Adv. Mater. Interfaces 4 (19):1700540. doi:10.1002/admi.201700540

144. C. Dong, S. Lu, S. Yao, R. Ge, Z. Wang, Z. Wang, P. An, Y. Liu, B. Yang, H. Zhang (2018) Colloidal Synthesis of Ultrathin Monoclinic $BiVO_4$ Nanosheets for Z-Scheme Overall Water Splitting under Visible Light. ACS Catal. 8 (9):8649-8658. doi:10.1021/acscatal.8b01645

145. J. Yu, A. Kudo (2006) Effects of Structural Variation on the Photocatalytic Performance of Hydrothermally Synthesized $BiVO_4$. Adv. Funct. Mater. 16 (16):2163-2169. doi:10.1002/adfm.200500799

146. K. Qin, Q. Zhao, H. Yu, X. Xia, J. Li, S. He, L. Wei, T. An (2021) A Review of Bismuth-Based Photocatalysts for Antibiotic Degradation: Insight into the Photocatalytic Degradation Performance, Pathways and Relevant Mechanisms. Environ. Res. 199:111360. doi:10.1016/j.envres.2021.111360

147. M. Xu, J. Yang, C. Sun, L. Liu, Y. Cui, B. Liang (2020) Performance Enhancement Strategies of Bi-Based Photocatalysts: A Review on Recent Progress. Chem. Eng. J. 389:124402. doi:10.1016/j.cej.2020.124402

148. J. Shi, E. A. Rubinstein, W. Li, J. Zhang, Y. Yang, T.-L. Lee, C. Qin, P. Yan, J. L. MacManus-Driscoll, D. O. Scanlon, K. H. L. Zhang (2022) Modulation of the Bi^{3+} $6s^2$ Lone Pair State in Perovskites for High-Mobility p-Type Oxide Semiconductors. Adv. Sci. 9 (6):2104141. doi:10.1002/advs.202104141

149. H. Kunioku, M. Higashi, O. Tomita, M. Yabuuchi, D. Kato, H. Fujito, H. Kageyama, R. Abe (2018) Strong Hybridization between Bi-6s and O-2p Orbitals in Sillén–Aurivillius Perovskite Bi_4MO_8X (M = Nb, Ta; X = Cl, Br), Visible Light Photocatalysts

Enabling Stable Water Oxidation. J. Mater. Chem. A 6 (7):3100-3107. doi:10.1039/C7TA08619A

150. A. Bhatia, G. Hautier, T. Nilgianskul, A. Miglio, J. Sun, H. J. Kim, K. H. Kim, S. Chen, G.-M. Rignanese, X. Gonze, J. Suntivich (2016) High-Mobility Bismuth-based Transparent p-Type Oxide from High-Throughput Material Screening. Chem. Mater. 28 (1):30-34. doi:10.1021/acs.chemmater.5b03794

151. M. W. Stoltzfus, P. M. Woodward, R. Seshadri, J.-H. Klepeis, B. Bursten (2007) Structure and Bonding in $SnWO_4$, $PbWO_4$, and $BiVO_4$: Lone Pairs vs Inert Pairs. Inorg. Chem. 46 (10):3839-3850. doi:10.1021/ic061157g

152. Z. Zhao, Z. Li, Z. Zou (2011) Electronic Structure and Optical Properties of Monoclinic Clinobisvanite $BiVO_4$. Phys. Chem. Chem. Phys. 13 (10):4746-4753. doi:10.1039/C0CP01871F

153. K. E. Kweon, G. S. Hwang (2013) Surface Structure and Hole Localization in Bismuth Vanadate: A First Principles Study. Appl. Phys. Lett. 103 (13):131603. doi:10.1063/1.4822270

154. I. D. Brown, K. K. Wu (1976) Empirical Parameters for Calculating Cation–Oxygen Bond Valences. Acta Crystallogr. Sect. B 32 (7):1957-1959. doi:10.1107/S0567740876006869

155. F. D. Hardcastle, I. E. Wachs (1991) Determination of Vanadium-Oxygen Bond Distances and Bond Orders by Raman Spectroscopy. J. Phys. Chem. 95 (13):5031-5041. doi:10.1021/j100166a025

156. S. M. Thalluri, C. Martinez Suarez, M. Hussain, S. Hernandez, A. Virga, G. Saracco, N. Russo (2013) Evaluation of the Parameters Affecting the Visible-Light-Induced Photocatalytic Activity of Monoclinic $BiVO_4$ for Water Oxidation. Ind. Eng. Chem. Res. 52 (49):17414-17418. doi:10.1021/ie402930x

157. D. Wang, H. Jiang, X. Zong, Q. Xu, Y. Ma, G. Li, C. Li (2011) Crystal Facet Dependence of Water Oxidation on $BiVO_4$ Sheets under Visible Light Irradiation. Chem. Eur. J. 17 (4):1275-1282. doi:10.1002/chem.201001636

158. T. Wang, L. Liu, G. Ge, M. Liu, W. Zhou, K. Chang, F. Yang, D. Wang, J. Ye (2018) Two-Dimensional Titanium Oxide Nanosheets Rich in Titanium Vacancies as an Efficient Cocatalyst for Photocatalytic Water Oxidation. J. Catal. 367:296-305. doi:10.1016/j.jcat.2018.09.026

159. D. Yao, C. Dong, Q. Bing, Y. Liu, F. Qu, M. Yang, B. Liu, B. Yang, H. Zhang (2019) Oxygen-Defective Ultrathin $BiVO_4$ Nanosheets for Enhanced Gas Sensing. ACS Appl. Mater. Interfaces 11 (26):23495-23502. doi:10.1021/acsami.9b05626

160. S. Zhang, S. Guo, Z. Chen, Y. Wang, H. Gao, J. Gómez-Herrero, P. Ares, F. Zamora, Z. Zhu, H. Zeng (2018) Recent Progress in 2D Group-VA Semiconductors: from Theory to Experiment. Chem. Soc. Rev. 47 (3):982-1021. doi:10.1039/C7CS00125H

161. P. Cai, S.-M. Zhou, D.-K. Ma, S.-N. Liu, W. Chen, S.-M. Huang (2015) Fe_2O_3-Modified Porous $BiVO_4$ Nanoplates with Enhanced Photocatalytic Activity. Nano-Micro Lett. 7 (2):183-193. doi:10.1007/s40820-015-0033-9

162. Y. Li, Z. Sun, S. Zhu, Y. Liao, Z. Chen, D. Zhang (2015) Fabrication of $BiVO_4$ Nanoplates with Active Facets on Graphene Sheets for Visible-Light Photocatalyst. Carbon 94:599-606. doi:10.1016/j.carbon.2015.07.042

163. L. Ren, L. Ma, L. Jin, J.-B. Wang, M. Qiu, Y. Yu (2009) Template-Free Synthesis of $BiVO_4$ Nanostructures: II. Relationship between Various Microstructures for Monoclinic $BiVO_4$ and Their Photocatalytic Activity for the Degradation of Rhodamine B under Visible Light. Nanotechnology 20 (40):405602. doi:10.1088/0957-4484/20/40/405602

164. S. Ni, T. Zhou, H. Zhang, Y. Cao, P. Yang (2018) BiOI/$BiVO_4$ Two-Dimensional Heteronanostructures for Visible-Light Photocatalytic Degradation of Rhodamine B. ACS Appl. Nano Mater. 1 (9):5128-5141. doi:10.1021/acsanm.8b01161

165. L. J. Wang, J. Y. Bai, Y. J. Zhang, F. Mao, Y. Liu, H. Yuan, P. F. Liu, H. G. Yang (2020) Controllable Synthesis of Conical $BiVO_4$ for Photocatalytic Water Oxidation. J. Mater. Chem. A 8 (5):2331-2335. doi:10.1039/C9TA12122F

166. G. Liu, J. C. Yu, G. Q. Lu, H.-M. Cheng (2011) Crystal Facet Engineering of Semiconductor Photocatalysts: Motivations, Advances and Unique Properties. Chem. Commun. 47 (24):6763-6783. doi:10.1039/C1CC10665A

167. J. Pan, G. Liu, G. Q. Lu, H.-M. Cheng (2011) On the True Photoreactivity Order of {001}, {010}, and {101} Facets of Anatase TiO_2 Crystals. Angew. Chem. Int. Ed. 50 (9):2133-2137. doi:10.1002/anie.201006057

168. H. G. Yang, C. H. Sun, S. Z. Qiao, J. Zou, G. Liu, S. C. Smith, H. M. Cheng, G. Q. Lu (2008) Anatase TiO_2 Single Crystals with a Large Percentage of Reactive Facets. Nature 453 (7195):638-641. doi:10.1038/nature06964

169. T. Ohno, K. Sarukawa, M. Matsumura (2002) Crystal Faces of Rutile and Anatase TiO_2 Particles and Their Roles in Photocatalytic Reactions. New J. Chem. 26 (9):1167-1170. doi:10.1039/B202140D

170. A. Selloni (2008) Anatase Shows its Reactive Side. Nat. Mater. 7 (8):613-615. doi:10.1038/nmat2241

171. J. Zhu, S. Wang, Z. Bian, S. Xie, C. Cai, J. Wang, H. Yang, H. Li (2010) Solvothermally Controllable Synthesis of Anatase TiO_2 Nanocrystals with Dominant {001} Facets and Enhanced Photocatalytic Activity. CrystEngComm 12 (7):2219-2224. doi:10.1039/C000128G

172. X. H. Yang, Z. Li, G. Liu, J. Xing, C. Sun, H. G. Yang, C. Li (2011) Ultra-Thin Anatase TiO_2 Nanosheets Dominated with {001} Facets: Thickness-Controlled Synthesis, Growth Mechanism and Water-Splitting Properties. CrystEngComm 13 (5):1378-1383. doi:10.1039/C0CE00233J

173. N. Murakami, Y. Kurihara, T. Tsubota, T. Ohno (2009) Shape-Controlled Anatase Titanium(IV) Oxide Particles Prepared by Hydrothermal Treatment of Peroxo Titanic Acid in the Presence of Polyvinyl Alcohol. J. Phy. Chem. C 113 (8):3062-3069. doi:10.1021/jp809104t

174. N. Wu, J. Wang, D. N. Tafen, H. Wang, J.-G. Zheng, J. P. Lewis, X. Liu, S. S. Leonard, A. Manivannan (2010) Shape-Enhanced Photocatalytic Activity of Single-Crystalline Anatase TiO_2 (101) Nanobelts. J. Am. Chem. Soc. 132 (19):6679-6685. doi:10.1021/ja909456f

175. C. H. Cho, M. H. Han, D. H. Kim, D. K. Kim (2005) Morphology Evolution of Anatase TiO_2 Nanocrystals under a Hydrothermal Condition (pH=9.5) and Their Ultra-High Photo-Catalytic Activity. Mater. Chem. Phys. 92 (1):104-111. doi:j.matchemphys.2004.12.036

176. W. E. Farneth, R. S. McLean, J. D. Bolt, E. Dokou, M. A. Barteau (1999) Tapping Mode Atomic Force Microscopy Studies of the Photoreduction of Ag^+ on Individual Submicrometer TiO_2 Particles. Langmuir 15 (25):8569-8573. doi:10.1021/la9908844

177. P. A. Morris Hotsenpiller, J. D. Bolt, W. E. Farneth, J. B. Lowekamp, G. S. Rohrer (1998) Orientation Dependence of Photochemical Reactions on TiO_2 Surfaces. J. Phy. Chem. B 102 (17):3216-3226. doi:10.1021/jp980104k

178. C. G. Read, E. M. P. Steinmiller, K.-S. Choi (2009) Atomic Plane-Selective Deposition of Gold Nanoparticles on Metal Oxide Crystals Exploiting Preferential Adsorption of Additives. J. Am. Chem. Soc. 131 (34):12040-12041. doi:10.1021/ja9036884

179. Y. Miseki, H. Kato, A. Kudo (2009) Water Splitting into H_2 and O_2 over Niobate and Titanate Photocatalysts with (111) Plane-Type Layered Perovskite Structure. Energy Environ. Sci. 2 (3):306-314. doi:10.1039/B818922F

Chapter 2. Lattice Distortion Engineering over Ultrathin Monoclinic $BiVO_4$ Nanoflakes Triggering AQE up to 69.4% in Visible-light-driven Water Oxidation

2.1. Introduction

As the global challenges of energy sustainability and drastic climate change become more critical, the solar-driven photocatalytic CO_2 reduction, water splitting, and N_2 fixation technologies for the production of clean and safe energy-containing chemicals are expected to step onto the stage as early as possible.[1-4] Nevertheless, the realization of these applications (fuel-forming reduction reactions) is greatly limited by the balancing reaction, i.e., water oxidation or oxygen evolution reaction (OER).[5,6] Due to its complex four-electron transfer process, unclear reaction mechanism, and sluggish reaction kinetics, designing a suitable and effective photocatalyst for achieving efficient water oxidation becomes quite a difficult task to accomplish, yet indispensable.[7-9]

Among many developments of photocatalytic materials, ultrathin 2D semiconductor nanomaterials have displayed excellent prospects for various photocatalytic applications owing to their unique 2D structural features and enormous potential for further innovations.[10-12] Bi-based materials usually possess layered crystals with either stacking van der Waals layers (e.g., BiOCl, BiOBr, and BiOI) or chemically bonded layer stacks (e.g., Bi_2WO_6, Bi_2MoO_6, and $BiVO_4$), which can facilitate the formation of ultrathin 2D structure.[11] Among other Bi-based materials, $BiVO_4$ stands out for its notable photocatalytic OER performance. In addition, it has been reported that the water oxidation activity of $BiVO_4$ is proportionally dependent on the degree of (040) facet exposure,[13] thus rendering ultrathin 2D $BiVO_4$ as an ideal OER photocatalyst. Unfortunately, the venture to tailor $BiVO_4$ into ultrathin 2D nanostructures encounters some extent of difficulty, due to its lacking of the intrinsic driving force for 2D anisotropic growth.[14,15]

It has been widely known that $BiVO_4$ possesses three types of crystal polymorphs: tetragonal zircon, tetragonal scheelite, and monoclinic scheelite.[16-18] Monoclinic scheelite $BiVO_4$ with an ideal bandgap of 2.4 eV is often distinguished for its superior photocatalytic performance under visible light irradiation due to its relatively more distorted crystal structure compared to the tetragonal scheelite $BiVO_4$ (the other

polymorph of $BiVO_4$ with a similar bandgap, however, with an orderly crystal structure).[18-20] This kind of structural variation is commonly encountered for Bi-based complex oxide due to the existence of lone pair electrons around the Bi $6s^2$ orbital.[16,20-24] Thalluri et al.[25] and Yu, Kudo[26] have separately reported the effect of lattice distortion degree over photocatalytic OER activities of prepared monoclinic $BiVO_4$ by controlling the calcination temperature and solution pH, respectively. However, the observed local structural variations are also accompanied by disparities in other vital properties such as morphology, particle size, optical bandgap, and degree of crystallinity, thus making it not easy to clarify the critical parameters which govern the overall photocatalytic water oxidation performance.

Here, in this work, we demonstrate a facile template-directed strategy to fabricate ultrathin 2D monoclinic $BiVO_4$ nanoflakes (BVO NFs) of about 2.3 nm with controlled lattice distortion, which was achieved through a simple introduction of sodium (Na^+) additive. Raman analysis and XRD Rietveld structure refinement indicate a greater degree of lattice distortion: the shrinking of V–O bonds and the elongation of the Bi–O bonds. The BVO NFs with more lattice distortion (BVO NFs A) demonstrated superior photocatalytic OER performances with remarkable apparent quantum efficiencies up to 69.4% over sacrificial Fe^{3+} solution. It is also unraveled through mechanistic investigations how the ultrathin 2D features and lattice distortion positively and synergistically affect the innate characteristics (charge carrier dynamics and surface properties) and overall photocatalytic OER performance of BVO NFs. In particular, the density functional theory (DFT) calculations emphasize the advantages of lattice distortion effect not only for enhancing the photogenerated holes transfer rate but also providing better wave function connection for the migration of electrons and delocalizing the electrons of the O 2p surficial state. This work provides critical insights into the morphology, dimension, and lattice distortion engineering in fabricating superior monoclinic $BiVO_4$ photocatalyst for efficient solar energy conversion.

2.2. Experimental section

2.2.1. Materials

Bismuth nitrate pentahydrate ($Bi(NO_3)_3 \cdot 5H_2O$, Guaranteed Reagent), D(−)-mannitol (Guaranteed Reagent), potassium bromide (KBr, Guaranteed Reagent), sodium metavanadate ($NaVO_3$, Practical Grade), ammonium metavanadate (NH_4VO_3,

Guaranteed Reagent), sodium bromide (NaBr, Guaranteed Reagent), sodium nitrate ($NaNO_3$, Guaranteed Reagent), lithium nitrate ($LiNO_3$, Wako Special Grade), silver nitrate ($AgNO_3$, Guaranteed Reagent), sodium sulfite (Na_2SO_3, Guaranteed Reagent), boric acid (H_3BO_3, Guaranteed Reagent), and potassium hydroxide (KOH, Guaranteed Reagent) were provided by FUJIFILM Wako Pure Chemical Corporation. Polyvinylpyrrolidone (PVP, MW: 10000) and potassium metavanadate (KVO_3, 98%) were purchased from Sigma-Aldrich. All chemicals were used directly as received without further purification. The ultrapure water with a resistivity of 18.2 MΩ cm^{-1} was supplied by a Millipore System (Millipore Q) and used in all experiments.

2.2.2. Preparation of $BiVO_4$ Photocatalysts

In general, ultrathin 2D monoclinic $BiVO_4$ nanoflakes (BVO NFs) were fabricated by a template-directed strategy through facile two-step hydrothermal treatment, as illustrated in **Figure 2.1**. Initially, BiOBr ultrathin nanosheets were prepared beforehand according to the reported procedure,[27,28] with slight modification. In detail, 5 mmol $Bi(NO_3)_3 \cdot 5H_2O$ and 1 g PVP (MW: 10000) were dissolved in sequence into 60 mL 0.075 M mannitol solution under magnetic stirring for about 30 min. Subsequently, 5 mmol KBr were added into the solution and stirred for another 30 min. The resulting white suspension was transferred into 100 mL Teflon-lined autoclave and hydrothermally treated at 160 °C for 2 hours. After cooling down to room temperature, the white precipitate was collected by centrifugation and washed several times using water and ethanol, and finally dried at 70 °C under vacuum to obtain BiOBr ultrathin nanosheets (BiOBr NS) which will act as the template for the subsequent reaction.

For the second step, 1 mmol of as-prepared BiOBr NS was dispersed in 50 mL water and ultrasonically treated for 30 min. After that, 1 mmol of $NaVO_3$ was added, and the solution was stirred for 30 min. The solution was then transferred into 100 mL Teflon-lined autoclave and subjected to another hydrothermal treatment (160 °C, 2 hours) which would trigger the ion exchange process. The ultrathin BiOBr NS consists of a layered structure of BiOBr stacked to each other by weak interlayer van der Waals force, where Br atoms terminate the dangling bonds of slices.[27,28] Through the ion exchange process, the terminative Br^- layer could be extracted and replaced by the VO_3^- to generate chemically bonded $[Bi_2O_2]^{2+}$-$[(VO_3)_2]^{2-}$ layered stacks of $BiVO_4$. The resulting yellow precipitate was collected and washed using water several times and finally dried at 70 °C under vacuum to obtain ultrathin 2D monoclinic BVO NFs. In order to probe the effect

of alkali additive, several kinds of vanadate (VO_3^-) precursors were employed during the ion exchange hydrothermal treatment. BVO NFs A and BVO NFs B denote the ultrathin 2D $BiVO_4$ nanoflakes samples which were synthesized by using $NaVO_3$ and NH_4VO_3, respectively. On some occasions, some additional alkali (especially Na^+) source was also introduced during the ion exchange process. For some activity comparison, BVO NFs C was also synthesized using KVO_3 with the same procedure as described above. Bulk $BiVO_4$ nanoparticles (BVO NPs) were also prepared through a simple aqueous processes.[25] In detail, 5 mmol of $Bi(NO_3)_3 \cdot 5H_2O$ were dissolved and stirred in an aqueous nitric acid solution (1 M, 100 mL) for about 30 min. Afterward, 5 mmol of NH_4VO_3 were added to the mixture, and the stirring continued for 20 h. The resulting $BiVO_4$ nanoparticles powder was then collected by centrifugation and washed with distilled water before drying at 70 °C under vacuum.

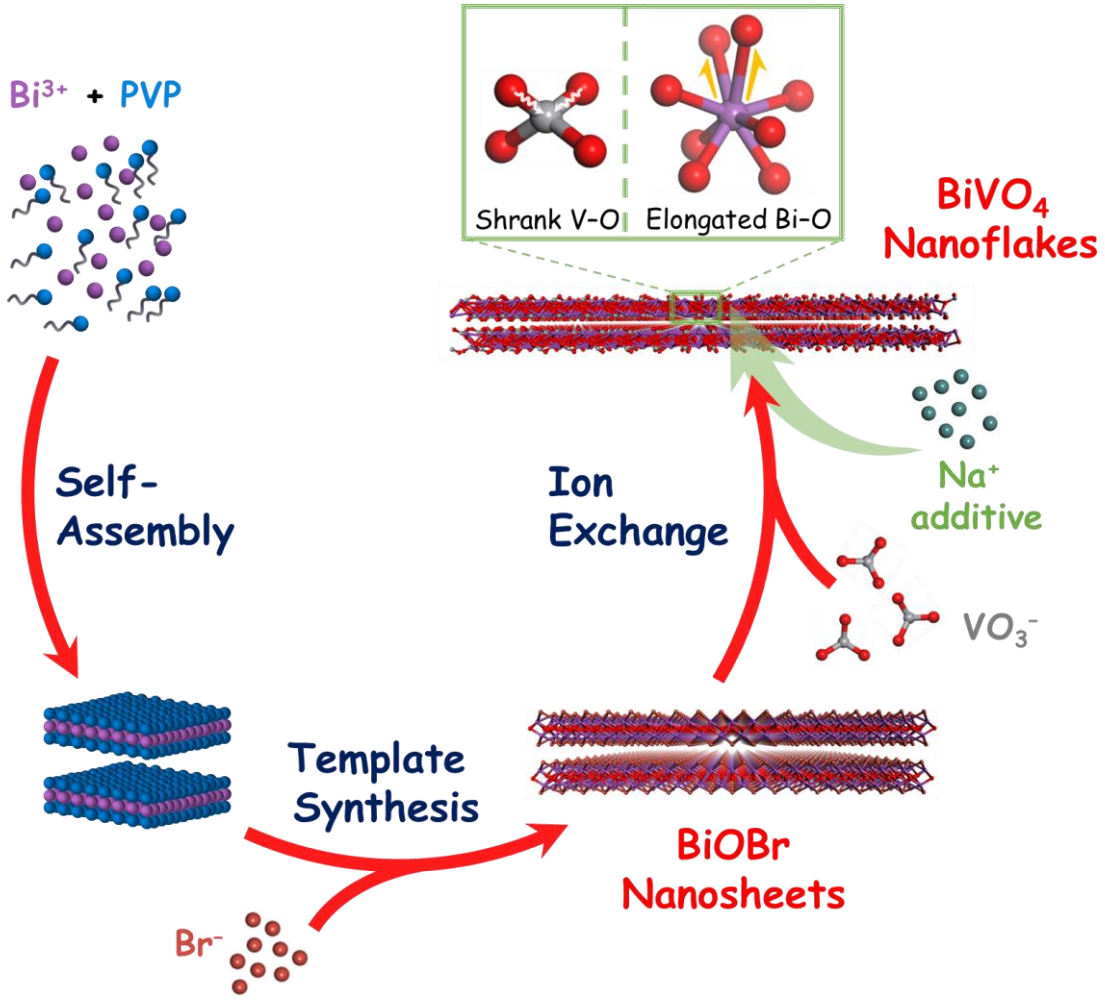

Figure 2.1. Fabrication process of ultrathin 2D BVO NFs through a template-directed method, including self-assembly, template synthesis, and ion exchange process.

2.2.3. Material Characterizations

The material crystal structures were determined using an X-ray diffractometer (X'pert powder, PANalytical B.V., Netherland) with Cu-Kα radiation (λ = 0.1541 nm) under 45 kV and 30 mA. High-resolution XRD spectra for the XRD Rietveld refinement were obtained using a Rigaku Ultima IV diffractometer equipped with monochromatic Cu-Kα radiation (λ = 0.1541 nm). XRD Rietveld refinement analysis of BVO NFs was performed using the GSAS II program to further determine the crystal structure variation. The morphologies and elemental compositions of the samples were characterized by transmission electron microscopy (TEM, JEOL JEM-2100F) and scanning electron microscopy (SEM, JEOL JSM-6701F), equipped with an energy dispersive spectrometer (EDS). Atomic force microscopy (AFM, Nanocute H, Japan) was carried out in tapping mode for analyzing the surface morphology and thickness of the samples. Raman spectra were collected by engaging the Raman microscope (NRS-1000, Japan) at room temperature with a green laser (532 nm) as the excitation source. Inductively coupled plasma optical emission spectrometry (ICP-OES, Agilent5800) was employed to determine the elemental composition of the prepared samples. The optical absorption properties were measured over a UV-vis spectrophotometer (UV-2600 Shimadzu), and the corresponding bandgaps were calculated according to Kubelka-Munk transformation. X-ray photoelectron spectroscopy (XPS) was performed by a PHI Quantera SXM, ULVAC-PHI in a theta probe using monochromatic Al-Kα X-rays at hν = 1486.6 eV. The observed peak positions were calibrated to the binding energy of the C−C bond in C 1s spectra (285.0 eV). Thermogravimetric (TG) measurement was performed on a DTG-60H unit (simultaneous DTA-TG apparatus) under a N_2 atmosphere.

2.2.4. Photocatalytic Activity Test

Photocatalytic O_2 evolution of $BiVO_4$ samples was carried out within a 290 mL Pyrex glass reactor connected to a closed gas circulation system. In a typical test, 100 mg of photocatalyst powders were dispersed in 100 mL $AgNO_3$ (or $Fe(NO_3)_3$) solution (30 mM) with ultrasonic treatment and constant stirring. The reactor was illuminated from the top side by visible light using a 300 W Xe lamp equipped with an L-42 cut-off filter. The system was degassed beforehand under dark conditions by evacuation to remove any dissolved air. A cooling water system was employed to maintain the temperature of the photocatalytic test system at around ~15 °C. The evolved O_2 was quantitatively

determined by online gas chromatography (GC-8A, Shimadzu, Japan) equipped with a thermal conductivity detector (TCD) and Ar carrier gas. The measurement of apparent quantum efficiency (AQE) was carried out under similar conditions as described above, except for the usage of monochromatic light irradiation. A series of bandpass filters (400 nm, 420 nm, 460 nm, 500 nm, 540 nm, 580 nm, and 600 nm) and a water filter were added together to the cut-off filter system in order to control the wavelength region of the monochromatic light and avoid possible damage caused by the heating effect of Xe lamp, respectively. The average light intensity was determined using a spectroradiometer (Ushio, USR-40, Japan). The AQE was estimated by using the following equation:

$$\mathrm{AQE} = \frac{4 \times \text{number of evolved } O_2 \text{ molecules}}{\text{number of incident photons}} \times 100\% \qquad (2\text{-}1)$$

2.2.5. Electrochemical Measurement

The electrochemical measurement was carried out by using a fluorine doped tin oxide (FTO) glass deposited (spin coating) by the BVO NFs A, BVO NFs B, or BVO NPs (2 mg of samples in 200 μL ethanol over an area of 1 cm^2) as the working electrode. The transient photocurrent responses under on-off cycling irradiation by manual chopping and electrochemical impedance spectroscopy (EIS) Nyquist plots under light irradiation were measured in 0.5 M Na_2SO_4 electrolyte using a bias potential at 1.23 V (vs RHE).

2.2.6. Computational Details for First-Principles Electronic Structure Calculations

The electronic structure calculations for just slabs of BVO NFs A and B were carried out by first-principles calculation based on the density functional theory (DFT) using norm-conserving pseudopotentials and an unrestricted spin (Local Spin Density: LSD) approach and including gradient corrections (GGA) on the exchange and correlation functional. The model slab with the dimension of 3a × (2b + vacant space (roughly 22 ~ 23 Å)) × 3c exposing the (010) facet was built based on the refined structure provided by the XRD Rietveld refinement for the calculations. The slabs of BVO NFs A and B are composed of 432 atoms in total indicated by following serial indices: Bi; 1~72, V; 73~144, O; 145~432. Among them, Bi1-Bi9 are located near the upper surface, Bi64-Bi72 near the lower surface, V73-V81 near the upper surface, V136-V144 near the lower surface, O145-O162 at the upper surface, and O415-O432 at the lower surface. In the inner part of the slab crystal, each Bi atom is surrounded by 8 oxygen atoms (BiO_8), while each V atom is surrounded by 4 oxygen atoms (VO_4). At the surface, the coordination of V atom

is preserved (VO_4), while Bi atom is unsaturated and only surrounded by 6 oxygen atoms (BiO_6). The recipe of the pseudopotentials for this electronic structure calculations are as follows: The exchange and correlation functional after Becke-Lee-Yang-Parr (BLYP) was used.[29,30] The valence-core interaction was modeled by norm-conserving pseudopotentials (NCPP) employing a plane-wave basis set with an energy cut-off of 80 Ry,[31] with the sampling of the Brillouin restricted to the Γ point. The electrons of Bi 5d, 6s, 6p; V 3d, 4s; O 2s, 2p were treated explicitly as valence electrons.

2.2.7. Statistical Analysis

The Raman shift positions (n = 4) in **Table 2.2** were evaluated with the assistance of SpetraGryph software and the presented means ± S.D. are the combination of the standard uncertainty of repeated measurements and resolution uncertainty, expanded by the factor of 2. The lattice parameters and bond lengths of BVO NFs samples as well as their corresponding uncertainties in **Table 2.3** were evaluated by the GSAS II suite. The means ± S.D. (n = 3) from repeated measurements were calculated in order to validate the data of photocatalytic O_2 evolution and wavelength-dependent AQE in **Figure 2.16, Figure 2.19**, and **Figure 2.20**.

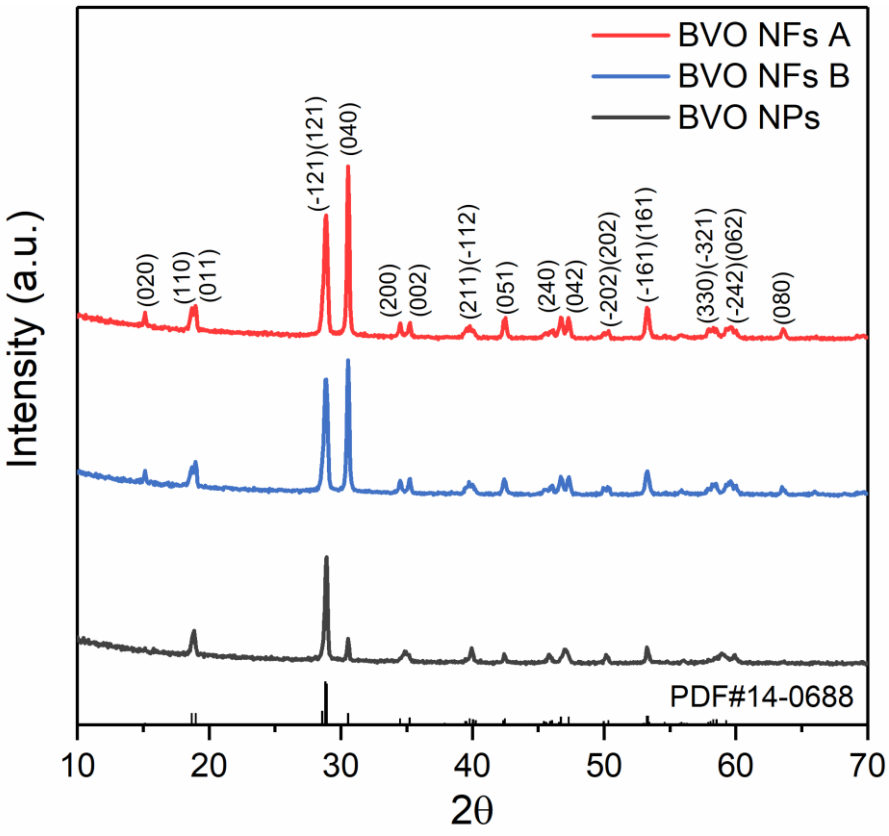

Figure 2.2. XRD patterns of ultrathin 2D BVO NFs and BVO NPs.

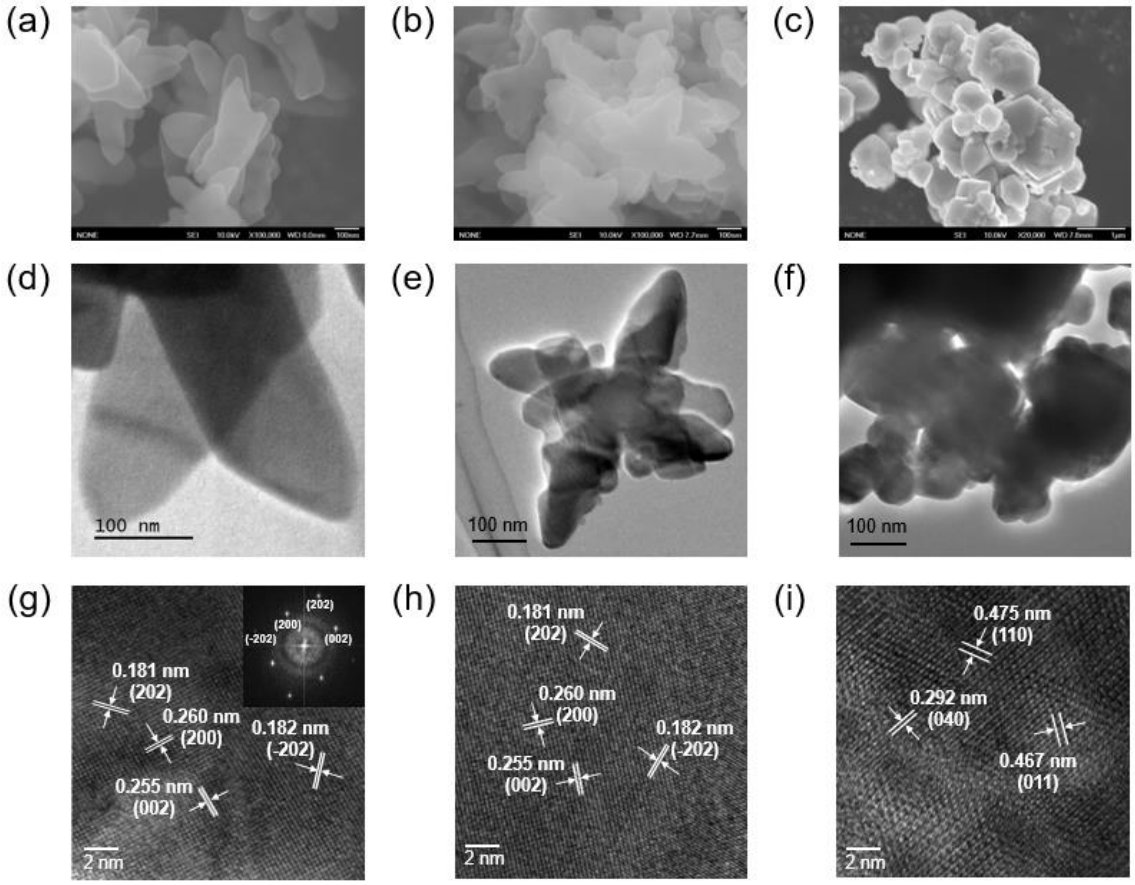

Figure 2.3. (a-c) SEM images, (d-f) TEM images, and (g-i) HR-TEM images of BVO NFs A, BVO NFs B, and BVO NPs, respectively. The inset of (g) is the corresponding SAED image.

2.3. Results and Discussion

2.3.1. Characterizations of Ultrathin 2D Monoclinic $BiVO_4$ Nanoflakes

The XRD pattern (**Figure 2.2**) confirms the pure monoclinic phase of $BiVO_4$ (JCPDS File No. 14-0688), in which BVO NFs samples exhibit intensive (040) peaks in comparison with bulk $BiVO_4$ nanoparticles (BVO NPs), indicating the preferential orientation of BVO NFs along the [010] direction, a typical feature of the crystal structure of 2D nanomaterials.[12,13,32] As can be inferred from the SEM and TEM images of the prepared samples (**Figure 2.3 a-c** and **Figure 2.3 d-f**), BVO NFs possess irregular plates or flake morphology with an average lateral size of 200-500 nm. Furthermore, high-resolution TEM (HR-TEM) images and the corresponding SAED images (**Figure 2.3 g-i**) signify the well-crystallized structure of BVO NFs. The observed interplanar d-spacings of 0.255, 0.260, 0.181, and 0.182 nm correspond to (002), (200), (202), and (-

202) lattice planes of monoclinic $BiVO_4$, respectively, further emphasizing that the monoclinic BVO NFs are oriented along the [010] zone axis. Hence, it can also be expected that the surface of the synthesized ultrathin 2D monoclinic BVO NFs is mainly composed of (010) facets. No noticeable microstructure variation can be observed over the SEM, TEM, and HR-TEM images of BVO NFs A and BVO NFs B. The atomic force microscopy (AFM) measurement and the corresponding height profiles (**Figure 2.4**) reveal that the as-prepared BVO NFs possess an average thickness of ~2.3 nm, which is pretty equal to the two-unit-cell packing thickness along the [010] zone axis of monoclinic $BiVO_4$. The Raman analysis of the BVO NFs samples (**Figure 2.5**) verifies the typical vibrational bands of $BiVO_4$,[26] further demonstrating the successful formation of monoclinic $BiVO_4$. The broad Raman band at 300-400 cm^{-1} can be deconvolved into two components located at ~ 325 and 365 cm^{-1} which can be ascribed to the asymmetric and symmetric deformation modes of VO_4^{3-} tetrahedron, respectively. The intense Raman band at 826 cm^{-1} can be associated with the stretching mode of the shorter V–O bonds. The weak band located at ~ 710 cm^{-1}, which corresponds to the stretching mode of the other V–O bonds cannot be clearly observed. The absence of this band and the merging of the bands of the asymmetric and symmetric VO_4^{3-} deformation modes in the Raman spectra might be attributed to the ultrathin thickness of BVO NFs.[26,33,34]

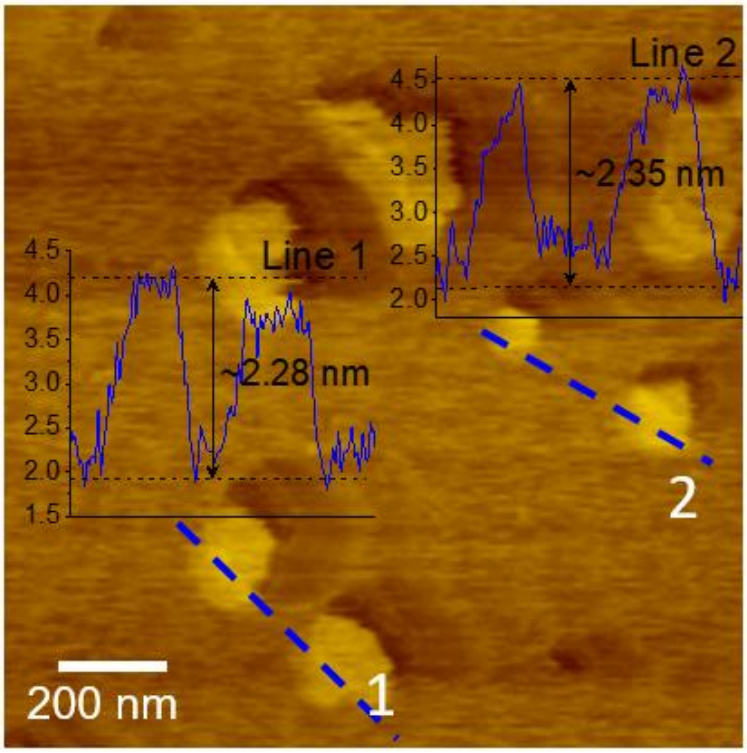

Figure 2.4. AFM image and height profiles of ultrathin 2D BVO NFs A.

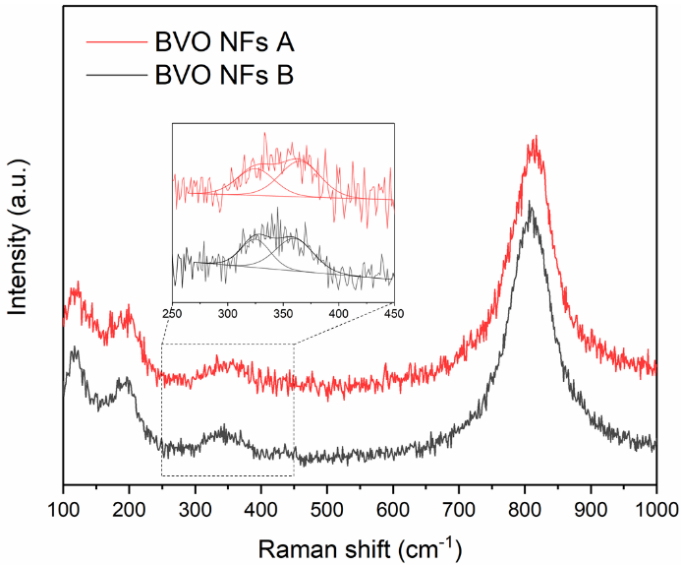

Figure 2.5. Raman spectra of BVO NFs samples.

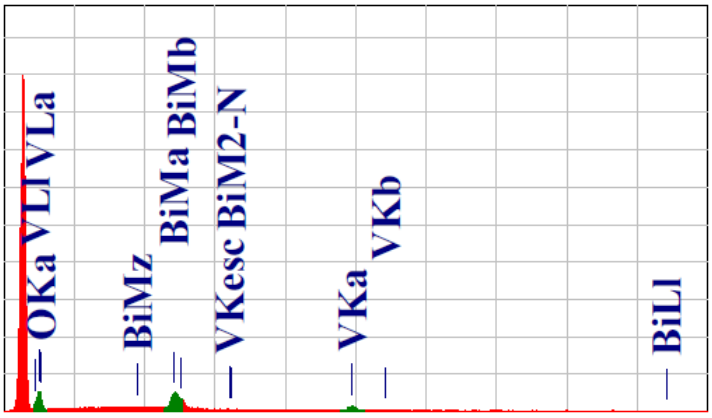

Figure 2.6. EDS of BVO NFs A. The highest peak on the left is the carbon peak originating from the carbon tape which was used as the substrate for attaching samples. The calculated Bi/V/O ratio is 1/1.2/3.7, which is pretty close to the stoichiometric ratio of $BiVO_4$. No Na atom's related signal can be observed from the EDS measurement.

Energy-dispersive X-ray spectroscopy (EDS), X-ray photoelectron spectroscopy (XPS), and inductively coupled plasma-optical emission spectroscopy (ICP-OES) were conducted to examine the chemical composition of the synthesized samples (**Figure 2.6**, **Figure 2.7**, and **Table 2.1**). The corresponding results reveal that the Bi/V molar ratio of the samples is close to the stoichiometric ratio of 1: 1, validating the successful formation of pure monoclinic $BiVO_4$. Only trace amount of Na can be detected from BVO NFs A even though a lot amount of Na^+ was added during the synthesis process, verifying the removability of Na^+ during the washing process. In addition, the Br element was undetected in all BVO NFs samples.

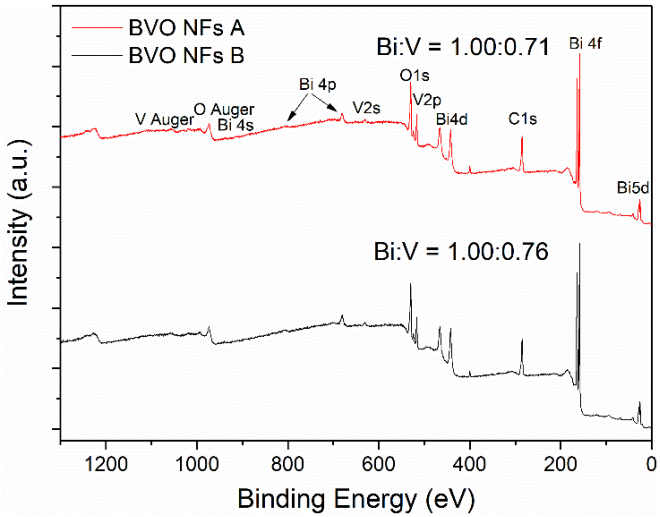

Figure 2.7. XPS spectra of BVO NFs samples. The source of the carbon signal is the carbon tape substrate. The higher detected Bi content on BVO NFs A might imply the higher amount of Bi-terminated surface since XPS is relatively surface-sensitive. No Na signal was detected from the XPS spectrum of BVO NFs A.

Table 2.1. Composition of the prepared $BiVO_4$ samples determined by ICP-OES. The analyzed samples were dissolved beforehand in HCl solution.

Sample	Bi (mg/L)	V (mg/L)	Na (mg/L)	Br (mg/L)	Bi: V
BVO NFs A	17.77	4.22	TA	-	1.00: 0.97
BVO NFs B	16.88	4.06	-	-	1.00: 0.98
BVO NP	17.97	4.23	-	-	1.00: 0.97

* TA = trace amount

The atomic distribution of BVO NFs A is analyzed by the elemental mapping, as shown in **Figure 2.8**, which indicates the homogenous distribution of Bi, V, and O throughout the sample. Thermogravimetric analysis (TGA, **Figure 2.9**) signifies the absence of any organic impurity within BVO NFs. The optical absorption properties of ultrathin 2D BVO NFs have been investigated by employing UV-Vis diffuse reflectance spectroscopy (**Figure 2.10**). The absorptions of BVO NFs samples exhibit a significant blue shift relative to the bulk BVO NPs (from 523.5 nm to 508.5 nm), which can be attributed to the quantum confinement effect of ultrathin 2D structure.[28,35] As can also be observed, the introduction of Na^+ additive doesn't yield any significant effect on the optical properties of BVO NFs samples. The non-zero absorption of both BVO NFs samples for wavelength larger than 500 nm might be attributed to the presence of defects. Mott-

Schottky plot of the as-synthesized BVO NFs A was utilized for determining the Fermi level or flat band potential of the corresponding sample (*x*-intercept of the linear part), which can give an estimate of the band positions in an aqueous environment. As shown in **Figure 2.11**, the Fermi level of BVO NFs A was calculated to be 0.09 V *vs*. RHE. It has been reported that for a typical n-type monoclinic $BiVO_4$, its conduction band minimum (CBM) position is located around 0.04 V above its Fermi level.[36] Therefore, it can be estimated that the CBM of BVO NFs A is located at 0.05 V *vs.* RHE. Based on the Tauc plot from optical absorption data, it is revealed that BVO NFs A possess a band gap of about 2.44 eV, which enable us to surmise the position of its valence band maximum (VBM) to be about 2.49 V *vs.* RHE. The corresponding band diagram of BVO NFs A can be seen in **Figure 2.12**, which indicates that it is thermodynamically possible for BVO NFs A to drive the OER and the reduction of sacrificial agents (Fe^{3+} or Ag^{+}). In order to verify the band positions, it might be necessary to employ the ultraviolet photoelectron spectroscopy (UPS) to accurately measure the VBM position.

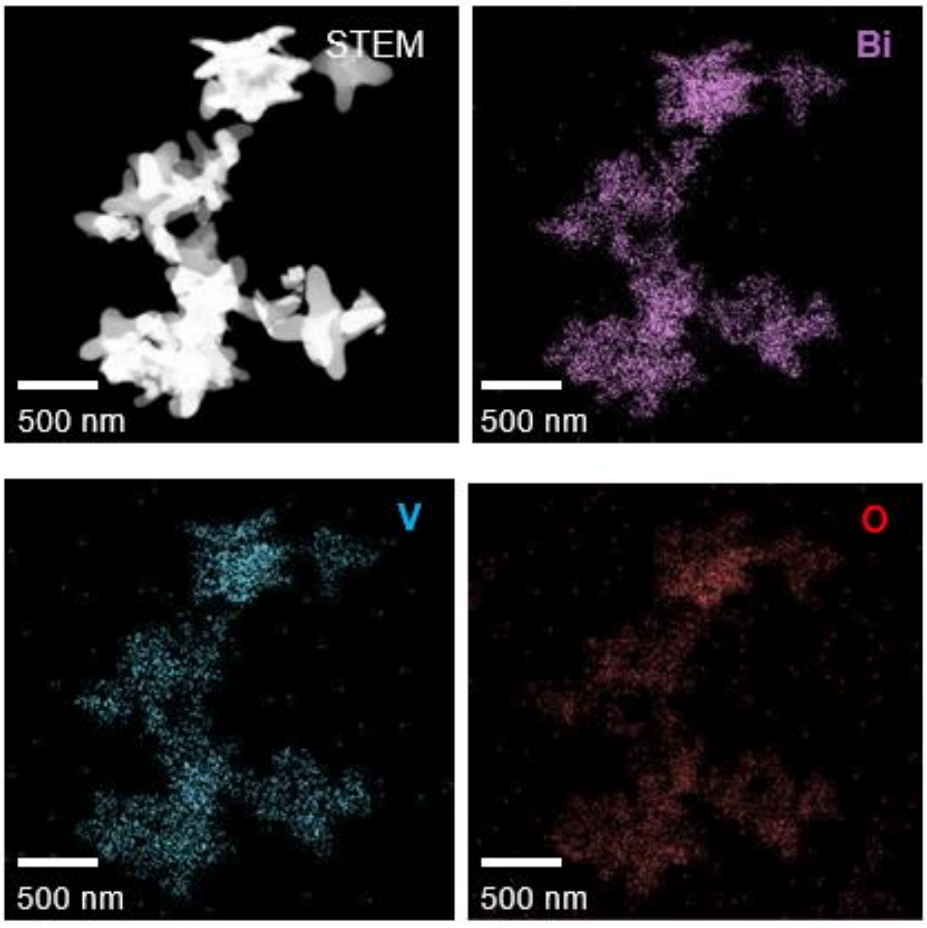

Figure 2.8. EDS elemental mapping images of ultrathin 2D BVO NFs A.

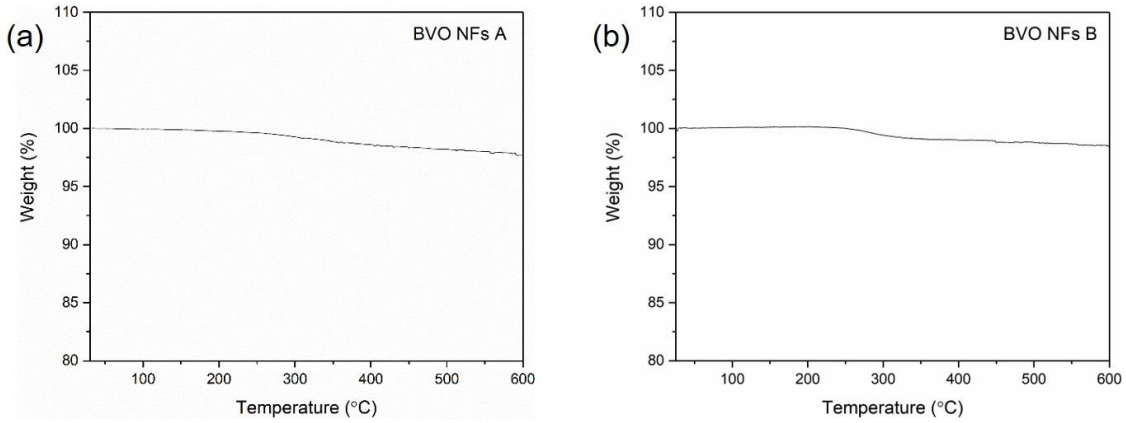

Figure 2.9. TG results of ultrathin 2D (a) BVO NFs A and (b) BVO NFs B. No obvious weight loss was observed throughout the measurement of both samples, signifying the absence of organic impurities within both BVO NFs samples.

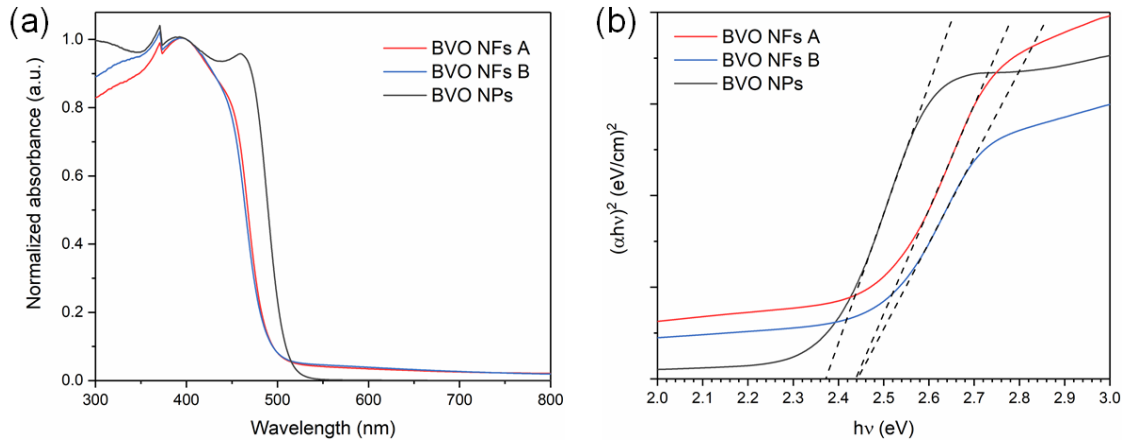

Figure 2.10. (a) UV-Vis DRS spectra and (b) Tauc plot of $(\alpha h\nu)^2$ versus photon energy ($h\nu$) based on the Kubelka-Munk transformation of the synthesized samples, revealing the possession of similar band gap of ~ 2.44 eV for both BVO NFs samples, which is very suitable for photocatalytic reaction under visible light irradiation; bulk BVO NPs exhibits a smaller bandgap of 2.37 eV.

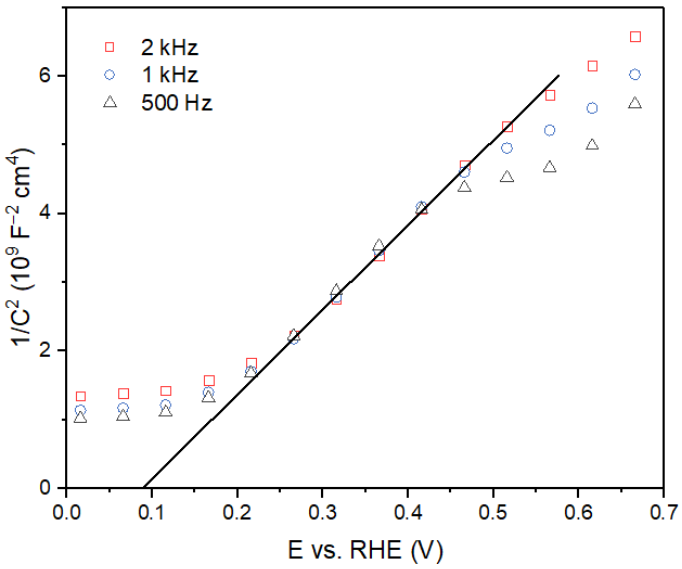

Figure 2.11. Mott-Schottky plot of the as-synthesized BVO NFs A. The Fermi level of BVO NFs A is estimated to be about 0.09 V vs. RHE.

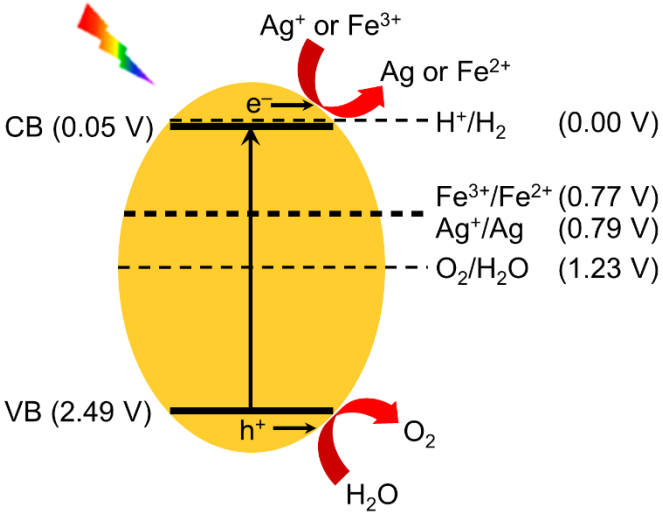

Figure 2.12. Band diagram of the as-prepared BVO NFs A.

2.3.2. Lattice Distortion Engineering upon the Introduction of Na^+ Additive

In this section, we are going to discuss the intrinsic effect of Na^+ additive for lattice distortion engineering over ultrathin 2D monoclinic BVO NFs. Through careful examination of the Raman spectra of BVO NFs samples, peculiarly by surveying the intense band located at 800-820 cm^{-1}, which corresponds to the stretching mode of the shorter V−O bonds, some crucial variations of the stretching Raman frequency could be pinpointed. As can be observed from **Figure 2.13**, the presence of Na^+ additive during the synthesis process would increase the shift position of the V−O vibrational mode,

which varies from 809.9(9) to 815.1(9) cm^{-1}. Interestingly, similar variation can also be observed for the BVO NFs B sample with some sodium salt (NaBr) added during the ion exchange process, verifying that such phenomenon was prompted by the introduction of Na^+ additive. Furthermore, this Raman shift can be correlated to the bond length of V−O by using the following empirical equation:[25,37]

$$\nu\ (cm^{-1}) = 21349 \exp(-1.9176\ R\ (Å)) \quad (2\text{-}2)$$

where ν is the stretching Raman frequency for V−O and *R* is the estimated bond length of V−O. Based on the above functional relationship, the stretching Raman shift position would have an inverse relationship with the V−O bond length. In other words, the higher the stretching frequency is, the smaller the metal−oxygen bond length would be. **Table 2.2** summarizes the stretching Raman shift positions of various BVO NFs samples and the corresponding V−O bond length. Based on Raman analysis, the introduction of Na^+ additive would shorten the V−O bond length of the ultrathin monoclinic BVO NFs from 1.7062(6) Å (BVO NFs B) to 1.7028(6) Å (BVO NFs A). The change of V−O bond length can be attributed to the $6s^2$ lone pair distortion around Bi^{3+} cation within the local structure of $BiVO_4$.[25] Unfortunately, it is not possible to extract the information about the Bi−O polyhedron from the Raman characterization. However, by considering the coordination state of bismuth cation, it could be deduced easily that the change in the V−O bond length would be alleviated by the reverse change in the Bi−O bond length to balance the structure.[26]

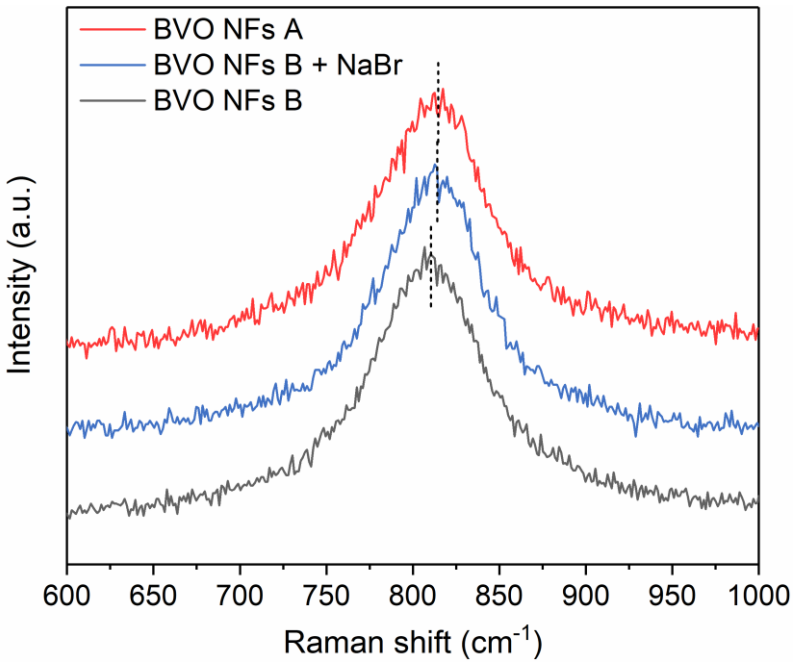

Figure 2.13. Focused Raman spectra of BVO NFs samples with and without Na^+ additive.

Table 2.2. Effect of Na^+ additive on the $V-O^I$ stretching Raman shift and estimated $V-O^I$ bond length of ultrathin 2D monoclinic BVO NFs.

Sample	Stretching Raman shift $V-O^I$ bond, ν (cm^{-1})	Estimated $V-O^I$ bond length, R (Å)*
BVO NFs A	815.1(9)	1.7028(6)
BVO NFs B + NaBr	814.4(11)	1.7033(7)
BVO NFs B	809.9(9)	1.7062(6)

* Calculated using the following empirical expression: ν (cm^{-1}) = 21349 exp (–1.9176 R (Å))

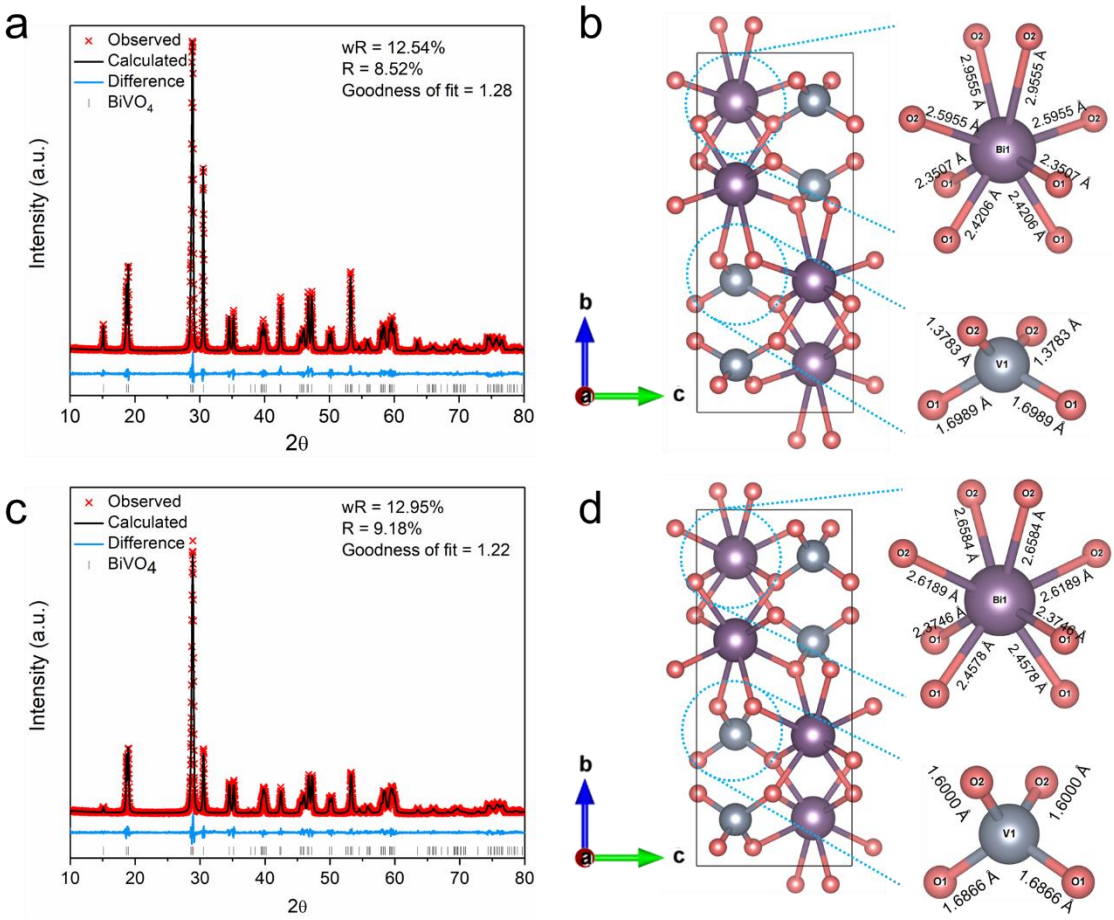

Figure 2.14. Rietveld refinement XRD patterns and the corresponding simulated lattice structure of (a-b) BVO NFs A and (c-d) BVO NFs B.

Table 2.3. Lattice properties of ultrathin 2D monoclinic BVO NFs obtained by XRD Rietveld refinement.

Samples	Lattice parameters					Unit-cell volume ($Å^3$)	Bond length (Å)	
	a (Å)	*b* (Å)	*c* (Å)	$\alpha = \gamma$ (deg)	β (deg)		V–O	Bi–O
BVO NFs A	5.1960(2)	11.7051(3)	5.0956(2)	90	90.37(1)	309.914(10)	1.3783(1) × 2	2.3507(1) × 2
							1.6989(1) × 2	2.4206(1) × 2
								2.5955(1) × 2
								2.9555(1) × 2
BVO NFs B	5.1940(3)	11.7049(4)	5.0967(3)	90	90.35(1)	309.854(17)	1.6000(1) × 2	2.3746(2) × 2
							1.6866(1) × 2	2.4578(2) × 2
								2.6189(1) × 2
								2.6584(2) × 2

The Rietveld refinements for XRD patterns of BVO NFs A and B were further employed in order to obtain more understanding about the lattice distortion effect. The corresponding results in **Figure 2.14** and **Table 2.3** demonstrate that both BVO NFs exhibit the typical features of monoclinic scheelite phase with unbalanced symmetry constraints and lattice distortion. As typical clinobisvanite structures, there are two types of V−O bonds and four types of Bi−O bonds with distinct lengths that exist within the VO_4 tetrahedrons and the BiO_8 octahedron, respectively, which is different from the symmetrical tetragonal scheelite that only has one type of V−O bond and two types of Bi−O bonds.[38-40] The lattice parameters and variations of V−O and Bi−O bond lengths, as summarized in **Table 2.3**, indicate that BVO NFs A comparatively has greater degree of lattice distortion than BVO NFs B. First of all, BVO NFs A has relatively longer cell parameter *a* and shorter *c* compared to BVO NFs B. Secondly, the β angle of BVO NFs A is bigger than that of BVO NFs B, implying a more slanted crystal structure of the former one. Thirdly and importantly, upon the introduction of Na^+ additive, the shorter V−O bonds become even shorter (1.6000(1) Å *vs.* 1.3783(1) Å), while the longer Bi−O bonds are elongated (2.6584(2) Å *vs.* 2.9555(1) Å) in response to balance the crystal structure. These results are consistent with the Raman analysis, which also signifies the shrinking of V−O bonds and the elongation of Bi−O bonds although the degree of change is more pronounced in the XRD Rietveld refinement.

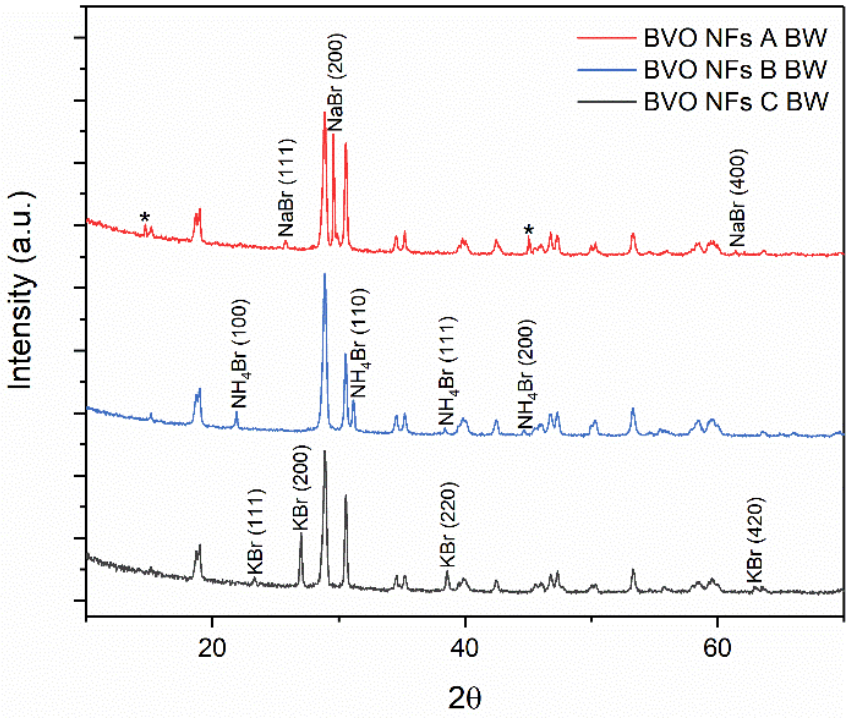

Figure 2.15. XRD spectra of BVO NFs A, BVO NFs B, and BVO NFs C samples before the washing process. The peaks marked with the asterisk sign (*) correspond to some sodium-containing compound (probably $NaBi_3V_2O_{10}$) that was formed during the ion exchange process.

In order to gain more comprehension on how the Na^+ additive is able to influence the local crystal structure, the prepared BVO NFs samples just before the washing process were examined using XRD analysis. The corresponding spectra (**Figure 2.15**) reveal the presence of NaBr, NH_4Br, and KBr within BVO NFs A, BVO NFs B, and BVO NFs C samples before washing, respectively, which is reasonable if we consider the remaining ions other than the composing elements of $BiVO_4$. Interestingly, only BVO NFs A before washing exhibits some distinct phases at 2θ: 14.69° and 45.04°, which cannot be associated with the bromide salt counterpart, i.e., NaBr. These phases are not observed on the XRD spectra of the other BVO NFs before washing, hinting that a sodium-containing compound is responsible for their existence. Such new phases might belong to the crystals of $NaBi_3V_2O_{10}$ along the (100) lattice planes.[41-44] According to Sinclair et.al.,[45] the formula $NaBi_3V_2O_{10}$ can be rewritten as $[(Na_{1/2}Bi_{1/2})O]\cdot[BiVO_4]$, and this material is composed of 'double $BiVO_4$-type layers' which contain Bi and Na ions in a highly distorted environment. Similar to the distorted monoclinic $BiVO_4$, it is reported that $NaBi_3V_2O_{10}$ also possesses several types of V−O and Bi−O bonds with varied bond

lengths.[42,45,46] Accordingly, we propose that the presence of the highly distorted $NaBi_3V_2O_{10}$ during the fabrication process of ultrathin monoclinic BVO NFs, peculiarly the ion exchange process, would influence the crystal formation process and induce more lattice distortion to the crystal structure of BVO NFs. The $NaBi_3V_2O_{10}$ phases would be removed afterward through the washing process, and the stable ultrathin 2D monoclinic BVO NFs with a greater degree of lattice distortion would be established as a result.

2.3.3. Photocatalytic Oxygen Evolution

Photocatalytic oxygen production of ultrathin 2D monoclinic BVO NFs in sacrificial $AgNO_3$ solution was evaluated. As shown in **Figure 2.16**, both BVO NFs without any cocatalyst exhibited comparatively superior photocatalytic water oxidation activities (~131.0 μmol/h and ~43.9 μmol/h), exceptionally higher than that of BVO NPs (~22.1 μmol/h). These results emphasize the advantage of ultrathin 2D nanoflakes morphology for boosting the photocatalytic water oxidation performance of monoclinic $BiVO_4$. Furthermore, the usage of sodium-containing vanadate precursor ($NaVO_3$) during the fabrication process resulted in a three-fold enhancement of the photocatalytic OER performance of BVO NFs A compared to BVO NFs B. The corresponding AQEs of BVO NFs A are 46.3% at 400 nm and 41.2% at 420 nm.

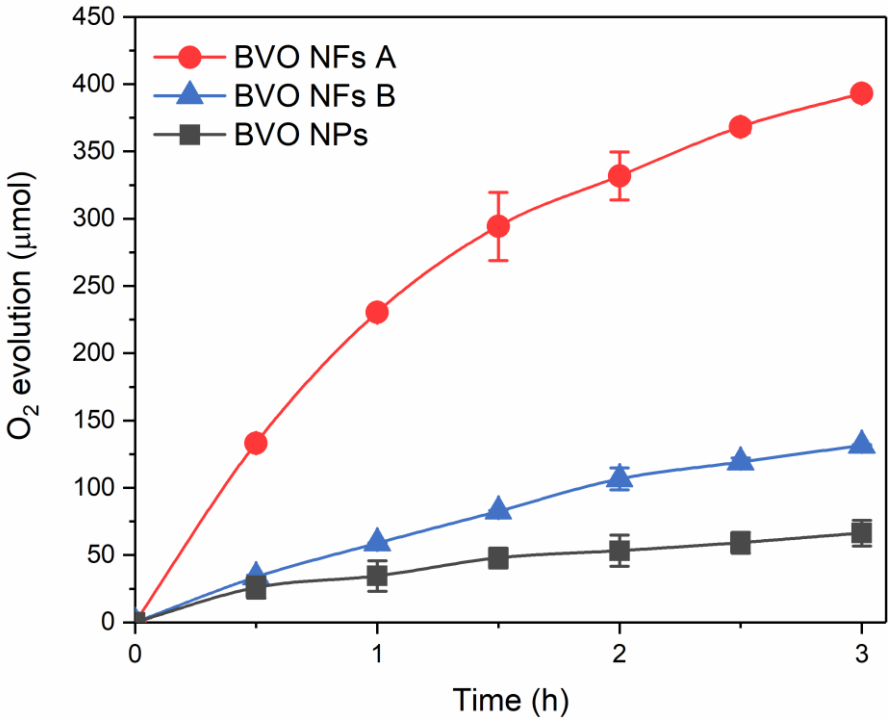

Figure 2.16. Photocatalytic O_2 evolution of $BiVO_4$ samples from aqueous solution of $AgNO_3$ (30 mM) under visible light illumination.

In order to further investigate the positive and exclusive effect of Na^+ additive on the fabrication of superior ultrathin 2D monoclinic BVO NFs, we carried out a series of performance tests for various BVO NFs (with or without some alkali additive during the fabrication process), whose results are shown in **Figure 2.17**. Interestingly, all the BVO NFs samples that employed the Na^+ additive during the synthesis process exhibited relatively better performance compared to those without any additive and with other alkali additives (i.e. Li^+ and K^+). Even though different Na^+ sources (NaBr, NaCl, and $NaNO_3$) were introduced during the fabrication process of BVO NFs B, the resulting photocatalytic OER performances were similarly enhanced (105.7 μmol/h, 104.6 μmol/h and 107.6 μmol/h, respectively). In contrast, the Li^+ additive (from $LiNO_3$) had a negative effect on the OER performance of BVO NFs B (37.5 μmol/h), while, on the other hand, the K^+ additive (from KVO_3) was able to slightly improve the OER performance (61.9 μmol/h), though not as significant as the Na^+ additive. These outcomes ascertain the importance, versatility, and exclusivity of Na^+ additive for synthesizing superior ultrathin 2D monoclinic BVO NFs. In order to rule out the possible effect of Na^+ additive during the photocatalytic reaction, external Na^+ salt ($NaNO_3$) was added into the reaction solution during the catalytic performance test. As shown in **Table 2.4**, the results indicate slight decreases on the photocatalytic OER activity for both BVO NFs A and BVO NFs B, thus verifying that the Na^+ additive doesn't induce any direct merit to the photocatalytic water oxidation process.

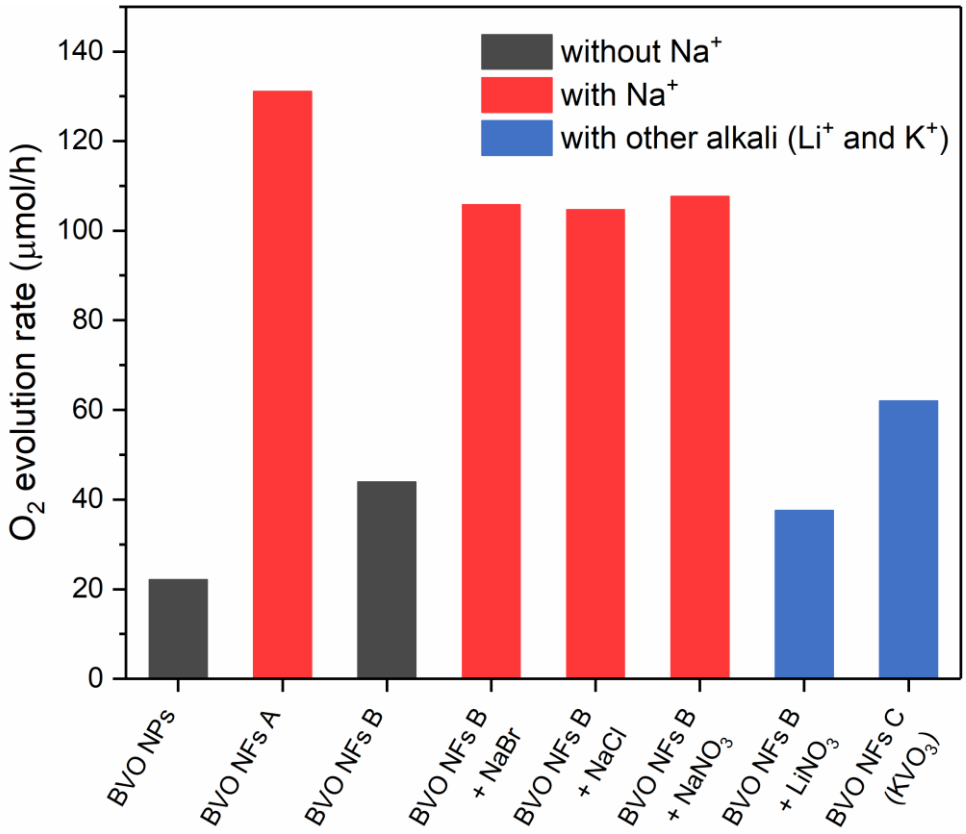

Figure 2.17. Effect of alkali additives (added during the ion-exchange process) on the visible-light-driven O_2 evolution rate over $BiVO_4$ samples.

Table 2.4. Effect of different reaction conditions on the photocatalytic OER activity of BVO NFs samples.

Samples	Reaction Condition			O_2 evolution rate (μmol/h)
	$AgNO_3$	$NaNO_3$*	$Fe(NO_3)_3$	
BVO NFs A	✓	-	-	131.0
BVO NFs A	✓	✓	-	118.3
BVO NFs A	-	-	✓	309.9
BVO NFs B	✓	-	-	43.9
BVO NFs B	✓	✓	-	36.5

* the added amount was 1 mmol

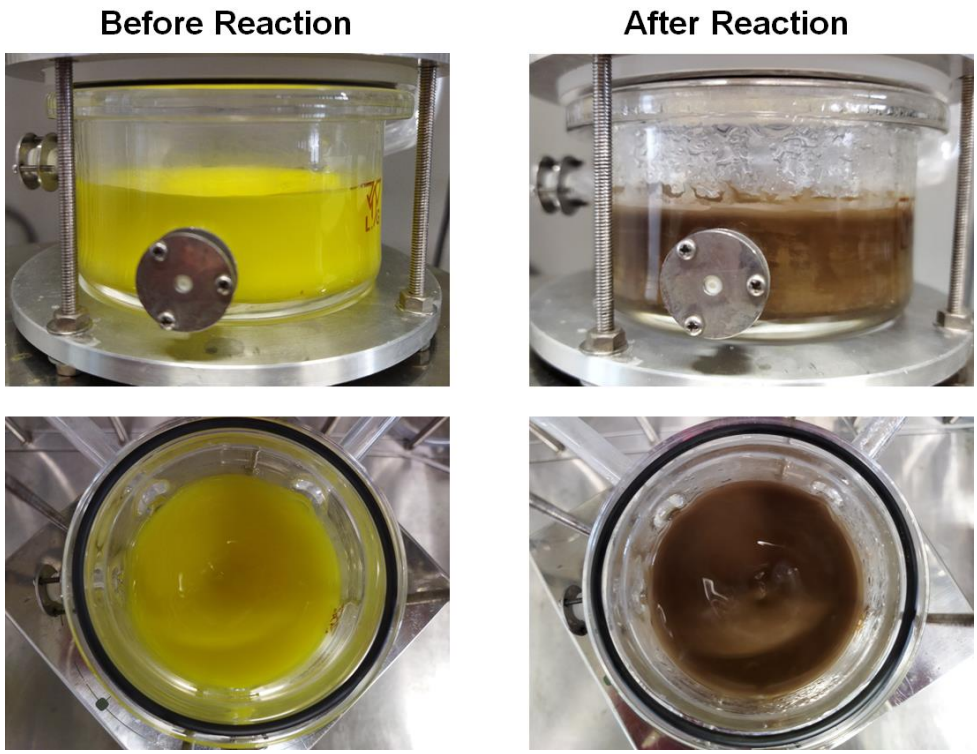

Figure 2.18. Photos of reaction solution before and after the photocatalytic OER test over $AgNO_3$ solution. The drastic change in the solution color indicates the severe photodeposition of Ag metal on the surface of the catalyst, which would significantly block the light absorption.

The usage of $AgNO_3$ sacrificial solution would lead to a severe deposition of Ag metal on the catalyst surface (see **Figure 2.18**), which would significantly hinder the light absorption and gradually decrease the oxygen evolution yield over time. In order to avoid such drawback and further evaluate the reducing ability of BVO NFs A, another activity test by using $Fe(NO_3)_3$ as sacrificial agent was performed (**Figure 2.19**). Encouragingly, BVO NFs A could demonstrate an even more remarkable photocatalytic OER activity up to 309.9 μmol/h, which corresponds to the AQEs of 69.4% at 400 nm and 62.4% at 420 nm, further emphasizing the superiority of ultrathin 2D monoclinic BVO NFs with greater lattice distortion for visible-light-driven water oxidation. **Figure 2.20** shows the dependence of AQE on incident light wavelength, which indicates that the AQEs of BVO NFs A follow the similar trend with its light absorption spectrum, thus confirming the key contribution of solar-driven photocatalytic process to the OER activity. **Table 2.5** shows the detailed calculation for the AQE measurement. Compared with the other representative cases using $BiVO_4$ photocatalyst, our work demonstrates outstanding performance towards visible-light-driven water oxidation (**Table 2.6**). In addition to its

remarkable photocatalytic OER performance, BVO NFs A also exhibits good durability and reusability, by which only a slight decrease of activity is observed after five cycles of photocatalytic OER test over $Fe(NO_3)_3$ solution (**Figure 2.21**, **Figure 2.22**, **Figure 2.23**, and **Figure 2.24**).

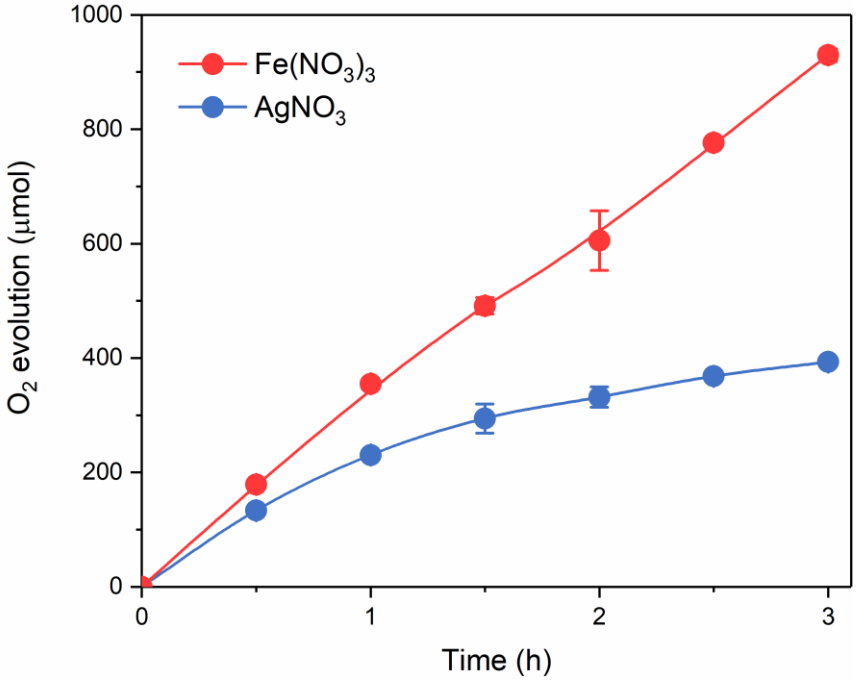

Figure 2.19. Effect of sacrificial agent on photocatalytic O_2 evolution of BVO NFs A.

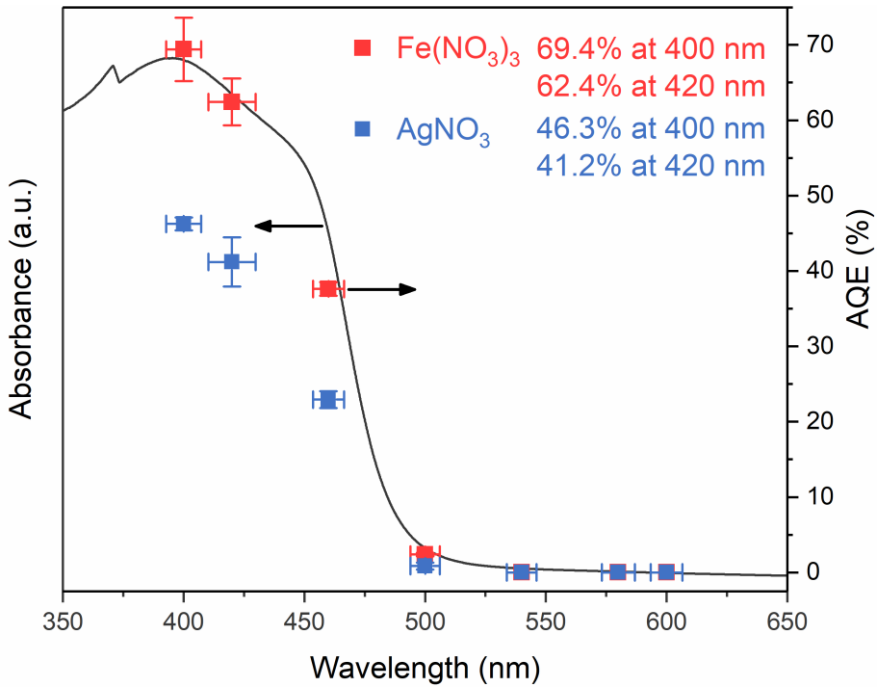

Figure 2.20. Wavelength-dependent apparent quantum efficiency (AQE) of photocatalytic O_2 evolution of BVO NFs A.

Table 2.5. Measurement of apparent quantum efficiency (AQE).

Wavelength (nm)	Number of incident photons (h^{-1})	Sacrificial Agent	Oxygen production rate (μmol/h)	Number of reacted electrons (h^{-1})	AQE (%)
400	1.992×10^{20}	$Fe(NO_3)_3$	57.41	1.383×10^{20}	69.4
		$AgNO_3$	38.25	9.214×10^{19}	46.3
420	1.002×10^{20}	$Fe(NO_3)_3$	25.95	6.250×10^{19}	62.4
		$AgNO_3$	17.13	4.127×10^{19}	41.2
460	2.802×10^{20}	$Fe(NO_3)_3$	43.75	1.054×10^{20}	37.6
		$AgNO_3$	26.68	6.426×10^{19}	22.9
500	6.237×10^{20}	$Fe(NO_3)_3$	6.19	1.491×10^{19}	2.39
		$AgNO_3$	2.18	5.252×10^{18}	0.84

Table 2.6. Comparison of oxygen evolution performance and AQE of the $BiVO_4$ samples reported in the representative literatures.

Photocatalyst	Light Source	Sacrificial agent	Oxygen production rate (μmol/h)	AQE	Refs.
Ultrathin $BiVO_4$ nanoflakes (100 mg)	300 W Xe Lamp (λ > 420 nm)	$AgNO_3$ (30 mM)	131.0	46.3% (400 nm) 41.2% (420 nm)	This work
		$Fe(NO_3)_3$ (30 mM)	309.9	69.4% (400 nm) 62.2% (420 nm)	
$BiVO_4$-Cl (100 mg)	300 W Xe Lamp (λ > 400 nm)	$AgNO_3$ (18.5 mM)	195*	34.6% (420 nm)	[47]
Conical $BiVO_4$ (35 mg)	300 W Xe Lamp	$AgNO_3$ (25 mM)	8.05	-	[48]
Ultrathin $BiVO_4$ nanosheets (20 mg)	300 W Xe Lamp (λ > 420 nm)	$AgNO_3$ (50 mM)	107.4	26.1% (420 nm)	[14]
$BiVO_4$ nanotubes (100 mg)	300 W Xe Lamp (λ > 420 nm)	$AgNO_3$ (50 mM)	20.4	3.5% (420 nm)	[49]
Oxygen-vacancy-rich $BiVO_4$ (200 mg)	300 W Xe Lamp (λ > 420 nm)	$AgNO_3$ (12.5 mM) $Fe(NO_3)_3$ (20 mM)	680* 176*	77.8% (420 nm) 19.6% (420 nm)	[8]
$BiVO_4$ nanofiber (50 mg)	300 W Xe Lamp	$AgNO_3$ (100 mM)	13.7	-	[50]
Decahedron $BiVO_4$ (200 mg)	300 W Xe Lamp	$Fe(NO_3)_3$ (4 mM)	-	71% (365 nm) 62% (420 nm)	[51]
Ti-doped $BiVO_4$ nanosheets (50 mg)	300 W Xe Lamp (λ > 420 nm)	$AgNO_3$ (50 mM)	5.14	-	[52]
24-faceted $BiVO_4$ polyhedron (100 mg)	300 W Xe Lamp (λ > 420 nm)	$AgNO_3$ (50 mM)	178.8	30.7% (420 nm)	[53]
30-faceted $BiVO_4$ polyhedron (100 mg)	300 W Xe Lamp (λ > 420 nm)	$NaIO_3$ (20 mM)	57.0	18.3% (430 nm)	[54]
[010]-dominant platelike $BiVO_4$ (100 mg)	300 W Xe Lamp (λ > 420 nm)	$AgNO_3$ (50 mM)	65	1.04% (400 nm)	[55]

* measured activity over the first hour

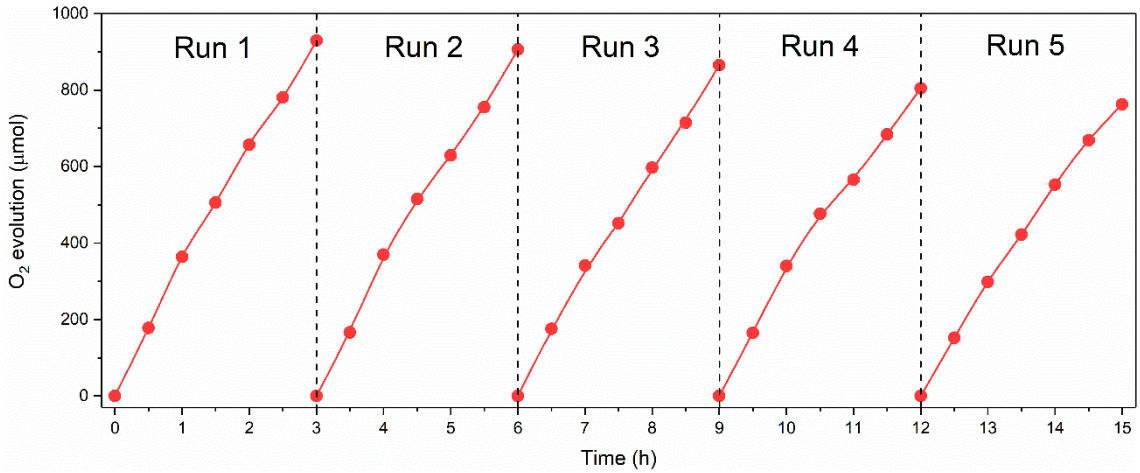

Figure 2.21. Cycle test for photocatalytic O_2 evolution of BVO NFs A over aqueous solution of $Fe(NO_3)_3$ (30 mM).

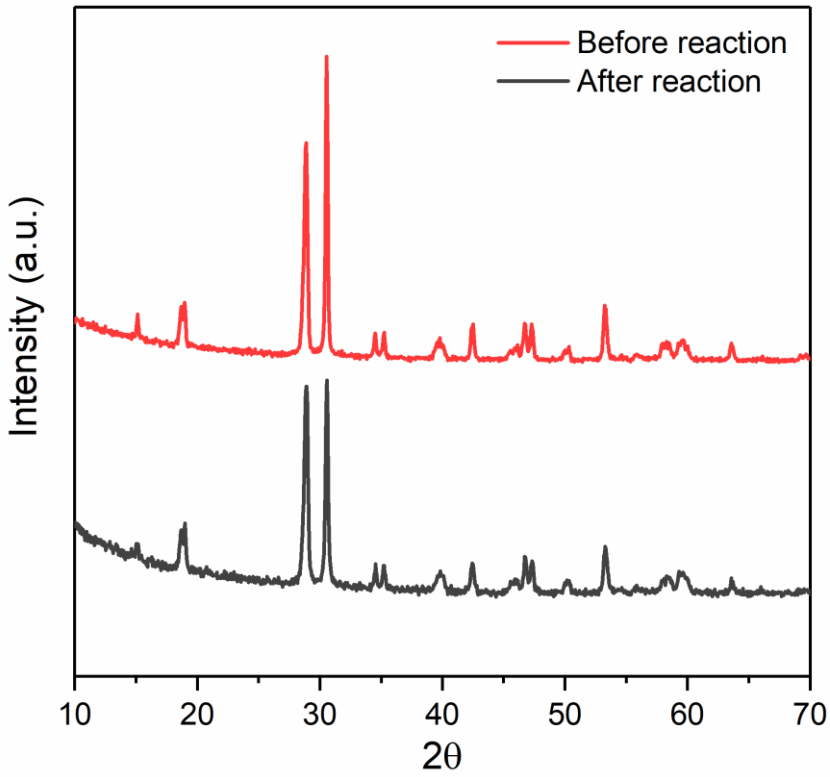

Figure 2.22. XRD spectra of BVO NFs A before and after five cycles of photocatalytic OER test over $Fe(NO_3)_3$ solution. Similar to the original BVO NFs A sample, the post-reaction sample also exhibits an intensive (040) peak, indicating that it maintains the 2D nanomaterial feature.

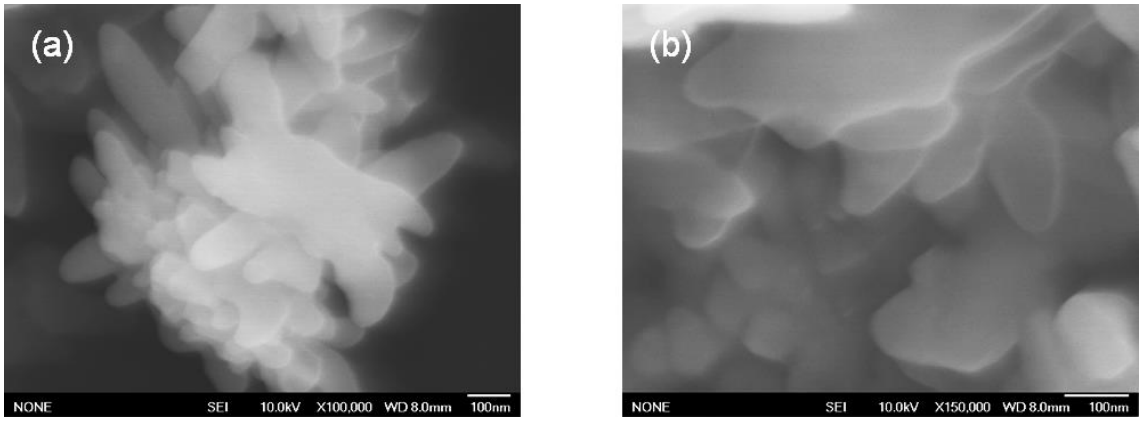

Figure 2.23. SEM images of BVO NFs A after five cycles of photocatalytic OER test over $Fe(NO_3)_3$ solution. Similar to the fresh one, the BVO NFs A sample after the cycling stability test still possesses the nanoflakes morphology.

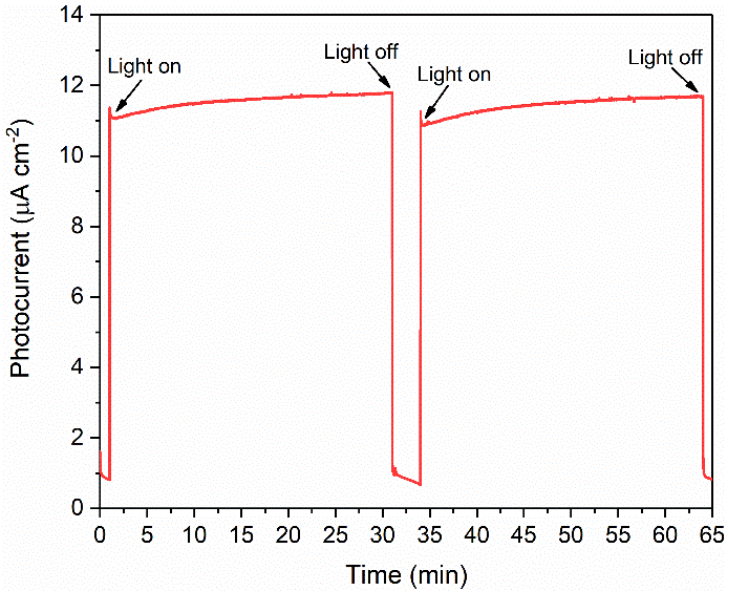

Figure 2.24. Long-term transient photocurrent response of BVO NFs A for sulfite (SO_3^{2-}) oxidation by using 1.0 M potassium borate (KB) buffer solution (pH 9.3) containing 0.2 M Na_2SO_3.[56] Sulfite oxidation was employed instead of water oxidation in order to avoid possible damage to the catalyst layer on top of the electrode surface by the generated O_2 bubble, which would result in a gradual decrease of photocurrent response over time.

2.3.4. Mechanistic Investigation

A series of fundamental investigations were performed to verify the advantages of 2D structure tailoring and lattice distortion engineering over BVO NFs. As shown in **Figure 2.25**, BVO NFs clearly showed enhanced transient photocurrent response compared with BVO NPs, indicating the improvement of electron-hole separation upon the morphology

modification from bulk nanoparticles to ultrathin 2D nanoflakes. This could be ascribed to the atomic thickness of the materials which would markedly reduce the required migration distance for the charge carriers to reach the catalytic surface. The transient photocurrent of BVO NFs A is nearly 2-times that of BVO NFs B, pronouncing the enhanced charge carriers dynamics of the former one compared to the latter one. Moreover, the Nyquist plots under light irradiation (**Figure 2.26**) indicate smaller resistance of BVO NFs A compared to BVO NFs B, suggesting a significantly improved electron conductivity along with the increase in lattice distortion degree.

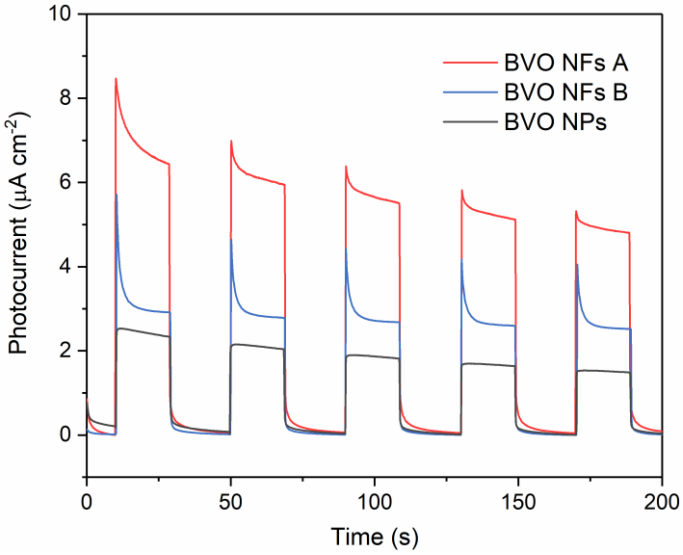

Figure 2.25. Transient photocurrent responses of BVO NFs and BVO NPs using a bias potential at 1.23 eV (vs. RHE) under on-off cycling irradiation by manual chopping.

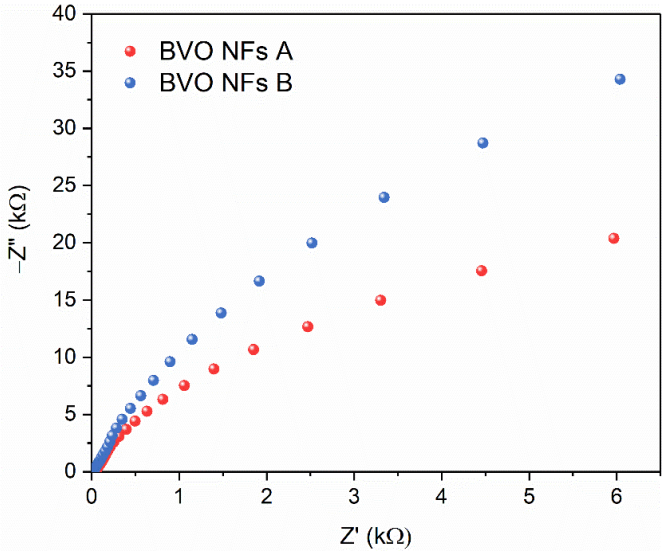

Figure 2.26. Electrochemical impedance spectroscopy (EIS) Nyquist plots of BVO NFs under light irradiation.

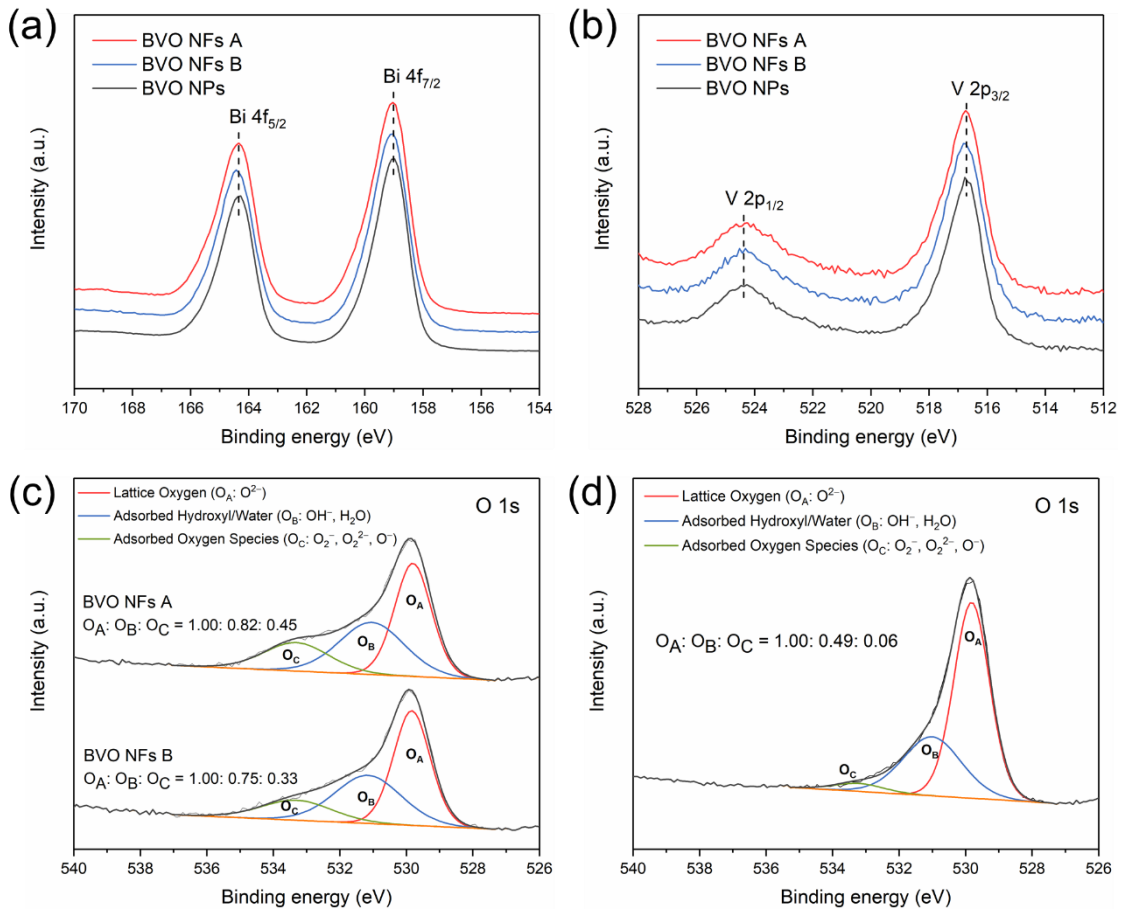

Figure 2.27. (a) Bi 4f and (b) V 2p high-resolution XPS spectra of various $BiVO_4$ samples. (c) O 1s high-resolution XPS spectra of BVO NFs and (d) BVO NPs.

Surface information and chemical state variations of each composing element on BVO NFs A, BVO NFs B, and BVO NPS were investigated using high-resolution X-ray photoelectron spectroscopy (XPS). There is no significant disparity between the Bi 4f and V 2p spectra of BVO NFs and BVO NPs samples (**Figure 2.27 a-b**), prompting the similar chemical environment of Bi and V atoms within the crystal structures of all samples. On the other hand, the XPS spectra of O 1s signify a noteworthy variation regarding the shoulder peak located at 531-536 eV (**Figure 2.27 c**). After the deconvolution and curve-fitting, the asymmetric XPS spectra of O 1s can be generally divided into three components with peaks centered at about 529.8 eV, 531.1 eV, and 533.3 eV, corresponding to lattice oxygen (O_A: O^{2-}), adsorbed hydroxyl or water (O_B: OH^-, H_2O), and chemisorbed or dissociated oxygen species (O_C: O_2^-, O_2^{2-}, O^-), respectively.[48,52,54] As can be observed, BVO NFs A possesses a moderately higher amount of O_B and O_C relative to BVO NFs B, suggesting that the surface of the former one is comparatively more active in interacting with hydroxyl or water and generating

oxygen species, which would be beneficial for the catalytic OER. The shortened V−O bonds and elongated Bi−O bonds are particularly located on the surface of the unit-cell of BVO NFs A (see **Figure 2.14 b, d**). Consequently, it is more likely that they would terminate the actual crystal structure of BVO NFs A along the (010) planes, thus enabling them to be exposed and strongly influence the catalytic surface behavior. At the same time, the atomic thickness of the ultrathin 2D monoclinic BVO NFs would enable most of the lattice atoms to act as the surface atoms, further intensifying this enhanced surface feature. In contrast, the O 1s XPS spectra of BVO NPs (**Figure 2.27 d**) reveal substantially lower amount of O_B and O_C, which can be attributed to its small surface area and thus less reactive sites to produce those species.

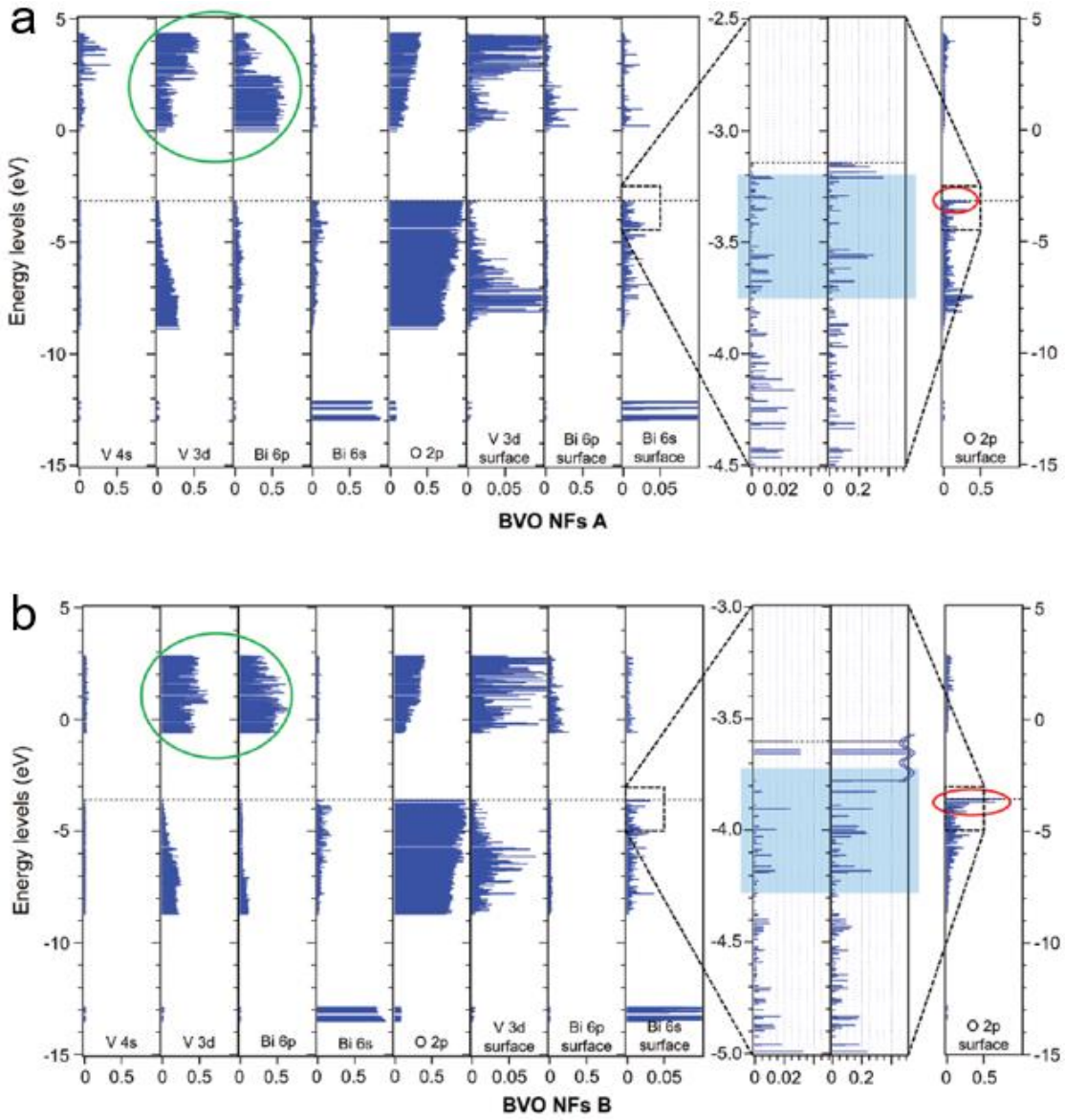

Figure 2.28. Theoretical intrinsic electronic structure properties of a slab model exposing (010) surface of (a) BVO NFs A and (b) BVO NFs B.

In order to understand the cause of the positive effects of lattice distortion more clearly, the electronic structures of BVO NFs A and BVO NFs B were investigated and compared by first-principles calculations within the local spin density approximation (GGA-LSD) using the refined crystal structural data provided by a XRD Rietveld analysis. As shown in **Figure 2.28**, what the electronic properties of BVO NFs A and BVO NFs B have in common is that the levels around the conduction band minimum (CBM) are mainly composed of Bi 6p and V 3d unoccupied states. Furthermore, the levels around the valence band maximum (VBM) mostly consist of O 2p and a small amount of Bi 6s occupied states, while the dominant components of Bi 6s are located at much lower energy range (roughly 9 eV below VBM), which correspond to the theoretical electronic properties (i.e. density of state profiles projected onto atomic orbitals) reported on the bulk crystal using a unit cell.[57] Some pivotal differences can be observed after a detailed and careful comparison of the electronic structures.

Firstly, the Bi 6p unoccupied states around the conduction band minimum (CBM) of BVO NFs A are stronger than those of BVO NFs B, while the otherwise situation can be observed for the unoccupied V 3d orbitals, as indicated by the green circles. It is worthy of note that the (010) surfaces of both BVO NFs contain the following atomic wave function connections: - V 3d - V 3d - V 3d - V 3d - (V-V atomic distance roughly 5.1~5.2 Å) and - Bi 6p - Bi 6p - Bi 6p - Bi 6p - (Bi-Bi atomic distance roughly 5.1 ~ 5.2 Å), which are important pathways for the photoexcited electrons. However, the V 3d wave function is significantly smaller (roughly one third times) than the Bi 6p wave function, which means that the migration of electrons would favor the Bi 6p pathways. In this case, the stronger Bi 6p components around the CBM of BVO NFs A system indicate better photogenerated electron mobility and therefore more advantages for accelerating the reduction reaction, compared to BVO NFs B which exhibits weaker Bi 6p and stronger V 3d orbitals.

Secondly, focusing on the vicinity of the VBM in BVO NFs systems around the surface, as indicated by the light blue shaded area, we can notice that the Bi 6s occupied states are hybridized with the O 2p occupied states. Comparing the similarity of the patterns between Bi 6s and O 2p components, more overlap of the orbitals can be found on BVO NFs A compared to BVO NFs B, suggesting the stronger Bi 6s and O 2p hybridization of the former one, which can be ascribed to the change in the extent of lattice distortion in accordance to the previous report.[26] The greater the degree of distortion, the more Bi 6s

and O 2p orbitals would overlap, and as a consequence, it would enable more efficient transfer of photogenerated holes between Bi 6s and O 2p occupied states, reduce the hole effective mass, elevate the photogenerated holes migration rate to the catalytic surface, and therefore suppress the charge carriers recombination.[22,24-26]

Thirdly, some strong surface levels of O 2p occupied states are observed in BVO NFs B system, as marked by the red circles. As indicated in our former studies,[58-61] the O 2p components deriving from the adsorbed water or hydroxyl group are usually small and mostly located below the surface levels. In this case, the presence of strong surface levels of O 2p band would lead the photogenerated holes to preferentially recombine with the high-energy surficial electrons, and thus blocking the oxidation process. On the other hand, the profile of the surface levels of BVO NFs A indicates weaker and milder peaks, which implies that the surface states are more delocalized. Therefore, it is considered that this not only suppresses inconvenient blocking for the oxidation process, but also brings higher mobility to the holes, enabling BVO NFs A to exhibit better oxidizing function.

On the basis of above results and discussions, the vital factors that stimulate the superior photocatalytic OER performance of ultrathin 2D monoclinic BVO NFs with greater lattice distortion can be summarized as follows. 1) From the aspect of charge carrier dynamics, the atomic thickness would shorten the required migration distance for photogenerated charge carriers to reach the catalytic surface. In addition, the existence of better wave function connection within CB region, greater hybridization between Bi 6s and O 2p orbitals, as well as the delocalization of surficial O 2p occupied states around the VBM would enable more swift transfer of photogenerated charge carriers and effectively suppress the charge carrier recombination. 2) The surface properties are modulated to benefit the catalytic water oxidation reaction as the consequence of the variation in lattice atomic coordination. Such a prominent surface feature would be further intensified by the ultrathin 2D features which expose more active (010) facet and enable most of the lattice atoms to act as the surface atoms to participate in the surface transformation. This notion will be addressed and discussed more profoundly in the next chapter. In brief, the ultrathin 2D feature and lattice distortion engineering act in concert, rendering a cooperative enhancement of visible-light-driven OER performance over $BiVO_4$ photocatalyst, as illustrated in **Figure 2.29**.

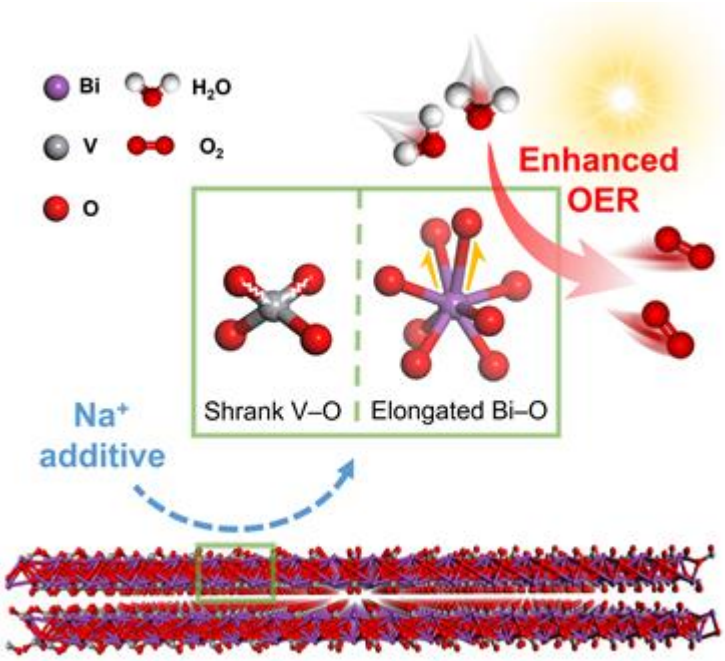

Figure 2.29. Schematic illustration of lattice distortion engineering (by Na^+ additive) over ultrathin 2D monoclinic $BiVO_4$ photocatalyst for more superior photocatalytic water oxidation.

2.4. Conclusions

In conclusion, simultaneous 2D structure tailoring and lattice distortion engineering over $BiVO_4$ photocatalyst were successfully performed through a facile template-directed strategy and simple introduction of Na^+ additive, respectively. In particular, the lattice distortion effect was characterized by the shrinking of V−O bonds and the elongation of Bi−O bonds. In-depth analysis unravels the cooperative contribution of the ultrathin 2D features and the lattice distortion effect to the modulation of charge carriers dynamics and catalytic surface features of the ultrathin 2D monoclinic $BiVO_4$ nanoflakes, yielding superior photocatalytic OER performance with remarkable apparent quantum efficiencies up to 69.4%. The findings of this work prompt the functional exploitation of dimensional modification and lattice distortion engineering in order to design and fabricate superior monoclinic $BiVO_4$ photocatalyst for various photocatalytic applications.

Reference

1. S. Chen, T. Takata, K. Domen (2017) Particulate Photocatalysts for Overall Water Splitting. Nat. Rev. Mater. 2 (10):17050. doi:10.1038/natrevmats.2017.50

2. D. Philo, H. El-Hosainy, S. Luo, H. Huang, F. Ichihara, J. Ye (2022) Artificial Photosynthesis: Fundamentals, Challenges, and Strategies. In: Wakayama Y, Ariga K (eds) System-Materials Nanoarchitectonics. Springer Japan, Tokyo, pp 233-263. doi:10.1007/978-4-431-56912-1_14

3. H. Lin, S. Luo, H. Zhang, J. Ye (2022) Toward Solar-Driven Carbon Recycling. Joule 6 (2):294-314. doi:10.1016/j.joule.2022.01.001

4. S. Luo, X. Ren, H. Lin, H. Song, J. Ye (2021) Plasmonic photothermal catalysis for solar-to-fuel conversion: current status and prospects. Chem. Sci. 12 (16):5701-5719. doi:10.1039/D1SC00064K

5. M. Kondo, H. Tatewaki, S. Masaoka (2021) Design of Molecular Water Oxidation Catalysts with Earth-Abundant Metal Ions. Chem. Soc. Rev. 50 (12):6790-6831. doi:10.1039/D0CS01442G

6. N. C. S. Selvam, L. Du, B. Y. Xia, P. J. Yoo, B. You (2021) Reconstructed Water Oxidation Electrocatalysts: The Impact of Surface Dynamics on Intrinsic Activities. Adv. Funct. Mater. 31 (12):2008190. doi:10.1002/adfm.202008190

7. G. Ge, M. Liu, C. Liu, W. Zhou, D. Wang, L. Liu, J. Ye (2019) Ultrathin FeOOH Nanosheets as an Efficient Cocatalyst for Photocatalytic Water Oxidation. J. Mater. Chem. A 7 (15):9222-9229. doi:10.1039/C9TA01740B

8. W. Han, H. Lin, F. Fang, Y. Zhang, K. Zhang, X. Yu, K. Chang (2021) The Effect of Fe(iii) Ions on Oxygen-Vacancy-Rich $BiVO_4$ on the Photocatalytic Oxygen Evolution Reaction. Catal. Sci. Technol. 11 (23):7598-7607. doi:10.1039/D1CY01559A

9. J. Li, C. A. Triana, W. Wan, D. P. Adiyeri Saseendran, Y. Zhao, S. E. Balaghi, S. Heidari, G. R. Patzke (2021) Molecular and Heterogeneous Water Oxidation Catalysts: Recent Progress and Joint Perspectives. Chem. Soc. Rev. 50 (4):2444-2485. doi:10.1039/D0CS00978D

10. T. Wang, L. Liu, G. Ge, M. Liu, W. Zhou, K. Chang, F. Yang, D. Wang, J. Ye (2018) Two-Dimensional Titanium Oxide Nanosheets Rich in Titanium Vacancies as an Efficient Cocatalyst for Photocatalytic Water Oxidation. J. Catal. 367:296-305. doi:10.1016/j.jcat.2018.09.026

11. J. Xiong, P. Song, J. Di, H. Li, Z. Liu (2019) Freestanding Ultrathin Bismuth-Based Materials for Diversified Photocatalytic Applications. J. Mater. Chem. A 7 (44):25203-25226. doi:10.1039/C9TA10144F

12. D. Yao, C. Dong, Q. Bing, Y. Liu, F. Qu, M. Yang, B. Liu, B. Yang, H. Zhang (2019) Oxygen-Defective Ultrathin $BiVO_4$ Nanosheets for Enhanced Gas Sensing. ACS Appl. Mater. Interfaces 11 (26):23495-23502. doi:10.1021/acsami.9b05626

13. D. Wang, H. Jiang, X. Zong, Q. Xu, Y. Ma, G. Li, C. Li (2011) Crystal Facet Dependence of Water Oxidation on $BiVO_4$ Sheets under Visible Light Irradiation. Chem. Eur. J. 17 (4):1275-1282. doi:10.1002/chem.201001636

14. C. Dong, S. Lu, S. Yao, R. Ge, Z. Wang, Z. Wang, P. An, Y. Liu, B. Yang, H. Zhang (2018) Colloidal Synthesis of Ultrathin Monoclinic $BiVO_4$ Nanosheets for Z-Scheme Overall Water Splitting under Visible Light. ACS Catal. 8 (9):8649-8658. doi:10.1021/acscatal.8b01645

15. Y. Du, Z. Yin, J. Zhu, X. Huang, X. J. Wu, Z. Zeng, Q. Yan, H. Zhang (2012) A General Method for The Large-Scale Synthesis of Uniform Ultrathin Metal Sulphide Nanocrystals. Nat. Commun. 3:1177. doi:10.1038/ncomms2181

16. M. A. Gaikwad, U. P. Suryawanshi, U. V. Ghorpade, J. S. Jang, M. P. Suryawanshi, J. H. Kim (2022) Emerging Surface, Bulk, and Interface Engineering Strategies on $BiVO_4$ for Photoelectrochemical Water Splitting. Small 18 (10):2105084. doi:10.1002/smll.202105084

17. J. H. Kim, J. S. Lee (2019) Elaborately Modified $BiVO_4$ Photoanodes for Solar Water Splitting. Adv. Mater. 31 (20):1806938. doi:10.1002/adma.201806938

18. Z. Wang, X. Huang, X. Wang (2019) Recent Progresses in the Design of $BiVO_4$-Based Photocatalysts for Efficient Solar Water Splitting. Catal. Today 335:31-38. doi:10.1016/j.cattod.2019.01.067

19. T. Liu, X. Zhou, M. Dupuis, C. Li (2015) The Nature of Photogenerated Charge Separation among Different Crystal Facets of $BiVO_4$ Studied by Density Functional Theory. Phys. Chem. Chem. Phys. 17 (36):23503-23510. doi:10.1039/C5CP04299B

20. M. Xu, J. Yang, C. Sun, L. Liu, Y. Cui, B. Liang (2020) Performance Enhancement Strategies of Bi-Based Photocatalysts: A Review on Recent Progress. Chem. Eng. J. 389:124402. doi:10.1016/j.cej.2020.124402

21. K. Qin, Q. Zhao, H. Yu, X. Xia, J. Li, S. He, L. Wei, T. An (2021) A Review of Bismuth-Based Photocatalysts for Antibiotic Degradation: Insight into the Photocatalytic Degradation Performance, Pathways and Relevant Mechanisms. Environ. Res. 199:111360. doi:10.1016/j.envres.2021.111360

22. J. Shi, E. A. Rubinstein, W. Li, J. Zhang, Y. Yang, T.-L. Lee, C. Qin, P. Yan, J. L. MacManus-Driscoll, D. O. Scanlon, K. H. L. Zhang (2022) Modulation of the Bi^{3+} $6s^2$ Lone Pair State in Perovskites for High-Mobility p-Type Oxide Semiconductors. Adv. Sci. 9 (6):2104141. doi:10.1002/advs.202104141

23. H. Kunioku, M. Higashi, O. Tomita, M. Yabuuchi, D. Kato, H. Fujito, H. Kageyama, R. Abe (2018) Strong Hybridization between Bi-6s and O-2p Orbitals in Sillén–Aurivillius Perovskite Bi_4MO_8X (M = Nb, Ta; X = Cl, Br), Visible Light Photocatalysts Enabling Stable Water Oxidation. J. Mater. Chem. A 6 (7):3100-3107. doi:10.1039/C7TA08619A

24. A. Bhatia, G. Hautier, T. Nilgianskul, A. Miglio, J. Sun, H. J. Kim, K. H. Kim, S. Chen, G.-M. Rignanese, X. Gonze, J. Suntivich (2016) High-Mobility Bismuth-based Transparent p-Type Oxide from High-Throughput Material Screening. Chem. Mater. 28 (1):30-34. doi:10.1021/acs.chemmater.5b03794

25. S. M. Thalluri, C. Martinez Suarez, M. Hussain, S. Hernandez, A. Virga, G. Saracco, N. Russo (2013) Evaluation of the Parameters Affecting the Visible-Light-Induced Photocatalytic Activity of Monoclinic $BiVO_4$ for Water Oxidation. Ind. Eng. Chem. Res. 52 (49):17414-17418. doi:10.1021/ie402930x

26. J. Yu, A. Kudo (2006) Effects of Structural Variation on the Photocatalytic Performance of Hydrothermally Synthesized $BiVO_4$. Adv. Funct. Mater. 16 (16):2163-2169. doi:10.1002/adfm.200500799

27. J. Di, C. Chen, C. Zhu, M. Ji, J. Xia, C. Yan, W. Hao, S. Li, H. Li, Z. Liu (2018) Bismuth Vacancy Mediated Single Unit Cell Bi_2WO_6 Nanosheets for Boosting Photocatalytic Oxygen Evolution. Appl. Catal. B 238:119-125. doi:10.1016/j.apcatb.2018.06.066

28. J. Di, X. Zhao, C. Lian, M. Ji, J. Xia, J. Xiong, W. Zhou, X. Cao, Y. She, H. Liu, K. P. Loh, S. J. Pennycook, H. Li, Z. Liu (2019) Atomically-Thin Bi_2MoO_6 Nanosheets with Vacancy Pairs for Improved Photocatalytic CO_2 Reduction. Nano Energy 61:54-59. doi:10.1016/j.nanoen.2019.04.029

29. A. D. Becke (1988) Density-Functional Exchange-Energy Approximation with Correct Asymptotic Behavior. Phys. Rev. A 38 (6):3098-3100. doi:10.1103/PhysRevA.38.3098

30. C. Lee, W. Yang, R. G. Parr (1988) Development of the Colle-Salvetti Correlation-Energy Formula into a Functional of the Electron Density. Phys. Rev. B 37 (2):785-789. doi:10.1103/PhysRevB.37.785

31. N. Troullier, J. L. Martins (1991) Efficient Pseudopotentials for Plane-Wave Calculations. Phys. Rev. B 43 (3):1993-2006. doi:10.1103/PhysRevB.43.1993

32. Y. Li, Z. Sun, S. Zhu, Y. Liao, Z. Chen, D. Zhang (2015) Fabrication of $BiVO_4$ Nanoplates with Active Facets on Graphene Sheets for Visible-Light Photocatalyst. Carbon 94:599-606. doi:10.1016/j.carbon.2015.07.042

33. A. Galembeck, O. L. Alves (2000) $BiVO_4$ Thin Film Preparation by Metalorganic Decomposition. Thin Solid Films 365 (1):90-93. doi:10.1016/S0040-6090(99)01079-2

34. J. Yu, A. Kudo (2005) Hydrothermal Synthesis of Nanofibrous Bismuth Vanadate. Chem. Lett. 34 (6):850-851. doi:10.1246/cl.2005.850

35. A. Cupo, V. Meunier (2017) Quantum Confinement in Black Phosphorus-Based Nanostructures. J. Phys. Condens. Matter 29 (28):283001. doi:10.1088/1361-648x/aa748c

36. J. Resasco, H. Zhang, N. Kornienko, N. Becknell, H. Lee, J. Guo, A. L. Briseno, P. Yang (2016) TiO_2/$BiVO_4$ Nanowire Heterostructure Photoanodes Based on Type II Band Alignment. ACS Central Science 2 (2):80-88. doi:10.1021/acscentsci.5b00402

37. I. D. Brown, K. K. Wu (1976) Empirical Parameters for Calculating Cation–Oxygen Bond Valences. Acta Crystallogr. Sect. B 32 (7):1957-1959. doi:10.1107/S0567740876006869

38. A. W. Sleight, H. y. Chen, A. Ferretti, D. E. Cox (1979) Crystal Growth and Structure of $BiVO_4$. Mater. Res. Bull. 14 (12):1571-1581. doi:10.1016/0025-5408(72)90227-9

39. W. I. F. David, A. M. Glazer, A. W. Hewat (1979) The Structure and Ferroelastic Phase Transition of $BiVO_4$. Phase Transit. 1 (2):155-169. doi:10.1080/01411597908213198

40. J. K. Cooper, S. Gul, F. M. Toma, L. Chen, P.-A. Glans, J. Guo, J. W. Ager, J. Yano, I. D. Sharp (2014) Electronic Structure of Monoclinic $BiVO_4$. Chem. Mater. 26 (18):5365-5373. doi:10.1021/cm5025074

41. D. C. Sinclair, C. J. Watson, R. A. Howie, J. M. S. Skakle, A. M. Coats, C. A. Kirk, E. E. Lachowski, J. Marr (1998) $NaBi_3V_2O_{10}$: A New Oxide Ion Conductor. J. Mater. Chem. 8 (2):281-282. doi:10.1039/A707760B

42. D. G. Porob, T. N. Guru Row (2000) A Novel Oxide Ion Conductor in a Doped Bi_2O_3-V_2O_5 System: Ab Initio Structure of a New Polymorph of $NaBi_3V_2O_{10}$ via Powder X-ray Diffraction. Chem. Mater. 12 (12):3658-3661. doi:10.1021/cm000444u

43. G. Yang, C. Yin, Y. Kang, S. Zhang, C. Li (2020) An Ultra-Low-Firing $NaBi_3V_2O_{10}$ Ceramic and Its Dielectric Properties at RF and Microwave Frequency Bands. J. Mater. Sci. Mater. Electron. 31 (9):7219-7225. doi:10.1007/s10854-020-03294-x

44. S. J. Patwe, S. N. Achary, A. K. Tyagi (2012) X-ray Powder Diffraction Data and Thermal Stability of a New High Temperature Phase of $NaBi_3V_2O_{10}$. Powder Diffr. 20 (1):51-57. doi:10.1154/1.1835960

45. D. C. Sinclair, E. Marinou, J. M. S. Skakle (1999) The Crystal Structure of a New Oxide Ion Conductor $NaBi_3V_2O_{10}$ and Oxide Ion Conductivity in $Pb_2Bi_2V_2O_{10}$. J. Mater. Chem. 9 (10):2617-2621. doi:10.1039/A904273C

46. R. Bliesner, S. Uma, A. Yokochi, A. W. Sleight (2001) Structure of $NaBi_3V_2O_{10}$ and Implications for Ionic Conductivity. Chem. Mater. 13 (11):3825-3826. doi:10.1021/cm010522t

47. Q. Zhang, M. Liu, W. Zhou, Y. Zhang, W. Hao, Y. Kuang, H. Liu, D. Wang, L. Liu, J. Ye (2021) A Novel Cl^- Modification Approach to Develop Highly Efficient Photocatalytic Oxygen Evolution over $BiVO_4$ with AQE of 34.6%. Nano Energy 81:105651. doi:10.1016/j.nanoen.2020.105651

48. L. J. Wang, J. Y. Bai, Y. J. Zhang, F. Mao, Y. Liu, H. Yuan, P. F. Liu, H. G. Yang (2020) Controllable Synthesis of Conical $BiVO_4$ for Photocatalytic Water Oxidation. J. Mater. Chem. A 8 (5):2331-2335. doi:10.1039/C9TA12122F

49. J. Hu, H. He, X. Zhou, Z. Li, Q. Shen, W. Luo, A. Alsaedi, T. Hayat, Y. Zhou, Z. Zou (2019) $BiVO_4$ Tubular Structures: Oxygen Defect-Rich and Largely Exposed Reactive {010} Facets Synergistically Boost Photocatalytic Water Oxidation and the Selective N-N Coupling Reaction of 5-amino-1H-tetrazole. Chem. Commun. 55 (39):5635-5638. doi:10.1039/C9CC01290G

50. M. Yu, C. Shang, G. Ma, Q. Meng, Z. Chen, M. Jin, L. Shui, Y. Zhang, Z. Zhang, M. Yuan, X. Wang, G. Zhou (2019) Synthesis and Characterization of Mesoporous $BiVO_4$ Nanofibers with Enhanced Photocatalytic Water Oxidation Performance. Appl. Surf. Sci. 481:255-261. doi:10.1016/j.apsusc.2019.03.056

51. Y. Zhao, C. Ding, J. Zhu, W. Qin, X. Tao, F. Fan, R. Li, C. Li (2020) A Hydrogen Farm Strategy for Scalable Solar Hydrogen Production with Particulate Photocatalysts. Angew. Chem. Int. Ed. 59 (24):9653-9658. doi:10.1002/anie.202001438

52. B. Peng, Y. Shi, X. Zhang, P. Lv (2021) Top-Down Fabrication of Ti Doped $BiVO_4$ Nanosheets for Efficient Water Oxidation under Visible Light. Catal. Sci. Technol. 11 (24):7898-7904. doi:10.1039/D1CY01670A

53. J. Hu, H. He, L. Li, X. Zhou, Z. Li, Q. Shen, C. Wu, A. M. Asiri, Y. Zhou, Z. Zou (2019) Highly Symmetrical, 24-Faceted, Concave BiVO4 Polyhedron Bounded by Multiple High-Index Facets for Prominent Photocatalytic O_2 Evolution under Visible Light. Chem. Commun. 55 (33):4777-4780. doi:10.1039/C9CC01366K

54. P. Li, X. Chen, H. He, X. Zhou, Y. Zhou, Z. Zou (2018) Polyhedral 30-Faceted BiVO4 Microcrystals Predominantly Enclosed by High-Index Planes Promoting Photocatalytic Water-Splitting Activity. Adv. Mater. 30 (1):1703119. doi:10.1002/adma.201703119

55. H. L. Tan, X. Wen, R. Amal, Y. H. Ng (2016) $BiVO_4$ {010} and {110} Relative Exposure Extent: Governing Factor of Surface Charge Population and Photocatalytic Activity. J. Phy. Chem. Let. 7 (7):1400-1405. doi:10.1021/acs.jpclett.6b00428

56. D. K. Lee, K.-S. Choi (2018) Enhancing Long-term Photostability of $BiVO_4$ Photoanodes for Solar Water Splitting by Tuning Electrolyte Composition. Nat. Energy 3 (1):53-60. doi:10.1038/s41560-017-0057-0

57. M. Oshikiri, M. Boero, J. Ye, Z. Zou, G. Kido (2002) Electronic Structures of Promising Photocatalysts $InMO_4$ (M=V, Nb, Ta) and $BiVO_4$ for Water Decomposition in the Visible Wavelength Region. J. Chem. Phy. 117 (15):7313-7318. doi:10.1063/1.1507101

58. K. Ishisone, N. Jiraborvornpongsa, T. Isobe, S. Matsushita, M. Wakumura, M. Oshikiri, A. Nakajima (2020) Experimental and Theoretical Investigation of WO_x Modification Effects on the Photocatalytic Activity of Titanium-Substituted Hydroxyapatite. Appl. Catal. B 264:118516. doi:10.1016/j.apcatb.2019.118516

59. M. Oshikiri, J. Ye, M. Boero (2014) The Role of Ni-Based Cocatalyst in Inhomogeneous RVO_4 Photocatalyst Systems (R = Y, Gd). J. Phy. Chem. C 118 (24):12845-12854. doi:10.1021/jp502099v

60. M. Oshikiri, J. Ye, M. Boero (2014) Inhomogeneous RVO_4 Photocatalyst Systems (R = Y, Ce, Pr, Nd, Sm, Eu, Gd, Tb, Dy, Ho, Er, Tm, Yb, Lu). J. Phy. Chem. C 118 (16):8331-8341. doi:10.1021/jp410565e

61. M. Oshikiri, M. Boero, A. Matsushita, J. Ye (2009) Water Adsorption onto Y and V Sites at the Surface of the YVO_4 Photocatalyst and Related Electronic Properties. J. Chem. Phy. 131 (3):034701. doi:10.1063/1.3170928

Chapter 3. New Insights into Water Oxidation Reaction over (010) Facet of Monoclinic $BiVO_4$: Unravelling the Key Role of Lattice Distortion

3.1. Introduction

Artificial photosynthesis for solar energy conversion into chemical energy is believed to be the most feasible and adaptable solution to the global problems of energy crisis and environmental pollution.[1-3] Nevertheless, the conquest to realize this technology has faced a great challenge, due to the difficulty of regulating the other half-reaction, i.e. water oxidation reaction into oxygen.[4-6] Fundamentally, oxygen evolution reaction (OER) is an energetically and kinetically demanding four-electron-transfer reaction, which requires joint efforts from multidisciplinary research fields in order to gain a complete understanding and comprehension of the corresponding catalytic mechanisms.[6-10]

Among many semiconductors, monoclinic $BiVO_4$ has been regarded as one of the most promising water oxidation photocatalyst candidates, due to its non-toxicity, abundant resources, low cost, photostability, visible light absorption ability (band gap energy of ~2.4 eV), and also deep valence band energy, which is favorable for driving the OER.[11-13] Unfortunately, to some extent, most reported $BiVO_4$ photocatalysts display a great dependence on metal-based cocatalysts for improving their OER activities, due to the lack of innate reactive sites on the surfaces of pure monoclinic $BiVO_4$.[13-23] Interestingly, some other reports indicate that the (010) facets of monoclinic $BiVO_4$ potentially possess the ability to efficiently trigger the catalytic water oxidation, which allows the corresponding $BiVO_4$ photocatalysts to reach satisfactory photocatalytic OER performances.[11,24,25] Wang et al. discovered that the photocatalytic water oxidation activity of $BiVO_4$ is proportionally correlated with the exposed surfaces of the (040) facet.[24] In a similar fashion, Dong et al. associate the superior OER activity of the as-prepared ultrathin monoclinic $BiVO_4$ nanosheets with their large-scale exposed (010) planes and active oxygen vacancy.[25] Noteworthily, despite the latter factor being removed through high-temperature annealing in air, the $BiVO_4$ nanosheets still display much higher OER performance compared to $BiVO_4$ nanoparticles, indicating the major contribution of the (010) facet to catalyze the water oxidation reaction.

Chapter 3

In the previous chapter, we have demonstrated an effective strategy by lattice distortion engineering over ultrathin 2D monoclinic $BiVO_4$ nanoflakes with more exposed (010) facets, which was able to demonstrate a superior visible-light-driven OER without any cocatalyst, triggering remarkable apparent quantum efficiencies up to 69.4%. According to the mechanistic investigations, it was found that the greater degree of lattice distortion would positively influence the charge carrier separation efficiency of the monoclinic $BiVO_4$ sample, by not only promoting the greater hybridization between Bi 6s and O 2p orbitals, but also providing better wave function connection within the CB region and triggering the delocalization of surficial O 2p occupied states around the VBM, thus adding more insights to the findings of some early reports about the effect of lattice distortion.[26,27] Intriguingly, we also observed a variation in the surface properties along with the change in the degree of lattice distortion, as recorded by the XPS analysis. Hence, it prompts us to believe that there is much more about the lattice distortion phenomenon which has not been unraveled yet and thus requires further in-depth study and comprehensive investigation, especially concerning its effect to the surface catalytic behavior of monoclinic $BiVO_4$ (010) facet, which would be another principal factor for determining the overall photocataytic OER performance.

In this work, by combining the means of experimental and theoretical study, I was able to investigate and unravel the critical role of lattice distortion for regulating more favorable catalytic water oxidation over the (010) facet of monoclinic $BiVO_4$. ATR-IR spectroscopy was firstly employed to identify the reaction intermediates structures, which allowed us to stipulate the surface OER pathways. First principle density functional theory (DFT) calculation was then performed to calculate the Gibbs free energy for the intermediate structures established on the (010) surface of $BiVO_4$ slab models, which evidently demonstrates the superiority of monoclinic $BiVO_4$ with greater lattice distortion by manifesting markedly diminished reaction energy barrier for the water oxidation process. Furthermore, by employing the first principal molecular dynamic (MD) simulations, some novel insights regarding the OER mechanism, i.e. oxidazibility of some key OER intermediates and spontaneous water dissociative adsorption process over the (010) surface are represented and discussed comprehensively.

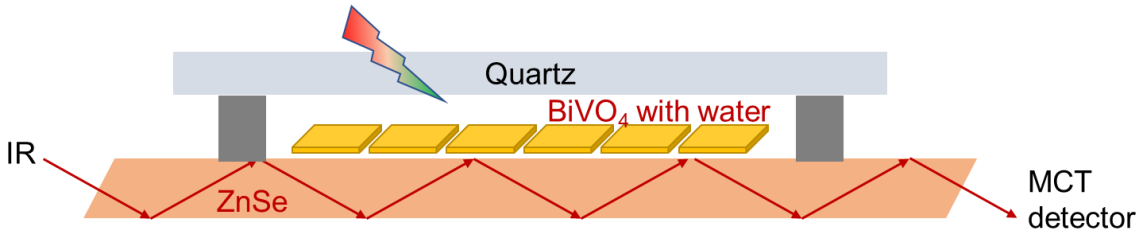

Figure 3.1. Schematic illustration for the ATR-IR setup.

3.2. Experimental Details

Attenuated total reflectance (ATR) Fourier transform infrared spectroscopy (FTIR) analysis was conducted in order to probe the reaction intermediates formed during the photocatalytic water oxidation over monoclinic $BiVO_4$ sample. In this study, BVO NFs A was used for the ATR-IR analysis and synthesized according to the procedure described in the previous chapter (see section 2.2.2). The schematic for the ATR-IR setup is shown in **Figure 3.1**. An internal reflection element of ZnSe (50mm × 20mm × 3 mm) was obtained from Pier Optics Co., Ltd. Japan as the substrate. A stainless steel ring with a thickness of 0.1 mm and an inner diameter of 16 mm was used as a separator between the ZnSe substrate and a quartz window, and 20 µL BVO NFs A suspension in water without a sacrificial agent was sealed therein. An FTIR spectrometer (FT/IR-6300, Jasco Inc.) with liquid nitrogen cooled MCT detector was used and purged with dry nitrogen before ATR-IR experiments. During the measurement, the sample system was illuminated by visible light using a xenon (Xe) lamp (LA-251 Xe, Hayashi Tokei, Japan) equipped with an L-42 filter. Before the light illumination, the setup was kept in the dark until the background was subtracted to be stable, generally after 5 minutes. The absorbance spectra were then obtained and recorded with a resolution of 4 cm^{-1} and repeated scans 32 times under light illumination at certain time intervals.

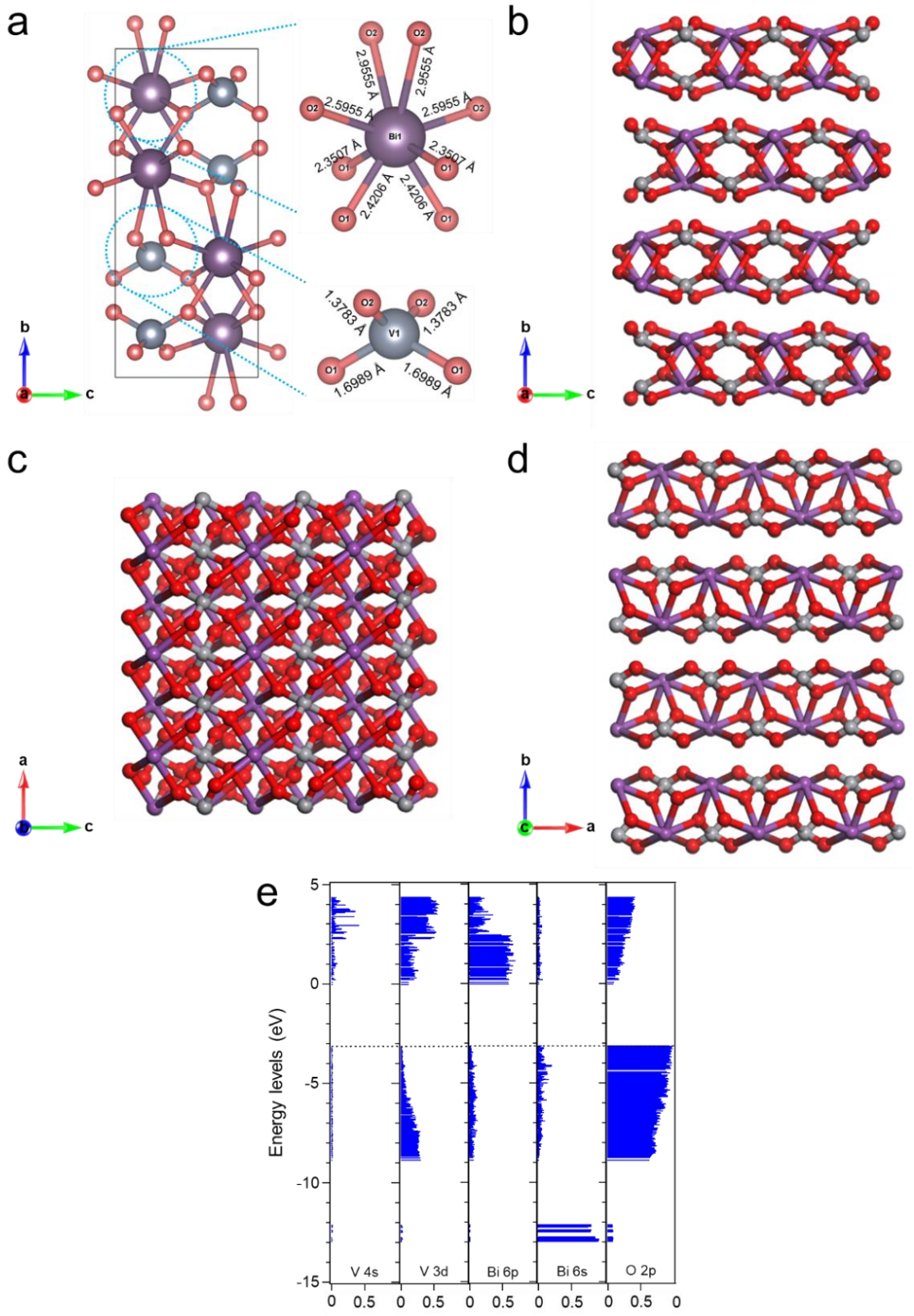

Figure 3.2. (a) Unit cell lattice configuration, (b) slab model with dimension of 3a × 2b × 3c viewed from [100], (c) [010], and (d) [100] directions (Bi: purple, V: gray, and O: red), and (e) theoretical electronic structure properties of BVO A. The broken lines in (e) indicate the highest occupied levels.

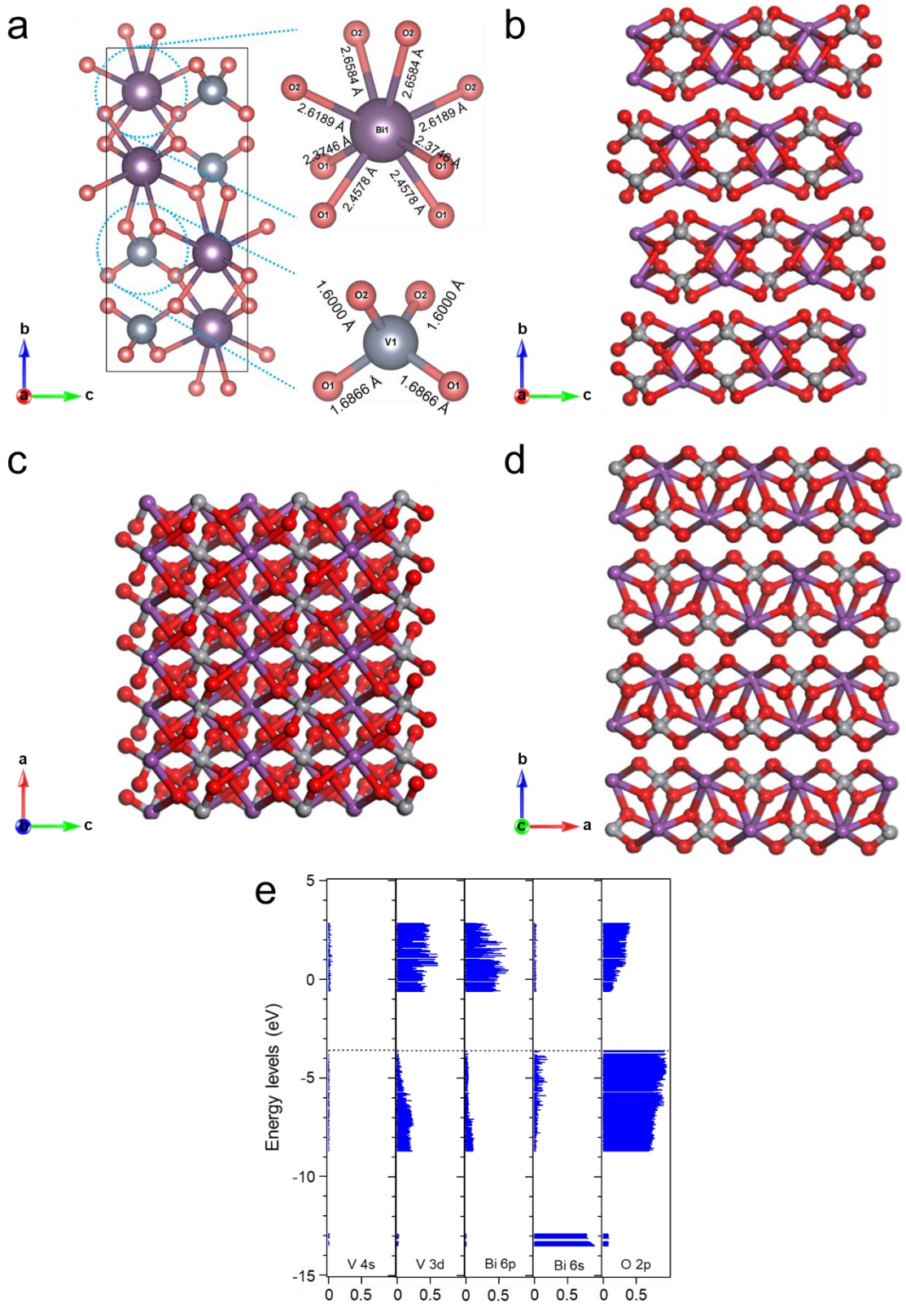

Figure 3.3. (a) Unit cell lattice configuration, (b) slab model with dimension of 3a × 2b × 3c viewed from [100], (c) [010], and (d) [100] directions (Bi: purple, V: gray, and O: red), and (e) theoretical electronic structure properties of BVO B. The broken lines in (e) indicate the highest occupied levels.

3.3. Computational Details

3.3.1. Structural Properties of Monoclinic $BiVO_4$ Slab Models

Two model slabs of monoclinic scheelite $BiVO_4$ with the dimension of 3a × (2b + ~16 Å vacuum spaces for reactant molecules) × 3c exposing the (010) facet, referred as BVO A and BVO B were initially constructed based on the refined structure provided by the XRD Rietveld refinement of BVO NFs A and BVO NFs B respectively (see Chapter 2, section 2.3.2). These slab models were utilized for the first principle calculations, which would be introduced in the following sections. In this regard, BVO A represents the monoclinic $BiVO_4$ with greater degree of lattice distortion compared to BVO B. As shown in **Figure 3.2 a** and **Figure 3.3 a**, there are two types of V−O bonds and four types of Bi−O bonds with distinct lengths that exist within the VO_4 tetrahedrons and the BiO_8 dodecahedron, respectively, which signifies the typical clinobisvanite structures.[28-30] In contrast to the more symmetrical tetragonal $BiVO_4$, the monoclinic $BiVO_4$ crystals tend to possess unbalance symmetry constraints and lattice distortion, due to the presence of lone-pair electron around the Bi $6s^2$ orbital, which is correlated to the hybridization of Bi 6s and O 2p orbital at the top of the valence band (VB).[31-36] Accordingly, the lattice parameters of the unit cell of BVO A are as follows: a = 5.1960 Å, b = 11.7051 Å, c = 5.0956 Å, β = 90.37°, while the lattice constants of BVO B are: a = 5.1940 Å, b = 11.7049 Å, c = 5.0967 Å, β = 90.35°.

Each model slab is composed of 432 atoms in total, which are indicated by the following serial indices: Bi; 1~72, V; 73~144, O; 145~432. Among them, Bi1–Bi9 are located near the upper surface, Bi64–Bi72 near the lower surface, V73–V81 near the upper surface, V136–V144 near the lower surface, O145–O162 at the upper surface, and O415–O432 at the lower surface. In the inner part of the slab crystal, each V atom is surrounded by 4 oxygen atoms (4c-V), while each Bi atom is surrounded by 8 oxygen atoms (8c-Bi). At the surface, the coordination of V atoms is preserved (4c-V), while each Bi atom is unsaturated and only surrounded by 6 oxygen atoms (6c-Bi). Snapshots of the crystal structure of BVO A and BVO B from the [100], [010], and [001] directions are shown in **Figure 3.2 b-d** and **Figure 3.3 b-d**, respectively.

As shown in **Figure 3.2 e** and **Figure 3.3 e**, the valence bands of both BVO A and BVO B slab models are primarily composed of O 2p orbitals (around 80-90%), while the conduction bands are dominated by Bi 6p and V 3d states. The levels around the

conduction band minimum (CBM) of the slab model are mainly composed of Bi 6p and V 3d unoccupied states. Furthermore, Bi 6s orbitals also hybridize with O 2p close to the valence band maximum (VBM) level, while the dominant components of Bi 6s are located at much lower energy (roughly 9 eV below VBM), which correspond to the theoretical electronic properties (i.e. density of state profiles projected onto atomic orbitals) reported on the bulk crystal using a unit cell.[37] The corresponding band gaps are quite similar, which is around 3.0 eV, an overestimated value compared to that of the actual materials (~2.4 eV).

3.3.2. Gibbs free energy Evaluation

The density functional theory (DFT) calculations for evaluating the Gibbs free energy of several water oxidation intermediate structure was performed using PWSCF code from the Quantum ESPRESSO package.[38,39] In order to imitate the configuration of some certain water oxidation intermediate species, some modifications to the slab models were conducted accordingly by introducing some external hydrogen and/or oxygen atoms into the proximity of surface atoms. The exchange and correlation potential were used in the generalized gradient approximation (GGA) in the scheme of Perdew, Burke and Ernzerrof (PBE).[40] All the geometry structures were relaxed until the energy converged to 1×10^{-5} Ry and 1×10^{-3} eV/Å for electronic and force convergence. The projector augmented wave (PAW) method[41] with a plane-wave cutoff energy of 55 Ry was used for the real-space integration grid. Brillouin zone was sampled by 3×3×1 k-points Monkhorst-Pack grid for optimization. The DFT-D3 method was employed for van der Waals correction.[42,43] The free energy change (ΔG) of each elementary reaction step was calculated according to the computational hydrogen electrode (CHE) model suggested by Nørskov et al.[44-46] In this method, the free energy change is defined as:

$$\Delta G = \Delta E + \Delta ZPE - T\Delta S \quad (3\text{-}1)$$

where ΔE is the reaction energy directly obtained from DFT calculations, ΔZPE and ΔS are the zero point energy difference and the entropy change between the products and reactants, respectively, and T is the temperature (298.15 K). The entropies and vibrational frequencies of molecules in the gas phase were taken from the NIST database,[44] while the vibrational frequencies of adsorbed species were computed to obtain ZPE contribution in the free energy expression. Only adsorbate vibrational modes were computed explicitly,

while the catalyst sheet was fixed (assuming that vibrations of the substrate were negligible).[46-49]

3.3.3. Dynamical Simulation and Electronic Structure Calculations

The molecular dynamic (MD) simulations within the Car-Parrinello framework (CPMD) based on DFT-GGA-LSD were conducted to probe the dynamic interactions between the catalytic surface of BVO A slab model and the reactant molecules. Employing the models, the CPMD based on a plane-wave basis set with an energy cut-off of 80 Ry, with the sampling of the Brillouin restricted to the Γ point, a fictitious electronic mass of 1200 a.u., and an integration step of 5.0 a.u. were achieved and we obtained equilibrium structure of the corresponding system at 300 K. Afterward, in order to investigate the charge carriers nature at the interface area of the inhomogeneous system, the electronic structure calculations were carried out by first-principles calculation based on the density functional theory (DFT) using norm-conserving pseudopotentials and an unrestricted spin (Local Spin Density, LSD) approach and including gradient corrections (GGA) on the exchange and correlation functional. The configuration of electrons and wave functions prepared for solving Kohn-Sham equations were almost the same as those in dynamical simulations but some unoccupied states were included in the calculation to investigate the energy levels of unoccupied states; the number of unoccupied states was about 25~30 % of the number of occupied states. The weight profiles of atomic orbital components were obtained by projecting the eigen-wave-function onto the corresponding atomic orbitals. The recipe of the pseudopotentials for both calculations are as follows: The exchange and correlation functional after Becke-Lee-Yang-Parr (BLYP) was used.[50,51] The valence-core interaction was modeled by norm-conserving pseudopotentials (NCPP) employing a plane-wave basis set with an energy cut-off of 80 Ry,[52] with the sampling of the Brillouin restricted to the Γ point. The electrons of Bi 5d, 6s, 6p; V 3d, 4s; O 2s, 2p were treated explicitly as valence electrons.

In order to imitate the actual inhomogeneous systems of monoclinic $BiVO_4$ during the photocatalytic water oxidation, several simulation scenarios were prepared, by which some liquid reactants and/or modifications were introduced to the system of BVO A slab model, depending on the objectives of the calculations. Specifically, there are two objectives to investigate, i.e. 1) the oxidazibility of some water oxidation key intermediates and 2) spontaneous dissociative adsorptive process of water molecules over

the (010) facet of BVO A. In all scenarios, 164 water (H_2O) molecules, 3 solvated Ag^+ and NO_3^- ions were added to the simulation system and the corresponding atoms were indicated by the following serial indices: O_{NO3} (oxygen atoms of NO_3^- ions); 433~441, O_{H2O} (oxygen atoms of water molecules and those of OH^-); 442~606, N; 607~609, Ag; 610~612, and H; 613~942. Furthermore, to probe the effect of the characteristic $BiVO_4$ (010) surface structure, Bi1-9, V73-81, O145-180 around the upper surface and Bi64-72, V136-144, O397-432 around the lower surface were fixed during the MD simulation in all scenarios. The detailed information regarding any further modification would be explained in the corresponding section.

3.4. Results and Discussion

3.4.1. Identification of Water Oxidation Intermediates

Attenuated total reflectance infrared (ATR-IR) spectroscopy analysis over a water suspension of BVO NFs A sample (prepared according to the procedure introduced in **Chapter 2**) irradiated with visible light (Xe lamp equipped with L-42 filter) was applied in order to gain some insight into the reaction intermediate structures, which could be utilized to deduce the water oxidation reaction mechanism. **Figure 3.4** displays the time-dependent ATR-IR spectra, with a reference spectrum taken before the irradiation as background, in the range of 1225-725 nm where the vibrational bands of water oxidation intermediates are most likely to appear. Three IR bands centered at 1151 cm^{-1}, 995 cm^{-1}, and 798 cm^{-1} are observed to grow upwardly while a band at 1120 cm^{-1} decreases along with visible light irradiation time. The upward bands at 1151 cm^{-1} correspond to the superoxide O_2^- species,[53-56] while the upward bands at 995 cm^{-1} can be ascribed to the surface peroxo[53,54] and/or metal=O (mostly likely V=O) species.[56-58] These above-mentioned intermediates are often encountered as primary intermediates for water oxidation reaction.

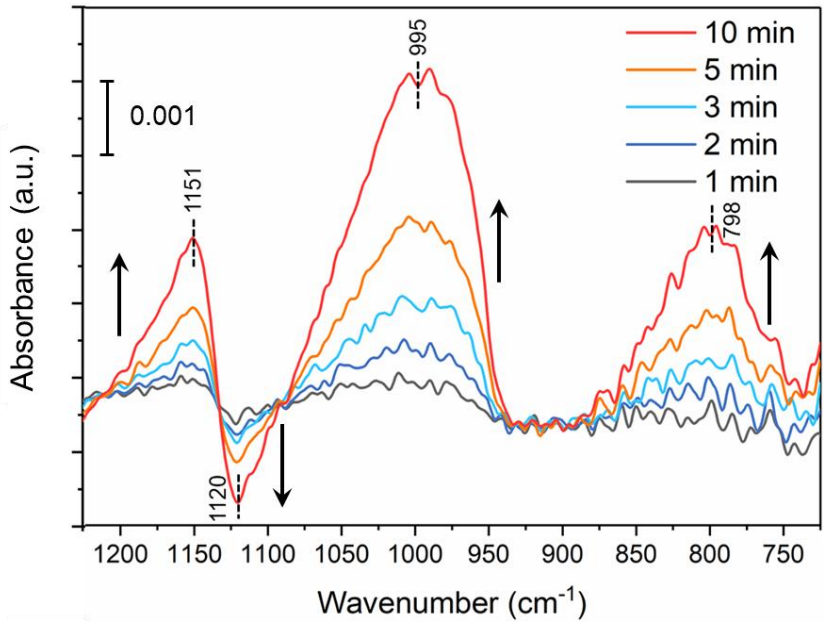

Figure 3.4. Time-dependent *in situ* ATR-IR spectra of BVO NFs A in contact with water suspension irradiated by visible light (LA-251 Xe lamp equipped with L-42 filter).

The assignment of the peak at 1120 cm^{-1} is a little hard because the vibrational peak of typical water oxidation intermediates do not usually appear in such an energy region, especially since this peak exhibit declining behavior along the illumination time, suggesting that the corresponding species was consumed by a photocatalytic process. In this regard, it might be plausible to associate this band with the O–H stretching vibrations of Bi–OH species.[59,60] This is consistent with the findings from the previous study, by which the O 1s high-resolution XPS spectra indicate the presence of abundant adsorbed hydroxyl (–OH) species on the surface of BVO NFs samples. The formation of V–OH on the surface of monoclinic $BiVO_4$ is quite unlikely since the surface V atoms are already fully coordinated with four oxygen atoms, while the exposed Bi sites on the surface are imperfectly oxygen coordinated,[61,62] thus rendering the possible formation of Bi–OH species. Accordingly, the Bi-OH species might have existed naturally on the surface of monoclinic $BiVO_4$ sample even before the light irradiation, allowing this species to act as the first OER intermediates and participate in the water oxidation reaction, thus explaining the downward direction of the corresponding peak.

The upward band at 798 cm^{-1} can be correlated with the O–O stretching mode of the bridged peroxo species (μ-peroxo), which can be assigned to the Bi–O–O–V structure. The assignment of this band to bridging O–O species is also supported by the early IR studies of metal-dioxygen complexes,[55,63-66] which report that the O–O stretching mode

of a bridged peroxo species is observed in a region of 740-920 cm^{-1}. For example, Nakamura et al. utilized an *in-situ* multiple internal reflection infrared (MIR-IR) spectroscopy to analyze a film of Pt-loaded rutile TiO_2 in contact with aqueous 0.01 M NaOH (pH 11.9) solution and observed a strong and growing band located at 812 cm^{-1}, which was later assigned as the bridge type surface peroxo Ti–O–O–Ti species.[63] In other work, by using the same technique, a characteristic band at 860 cm^{-1} was assigned for the same Ti–O–O–Ti species over anatase TiO_2 particles in contact with $FeCl_3$ aqueous solution.[66] Hence, it is reasonable to assign the observed 798 cm^{-1} band in this study to the unique lattice bridging Bi–O–O–V species. The two last-mentioned reaction intermediate structures (Bi–OH and Bi–O–O–V) are not commonly encountered over other oxide semiconductors, by which I speculate that they would play critical roles during the catalytic OER process.

3.4.2. Gibbs Free Energy of Water Oxidation Intermediates on (010) Facet of Monoclinic $BiVO_4$

Considering the existence of the above-mentioned intermediate structures, DFT calculations were performed to acquire Gibbs free energy diagram over the water oxidation reaction. The stipulated OER pathways are described as follows. Initially, the unsaturated Bi site on the surface adsorbs a water molecule to form Bi–OH species and release a proton (Step 1). As the reaction proceeds, the OH moiety gets further dehydrogenated and forms an electrophilic O adatom which promptly gains an electron by bonding with an adjacent O atom to establish the μ-peroxo intermediate of Bi–O–O–V structure (Step 2). Afterwards, a second H_2O molecule is adsorbed on the previous Bi site which is still unsaturated, another H adatom is removed, and accordingly the Bi–OH structure is once again formed (Step 3). After the last proton is removed, the resulting O adatom further interacts with the peroxo group to form the superoxo intermediate (Step 4). After a quick rearrangement, an O_2 molecule is finally generated and desorbed from the catalytic surface (Step 5). **Figure 3.5** and **Table 2.2** shows the calculated Gibbs free energy for the intermediate structures as well as the energy barrier of each water oxidation elementary step over the (010) facets of BVO A and BVO B slab models.

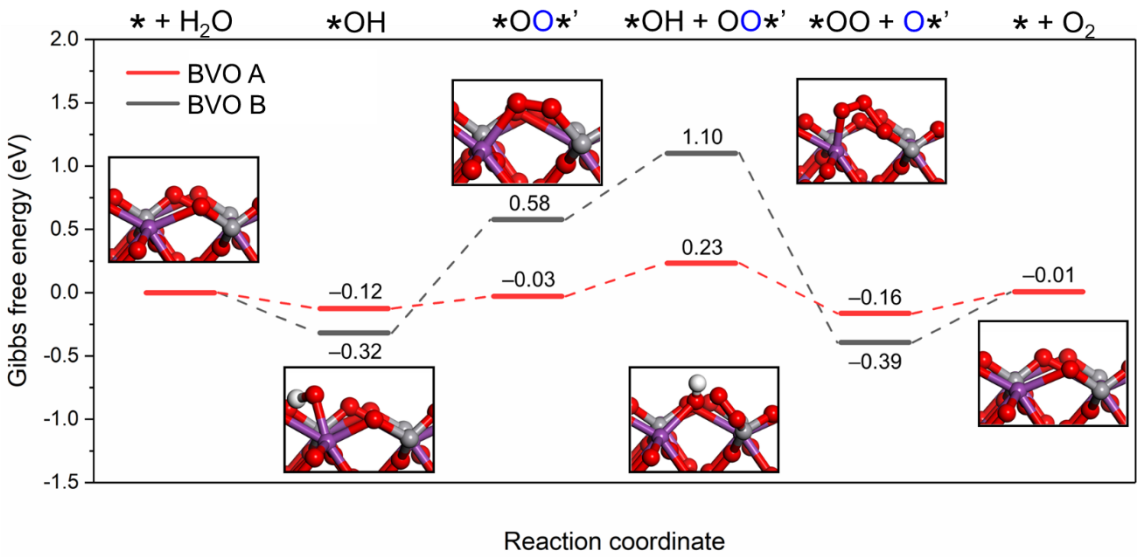

Figure 3.5. Energy profiles for OER over (010) facets of BVO A and BVO B. The *, *', and blue O on top of the diagram correspond to the Bi site, V site, and lattice oxygen, respectively.

Table 3.1. Calculated Gibbs free energies differences of the water oxidation elementary steps over (010) surfaces of BVO A and BVO B slab models. The *, *', and blue O correspond to the Bi site, V site, and lattice oxygen, respectively.

Step	Reactions	ΔG BVO $A_{(010)}$ (eV)	ΔG BVO $B_{(010)}$ (eV)
1	* + H_2O + h^+ → *OH + H^+	–0.12	–0.32
2	*OH + h^+ → *OO*' + H^+	0.09	0.90
3	*OO*' + H_2O + h^+ → *OH + OO*' + H^+	0.26	0.52
4	*OH + OO*' + h^+ → *OO + O*' + H^+	–0.39	–1.49
5	*OO → * + O_2	0.17	0.40

The first step of water dissociative adsorption is found to be exothermic over the (010) facets of both BVO A and BVO B, which indicates that this reaction is relatively favorable to occur. On the other hand, the detailed calculations also reveal that the formation of the Bi–O–O–V structure (Step 2) and the following water dissociation

process (Step 3) are thermodynamically unfavorable with high positive Gibbs free energy and hence are considered as the rate-determining steps for the overall water oxidation process. Interestingly, the corresponding energy barriers for both steps are much lower on BVO A with a total energy barrier of 0.35 eV (0.09 + 0.26 eV), compared to BVO B that has a total energy barrier of 1.42 eV (0.90 + 0.52 eV), indicating that the formation of the corresponding intermediate structures is more favorable to occur on the surface of the former one. As the reaction continues, the free-energy profiles for the proton removal and formation of superoxo species drop down-hill for both BVO A and BVO B. Noteworthily, the surface of BVO B is more susceptible to surface poisoning due to the high required energy for the desorption of O_2 molecule (0.38 eV), compared to BVO A which needs relatively less energy (0.15 eV). From the thermodynamic point of view, the overall calculations for the water oxidation processes indicate that the OER would occur more easily on the surface of BVO A which exhibits greater degree of lattice distortion compared to BVO B, suggesting the benefits of lattice distortion effect over the catalytic surface reaction of water oxidation process. As previously found, monoclinic $BiVO_4$ with greater degree of lattice distortion manifests lattice configuration with shrank V−O bonds and elongated Bi−O bonds. The corresponding altered bonds are particularly located on the surface of the unit-cell of BVO A (compare **Figure 3.2 a** and **Figure 3.3 b**). Consequently, it is more likely that they would terminate the crystal structure of monoclinic $BiVO_4$ along the (010) planes in the actual system, thus enabling them to be exposed and strongly influence the catalytic surface behavior.

3.4.3. Oxidizability of Water Oxidation Key Intermediates

In order to gain more understanding of the water oxidation process, some simulation models in which some reactant molecules were brought into contact with the (010) surface of the monoclinic BVO A slab were prepared to mimic the real system and the details of the dynamical behavior on the surface were theoretically observed by Car-Parinello Molecular Dynamics (CPMD) simulation, which is quite popular among the first principles approaches.[67] First-principal MD simulation is an effective tool to analyze the atomic and molecular interaction at the interface of any material surfaces and reactant molecules, which might provide some valuable information regarding the catalytic reaction mechanism. In this study, both the global and the local detailed electronic properties of the inhomogeneous system when important adsorbate structures

regarded as the key reaction intermediates appeared at the interface area were also investigated.

In a former work, Oshikiri et al. inspected the water molecule adsorption behavior over (100) $BiVO_4$ surfaces at 300 K using the MD simulation, by which no dissociative water molecule adsorption could be observed at the exposed Bi sites, which were actually expected to be reactive since they were imperfectly oxygen coordinated.[61,68] On the other hand, dissociative adsorptions of water molecules at room temperature were successfully observed at the exposed three-fold oxygen-coordinated V sites of other vanadate materials (YVO_4 and $InVO_4$).[61,62,68-70] Intriguingly, based on the previously discussed ATR-IR analysis, possible participation of bismuth hydroxyl (Bi–OH) species as the first intermediate for water oxidation reaction is considered, which quite contradicts the above-mentioned notions, since it might signify the active participation of Bi sites during the water oxidation reaction. In this case, the MD simulation study was used to probe the possibility of Bi sites serving as the reactive sites for triggering the water oxidation reaction, by comparing the behavior of Bi and V sites on the surface of BVO A model slab.

Unfortunately, due to the limited time for the simulation, it was difficult to observe the –V–OH and –Bi–OH structures being formed on $BiVO_4$ (010) facet by a spontaneous dissociative adsorption of a water molecule. Therefore, in order to save the time and cost for the calculation, another model was prepared in which V–OH and Bi–OH structures were deliberately created on the (010) surface of BVO A slab and the corresponding O 2p energy levels of both species were also calculated. For doing that, one of the water molecules was firstly broken down into H^+ and OH^- ions, with a consideration that those ions would also appear in the actual situation for any aqueous solution. Afterward, the H^+ and OH^- ion were attached to one surficial 4c-V site and 6c-Bi site, respectively to form –V140–O_{lat}422–H and –Bi67–O_{H2O}473–H at the surface of the model slab (see **Figure 3.6 a**, **c**). A thermal equilibrium state at 300K was roughly obtained (indicating the possible formation and stabilization of such structures) and the corresponding electronic properties were then investigated.

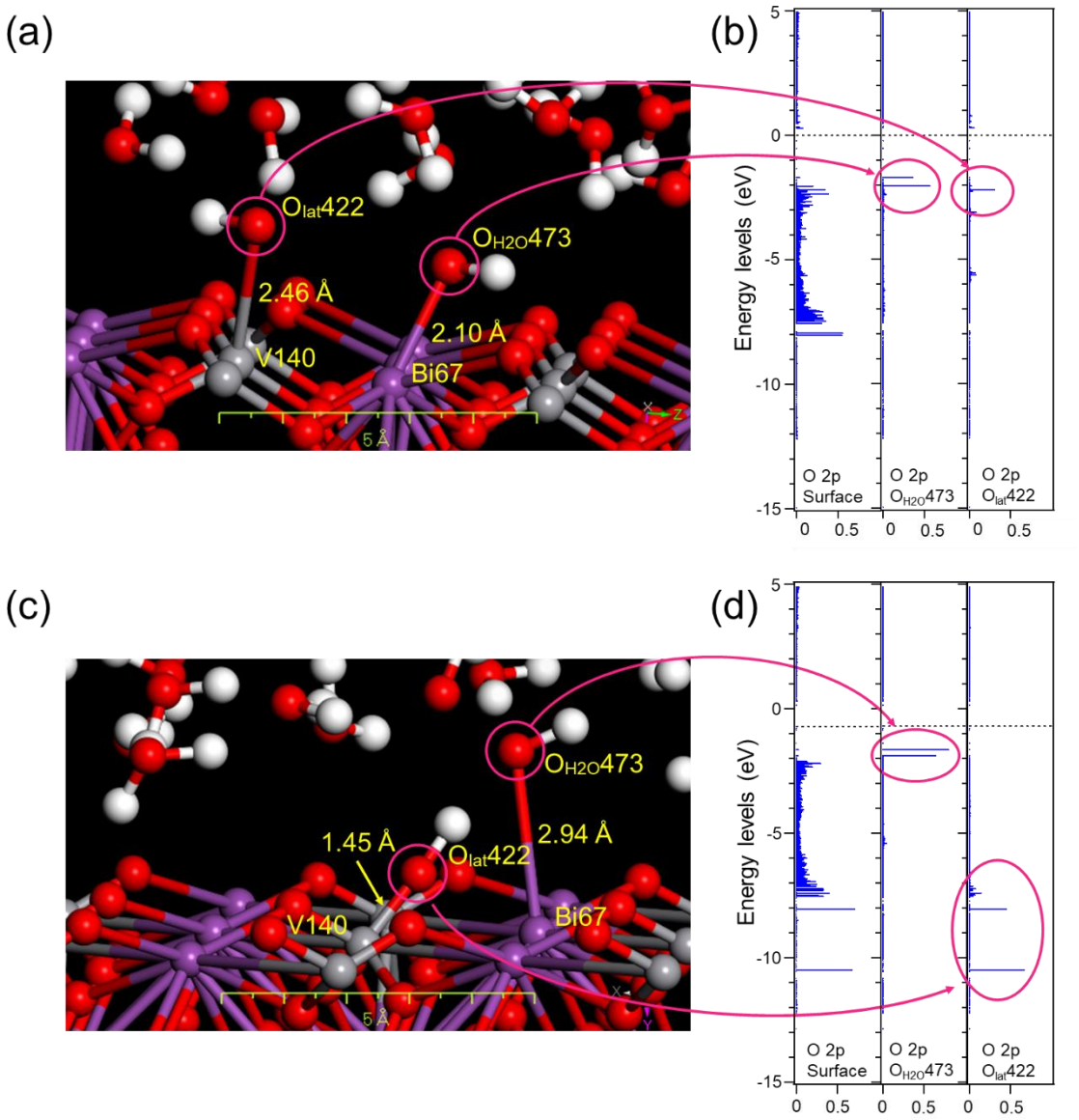

Figure 3.6. Geometry and O 2p energy levels at the moment when –Bi–OH and –V–OH structures were formed on the surface of BVO A slab with the minimum value of (a-b) Bi–O atomic distance (2.10 Å) and (c-d) V–O atomic distance (1.45 Å).

Figure 3.6 a-b displays the geometry and the corresponding electronic properties (O 2p energy levels) at the moment when the Bi–O atomic distance of the –Bi–OH indicated a local minimum value (2.10 Å), by which the V–O length of the adjacent –V–OH species was 2.46 Å. In this situation, both the O 2p energy levels of –Bi–OH ($O_{H2O}473$) and –V–OH ($O_{lat}422$) species are located at around the top of the O 2p band formed by the surficial O atoms, signifying that it would be possible for the O^{2-} ions belonging to both species to readily donate some electrons and participate in the oxidation process. Interestingly, when the V–O atomic distance reached a local minimum value (1.45 Å) while the Bi–O

distance was extended to 2.94 Å (as shown in **Figure 3.6 c**), which occurred about 0.86 picoseconds after the above-mentioned situation, some important variation can be discerned. While the O 2p energy levels of Bi–OH species are still located at around the top of the surficial O 2p band (**Figure 3.6 d)**, hence preserving its advantage to be easily oxidized, in contrast, the O 2p energy level of –V–OH moves down dramatically as the V–O atomic distance decreases, therefore prohibiting the oxidation of such species. Accordingly, it can be concluded that the –Bi–OH species is relatively more vulnerable to the oxidation process and consequently, it would be able to act as the pioneer for the water oxidation reaction, in accordance with the finding in our previous work. Under these circumstances, even though the surficial oxygen atom from the 4c-V (in the original structure) is actually able to disconnect from the adjacent Bi site and adsorb a proton to stabilize the structure, the resulting –V–OH species would not be able to easily proceed with further water oxidation process, since the opportunity for the corresponding oxygen atom to donate electrons is quite less. In contrast, the surficial 6c-Bi sites would be able to participate in the OER more readily, as long as it can adsorb the hydroxyl ion or undergo the dissociation adsorption of water and thus form the active Bi–OH species. Accordingly, spontaneous dissociative adsorption of water molecules over Bi sites on the surface of monoclinic $BiVO_4$ becomes very essential to the overall water oxidation process.

In addition to –Bi–OH species, a unique bridged-peroxo structure (–Bi–O–O–V–) was also observed by the ATR-IR analysis and regarded as one of the water oxidation reaction intermediates, i.e. the oxidation product of –Bi–OH species. In order to probe whether this –Bi–O–O–V– structure could be further oxidized, it was artificially established on the surface of BVO A slab model, by stripping one O^{2-} ion ($O_{H2O}473$) from a water molecule and taking that ion into the vicinity of the exposed 6c-Bi67 site to be adsorbed. After some time, the –Bi67–$O_{H2O}473$–$O_{lat}422$–V140– structure on the surface was stabilized into the structure as displayed in **Figure 3.7 a**, where the $O_{lat}422$–$O_{H2O}473$ atomic distance was 1.43 Å. The O–O distance roughly oscillated in the range of 1.3~1.7 Å during the MD simulation, which is longer than that of normal oxygen gaseous molecule (1.21 Å). As depicted on **Figure 3.7 b**, the electronic properties also elucidate that both oxygen atoms ($O_{lat}422$ and $O_{H2O}473$) forming the bridging oxygen-like molecule possess high enough O 2p energy levels which would enable this species to donate electrons and thus be further oxidized by the photogenerated holes.

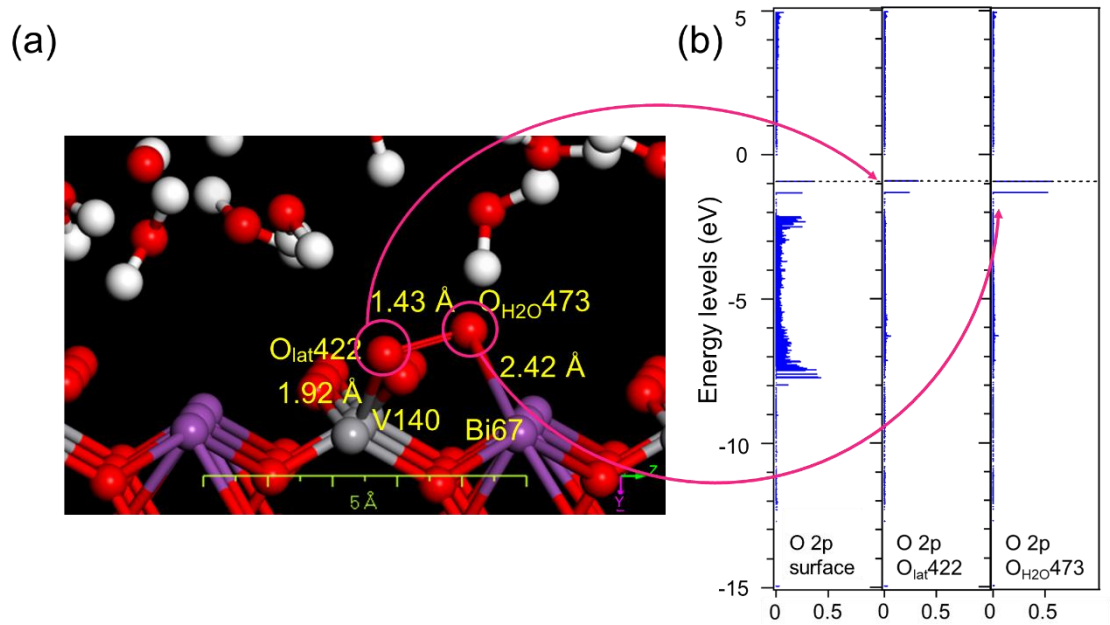

Figure 3.7. (a) Geometry and (b) the corresponding O 2p energy levels of the lower surface when the –Bi–O–O–V– structure was stabilized on the surface of BVO A slab.

3.4.4. Spontaneous Dissociative Adsorption of Water Molecules over (010) Facet of Monoclinic $BiVO_4$

Another scenario for the MD simulation was performed where some spontaneous dissociative adsorptions of water molecules over the Bi sites were successfully observed. The corresponding simulation model accommodates a (010) surface of BVO A slab, exposing not only the original 4c-V and 6c-Bi structures but also an artificial 7c-Bi species (Bi5) which was formed by carefully shifting one surficial oxygen atom (O_{lat}156), derived from one of the 4c-V structures (V78), on the surface without applying much stress to the overall monoclinic $BiVO_4$ crystal system. In order to stabilize the resulting 3c-V structure due to the oxygen shifting, it was connected to one NO_3^- ion to reform the 4c-V structure. **Figure 3.8** shows two crucial moments during the water molecule dissociative adsorption process over the (010) facet of BVO A slab.

In detail, firstly, one water molecule came close to the 7c-Bi site (Bi5), by which it extracted one proton (H^+) from the water molecule to produce a –Bi5–O_{lat}156H species and OH^- ion. Afterward, the OH^- ion approached the vicinity of the water molecule (H–O_{H2O}503–H), which had been adsorbed beforehand by another neighboring 6c-Bi site (Bi4), and as a consequence, the –Bi4–(H)O_{H2O}503--H--OH structure was formed temporally on the surface (**Figure 3.8 a**). The temporal intermediate structure was then

transformed into –Bi4–O_{H2O}503H species and H_2O molecule soon later. At this moment, two water molecules had successfully been dissociated at two different Bi sites (see **Figure 3.8 b**). This kind of process is predicted to repeat itself one after another, which demonstrated the natural production process of active –Bi–OH species by the dynamic interaction between the catalytic (010) surface of monoclinic $BiVO_4$, water molecules, and hydroxyl ions, as also illustrated in **Figure 3.9**.

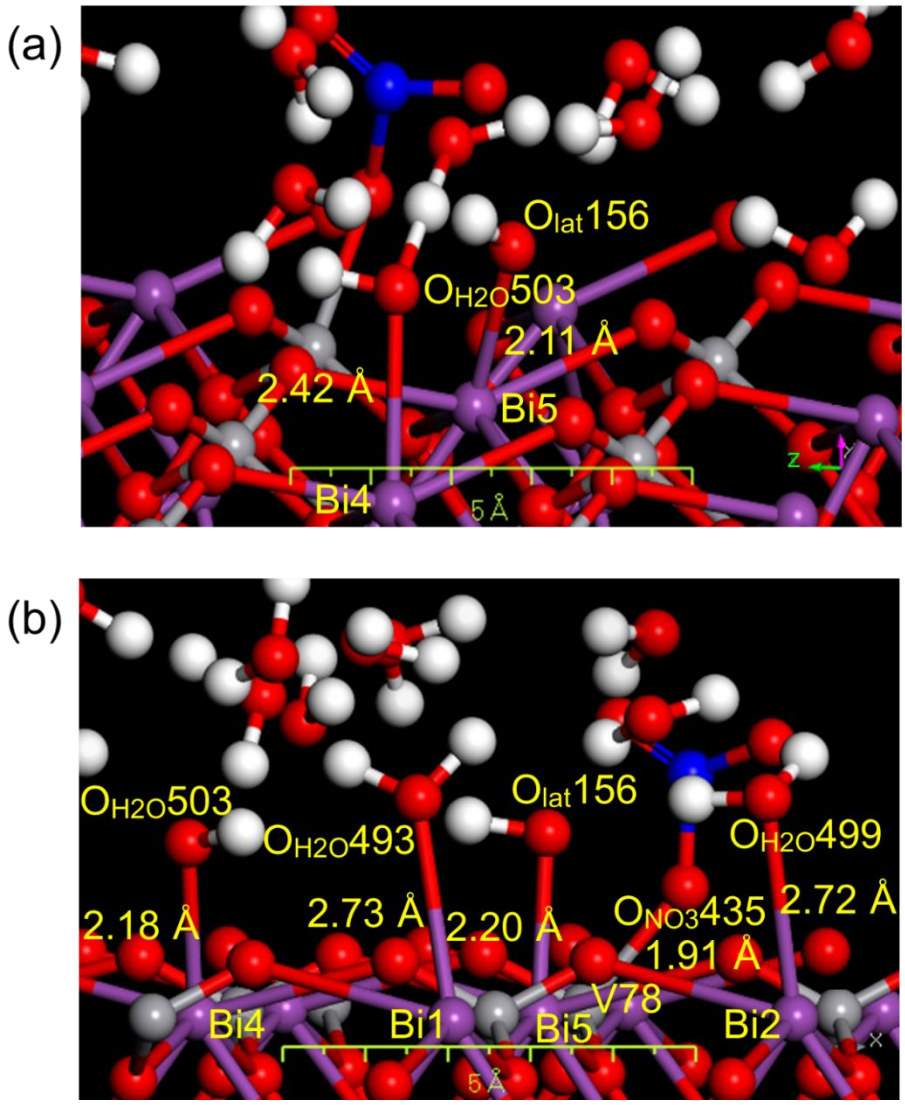

Figure 3.8. Two different geometries during the dissociative adsorptions of water molecules over the (010) surface of BVO A slab: (a) when the Bi4–(H–O_{H2O}503--H)--OH structure was formed and (b) when two –Bi–OH structures (–Bi5–O_{lat}156H and –Bi4–O_{H2O}503H) were formed.

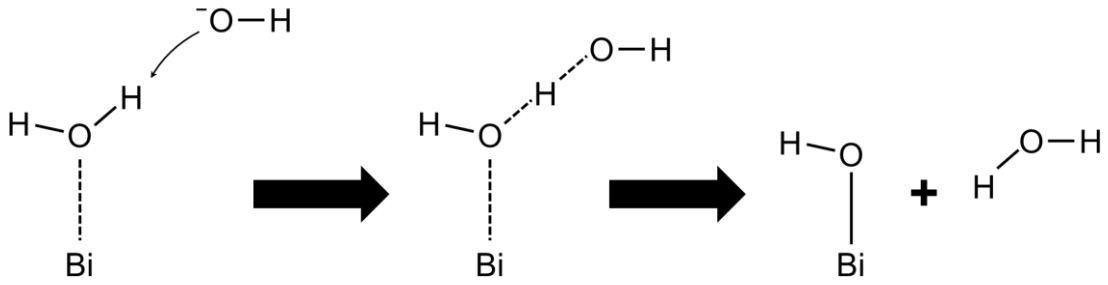

Figure 3.9. Spontaneous dissociative adsorption of water molecules over the surficial Bi site on the (010) facet of BVO A slab.

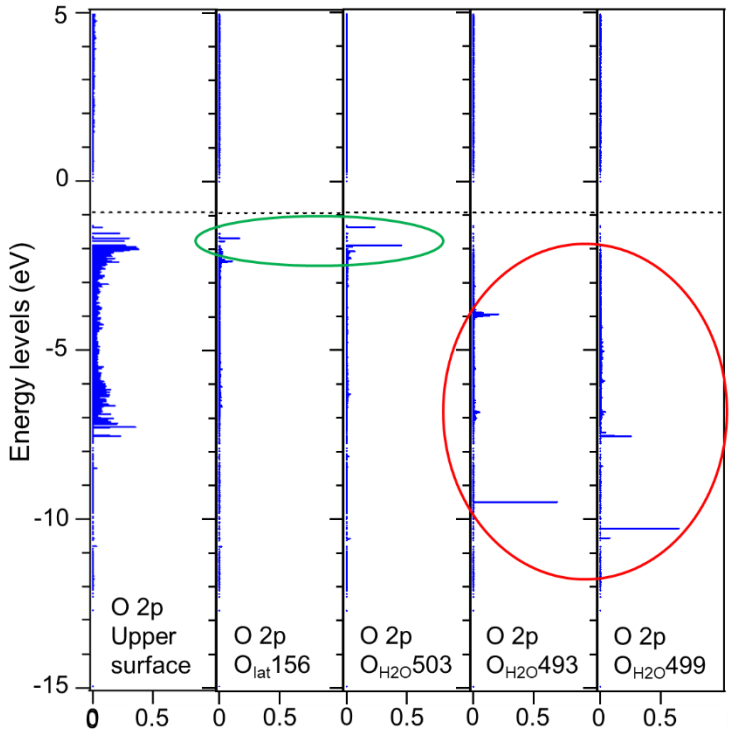

Figure 3.10. O 2p energy levels during the moment when two –Bi–OH structures were formed, as represented in **Figure 3.8 b**.

At the same moment when two –Bi–OH structures were formed (**Figure 3.8 b**), there were two water molecules (H_2O493 and H_2O499) being undissociatively adsorbed on two other 6c-Bi sites (Bi1 and Bi2). Herein, the electronic properties (O 2p energy bands) of those structures are shown in **Figure 3.10**. The O 2p component profiles of those abovementioned –Bi–OH structures (O_{lat}156 and O_{H2O}503), as circled in green, reveal similar tendency with the previous result, by which both species would be easily oxidized, since their energy levels are particularly located on top of the valence band. Nonetheless, the undissociated adsorbed water molecules shouldn't be oxidized, since their O 2p

energy levels (O_{H2O}493 and O_{H2O}499) are considerably low, as marked by the red circle. According to our previous findings, an H_2O molecule adsorbed onto the 6c-Bi site is relatively stable, where the distances between the O atoms belonging to H_2O molecules and the Bi atoms at the surface range between 2.7 and 3.0 Å.[61] Hence, in order for those water molecules to participate in the OER, they would need to undergo the previously described process, where some hydroxyl ion trigger some structure transformation to generate the –Bi–OH species which is more susceptible to the oxidation process. Such findings combined with the previous results encourage us to conclude that the existence and/or formation of –Bi–OH species by the assistance of hydroxyl ion within the (010) surface of monoclinic $BiVO_4$ are essential for the water oxidation reaction.

3.5. Conclusion

In summary, a combination of experimental and theoretical approaches was utilized to gain some new insights into water oxidation reaction over (010) facet of monoclinic $BiVO_4$, by which the key role of lattice distortion was unraveled and highlighted. By ATR-IR analysis, some water oxidation intermediates including the active Bi–OH and unique bridged Bi–O–O–V species were firstly identified, thus allowing the stipulation of possible water oxidation mechanism. Correspondingly, the DFT calculations for Gibbs free energy indicate the favorable water oxidation process over the (010) surface of $BiVO_4$ slab model with greater degree of lattice distortion, thus elucidating the additional benefit of lattice distortion effect over the catalytic surface features of monoclinic $BiVO_4$ for driving more efficient OER. In addition, by employing the first-principal molecular dynamic simulations and the corresponding electronic structure calculations, the observed key intermediates (Bi–OH and Bi–O–O–V species) were found to possess high enough O 2p energy levels, thus enabling them to readily donate some electrons and be oxidized by the photogenerated holes. Lastly, some spontaneous dissociative adsorption process of water molecules over the unsaturated 6c-Bi sites was also demonstrated, by which hydroxyl ion (OH^-) would play a critical role in triggering the transformation of undissociatively adsorbed water molecules into the active –Bi–OH species. The findings of this study deepens the understanding of water oxidation reaction over monoclinic $BiVO_4$ and might provide some inspiration for the rational design of superior $BiVO_4$-based material for more efficient photocatalytic OER.

References

1. J. Liu, Y. Zou, B. Jin, K. Zhang, J. H. Park (2019) Hydrogen Peroxide Production from Solar Water Oxidation. ACS Energy Lett. 4 (12):3018-3027. doi:10.1021/acsenergylett.9b02199

2. Z. Wang, C. Li, K. Domen (2019) Recent Developments in Heterogeneous Photocatalysts for Solar-Driven Overall Water Splitting. Chem. Soc. Rev. 48 (7):2109-2125. doi:10.1039/C8CS00542G

3. H. Lin, S. Luo, H. Zhang, J. Ye (2022) Toward Solar-Driven Carbon Recycling. Joule 6 (2):294-314. doi:10.1016/j.joule.2022.01.001

4. M. Kondo, H. Tatewaki, S. Masaoka (2021) Design of Molecular Water Oxidation Catalysts with Earth-Abundant Metal Ions. Chem. Soc. Rev. 50 (12):6790-6831. doi:10.1039/D0CS01442G

5. N. C. S. Selvam, L. Du, B. Y. Xia, P. J. Yoo, B. You (2021) Reconstructed Water Oxidation Electrocatalysts: The Impact of Surface Dynamics on Intrinsic Activities. Adv. Funct. Mater. 31 (12):2008190. doi:10.1002/adfm.202008190

6. J. Li, C. A. Triana, W. Wan, D. P. Adiyeri Saseendran, Y. Zhao, S. E. Balaghi, S. Heidari, G. R. Patzke (2021) Molecular and Heterogeneous Water Oxidation Catalysts: Recent Progress and Joint Perspectives. Chem. Soc. Rev. 50 (4):2444-2485. doi:10.1039/D0CS00978D

7. G. Ge, M. Liu, C. Liu, W. Zhou, D. Wang, L. Liu, J. Ye (2019) Ultrathin FeOOH Nanosheets as an Efficient Cocatalyst for Photocatalytic Water Oxidation. J. Mater. Chem. A 7 (15):9222-9229. doi:10.1039/C9TA01740B

8. W. Han, H. Lin, F. Fang, Y. Zhang, K. Zhang, X. Yu, K. Chang (2021) The Effect of Fe(iii) Ions on Oxygen-Vacancy-Rich $BiVO_4$ on the Photocatalytic Oxygen Evolution Reaction. Catal. Sci. Technol. 11 (23):7598-7607. doi:10.1039/D1CY01559A

9. W. Zhang, K. Zhou (2017) Ultrathin Two-Dimensional Nanostructured Materials for Highly Efficient Water Oxidation. Small 13 (32). doi:10.1002/smll.201700806

10. J. Yang , D. Wang , X. Zhou, C. Li (2013) A Theoretical Study on the Mechanism of Photocatalytic Oxygen Evolution on $BiVO_4$ in Aqueous Solution. Chem. Eur. J. 19 (4):1320-1326. doi:10.1002/chem.201202365

11. H. L. Tan, X. Wen, R. Amal, Y. H. Ng (2016) $BiVO_4$ {010} and {110} Relative Exposure Extent: Governing Factor of Surface Charge Population and Photocatalytic Activity. J. Phy. Chem. Let. 7 (7):1400-1405. doi:10.1021/acs.jpclett.6b00428

12. M. D. Bhatt, J. Y. Lee (2021) Theoretical Insights into the Mechanism of Oxygen Evolution Reaction (OER) on Pristine $BiVO_4$ (001) and $BiVO_4$ (110) Surfaces in Acidic Medium Both in the Gas and Solution (Water) Phases. Nanotechnology 32 (33):335401. doi:10.1088/1361-6528/abfcfd

13. Q. Zhang, M. Liu, W. Zhou, Y. Zhang, W. Hao, Y. Kuang, H. Liu, D. Wang, L. Liu, J. Ye (2021) A Novel Cl^- Modification Approach to Develop Highly Efficient Photocatalytic Oxygen Evolution over $BiVO_4$ with AQE of 34.6%. Nano Energy 81:105651. doi:10.1016/j.nanoen.2020.105651

14. R. Li, H. Han, F. Zhang, D. Wang, C. Li (2014) Highly Efficient Photocatalysts Constructed by Rational Assembly of Dual-Cocatalysts Separately on Different Facets of $BiVO_4$. Energy Environ. Sci. 7 (4):1369-1376. doi:10.1039/C3EE43304H

15. R. Li, F. Zhang, D. Wang, J. Yang, M. Li, J. Zhu, X. Zhou, H. Han, C. Li (2013) Spatial Separation of Photogenerated Electrons and Holes among {010} and {110} Crystal Facets of $BiVO_4$. Nat. Commun. 4 (1):1432. doi:10.1038/ncomms2401

16. Y. Zhang, L. Shi, Z. Geng, T. Ren, Z. Yang (2019) The Improvement of Photocatalysis O_2 Production over $BiVO_4$ with Amorphous FeOOH Shell Modification. Sci. Rep. 9 (1):19090. doi:10.1038/s41598-019-54940-2

17. R. Hu, L. Meng, J. Zhang, X. Wang, S. Wu, Z. Wu, R. Zhou, L. Li, D.-S. Li, T. Wu (2020) A High-Activity Bimetallic OER Cocatalyst for Efficient Photoelectrochemical Water Splitting of $BiVO_4$. Nanoscale 12 (16):8875-8882. doi:10.1039/D0NR01616K

18. M. Kaur, M. Chhetri, C. N. R. Rao (2020) Photoelectrochemical OER Activity by Employing $BiVO_4$ with Manganese Oxide Co-Catalysts. Phys. Chem. Chem. Phys. 22 (2):811-817. doi:10.1039/C9CP05293C

19. T. Palaniselvam, L. Shi, G. Mettela, D. H. Anjum, R. Li, K. P. Katuri, P. E. Saikaly, P. Wang (2017) Vastly Enhanced $BiVO_4$ Photocatalytic OER Performance by $NiCoO_2$ as Cocatalyst. Adv. Mater. Interfaces 4 (19):1700540. doi:10.1002/admi.201700540

20. J.-B. Pan, B.-H. Wang, J.-B. Wang, H.-Z. Ding, W. Zhou, X. Liu, J.-R. Zhang, S. Shen, J.-K. Guo, L. Chen, C.-T. Au, L.-L. Jiang, S.-F. Yin (2021) Activity and Stability

Boosting of an Oxygen-Vacancy-Rich $BiVO_4$ Photoanode by NiFe-MOFs Thin Layer for Water Oxidation. Angew. Chem. Int. Ed. 60 (3):1433-1440. doi:10.1002/anie.202012550

21. S. Wang, T. He, J.-H. Yun, Y. Hu, M. Xiao, A. Du, L. Wang (2018) New Iron-Cobalt Oxide Catalysts Promoting $BiVO_4$ Films for Photoelectrochemical Water Splitting. Adv. Funct. Mater. 28 (34):1802685. doi:10.1002/adfm.201802685

22. Y. Qi, J. Zhang, Y. Kong, Y. Zhao, S. Chen, D. Li, W. Liu, Y. Chen, T. Xie, J. Cui, C. Li, K. Domen, F. Zhang (2022) Unraveling of Cocatalysts Photodeposited Selectively on Facets of $BiVO_4$ to Boost Solar Water Splitting. Nat. Commun. 13 (1):484. doi:10.1038/s41467-022-28146-6

23. X. Meng, S. Xu, C. Zhang, P. Feng, R. Li, H. Guan, Y. Ding (2022) Prussian Blue Type Cocatalysts for Enhancing the Photocatalytic Water Oxidation Performance of $BiVO_4$. Chem. Eur. J. 28 (51):e202201407. doi:10.1002/chem.202201407

24. D. Wang, H. Jiang, X. Zong, Q. Xu, Y. Ma, G. Li, C. Li (2011) Crystal Facet Dependence of Water Oxidation on $BiVO_4$ Sheets under Visible Light Irradiation. Chem. Eur. J. 17 (4):1275-1282. doi:10.1002/chem.201001636

25. C. Dong, S. Lu, S. Yao, R. Ge, Z. Wang, Z. Wang, P. An, Y. Liu, B. Yang, H. Zhang (2018) Colloidal Synthesis of Ultrathin Monoclinic $BiVO_4$ Nanosheets for Z-Scheme Overall Water Splitting under Visible Light. ACS Catal. 8 (9):8649-8658. doi:10.1021/acscatal.8b01645

26. S. M. Thalluri, C. Martinez Suarez, M. Hussain, S. Hernandez, A. Virga, G. Saracco, N. Russo (2013) Evaluation of the Parameters Affecting the Visible-Light-Induced Photocatalytic Activity of Monoclinic $BiVO_4$ for Water Oxidation. Ind. Eng. Chem. Res. 52 (49):17414-17418. doi:10.1021/ie402930x

27. J. Yu, A. Kudo (2006) Effects of Structural Variation on the Photocatalytic Performance of Hydrothermally Synthesized $BiVO_4$. Adv. Funct. Mater. 16 (16):2163-2169. doi:10.1002/adfm.200500799

28. A. W. Sleight, H. y. Chen, A. Ferretti, D. E. Cox (1979) Crystal Growth and Structure of $BiVO_4$. Mater. Res. Bull. 14 (12):1571-1581. doi:10.1016/0025-5408(72)90227-9

29. W. I. F. David, A. M. Glazer, A. W. Hewat (1979) The Structure and Ferroelastic Phase Transition of $BiVO_4$. Phase Transit. 1 (2):155-169. doi:10.1080/01411597908213198

30. J. K. Cooper, S. Gul, F. M. Toma, L. Chen, P.-A. Glans, J. Guo, J. W. Ager, J. Yano, I. D. Sharp (2014) Electronic Structure of Monoclinic $BiVO_4$. Chem. Mater. 26 (18):5365-5373. doi:10.1021/cm5025074

31. K. Qin, Q. Zhao, H. Yu, X. Xia, J. Li, S. He, L. Wei, T. An (2021) A Review of Bismuth-Based Photocatalysts for Antibiotic Degradation: Insight into the Photocatalytic Degradation Performance, Pathways and Relevant Mechanisms. Environ. Res. 199:111360. doi:10.1016/j.envres.2021.111360

32. M. A. Gaikwad, U. P. Suryawanshi, U. V. Ghorpade, J. S. Jang, M. P. Suryawanshi, J. H. Kim (2022) Emerging Surface, Bulk, and Interface Engineering Strategies on $BiVO_4$ for Photoelectrochemical Water Splitting. Small 18 (10):2105084. doi:10.1002/smll.202105084

33. M. Xu, J. Yang, C. Sun, L. Liu, Y. Cui, B. Liang (2020) Performance Enhancement Strategies of Bi-Based Photocatalysts: A Review on Recent Progress. Chem. Eng. J. 389:124402. doi:10.1016/j.cej.2020.124402

34. J. Shi, E. A. Rubinstein, W. Li, J. Zhang, Y. Yang, T.-L. Lee, C. Qin, P. Yan, J. L. MacManus-Driscoll, D. O. Scanlon, K. H. L. Zhang (2022) Modulation of the Bi^{3+} $6s^2$ Lone Pair State in Perovskites for High-Mobility p-Type Oxide Semiconductors. Adv. Sci. 9 (6):2104141. doi:10.1002/advs.202104141

35. H. Kunioku, M. Higashi, O. Tomita, M. Yabuuchi, D. Kato, H. Fujito, H. Kageyama, R. Abe (2018) Strong Hybridization between Bi-6s and O-2p Orbitals in Sillén–Aurivillius Perovskite Bi_4MO_8X (M = Nb, Ta; X = Cl, Br), Visible Light Photocatalysts Enabling Stable Water Oxidation. J. Mater. Chem. A 6 (7):3100-3107. doi:10.1039/C7TA08619A

36. A. Bhatia, G. Hautier, T. Nilgianskul, A. Miglio, J. Sun, H. J. Kim, K. H. Kim, S. Chen, G.-M. Rignanese, X. Gonze, J. Suntivich (2016) High-Mobility Bismuth-based Transparent p-Type Oxide from High-Throughput Material Screening. Chem. Mater. 28 (1):30-34. doi:10.1021/acs.chemmater.5b03794

37. M. Oshikiri, M. Boero, J. Ye, Z. Zou, G. Kido (2002) Electronic Structures of Promising Photocatalysts $InMO_4$ (M=V, Nb, Ta) and $BiVO_4$ for Water Decomposition in the Visible Wavelength Region. J. Chem. Phy. 117 (15):7313-7318. doi:10.1063/1.1507101

38. P. Giannozzi, S. Baroni, N. Bonini, M. Calandra, R. Car, C. Cavazzoni, D. Ceresoli, G. L. Chiarotti, M. Cococcioni, I. Dabo, A. Dal Corso, S. de Gironcoli, S. Fabris, G. Fratesi, R. Gebauer, U. Gerstmann, C. Gougoussis, A. Kokalj, M. Lazzeri, L. Martin-Samos, N. Marzari, F. Mauri, R. Mazzarello, S. Paolini, A. Pasquarello, L. Paulatto, C. Sbraccia, S. Scandolo, G. Sclauzero, A. P. Seitsonen, A. Smogunov, P. Umari, R. M. Wentzcovitch (2009) QUANTUM ESPRESSO: A Modular and Open-Source Software Project for Quantum Simulations of Materials. J. Phys. Condens. Matter 21 (39):395502. doi:10.1088/0953-8984/21/39/395502

39. P. Giannozzi, O. Andreussi, T. Brumme, O. Bunau, M. Buongiorno Nardelli, M. Calandra, R. Car, C. Cavazzoni, D. Ceresoli, M. Cococcioni, N. Colonna, I. Carnimeo, A. Dal Corso, S. de Gironcoli, P. Delugas, R. A. DiStasio, A. Ferretti, A. Floris, G. Fratesi, G. Fugallo, R. Gebauer, U. Gerstmann, F. Giustino, T. Gorni, J. Jia, M. Kawamura, H. Y. Ko, A. Kokalj, E. Küçükbenli, M. Lazzeri, M. Marsili, N. Marzari, F. Mauri, N. L. Nguyen, H. V. Nguyen, A. Otero-de-la-Roza, L. Paulatto, S. Poncé, D. Rocca, R. Sabatini, B. Santra, M. Schlipf, A. P. Seitsonen, A. Smogunov, I. Timrov, T. Thonhauser, P. Umari, N. Vast, X. Wu, S. Baroni (2017) Advanced Capabilities for Materials Modelling with Quantum ESPRESSO. J. Phys. Condens. Matter 29 (46):465901. doi:10.1088/1361-648x/aa8f79

40. J. P. Perdew, K. Burke, M. Ernzerhof (1996) Generalized Gradient Approximation Made Simple. Phys. Rev. Lett. 77 (18):3865-3868. doi:10.1103/PhysRevLett.77.3865

41. G. Kresse, D. Joubert (1999) From Ultrasoft Pseudopotentials to the Projector Augmented-Wave Method. Phys. Rev. B 59 (3):1758-1775. doi:10.1103/PhysRevB.59.1758

42. S. Grimme (2006) Semiempirical GGA-Type Density Functional Constructed with a Long-Range Dispersion Correction. J. Comput. Chem. 27 (15):1787-1799. doi:10.1002/jcc.20495

43. V. Barone, M. Casarin, D. Forrer, M. Pavone, M. Sambi, A. Vittadini (2009) Role and Effective Treatment of Dispersive Forces in Materials: Polyethylene and Graphite Crystals as Test Cases. J. Comput. Chem. 30 (6):934-939. doi:10.1002/jcc.21112

44. J. K. Nørskov, J. Rossmeisl, A. Logadottir, L. Lindqvist, J. R. Kitchin, T. Bligaard, H. Jónsson (2004) Origin of the Overpotential for Oxygen Reduction at a Fuel-Cell Cathode. J. Phy. Chem. B 108 (46):17886-17892. doi:10.1021/jp047349j

45. J. Rossmeisl, A. Logadottir, J. K. Nørskov (2005) Electrolysis of Water on (Oxidized) Metal Surfaces. Chem. Phys. 319 (1):178-184. doi:10.1016/j.chemphys.2005.05.038

46. A. A. Peterson, F. Abild-Pedersen, F. Studt, J. Rossmeisl, J. K. Nørskov (2010) How Copper Catalyzes the Electroreduction of Carbon Dioxide into Hydrocarbon Fuels. Energy Environ. Sci. 3 (9):1311-1315. doi:10.1039/C0EE00071J

47. D.-H. Lim, J. Wilcox (2012) Mechanisms of the Oxygen Reduction Reaction on Defective Graphene-Supported Pt Nanoparticles from First-Principles. J. Phy. Chem. C 116 (5):3653-3660. doi:10.1021/jp210796e

48. Z. Gu, P. B. Balbuena (2006) Dissolution of Oxygen Reduction Electrocatalysts in an Acidic Environment: Density Functional Theory Study. J. Phy. Chem. A 110 (32):9783-9787. doi:10.1021/jp063447o

49. Y. Wang, H. Yuan, Y. Li, Z. Chen (2015) Two-Dimensional Iron-Phthalocyanine (Fe-Pc) Monolayer as a Promising Single-Atom-Catalyst for Oxygen Reduction Reaction: A Computational Study. Nanoscale 7 (27):11633-11641. doi:10.1039/C5NR00302D

50. A. D. Becke (1988) Density-Functional Exchange-Energy Approximation with Correct Asymptotic Behavior. Phys. Rev. A 38 (6):3098-3100. doi:10.1103/PhysRevA.38.3098

51. C. Lee, W. Yang, R. G. Parr (1988) Development of the Colle-Salvetti Correlation-Energy Formula into a Functional of the Electron Density. Phys. Rev. B 37 (2):785-789. doi:10.1103/PhysRevB.37.785

52. N. Troullier, J. L. Martins (1991) Efficient Pseudopotentials for Plane-Wave Calculations. Phys. Rev. B 43 (3):1993-2006. doi:10.1103/PhysRevB.43.1993

53. R. Nakamura, A. Imanishi, K. Murakoshi, Y. Nakato (2003) In Situ FTIR Studies of Primary Intermediates of Photocatalytic Reactions on Nanocrystalline TiO_2 Films in Contact with Aqueous Solutions. J. Am. Chem. Soc. 125 (24):7443-7450. doi:10.1021/ja029503q

54. G. Mattioli, F. Filippone, A. Amore Bonapasta (2006) Reaction Intermediates in the Photoreduction of Oxygen Molecules at the (101) TiO_2 (Anatase) Surface. J. Am. Chem. Soc. 128 (42):13772-13780. doi:10.1021/ja062145x

55. M. Zhang, M. de Respinis, H. Frei (2014) Time-Resolved Observations of Water Oxidation Intermediates on a Cobalt Oxide Nanoparticle Catalyst. Nat. Chem. 6 (4):362-367. doi:10.1038/nchem.1874

56. Q. Ding, Y. Liu, T. Chen, X. Wang, Z. Feng, X. Wang, M. Dupuis, C. Li (2020) Unravelling the Water Oxidation Mechanism on $NaTaO_3$-Based Photocatalysts. J. Mater. Chem. A 8 (14):6812-6821. doi:10.1039/C9TA14235E

57. A. Venugopal, R. Kas, K. Hau, W. A. Smith (2021) Operando Infrared Spectroscopy Reveals the Dynamic Nature of Semiconductor–Electrolyte Interface in Multinary Metal Oxide Photoelectrodes. J. Am. Chem. Soc. 143 (44):18581-18591. doi:10.1021/jacs.1c08245

58. Y. Kera, K. Hirota (1969) Infrared Spectroscopic Study of Oxygen Species in Vanadium Pentoxide with Reference to Its Activity in Catalytic Oxidation. J. Phys. Chem. 73 (11):3973-3981. doi:10.1021/j100845a070

59. S. Labib (2017) Preparation, Characterization and Photocatalytic Properties of Doped and Undoped Bi_2O_3. J. Saudi Chem. Soc. 21 (6):664-672. doi:10.1016/j.jscs.2015.11.003

60. M. Ashokkumar, S. Muthukumaran (2014) Microstructure and Band Gap Tailoring of $Zn_{0.96-x}Cu_{0.04}Co_xO$ ($0 \leqslant x \leqslant 0.04$) Nanoparticles Prepared by Co-precipitation Method. J. Alloys Compd. 587:606-612. doi:10.1016/j.jallcom.2013.10.246

61. M. Oshikiri, M. Boero (2006) Water Molecule Adsorption Properties on the $BiVO_4$ (100) Surface. J. Phy. Chem. B 110 (18):9188-9194. doi:10.1021/jp0555100

62. M. Oshikiri, M. Boero, A. Matsushita, J. Ye (2009) Water Adsorption onto Y and V Sites at the Surface of the YVO_4 Photocatalyst and Related Electronic Properties. J. Chem. Phy. 131 (3):034701. doi:10.1063/1.3170928

63. R. Nakamura, Y. Nakato (2004) Primary Intermediates of Oxygen Photoevolution Reaction on TiO_2 (Rutile) Particles, Revealed by in Situ FTIR Absorption and Photoluminescence Measurements. J. Am. Chem. Soc. 126 (4):1290-1298. doi:10.1021/ja0388764

64. R. D. Jones, D. A. Summerville, F. Basolo (1979) Synthetic Oxygen Carriers Related to Biological Systems. Chem. Rev. 79 (2):139-179. doi:10.1021/cr60318a002

65. K. Nakamoto, Y. Nonaka, Ishiguro, M. W. Urban, M. Suzuki, M. Kozuka, Y. Nishida, S. Kida (1982) Resonance Raman and Infrared Spectra of Molecular Oxygen Adducts of N,N'-ethylenebis(2,2-diacetylethylideneaminato)cobalt(II). J. Am. Chem. Soc. 104 (12):3386-3391. doi:10.1021/ja00376a024

66. E. Tsuji, K.-i. Fukui, A. Imanishi (2011) *In-situ* MIR-IR Observation of Peroxo Species on Anatase TiO_2 Particle during Oxygen Photoevolution Reaction. Electrochemistry 79 (10):787-789. doi:10.5796/electrochemistry.79.787

67. K. Ishisone, N. Jiraborvornpongsa, T. Isobe, S. Matsushita, M. Wakumura, M. Oshikiri, A. Nakajima (2020) Experimental and Theoretical Investigation of WO_x Modification Effects on the Photocatalytic Activity of Titanium-Substituted Hydroxyapatite. Appl. Catal. B 264:118516. doi:10.1016/j.apcatb.2019.118516

68. M. Oshikiri, M. Boero, A. Matsushita, J. Ye (2009) Water Molecule Adsorption Properties on Surfaces of MVO_4 (M = In, Y, Bi) Photo-Catalysts. J. Electroceram. 22 (1):114-119. doi:10.1007/s10832-007-9380-3

69. M. Oshikiri, J. Ye, M. Boero (2014) Inhomogeneous RVO_4 Photocatalyst Systems (R = Y, Ce, Pr, Nd, Sm, Eu, Gd, Tb, Dy, Ho, Er, Tm, Yb, Lu). J. Phy. Chem. C 118 (16):8331-8341. doi:10.1021/jp410565e

70. M. Oshikiri, M. Boero, A. Matsushita, J. Ye (2008) Dissociation of Water Molecule at Three-Fold Oxygen Coordinated V Site on the $InVO_4$ (001) Surface. Appl. Surf. Sci. 255 (3):679-681. doi:10.1016/j.apsusc.2008.07.041

Chapter 4. Oxygen Vacancy-Mediated Size Engineering of Pd Cocatalyst over Monoclinic $BiVO_4$ for Visible-Light-Driven H_2O_2 Synthesis

4.1. Introduction

Artificial photosynthesis technology offers some appealing method to produce green energy stocks through solar energy harvesting and conversion process for tackling the global challenges in energy and environmental sustainability.[1,2] Accordingly, solar-driven water splitting for hydrogen (H_2) generation has become the center of photocatalytic research all over the world for these past several decades.[3] Nevertheless, H_2 fuel still exerts some drawbacks, such as poor storability and transportability, which might hinder its practical application.[4,5] Concerning those issues, hydrogen peroxide (H_2O_2), on the other hand, has displayed great potential as an alternative liquid energy carrier since it is relatively more cost-effective (can operate in a membrane-free system) and easily transportable (fully soluble in water).[3,6-9] Furthermore, H_2O_2 has also been applied in many other areas, including pulp and textile bleaching, medical disinfection, organic synthesis, wastewater treatment, and many other industrial fields,[1,7,8,10] rendering the development of superior photocatalytic materials for the synthesis of H_2O_2 becomes a very attractive and important topic to research.[11,12]

N-type monoclinic $BiVO_4$ is widely known as one of the most promising oxide photocatalysts with good visible-light absorption ability and suitable band positions for driving the oxygen evolution reaction (OER) and oxygen reduction reaction (ORR) for H_2O_2 production.[13-17] However, while the former reaction can be considered its best forte with many scientific reports and studies, the latter one has been scarcely applied and realized over $BiVO_4$ photocatalysts.[3,18] This has to do with the fact that the pristine surface of monoclinic $BiVO_4$ is quite inactive for catalyzing the O_2 conversion into H_2O_2.[12,19,20] With that being the case, the surface modulation strategy to generate external reactive sites by the means of cocatalyst loading might be an ideal approach for promoting solar-driven H_2O_2 production over monoclinic $BiVO_4$ photocatalyst.[21,22] Among many available metal cocatalyts for particulate photocatalysis, palladium (Pd) has shown the best potential for driving the two electron reduction of O_2 to generate H_2O_2, in competition with Au metal.[9,18,21,23] Interestingly, in contrast to Au which tends to

manifest weak combination with O_2 molecules, Pd cocatalyst can strongly interact with O_2 molecules by forming the bridge-oxygen adsorption model, thus facilitating more effective electron transfer to reduce the adsorbed O_2 molecules.[21,24,25]

Concerning the cocatalyst loading strategy, the impregnation method is often utilized in most cases, resulting in a random distribution of cocatalysts over the photocatalyst surfaces without being able to control the location of cocatalysts.[26] Intriguingly, monoclinic $BiVO_4$ possesses a special trait that enables the selective photodeposition of reduction and oxidation cocatalysts into different anisotropic facets, due to its spatial charge separation nature.[26-29] In detail, upon the light illumination, the photogenerated electrons and holes will be transferred and accumulated on the (010) and (011)/(110) facets, respectively, enabling the former facet to catalyze the reduction reaction, while the latter drive the oxidation reaction.[27] Accordingly, the assemble of well-dispersed Pd cocatalyst over the (010) reduction facets of monoclinic $BiVO_4$ via photodeposition process is an interesting topic to further investigate, which might provide a breakthrough for fabricating a superior photocatalyst for high performance H_2O_2 production. Unfortunately, photodeposition method also comes with some shortcomings, especially the difficulty and complexity of controlling the size of photodeposited metal cocatalyst, which actually is the decisive factor for determining whether the surface reaction can proceed efficiently.[30,31] In general, a smaller size of cocatalyst with high dispersion is preferable since it can provide more active sites to drive the reaction.[32,33]

In this work, we demonstrate a functional surface modulation technique by introducing oxygen vacancy (O_v) into the crystal of monoclinic $BiVO_4$, which can exert a practical size engineering effect on the photodeposited Pd cocatalyst. By simply adjusting the pH of hydrothermal solution, various $BiVO_4$ photocatalyst with different degrees of oxygen vacancy were successfully fabricated. The oxygen vacancies on the (010) reduction facets are expected to function as a charge redistributor, enabling more effective electrostatic interaction with the $PdCl_4^{2-}$ precursor, by which higher concentration of oxygen vacancies would render smaller size of Pd cocatalysts. Under visible light irradiation, the optimized Pd/$BiVO_4$ sample demonstrated an excellent H_2O_2 synthesis, up to 2.35 mM/h, accomplishing the state-of-the-art AQE of 19.2% at 420 nm in photocatalytic H_2O_2 production over $BiVO_4$-based materials. This work sheds new light into the rational design of metal-semiconductor composites for more efficient H_2O_2 photosynthesis.

4.2. Experimental Section

4.2.1. Materials

Bismuth nitrate pentahydrate ($Bi(NO_3)_3 \cdot 5H_2O$, Guaranteed Reagent), ammonium metavanadate (NH_4VO_3, Guaranteed Reagent), nitric acid 69% (HNO_3, Guaranteed Reagent), hydrochloric acid 36% (HCl, Guaranteed Reagent), ammonia solution 25% (NH_3, Wako 1st Grade), palladium chloride ($PdCl_2$, Guaranteed Reagent), hydrogen tetrachloroaurate (III) tetrahydrate 99.9% ($HAuCl_4.4H_2O$), hydrogen hexachloroplatinate (IV) hexahydrate 99.9% ($H_2PtCl_6.6H_2O$), citric acid ($C_6H_8O_7$, Wako Special Grade), trisodium citrate anhydrous ($C_6H_5O_7Na_3$, Wako Special Grade), potassium hydrogen phthalate ($C_8H_5KO_4$, Guaranteed Reagent), potassium iodide (KI, Wako 1st Grade), hydrogen peroxide 30% (H_2O_2, Guaranteed Reagent), methanol 99.8% (CH_3OH, Guaranteed Reagent), ethanol 95% (C_2H_5OH, Guaranteed Reagent), isopropanol (IPA, $(CH_3)_2CHOH$, Japanese Pharmacopoeia) were purchased from FUJIFILM Wako Pure Chemical Corporation. All chemicals were used directly as received without further purification. The ultrapure water with a resistivity of 18.2 $M\Omega\ cm^{-1}$ was supplied by a Millipore System (Millipore Q) and used in all experiments.

4.2.2. Catalyst Preparation

Monoclinic $BiVO_4$ photocatalyst was prepared by a facile hydrothermal method according to the reported procedure,[34,35] with slight modification. Initially, 5.0 mmol of $Bi(NO_3)_3 \cdot 5H_2O$ and 5.0 mmol of NH_4VO_3 were dissolved in sequence in 60 mL of 2.0 M nitric acid solution. The above mixture was stirred until the color of the solution became yellow gold, signifying the complete dissolution. The pH of the solution were then adjusted to a certain value (0.75, 1.5, 2.0, 2.2, 2.3, 2.4, and 2.6) by adding ammonia solution (25 wt.%) drop by drop under stirring, which would gradually change the color to orange. A yellow or orange $BiVO_4$ slurry was obtained after stirring for about 2 h under room temperature (higher pH would yield more orange color). Afterward, the mixture (about 70 mL) was transferred to a Teflon-lined stainless-steel autoclave with a capacity of 100 mL, and hydrothermally treated at 180 °C for 24 h in the oven. After the autoclaves were cooled to room temperature, some yellow or orange precipitates were obtained. The precipitates were then collected by centrifugation, washed with pure water several times, and dried under vacuum at 70 °C overnight to obtain monoclinic $BiVO_4$ powder samples, which can be referred as BVO-*x* (*x* denotes the pH used during the synthesis process).

The selective photodeposition of Pd metal on the (010) facet of $BiVO_4$ photocatalyst was conducted according to the following procedure. 300 mg of the as-prepared $BiVO_4$ samples were initially dispersed in 100 mL pure water by ultrasonic treatment for about 15 min, followed by the addition of H_2PdCl_4 stock (prepared beforehand by dissolving $PdCl_2$ powder in HCl diluted solution) with metal loading amount of 0.3 wt% and stirring for 5-10 min. The mixture was then illuminated from the top side by using a full spectrum of 300 W Xe lamp for 1 h in an ice bath under atmospheric condition. The resultant precipitation was collected by centrifugation, washed several times using pure water, and finally dried at 70 °C under vacuum to obtain well-dispersed Pd on the (010) surface of BVO-*x* photocatalyst. For comparison, some other metal-$BiVO_4$ composites were also prepared by utilizing some organic aqueous solution (methanol, ethanol, and isopropyl alcohol (IPA)) and some other noble metals (Au and Pt) during the photodeposition process with the same procedure as described above.

4.2.3. Material Characterizations

The morphologies of the samples were investigated by scanning electron microscopy (SEM, JEOL JSM-6701F, Japan). The elemental distribution by STEM-EDS mapping was analysed using the transmission electron microscopy (TEM, JEOL JEM-3100FEF, Japan), equipped with an energy dispersive spectrometer (EDS). The crystal structures of the materials were characterized using X-ray diffractometer (X'pert powder, PANalytical B.V., Netherland) with Cu-Kα radiation (λ = 0.1541 nm) under 40 kV and 30 mA. The optical properties of the materials were measured over a UV-vis spectrophotometer (UV-2600 Shimadzu, Japan), and the corresponding band gaps were calculated according to the Kubelka-Munk transformation. The Brunner−Emmet−Teller (BET) tests to probe the specific surface area of the as-synthesized samples were performed by a surface area analyzer (Belsorp-Mini II, Japan) with N_2 analysis adsorptive at 77.2 K. The surface element chemical status of the samples was identified by X-ray photoelectron spectroscopy (Escalab 250 Xi, Thermo Scientific, Japan) in a theta probe using monochromatic Al-Kα X-rays at hν = 1486.6 eV. The observed peak positions were calibrated to the binding energy of the C−C bond in C 1s spectra (284.6 eV). The elemental composition of the prepared samples was analyzed using inductively coupled plasma optical emission spectrometry (ICP-OES, Agilent5800, USA). The photoluminescence (PL) properties were investigated using a fluorescence spectrophotometer (Jasco FP-8550, Japan).

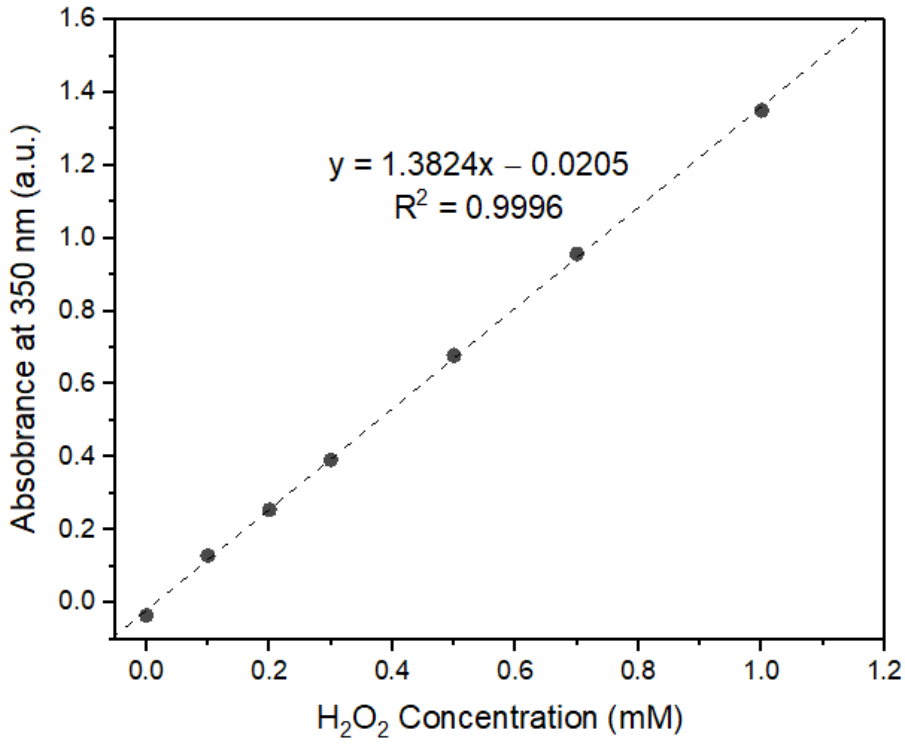

Figure 4.1. Calibration curve for H_2O_2 concentration measurement.

4.2.4. Photocatalytic Activity Test

Photocatalytic performances of the as-prepared samples were evaluated through photocatalytic ORR for the production of H_2O_2. Typically, 80 mg of photocatalyst powders were initially dispersed in 80 mL citric buffer solution (0.2 M, pH ≈ 3) inside a 180 mL Pyrex glass reactor with ultrasonic treatment. The reactor was then placed inside an ice bath to keep the low temperature (~15 °C) and the reactant solution was stirred mildly. Before irradiation, the mixture was purged continuously by a constant flow of O_2 (300 mL min^{-1}) for about 30 min under dark condition, in order to reach saturated solution of dissolved oxygen. Afterwards, the above solution was then illuminated from the top side by visible light using a 300 W Xe lamp equipped with an L-42 cut-off filter for 1 h, while still keeping the O_2 gas flow. During the illumination, 1 mL of the suspension was collected at designated time points and then centrifuged to remove the catalyst. The actual concentration of produced H_2O_2 was accurately measured by a colorimetric iodine method.[36-38] Specifically, 0.6 mL of the supernatant was initially separated and then added by 1.2 mL of potassium hydrogen phthalate solution (0.1 M) and 1.2 mL of potassium iodide solution (0.4 M) in sequence. After standing for 2 min, the absorbance of the above mixture was tested at wavelength of 350 nm using the UV-2600

spectrophotometer (Shimadzu, Japan). **Figure 4.1** shows a standard calibration curve of H_2O_2 concentration and absorbance (at 350 nm) for the measurement by colorimetric method. The measurement of apparent quantum efficiency (AQE) was carried out under similar conditions as described above, except for the usage of monochromatic light irradiation. A series of bandpass filters (420 nm, 460 nm, 500 nm, 540 nm, 580 nm, and 600 nm) were utilized in order to control the wavelength region of the monochromatic light. The average light intensity was determined using a spectroradiometer (Ushio, USR-40, Japan). The AQE was estimated by using the following equation:

$$\text{AQE} = \frac{2 \times \text{number of evolved } H_2O_2 \text{ molecules}}{\text{number of incident photons}} \times 100\% \quad (4\text{-}1)$$

4.2.5. Statistical Analysis

The average size of photodeposited Pd nanoparticles were evaluated by measuring 100 random nanoparticle samples in **Figure 4.8 a, c, and e**, while the presented means ± S.D. are the combination of the standard uncertainty of repeated measurements expanded by the factor of 3. The means ± S.D. (n = 4) from repeated measurements were calculated in order to validate the data of photocatalytic H_2O_2 production and wavelength-dependent AQE as can be found in **Figure 2.16**, **Figure 4.15**, **Figure 4.16**, **Figure 4.17**, and **Figure 4.18**.

4.3. Results and Discussion

4.3.1. Characterizations of Pure Monoclinic $BiVO_4$ (BVO-*x*)

A series of monoclinic $BiVO_4$ photocatalysts were fabricated using facile hydrothermal method[34,35] by varying the pH of the reactant solution. Herein, we are going to firstly discuss about the structural and chemical properties of the pure monoclinic $BiVO_4$ samples. **Figure 4.2** displays the SEM images of the as-synthesized BVO-*x* samples, which indicates the variation of morphology as the pH changes. At relatively lower pH (0.75 and 1.5), the monoclinic $BiVO_4$ microparticles exhibit a decahedral structure with clearly distinguished (010) and (011)/(110) facets.[3,15,34] As the pH increases, the $BiVO_4$ particles apparently experiences some deformation process, thus resulting in defective decahedral morphology (pH 2.0 and 2.3), irregular microparticles (pH 2.4), and hyperbranced rod-like microparticles (pH 2.6). As displayed in **Figure 4.3,** the XRD spectra confirms the pure monoclinic phase of $BiVO_4$ (JCPDS File No. 14-0688) for all prepared BVO-*x* samples. The BET tests for some selected samples, whose results are

summarized in **Table 4.1**, indicate the increasing tendency of the surface area as the pH increases, which can be ascribed to the alteration of the $BiVO_4$ particles morphology.

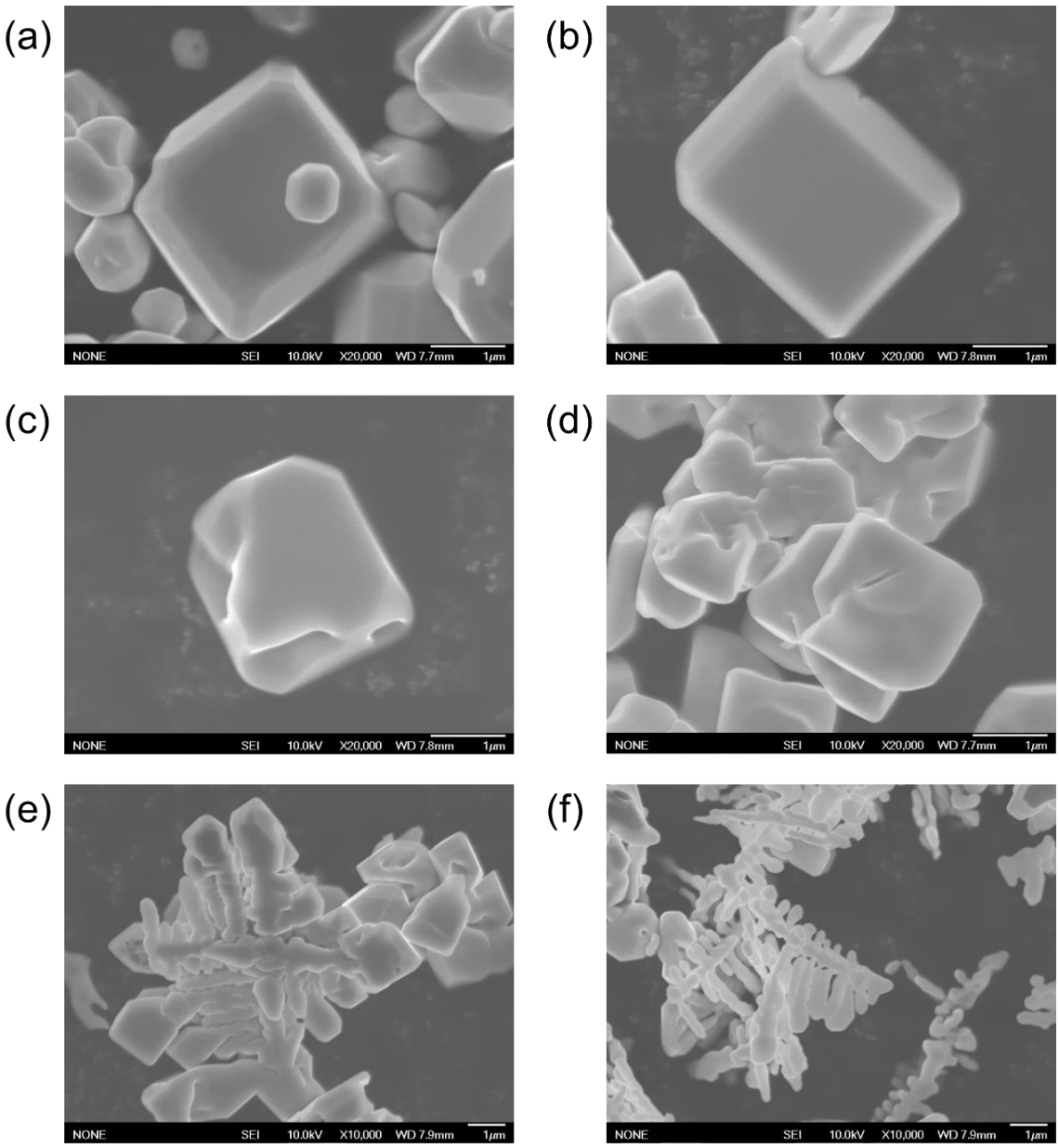

Figure 4.2. SEM images of pure monoclinic BVO-*x* samples synthesized at pH (a) 0.75 (regular deecahedron), (b) 1.5 (regular decahedron), (c) 2.0 (defective dodecahedron), (d) 2.3 (defective decahedron), (e) 2.4 (irregular microparticles), and (f) 2.60 (hyperbranched rod-like microparticles).

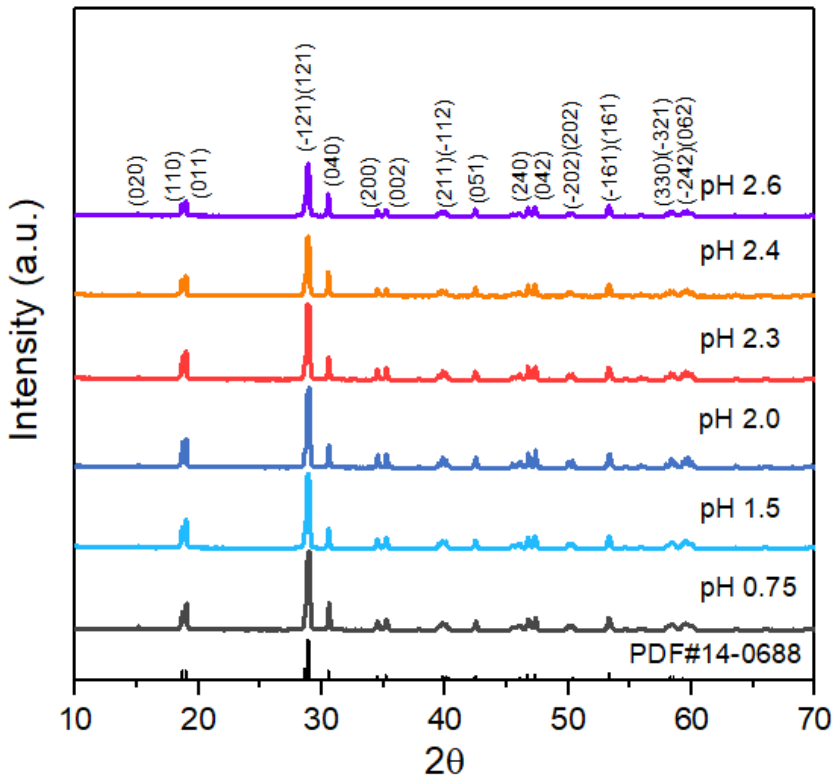

Figure 4.3. XRD spectra of the as-prepared monoclinic BVO-*x* samples synthesized at various pH.

Table 4.1. Effect of pH on the morphology, BET surface area, band gap, V^{4+} and oxygen vacancy (O_v) concentrations (at%), average Pd particle size, and H_2O_2 synthesis rate of some selected BVO-*x* photocatalysts.

Sample	Morphology	BET surface area (m^2/g)	Band gap (eV)	V^{4+} (at%)	O_v (at%)*	Average Pd particle size (nm)	H_2O_2 production rate (mM/h)
BVO-1.5	Regular decahedron	0.35	2.35	26.7	3.3	20.2 ± 1.3	1.42
BVO-2.0	Defective decahedron	0.52	2.35	33.4	4.2	16.1 ± 1.1	1.59
BVO-2.3	Defective decahedron	0.69	2.35	44.1	5.5	10.3 ± 0.6	2.35
BVO-2.6	Hyperbranched rod-like	1.45	2.37	56.8	7.1	*undetected*	1.43

* estimated to be one eighth of the V^{4+} concentration (at%)

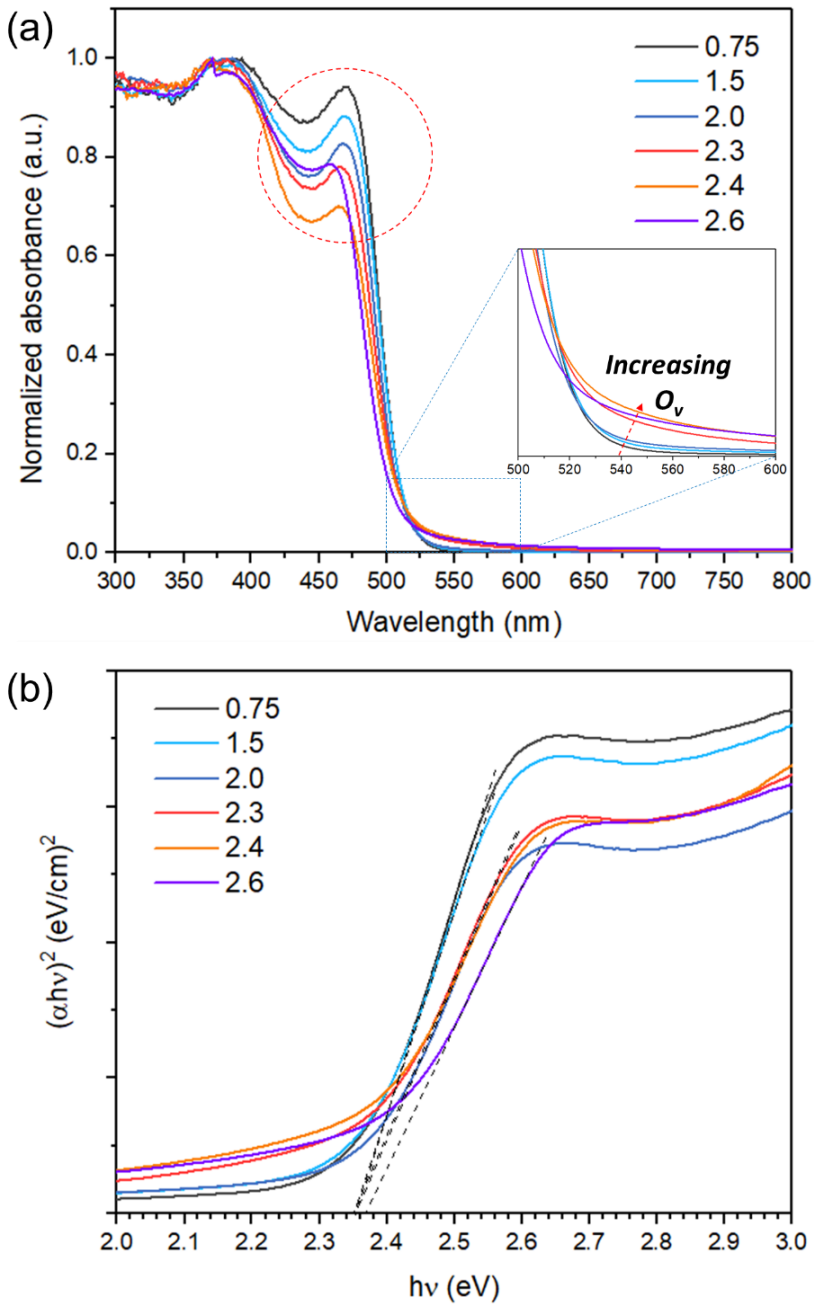

Figure 4.4. (a) UV-Vis and (b) plot of $(\alpha h\nu)^2$ versus photon energy ($h\nu$) based on the Kubelka-Munk transformation of pure $BiVO_4$ samples synthesized at various pH.

The optical absorption properties of the as-synthesized monoclinic $BiVO_4$ samples were investigated by employing UV-Vis diffuse reflectance spectroscopy (**Figure 4.4 a**). All the monoclinic $BiVO_4$ samples exhibit UV to visible light absorption with the absorption edge around 530 nm. The absorption of $BiVO_4$ sample synthesized at pH 2.6 indicates a slight blue shift compared to the other samples. By employing the Kubelka-Munk transformation (**Figure 4.4 b**), the band gaps of all $BiVO_4$ samples were calculated to be ~2.35 eV (2.37 eV for BVO-2.6), which is perfectly suitable for driving visible-

light-driven photocatalytic reaction.[39] Intriguingly, some unique absorption peaks around 440-490 nm are observed for all $BiVO_4$ samples, as circled in red, which signifies a decreasing tendency as the pH becomes less acidic; the peak completely disappears for BVO-2.6, while another unique absorption behavior emerges but at slightly lower wavelength. Considering the morphology changes, as has been previously discussed, the former unique absorption peak can be assigned to the decahedron structure of the monoclinic $BiVO_4$ crystals, which experiences deformation along the increasing pH, thus explaining the above mentioned peak decreasing behavior. Correspondingly, the emerging absorption peak of BVO-2.6 might derive from its rod-like structure. In this case, it can be deduced that different morphologies of $BiVO_4$ photocatalyst would result in different absorption characteristics, which might affect the overall photocatalytic performance. More importantly, focusing on the absorption tail region (530-600 nm), the as-prepared samples develop some non-zero absorption behavior which becomes more obvious as the pH increases, as represented in the inset of **Figure 4.4 a**. This extended absorption towards to near infrared region implies the existence of trap states induced by defects, which in this case are oxygen vacancies.[40-44] Accordingly, the colors of the $BiVO_4$ powders gradually change from light yellow to orange with the increasing pH (see **Figure 4.5**), suggesting the higher concentration of oxygen vacancy.[44-47]

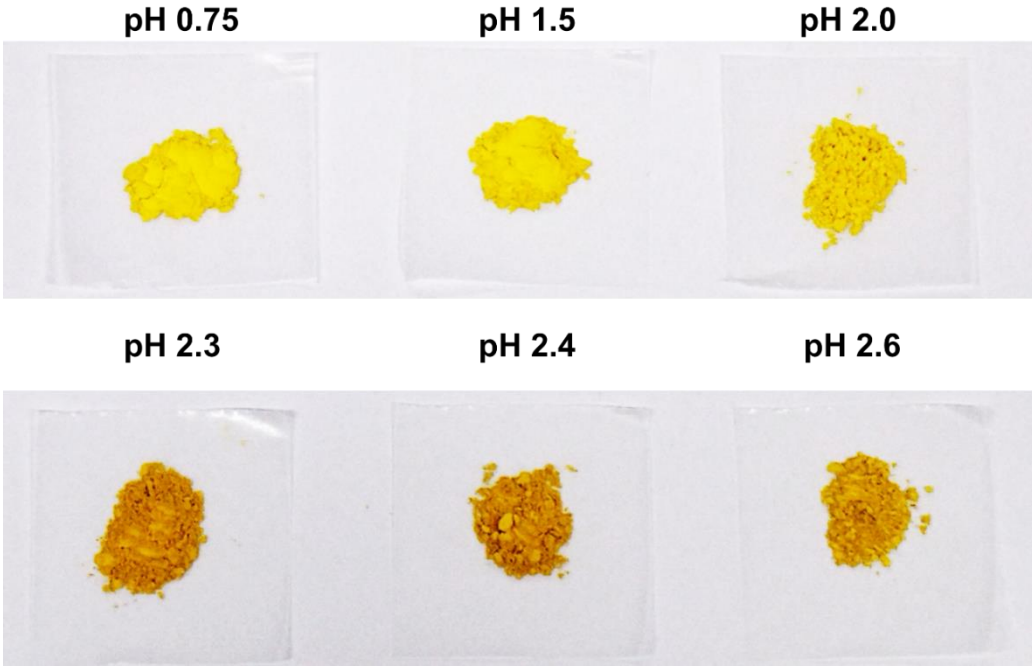

Figure 4.5. Photos of the monoclinic $BiVO_4$ powders synthesized at different pH, signifying the gradual change of color from light yellow to orange as the pH of reactant solution increases, due to the existence of oxygen vacancies.

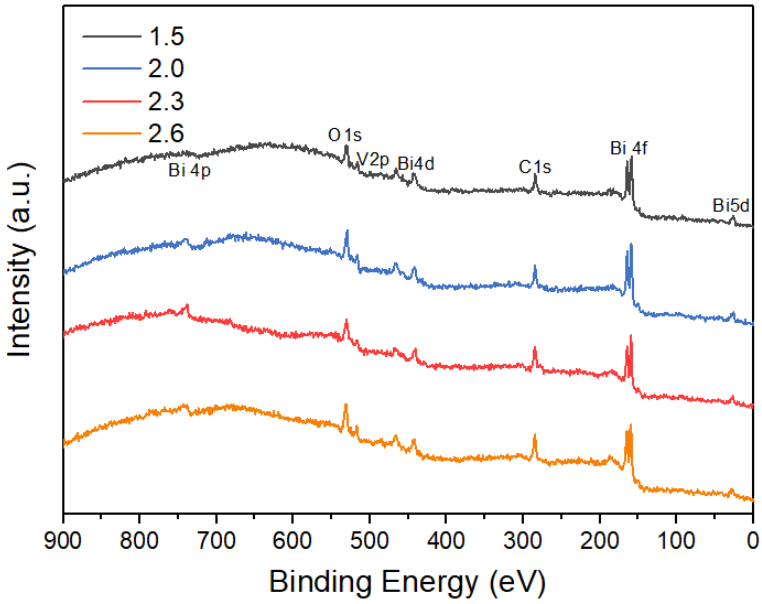

Figure 4.6. Wide-scan XPS spectra of the as-prepared BVO-*x* samples. The C 1s signal derives from the carbon tape substrate.

The surface chemistry of the as-synthesized monoclinic $BiVO_4$ samples are investigated by XPS analysis. **Figure 4.6** shows the wide-range XPS spectra of several selected BVO-*x* samples, which reveals the sole existence of $BiVO_4$ composing elements (Bi, V, and O) for all samples obtained at different pH. Noteworthily, the high-resolution XPS spectra of Bi 4f and V 2p orbitals reveal some pivotal variations. As depicted in **Figure 4.7 a**, the Bi 4f spectra exhibit two intensive peaks with a peak splitting of 5.3 eV, corresponding to the 3+ oxidation state of Bi, while the V 2p peaks with a peak splitting of around 7.6 eV (**Figure 4.7 b**) represent the V^{5+} cations in the $BiVO_4$ crystal lattice. Interestingly, those peak positions are shifted to lower binding energy with the increasing pH, thus indicating the higher electron density and lower valence states of both Bi and V species, which can be attributed to the partial reduction of Bi^{3+} and V^{5+} ions and also the existence of oxygen vacancies.[47-51] The greater XPS peak shift as the pH increases can be attributed to the higher oxygen vacancy level within the crystal of monoclinic $BiVO_4$,[47,52] in agreement with the previously discussed UV-Vis results. In addition, the asymmetric V $2p_{3/2}$ peaks of the $BiVO_4$ samples with abundant oxygen vacancies can be further fitted into two components of V^{5+} (516.8 eV) and V^{4+} (516.0 eV), by which the later species has been reported to have close connection with the existence of oxygen vacancies.[48,49,53] In this case, the observed concentration of V^{4+} can be utilized to represent the surface oxygen vacancy concentration, since they are linearly correlated.[54] As displayed in

Figure 4.7 c, the quantity of V^{4+} fraction becomes larger as the pH of hydrothermal solution becomes less acidic, hence prompting the formation of more oxygen vacancies. In an ideal condition, the formation of one oxygen vacancy would reduce two V^{5+} into two V^{4+} ions on average by considering the charge balance.[54] Since the total number of oxygen atom is four times that of vanadium atom in a perfectly stoichiometric $BiVO_4$ crystal, the oxygen vacancy concentration (with respect to the total number of oxygen) can thus be estimated using the following equation:

$$O_v\ (at\%) = ½ \times ¼ \times V^{4+}\ (at\%) = ⅛\ V^{4+}\ (at\%) \qquad (4\text{-}2)$$

The calculated oxygen vacancy concentrations on the surface of some selected BVO-*x* samples are summarized in **Table 4.1**, which steadily elevate as the pH becomes less acidic.

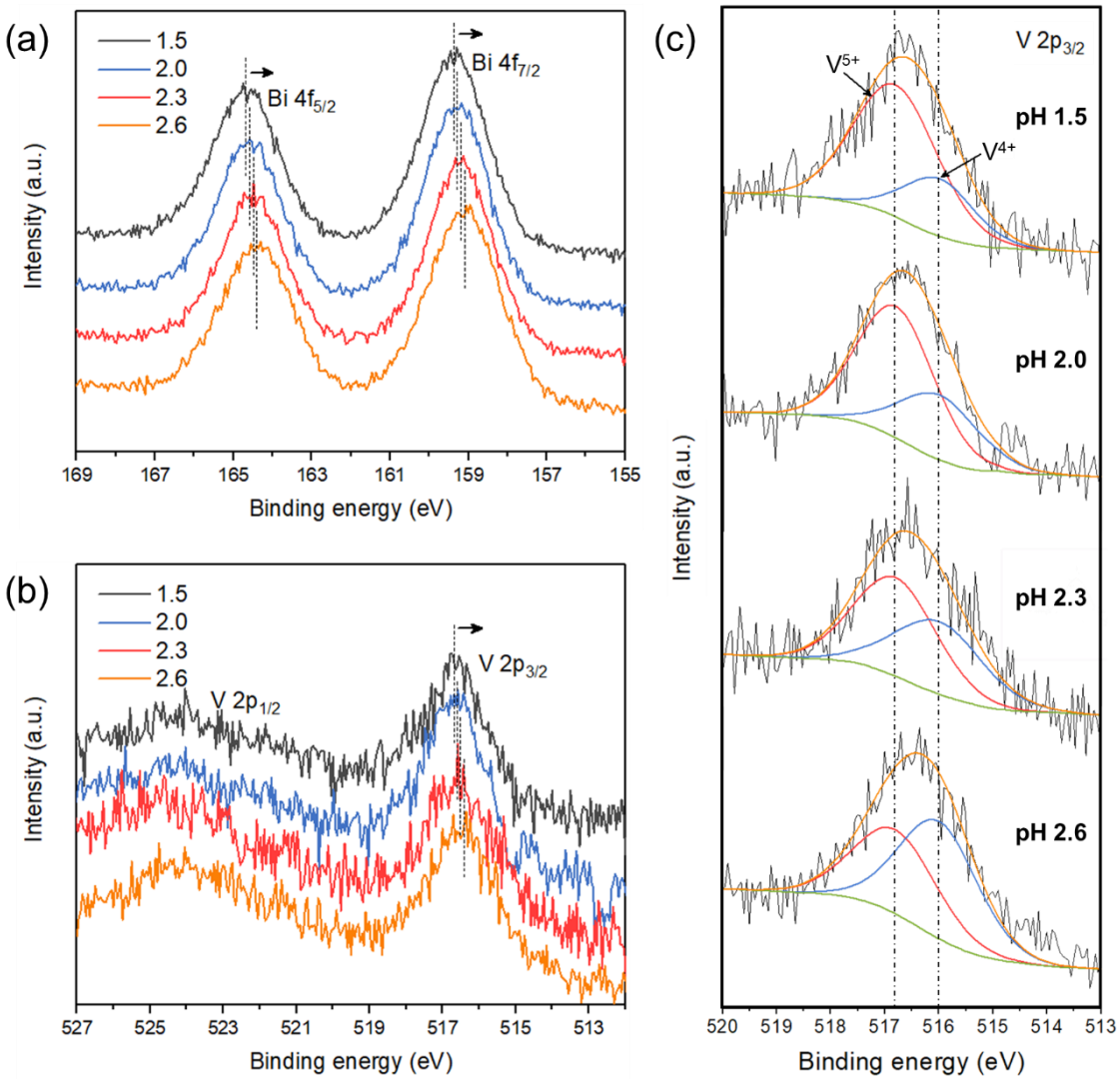

Figure 4.7. (a) Bi 4f and (b) V 2p XPS spectra, as well as (c) V $2p_{3/2}$ peak deconvolution of monoclinic $BiVO_4$ samples synthesized at various pH.

4.3.2. Characterizations of Pd-Photodeposited $BiVO_4$ (Pd/BVO-*x*)

Following the fabrication of the pure monoclinic $BiVO_4$ (BVO-*x*), photodeposition of Pd metal was conducted in pure water under atmospheric condition by using H_2PdCl_4 as precursor. The amount of Pd metal added was fixed to be 0.3 wt% of the monoclinic $BiVO_4$ host photocatalyst. **Figure 4.8 a, c, e** show the SEM images of the products upon Pd photodeposition process, revealing the homogenous distribution of Pd nanoparticles over the (010) facets of all samples. The elemental distribution by the STEM-EDS mapping also confirms the selective photodeposition and well-dispersion of Pd over the (010) reductive facets, as can be seen in **Figure 4.9**. Successful photodeposition of Pd cocatalysts is also confirmed by the UV-Vis, XPS, and ICP-OES analysis (**Figure 4.10**, **Figure 4.11**, and **Table 2.1**). Another Pd/BVO-2.3 sample was also prepared via photodeposition in 10% methanol aqueous solution for some comparison. The corresponding SEM image of this sample (**Figure 4.12**) shows that the Pd cocatalyst is also selectively photodeposited over the (010) facets, however it tends to aggregate with relatively poor dispersion, in contrast to the Pd/BVO samples which were prepared via photodeposition in pure water. Other groups that utilized methanol or other organic sacrificial solution for photodepositing noble metals over some semiconductors, including monoclinic $BiVO_4$, have also encountered similar larger particle size and poorly dispersive behavior of the resulting nanoparticles,[18,21,31,55-57] which might be attributed to the more rapid rate of photodeposition as the consequence of hole scavenging by the organic compounds, thus inducing the accumulation of electrons to reduce the noble metal precursors. Intriguingly, by comparing the corresponding Pd particle size distribution over various Pd/BVO-*x* samples prepared via photodeposition in pure water (**Figure 4.8 b, d, f**), some downsizing phenomena is observed along with the increasing pH. Specifically, the average Pd particles size are 20.2, 16.1, and 10.3 nm for the Pd/BVO-1.5, Pd/BVO-2.0, and Pd/BVO-2.3, respectively. On the other hand, the photodeposited Pd cannot be observed by the SEM analysis for the Pd/BVO-2.6 sample, suggesting the formation of cluster to single atom Pd metals, which would require other advanced characterization techniques in order to observe and analyze them. This size engineering effect can be correlated to the presence of oxygen vacancies within the crystal of monoclinic $BiVO_4$ samples.

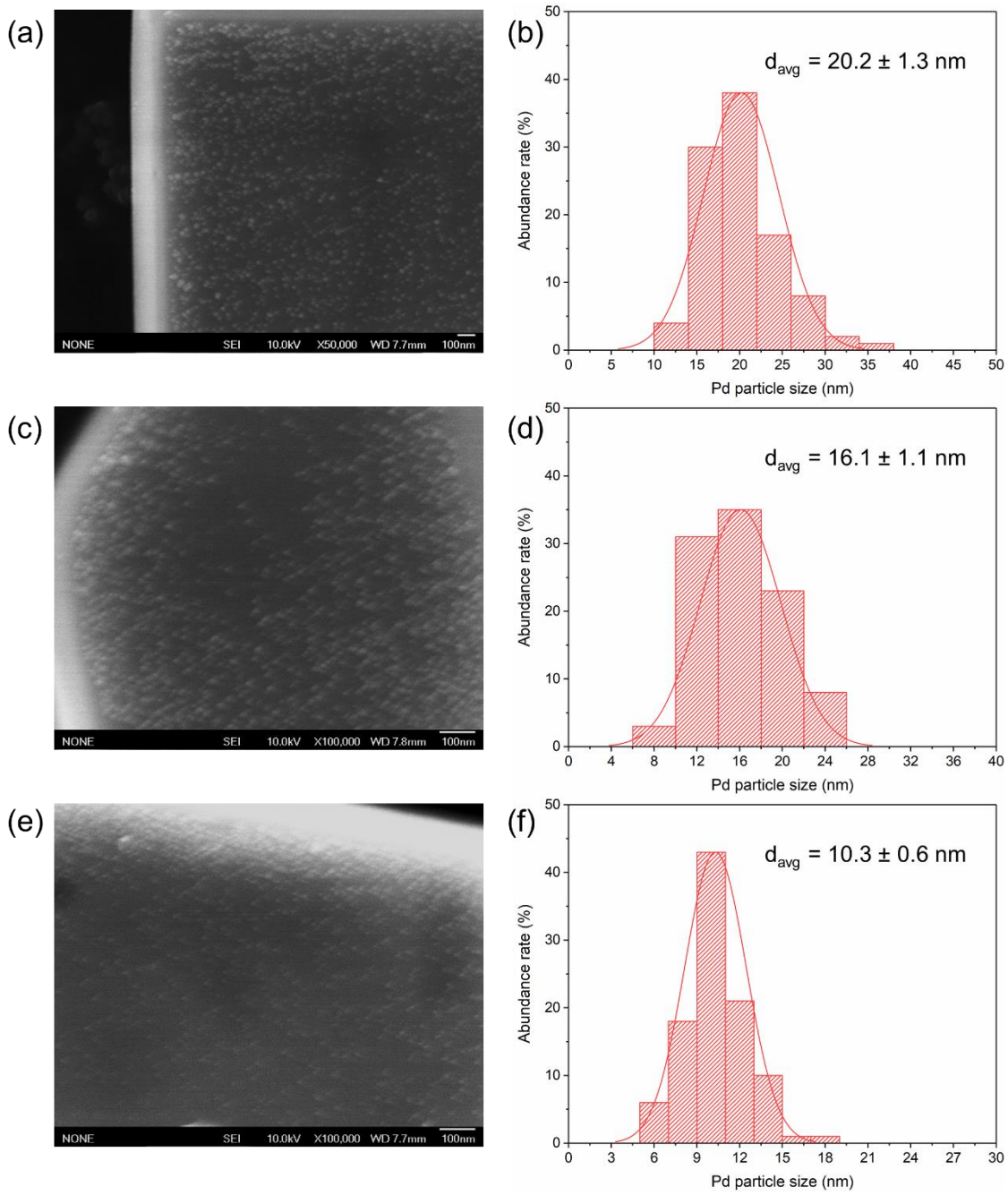

Figure 4.8. SEM images and Pd (white dots) particle size distributions of (a-b) Pd/BVO-1.5, (c-d) Pd/BVO-2.0, (e-f) Pd/BVO-2.3 prepared via photodeposition in pure water (loading amount: 0.3 wt%).

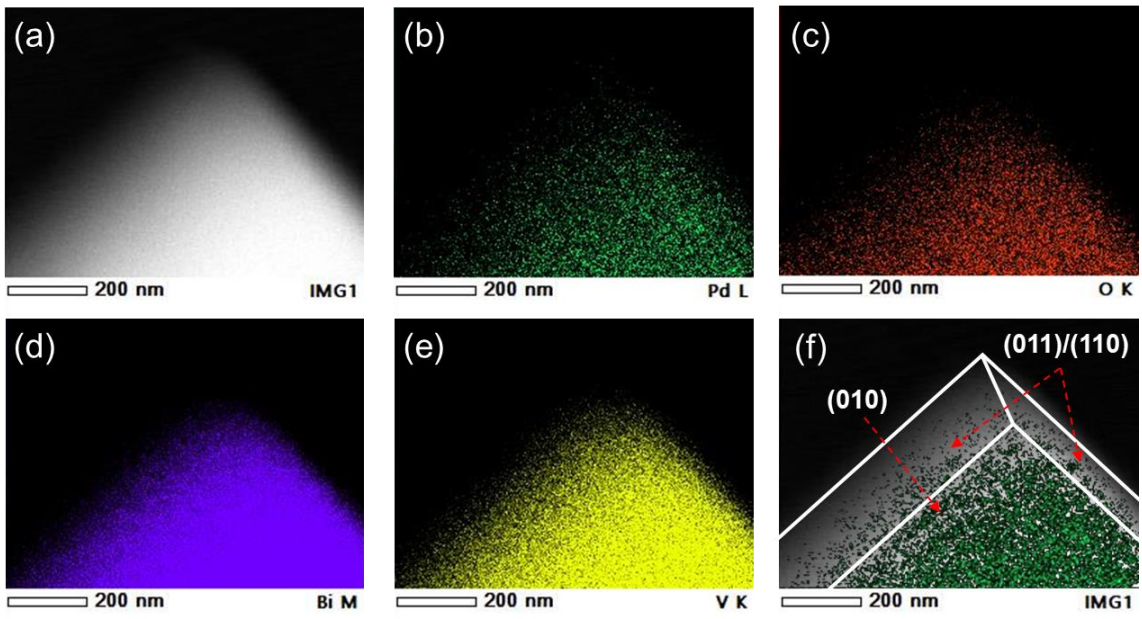

Figure 4.9. (a) STEM image and (b) Pd, (c) O, (d) Bi, and (e) V elemental mapping images, as well as (f) STEM and Pd mapping overlay image of the Pd/BVO-2.3 prepared via photodeposition in pure water. Compared with other elements, the Pd is preferentially distributed in a more designated region, prompting the selective photodeposition of Pd over the (010) reductive facet of monoclinic $BiVO_4$ sample.

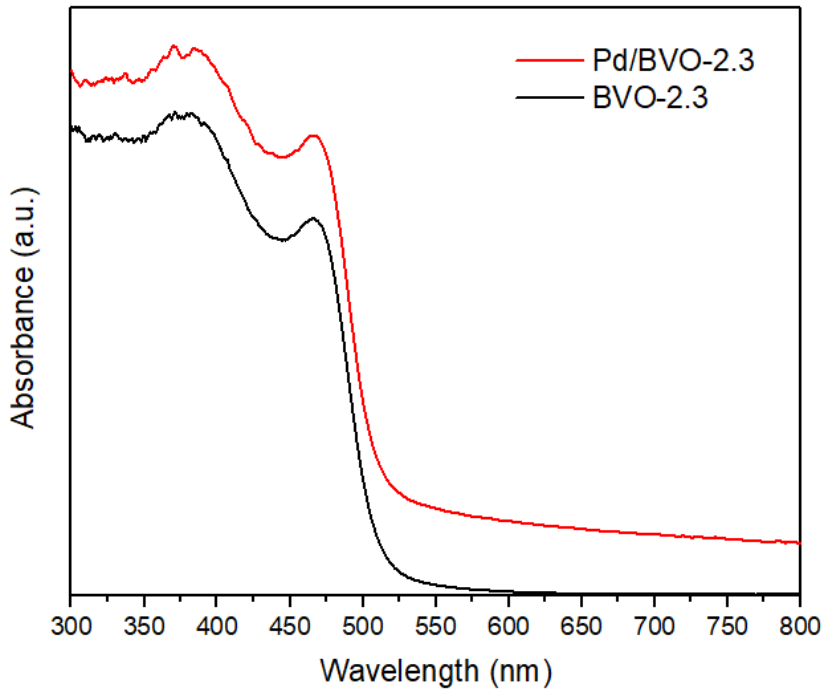

Figure 4.10. UV–vis absorbance spectra of BVO-2.3 before and after Pd photodeposition in pure water. The increase of absorbance over a wide range of wavelengths indicates the existence of Pd cocatalyst on the surface of the monoclinic $BiVO_4$ sample.

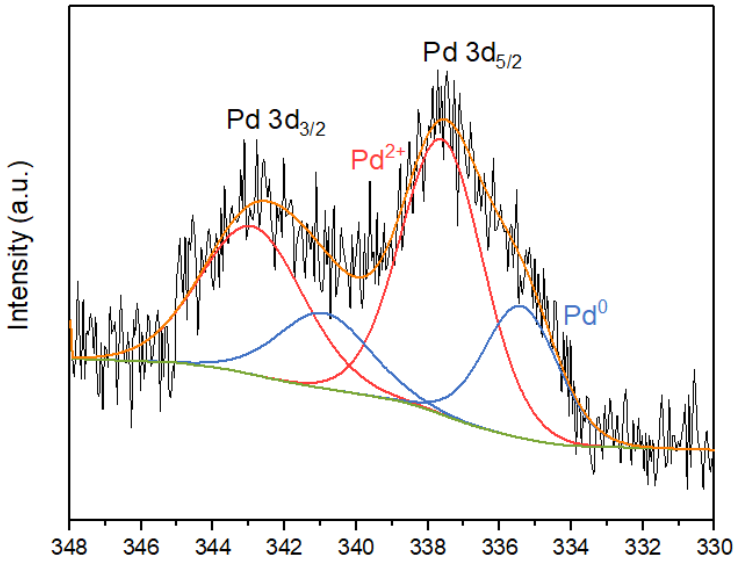

Figure 4.11. Pd 3D XPS spectra of Pd/BVO-2.3, indicating the existence of two Pd species with different valence states, i.e. Pd^0 (metal) and Pd^{2+} (oxide) with the major contribution of the latter species. The formation of palladium oxide species instead of the metallic one might be related to the usage of non-sacrificial solution and atmospheric (oxygen-rich) condition for the Pd photodeposition process.[31] It has been reported that oxidized Pd catalysts exhibit superior activity and selectivity for catalytic H_2O_2 synthesis from H_2 and O_2 in comparison to their reduced counterparts.[58,59] Further in-depth study and investigation would be required to analyze the effect Pd oxidation state to the surface catalytic H_2O_2 generation via photocatalytic ORR.

Table 4.2. Composition of the as-prepared Pd/BVO-*x* samples determined by ICP-OES. The analyzed samples were dissolved beforehand in Aqua regia and H_2SO_4 solution solution. Based on the feeding of H2PdCl4 precursor, the theoretical loading amount of Pd is 0.3 wt%, equal to 0.9 at%. In all Pd/BVO-*x* samples, the observed Pd content are about 1 at%, by which reasonable agreement with the theoretical content can be inferred.

Sample	Bi (mg/L)	V (mg/L)	Pd (mg/L)	Bi: V: Pd
Pd/BVO-1.5	13.39	3.23	0.05	1.00: 0.99: 0.01
Pd/BVO-2.0	12.60	3.07	0.05	1.00: 1.00: 0.01
Pd/BVO-2.3	15.80	3.88	0.07	1.00: 1.01: 0.01
Pd/BVO-2.6	13.51	3.33	0.06	1.00: 1.01: 0.01

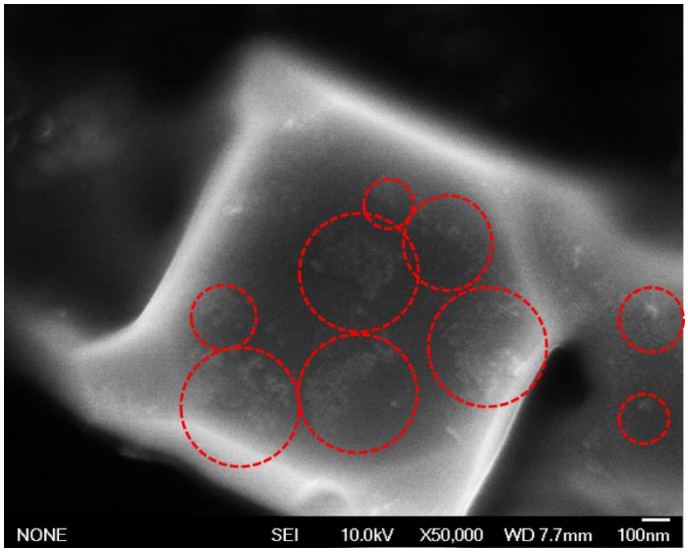

Figure 4.12. SEM image of Pd/BVO-2.3 sample prepared via photodeposition in 10% methanol solution. The Pd cocatalyst is also selectively photodeposited on the (010) facet, however it tends to be more aggregated and not well-dispersed, as circled in red.

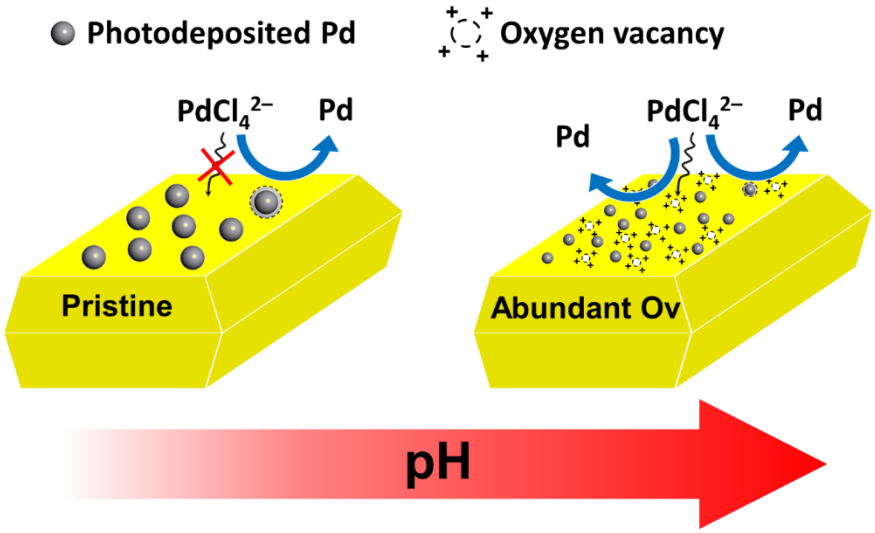

Figure 4.13. Schematic of the Pd photodeposition process over the (010) facet of monoclinic $BiVO_4$ with and without oxygen vacancies. The presence of oxygen vacancy enables $PdCl_4^{2-}$ precursor to interact more freely with the reduction facet, thus exhibiting a downsizing effect to the photodeposited Pd.

Recently, Zhao et al. has demonstrated that the (010) facets of monoclinic $BiVO_4$ tend to have positive charge under dark condition, while it becomes negatively charged under light irradiation,[34] due to the accumulation of photogenerated electrons induced by the spatial charge separation nature of monoclinic $BiVO_4$.[26,27] Consequently, the reduction of positively charged Fe^{3+} ions can take place favorably on the (010) facets, while the

same facets would also repel the negatively charged shuttle of $Fe(CN)_6^{3-}$ and thus hindering its reduction reaction, even though both ions have identical reduction potential.[34] In our current study, $PdCl_4^{2-}$ complex species was used as the precursor for Pd photodeposition. Accordingly, it would be quite difficult for the negative charged $PdCl_4^{2-}$ ion to effectively reach a perfect (010) facet (without defects) and be reduced during the illumination process. This notion can explain the relatively larger size of photodeposited Pd nanoparticles over the (010) surfaces of pristine monoclinic $BiVO_4$, because the reduction reaction would preferably take place over the already available Pd metal sites with more uniform charge distribution, especially since the photogenerated electrons from the $BiVO_4$ would be transferred and trapped by Pd particles once nucleated.[32] Interestingly, it has been reported that the introduction of oxygen vacancy would induce a significant charge density redistribution, thus affecting the electrostatic interactions.[60] In this regard, the presence of oxygen vacancies would make the catalytic surface becomes relatively more positive, peculiarly in the region close to the vacancy, which would significantly decrease the repel force, thus increasing the probability for $PdCl_4^{2-}$ ion to be homogenously adsorbed and reduced over the surface of monoclinic $BiVO_4$. Higher density of oxygen vacancy on the photocatalysis surface would provide more reduction sites for the Pd photodeposition process, thus enabling the formation of smaller Pd cocatalyst on the (010) surface of monoclinic $BiVO_4$, as encountered in this work. Accordingly, it is reasonable to expect an even smaller size of Pd (cluster to single atom) on Pd/BVO-2.6 sample which evidently contains higher concentration of oxygen vacancy, in addition to its larger specific surface area which would allow more efficient adsorption process for the $PdCl_4^{2-}$ precursor. **Figure 4.13** illustrates the size engineering effect of oxygen vacancy on photodeposited Pd over the (010) facet of monoclinic $BiVO_4$.

4.3.3. Photocatalytic H_2O_2 Production and Factors behind the Performances

Photocatalytic H_2O_2 synthesis of the as-prepared samples in citric buffer solution was evaluated under visible light irradiation. As depicted in **Figure 2.16 a**, the photocatalytic performances of various Pd/BVO-*x* samples indicated increasing and decreasing behaviors along with the pH variation, by which Pd/BVO-2.3 exhibited the highest H_2O_2 production of 2.35 mM after one-hour visible light irradiation, achieving, to the best of our knowledge, the state-of-the-art AQE of 19.2% at 420 nm in photocatalytic H_2O_2 production over $BiVO_4$-based materials. Below pH 2.3, as it became less acidic, the corresponding H_2O_2 evolution activity increased gradually (see **Figure 2.16 b**). However,

for the pH more than 2.3, the corresponding H_2O_2 generation rate started to decline. In detail, the accumulated concentration of H_2O_2 within 1 h were 1.27 mM, 1.42 mM, 1.62 mM, 1.85 mM, 1.96 mM, and 1.43 mM for Pd/BVO-0.75, Pd/BVO-1.5, Pd/BVO-2.0, Pd/BVO-2.2, Pd/BVO-2.4, and Pd/BVO-2.6 samples, respectively.

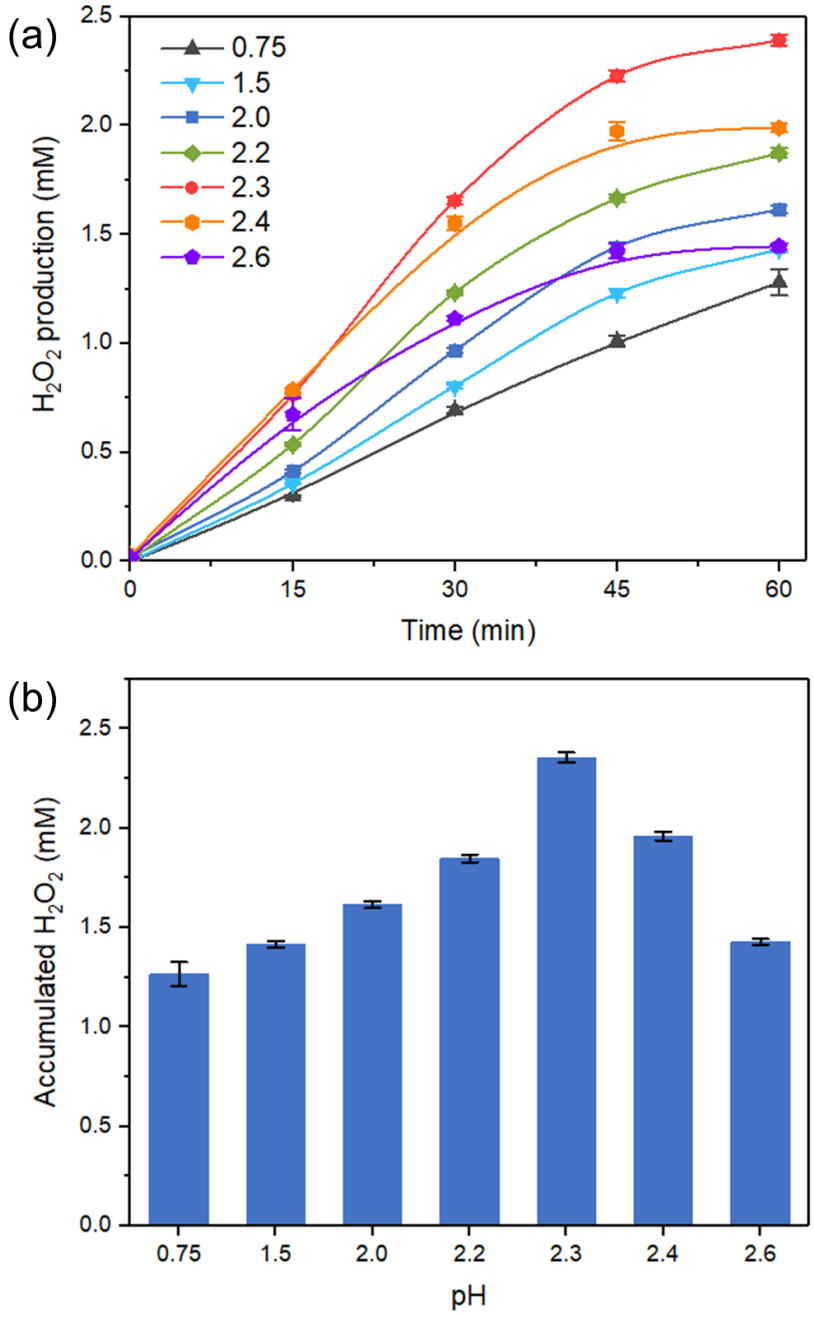

Figure 4.14. (a) Time-dependent H_2O_2 production course of Pd/BVO-*x* samples with different hydrothermal pH and (b) effect of hydrothermal pH on the accumulated H_2O_2 concentration after 1 h of light illumination activity test. Reaction condition: 80 mg catalyst, 80 mL citric buffer solution, O_2 flow rate: 300 mL/min, and light source: 300 W Xe Lamp equipped with L-42 cut-off filter.

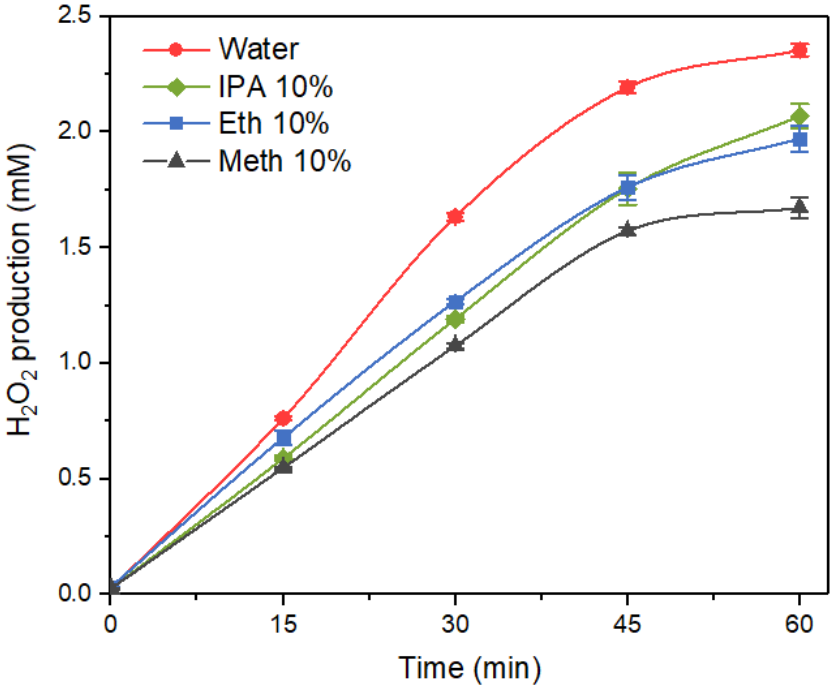

Figure 4.15. Time-dependent H_2O_2 production of Pd/BVO-2.3 samples prepared via photodeposition in pure water and 10% organic aqueous solutions (methanol, ethanol, and isopropanol (IPA)).

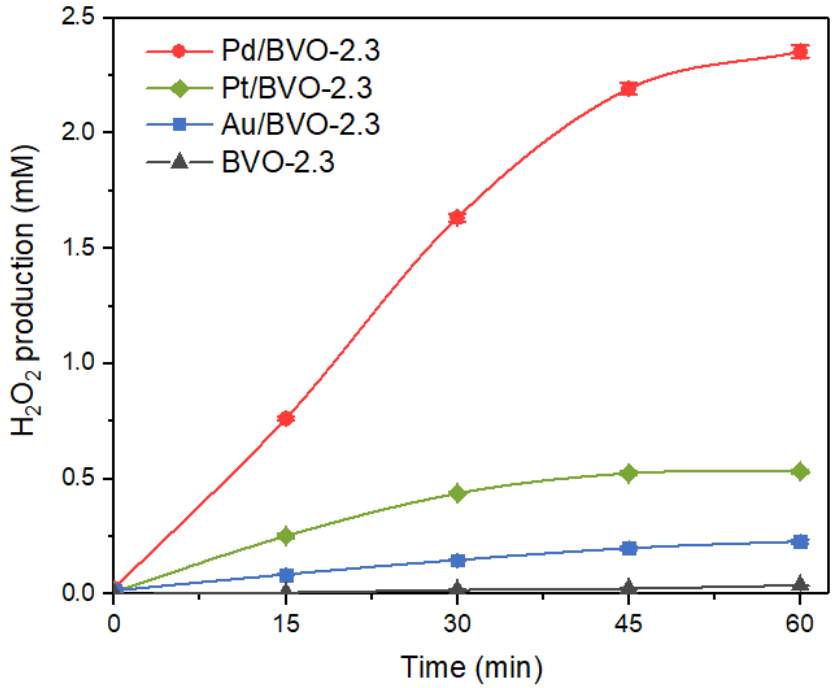

Figure 4.16. Time-dependent H_2O_2 production of various BVO-2.3 samples loaded with various metal cocatalysts (prepared via photodeposition in pure water with loading amount of 0.3 wt%).

Some other Pd/BVO-2.3 samples were also prepared through photodeposition in several organic aqueous solutions. As represented in **Figure 4.15**, those samples were found to exhibit minor photocatalytic performance compared to the sample prepared in pure water, with H_2O_2 production of 1.63 mM, 1.97 mM, and 2.07 mM within 1 hour of testing for the Pd/BVO-2.3 samples prepared in methanol, ethanol, and isopropanol (IPA) 10% aqueous solutions, respectively. The decrease in photocatalytic activity might be attributed to the aggregation and poor dispersion of Pd cocatalyst over the surface of monoclinic $BiVO_4$, when organic compound is used as sacrificial agent for the photodeposition process, as has been addressed earlier. Furthermore, some other metals (Au and Pt) were also employed to modify the BVO-2.3 and the corresponding H_2O_2 generation performances were compared (see **Figure 4.16**). The observed activities of both Pt/BVO-2.3 (0.53 mM/h) and Au/BVO-2.3 (0.23 mM/h) were substantially lower than that of Pd/BVO-2.3, thus suggesting the superiority of Pd cocatalyst over other metals, in accordance to the previous report.[18] In addition, as formerly expected, pure monoclinic BVO-2.3 sample (without any cocatalyst), due to the absence of active sites for the catalytic ORR, was only able to generate almost negligible amount of H_2O_2, up to 38 μM/h, thus confirming the vital factor of Pd cocatalyst for providing the reactive centers for more efficient H_2O_2 evolution reaction with about 62 fold enhancement.

Figure 4.17 display the results of several control experiments over the Pd/BVO-2.3 sample in order to probe the origin of the superior H_2O_2 production. When the reactant suspension was purged by the N_2 gas, the 60-min H_2O_2 production decreased significantly to 115 μM, corresponding to about 5% of its activity under O_2 bubbling, thus suggesting the major contribution of ORR to the synthesis of H_2O_2. This subsidiary H_2O_2 production without O_2 gas bubbling might derive from the remaining dissolved oxygen in the solution which was not able to be completely removed by the N_2 purging. Without the presence of catalyst and light illumination, no H_2O_2 production was observed, indicating that the H_2O_2 generation proceeded solely through the photocatalytic reaction. In addition to that, the corresponding AQE values of H_2O_2 evolution over Pd/BVO-2.3 as a function of absorption wavelength is practically in good accordance with the UV-Vis DRS pattern of BVO-2.3 (**Figure 4.18** and **Table 2.5**), thus confirming the key contribution of solar-driven photocatalytic process to the H_2O_2 generation. Compared with the other representative cases using $BiVO_4$ photocatalyst (**Table 4.4**), our work demonstrates outstanding performance towards visible-light-driven artificial photosynthesis of H_2O_2.

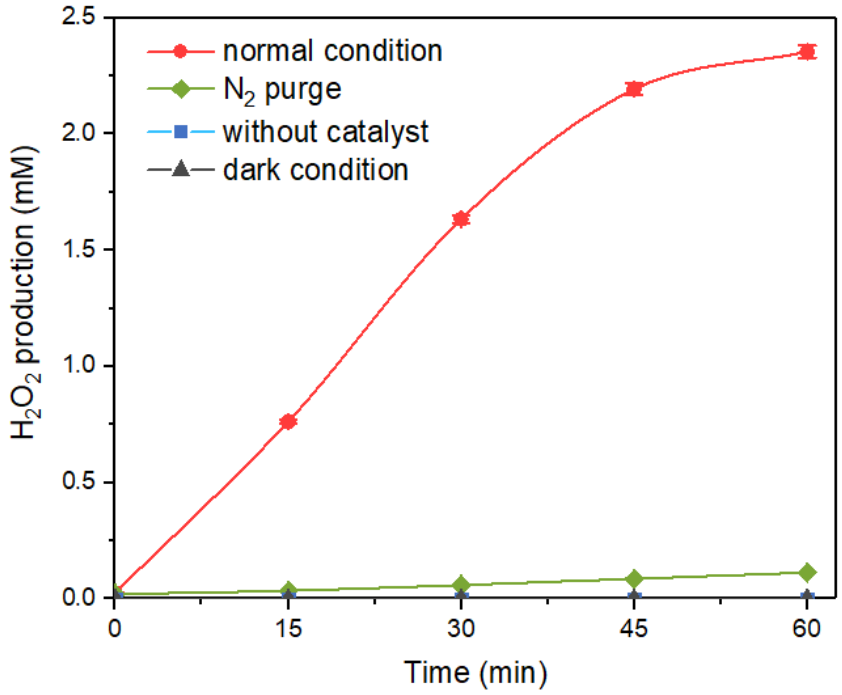

Figure 4.17. Time-dependent H_2O_2 production of Pd/BVO-2.3 under various test conditions. Normal condition: 80 mg catalyst (0.3 wt% photodeposited Pd), 80 mL citric buffer solution, O_2 purge (300 mL/min), and 300 W Xe lamp (equipped with L-42 cut-off filter). For N_2 purge condition, the flow rate of N_2 was 300 mL/min.

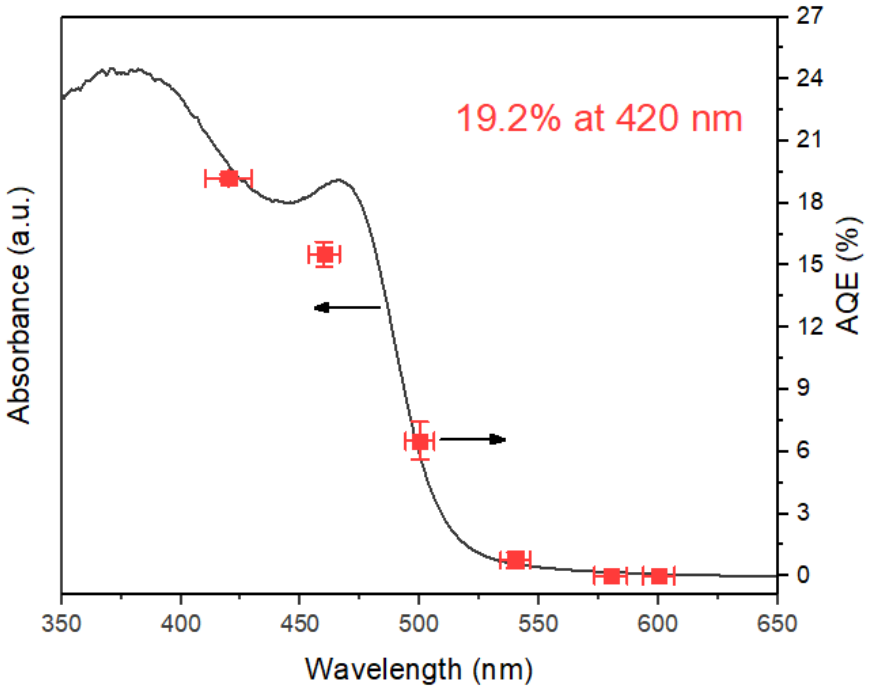

Figure 4.18. Wavelength-dependent apparent quantum efficiency (AQE) of photocatalytic H_2O_2 production of monoclinic $BiVO_4$ synthesized at pH 2.3 with 0.3 wt% Pd (via photodeposition in pure water).

Table 4.3. Measurement of apparent quantum efficiency (AQE).

Wavelength (nm)	Number of incident photons (h^{-1})	H_2O_2 production rate (μmol/h)	Number of reacted electrons (h^{-1})	AQE (%)
420	1.469×10^{20}	23.42	2.821×10^{19}	19.2
460	1.884×10^{20}	24.29	2.926×10^{19}	15.5
500	1.756×10^{20}	9.49	1.143×10^{19}	6.51
540	3.437×10^{20}	0.77	9.228×10^{17}	0.53

Table 4.4. Performance comparison of solar driven H_2O_2 synthesis over $BiVO_4$-based photocatalyst reported in the representative literatures.

Photocatalyst	Experimental conditions			H_2O_2 synthesis rate (μM/h)	AQE (420 nm)	Refs.
	Test solution*	Gas	Light source			
Pd/$BiVO_4$-O_v (80 mg)	CBS (80 mL, 0.2 M, pH ≈ 3.0)	O_2	300 W Xe Lamp (λ > 420 nm)	2354	19.2%	This work
CoO*x*/Mo:BiVO4/Pd (24 mg)	PBS (12 mL, 1 M, pH ≈ 7.4)	O_2	AM 1.5 G	1425	5.8%	[3]
Au/$BiVO_4$ (50 mg)	Water (30 mL)	O_2	2 kW Xe lamp (λ > 420 nm)	12	0.24%	[9]
$BiVO_4$ (010)-AuPd (80 mg)	CBS (80 mL, 0.2 M, pH ≈ 3.0)	O_2	LED Lamp (20 mW/cm^2, 420 nm)	1146	11.38%	[21]
CN-Au/$BiVO_4$ (80 mg)	CBS (80 mL, 0.2 M, pH ≈ 3.0)	O_2	LED Lamp (50 mW/cm^2, 420 nm)	676	6.7%	[12]
Cu@Au/$BiVO_4$ (100 mg)	5% methanol solution (130 mL)	O_2	LED Lamp (12.5 mW/cm^2, 420 nm)	65	0.88%	[20]
PO_4^{3-} coated Pd-$BiVO_4$	10% methanol solution (50 mL)	O_2	300 W Xe Lamp (λ > 420 nm)	300	-	[18]
Plate-$BiVO_4$/CoO_x (50 mg)	10% methanol solution (150 mL)	O_2	300 W Xe Lamp (λ > 420 nm)	5	-	[61]

* *Note*: CBS: citric buffer solution; PBS: phosphate buffer solution

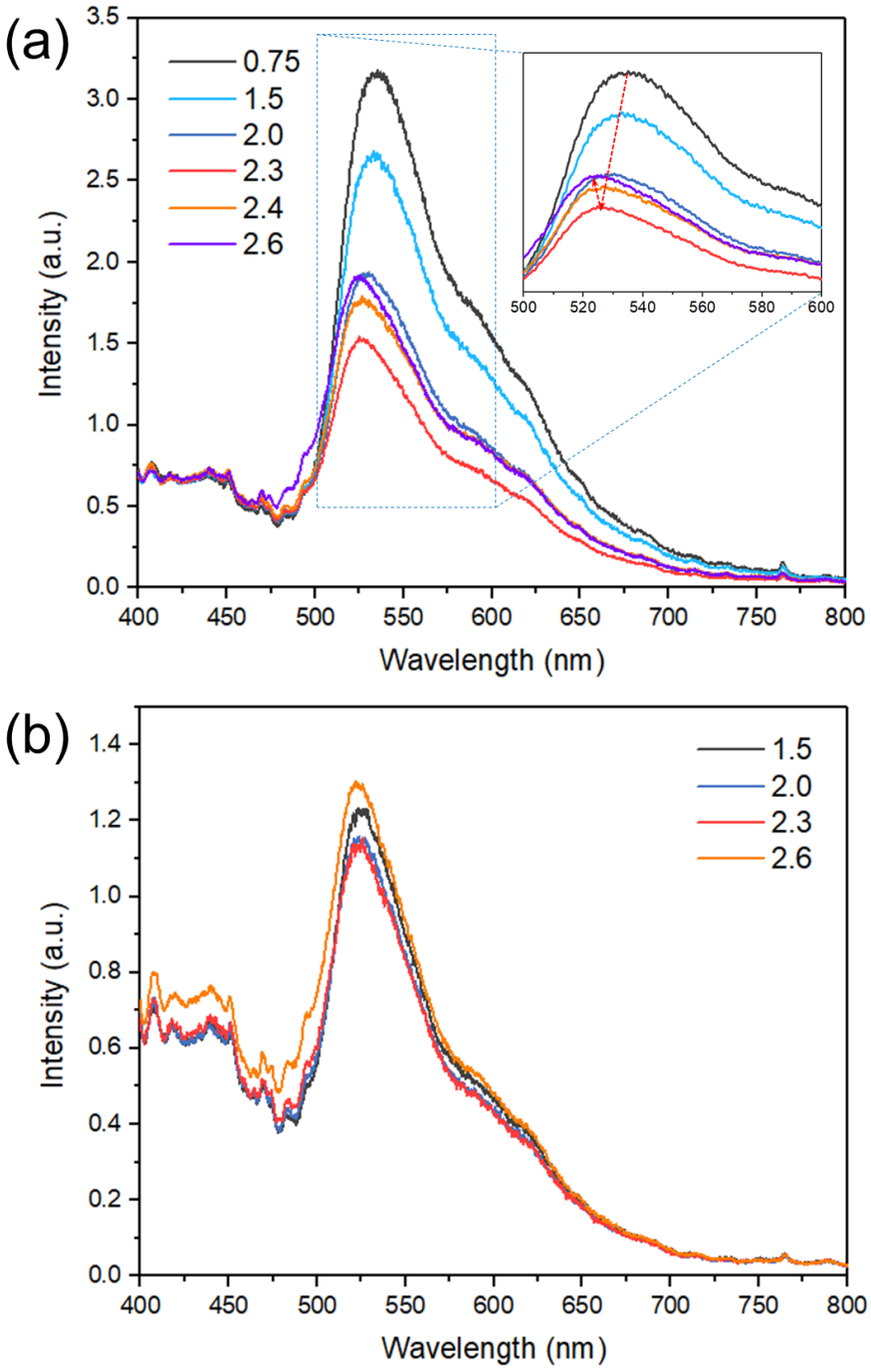

Figure 4.19. Steady-state photoluminescence (PL) spectra of various (a) BVO-*x* and (b) Pd/BVO-*x* samples with excitation wavelength of 350 nm.

In order to obtain better understanding regarding the factors behind the photocatalytic performances, photoluminescence (PL) analysis over the as-prepared BVO-*x* and Pd/BVO-*x* samples was utilized to investigate the photogenerated charge carrier dynamics and separation. As displayed in **Figure 4.19 a**, the emission peaks of BVO-*x*, deriving from the radiative recombination of electron-hole pairs, slightly blue-shift as the

pH increases, from 535 nm for pH 0.75 to 526 nm for pH 2.3 and 523 nm for pH 2.6, which might be attributed to the formation of more oxygen vacancies[62] and/or the morphology transformation. More importantly, BVO-2.3 exhibited a lower emission peak intensity in comparison to other BVO-*x* samples, thus indicating the suppression of electron-holes recombination in BVO-2.3 sample. In this case, the oxygen vacancies might facilitate more efficient charge carrier transfer and separation, since they could take the role of electron trap centers, especially those on the surface.[63,64] However, higher concentration of oxygen vacancies in the bulk of monoclinic $BiVO_4$ would produce the otherwise situation, where the oxygen defects would rather act as recombination centers for the charge carriers,[64,65] thus explaining the increasing in PL intensity for the BVO-*x* samples synthesized at pH more than 2.3. After Pd photodeposition, the as-prepared Pd/BVO-*x* samples showed markedly lower PL emission peak intensities (**Figure 4.19 b**), prompting the great contribution of Pd cocatalyst for capturing the electrons and inhibit the recombination. Notably, Pd/BVO-2.6 showed higher peak intensity compared to others, indicating that it maintains the drawback of oxygen vacancy with an excessive amount, which promoted the undesired electron-hole recombination. Nonetheless, considering the similar emission peak intensities for Pd/BVO-1.5, Pd/BVO-2.0, and Pd/BVO-2.3 samples, it might be more reasonable to speculate that the enhancement of charge carrier dynamics might only serve as a minor factor for the activity improvement.

Based on the above discussions, we propose the central role of Pd cocatalyst size for determining the corresponding photocatalytic H_2O_2 production, by which a downsizing effect of oxygen vacancy on the well-dispersed photodeposited Pd over (010) surface of monoclinic $BiVO_4$ was observed. Accordingly, by further reducing the size of the Pd cocatalyst, more potential catalytic sites would be generated, thus enabling more swift and efficient catalytic ORR for the H_2O_2 evolution. Regardless of that, the size of Pd cocatalyst was found to have no strong correlation with its ability to suppress the recombination of photogenerated charge carriers. On the other hand, overabundant oxygen vacancy within the crystal of monoclinic $BiVO_4$ would be rather harmful to the charge carrier separation efficiency, as mentioned earlier, thus negatively affecting the overall photocatalytic performance. In this case, the superior photocatalytic H_2O_2 production performance of the optimized sample (Pd/BVO-2.3) resulted from the proper balance between the enhanced surface catalytic reaction of downsized Pd cocatalyst and charge recombination induced by oxygen vacancy, as illustrated in **Figure 4.20**.

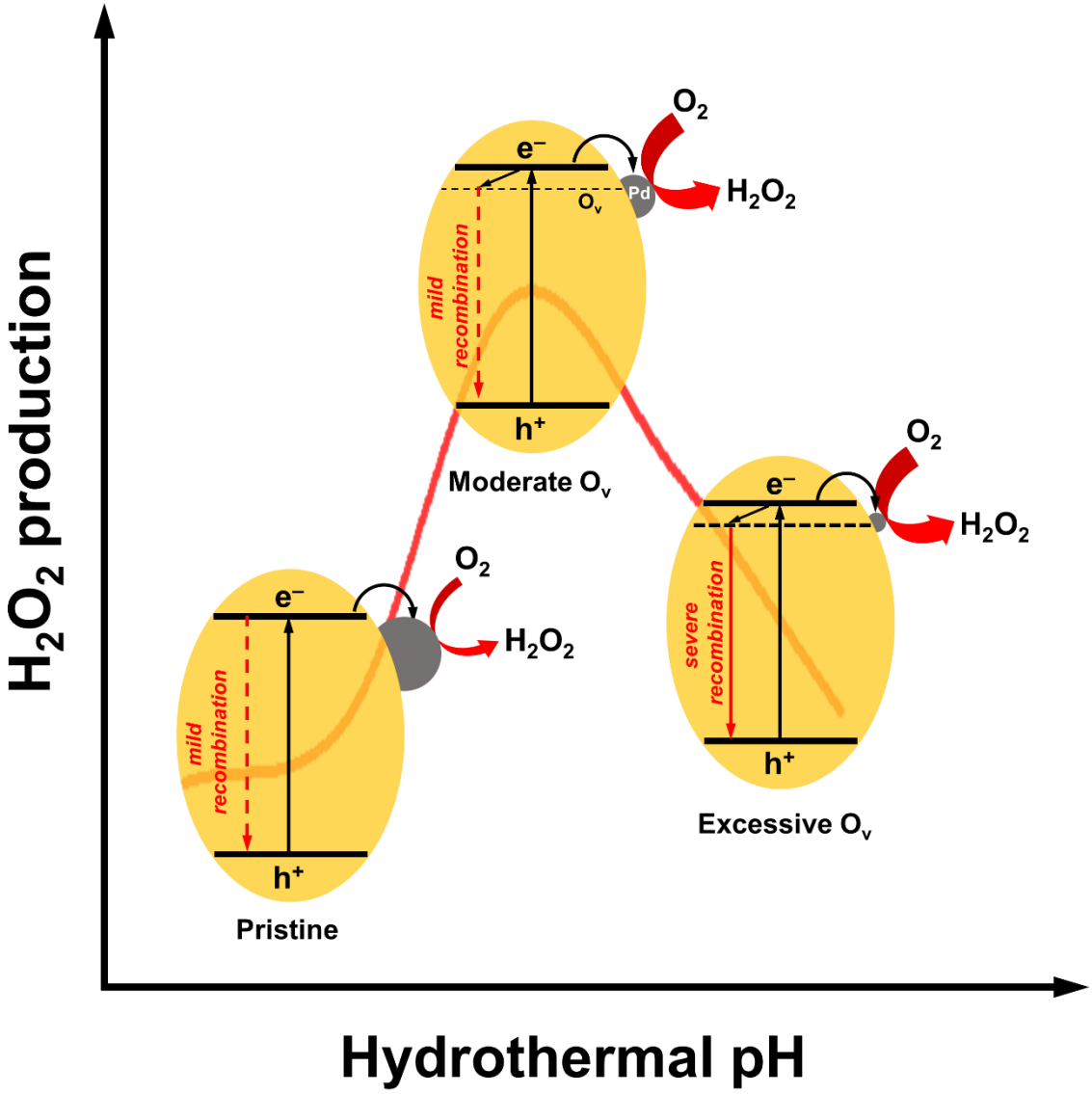

Figure 4.20. Schematic illustration of the trade-off between enhanced surface catalytic reaction kinetic of downsized Pd cocatalyst and charge recombination by oxygen vacancy for regulating the photocatalytic H_2O_2 production over Pd/BVO-*x* as the function of hydrothermal pH.

4.4. Conclusion

In summary, an effective oxygen vacancy-mediated size engineering strategy was successfully applied and demonstrated over the homogenously distributed palladium cocatalyst photodeposited on the (010) surface of monoclinic $BiVO_4$. The manipulation of oxygen vacancy level was accomplished by simply adjusting the pH of the hydrothermal solution for the fabrication of pure monoclinic $BiVO_4$ samples, by which higher pH would generate more oxygen vacancy. It is proposed that the oxygen vacancy

would serve as surface charge redistributor and positively influence the electrostatic interaction between the (010) surface of monoclinic $BiVO_4$ and the negative $PdCl_4^{2-}$ precursor ions, thus yielding smaller size of Pd cocatalysts. An appropriate trade-off between the enhanced surface catalytic reaction kinetic as the result of downsized Pd cocatalyst and charge recombination by oxygen vacancy in the bulk material of monoclinic $BiVO_4$ bestowed the optimized sample with an outstanding visible-light-driven H_2O_2 evolution performance of 2.35 mM within 1 h illumination, corresponding to a high AQE of 19.2% at 420 nm. The findings in this study highlight and prompt the importance of surface modulation and optimization for fabricating superior monoclinic $BiVO_4$ photocatalysts for efficient solar-driven H_2O_2 synthesis via ORR.

References

1. J. Liu, Y. Zou, B. Jin, K. Zhang, J. H. Park (2019) Hydrogen Peroxide Production from Solar Water Oxidation. ACS Energy Lett. 4 (12):3018-3027. doi:10.1021/acsenergylett.9b02199

2. Z. Wang, C. Li, K. Domen (2019) Recent Developments in Heterogeneous Photocatalysts for Solar-Driven Overall Water Splitting. Chem. Soc. Rev. 48 (7):2109-2125. doi:10.1039/C8CS00542G

3. T. Liu, Z. Pan, J. J. M. Vequizo, K. Kato, B. Wu, A. Yamakata, K. Katayama, B. Chen, C. Chu, K. Domen (2022) Overall Photosynthesis of H_2O_2 by an Inorganic Semiconductor. Nat. Commun. 13 (1):1034. doi:10.1038/s41467-022-28686-x

4. Y. Shiraishi, T. Takii, T. Hagi, S. Mori, Y. Kofuji, Y. Kitagawa, S. Tanaka, S. Ichikawa, T. Hirai (2019) Resorcinol–Formaldehyde Resins as Metal-Free Semiconductor Photocatalysts for Solar-to-Hydrogen Peroxide Energy Conversion. Nat. Mater. 18 (9):985-993. doi:10.1038/s41563-019-0398-0

5. C. Xia, Y. Xia, P. Zhu, L. Fan, H. Wang (2019) Direct Electrosynthesis of Pure Aqueous H_2O_2 Solutions up to 20% by Weight Using a Solid Electrolyte. Science 366 (6462):226-231. doi:10.1126/science.aay1844

6. S. Fukuzumi, Y.-M. Lee, W. Nam (2018) Solar-Driven Production of Hydrogen Peroxide from Water and Dioxygen. Chem. Eur. J. 24 (20):5016-5031. doi:10.1002/chem.201704512

7. H. Hou, X. Zeng, X. Zhang (2020) Production of Hydrogen Peroxide by Photocatalytic Processes. Angew. Chem. Int. Ed. 59 (40):17356-17376. doi:10.1002/anie.201911609

8. Y. Xue, Y. Wang, Z. Pan, K. Sayama (2021) Electrochemical and Photoelectrochemical Water Oxidation for Hydrogen Peroxide Production. Angew. Chem. Int. Ed. 60 (19):10469-10480. doi:10.1002/anie.202011215

9. H. Hirakawa, S. Shiota, Y. Shiraishi, H. Sakamoto, S. Ichikawa, T. Hirai (2016) Au Nanoparticles Supported on $BiVO_4$: Effective Inorganic Photocatalysts for H_2O_2 Production from Water and O_2 under Visible Light. ACS Catal. 6 (8):4976-4982. doi:10.1021/acscatal.6b01187

10. J. M. Campos-Martin, G. Blanco-Brieva, J. L. G. Fierro (2006) Hydrogen Peroxide Synthesis: An Outlook beyond the Anthraquinone Process. Angew. Chem. Int. Ed. 45 (42):6962-6984. doi:10.1002/anie.200503779

11. P. Nikačević, F. S. Hegner, J. R. Galán-Mascarós, N. López (2021) Influence of Oxygen Vacancies and Surface Facets on Water Oxidation Selectivity toward Oxygen or Hydrogen Peroxide with $BiVO_4$. ACS Catal. 11 (21):13416-13422. doi:10.1021/acscatal.1c03256

12. H. Shi, Y. Li, X. Wang, H. Yu, J. Yu (2021) Selective Modification of Ultra-thin g-C_3N_4 Nanosheets on the (110) Facet of Au/$BiVO_4$ for Boosting Photocatalytic H_2O_2 production. Appl. Catal. B 297:120414. doi:10.1016/j.apcatb.2021.120414

13. H. L. Tan, X. Wen, R. Amal, Y. H. Ng (2016) $BiVO_4$ {010} and {110} Relative Exposure Extent: Governing Factor of Surface Charge Population and Photocatalytic Activity. J. Phy. Chem. Let. 7 (7):1400-1405. doi:10.1021/acs.jpclett.6b00428

14. M. D. Bhatt, J. Y. Lee (2021) Theoretical Insights into the Mechanism of Oxygen Evolution Reaction (OER) on Pristine $BiVO_4$ (001) and $BiVO_4$ (110) Surfaces in Acidic Medium Both in the Gas and Solution (Water) Phases. Nanotechnology 32 (33):335401. doi:10.1088/1361-6528/abfcfd

15. Q. Zhang, M. Liu, W. Zhou, Y. Zhang, W. Hao, Y. Kuang, H. Liu, D. Wang, L. Liu, J. Ye (2021) A Novel Cl^- Modification Approach to Develop Highly Efficient Photocatalytic Oxygen Evolution over $BiVO_4$ with AQE of 34.6%. Nano Energy 81:105651. doi:10.1016/j.nanoen.2020.105651

16. Z.-F. Huang, L. Pan, J.-J. Zou, X. Zhang, L. Wang (2014) Nanostructured Bismuth Vanadate-Based Materials for Solar-Energy-Driven Water Oxidation: A Review on Recent Progress. Nanoscale 6 (23):14044-14063. doi:10.1039/C4NR05245E

17. X. Shi, Y. Zhang, S. Siahrostami, X. Zheng (2018) Light-Driven $BiVO_4$–C Fuel Cell with Simultaneous Production of H_2O_2. Advanced Energy Materials 8 (23):1801158. doi:10.1002/aenm.201801158

18. K. Fuku, R. Takioka, K. Iwamura, M. Todoroki, K. Sayama, N. Ikenaga (2020) Photocatalytic H_2O_2 Production from O_2 under Visible Light Irradiation over Phosphate Ion-Coated Pd Nanoparticles-Supported $BiVO_4$. Appl. Catal. B 272:119003. doi:10.1016/j.apcatb.2020.119003

19. A. Nadar, S. S. Gupta, Y. Kar, S. Shetty, A. P. van Bavel, D. Khushalani (2020) Evaluating the Reactivity of $BiVO_4$ Surfaces for Efficient Electrocatalytic H_2O_2 Production: A Combined Experimental and Computational Study. J. Phy. Chem. C 124 (7):4152-4161. doi:10.1021/acs.jpcc.9b11418

20. K. Wang, M. Wang, J. Yu, D. Liao, H. Shi, X. Wang, H. Yu (2021) $BiVO_4$ Microparticles Decorated with Cu@Au Core-Shell Nanostructures for Photocatalytic H_2O_2 Production. ACS Appl. Nano Mater. 4 (12):13158-13166. doi:10.1021/acsanm.1c02688

21. H. Shi, Y. Li, K. Wang, S. Li, X. Wang, P. Wang, F. Chen, H. Yu (2022) Mass-Transfer Control for Selective Deposition of Well-Dispersed AuPd Cocatalysts to Boost Photocatalytic H_2O_2 Production of $BiVO_4$. Chem. Eng. J. 443:136429. doi:10.1016/j.cej.2022.136429

22. X. Wang, Z. Li, Y. Qu, T. Yuan, W. Wang, Y. Wu, Y. Li (2019) Review of Metal Catalysts for Oxygen Reduction Reaction: From Nanoscale Engineering to Atomic Design. Chem 5 (6):1486-1511. doi:10.1016/j.chempr.2019.03.002

23. X. Meng, P. Zong, L. Wang, F. Yang, W. Hou, S. Zhang, B. Li, Z. Guo, S. Liu, G. Zuo, Y. Du, T. Wang, V. A. L. Roy (2020) Au-Nanoparticle-Supported ZnO as Highly Efficient Photocatalyst for H_2O_2 Production. Catal. Commun. 134:105860. doi:10.1016/j.catcom.2019.105860

24. J. S. Jirkovský, I. Panas, E. Ahlberg, M. Halasa, S. Romani, D. J. Schiffrin (2011) Single Atom Hot-Spots at Au–Pd Nanoalloys for Electrocatalytic H_2O_2 Production. J. Am. Chem. Soc. 133 (48):19432-19441. doi:10.1021/ja206477z

25. M. Ledendecker, E. Pizzutilo, G. Malta, G. V. Fortunato, K. J. J. Mayrhofer, G. J. Hutchings, S. J. Freakley (2020) Isolated Pd Sites as Selective Catalysts for

Electrochemical and Direct Hydrogen Peroxide Synthesis. ACS Catal. 10 (10):5928-5938. doi:10.1021/acscatal.0c01305

26. R. Li, H. Han, F. Zhang, D. Wang, C. Li (2014) Highly Efficient Photocatalysts Constructed by Rational Assembly of Dual-Cocatalysts Separately on Different Facets of $BiVO_4$. Energy Environ. Sci. 7 (4):1369-1376. doi:10.1039/C3EE43304H

27. R. Li, F. Zhang, D. Wang, J. Yang, M. Li, J. Zhu, X. Zhou, H. Han, C. Li (2013) Spatial Separation of Photogenerated Electrons and Holes among {010} and {110} Crystal Facets of $BiVO_4$. Nat. Commun. 4 (1):1432. doi:10.1038/ncomms2401

28. T. Liu, X. Zhou, M. Dupuis, C. Li (2015) The Nature of Photogenerated Charge Separation among Different Crystal Facets of $BiVO_4$ Studied by Density Functional Theory. Phys. Chem. Chem. Phys. 17 (36):23503-23510. doi:10.1039/C5CP04299B

29. Y. Qi, J. Zhang, Y. Kong, Y. Zhao, S. Chen, D. Li, W. Liu, Y. Chen, T. Xie, J. Cui, C. Li, K. Domen, F. Zhang (2022) Unraveling of Cocatalysts Photodeposited Selectively on Facets of $BiVO_4$ to Boost Solar Water Splitting. Nat. Commun. 13 (1):484. doi:10.1038/s41467-022-28146-6

30. C. Tossi, L. Hällström, J. Selin, M. Vaelma, E. See, J. Lahtinen, I. Tittonen (2019) Size- and Density-Controlled Photodeposition of Metallic Platinum Nanoparticles on Titanium Dioxide for Photocatalytic Applications. J. Mater. Chem. A 7 (24):14519-14525. doi:10.1039/C8TA09037H

31. K. Wenderich, G. Mul (2016) Methods, Mechanism, and Applications of Photodeposition in Photocatalysis: A Review. Chem. Rev. 116 (23):14587-14619. doi:10.1021/acs.chemrev.6b00327

32. L. Huang, X. Liu, H. Wu, X. Wang, H. Wu, R. Li, L. Shi, C. Li (2020) Surface State Modulation for Size-Controllable Photodeposition of Noble Metal Nanoparticles on Semiconductors. J. Mater. Chem. A 8 (40):21094-21102. doi:10.1039/C9TA14181B

33. Y. Jin-nouchi, T. Akita, H. Tada (2010) Ultrafast Photodeposition of Size-Controlled PbS Quantum Dots on TiO_2. ChemPhysChem 11 (11):2349-2352. doi:10.1002/cphc.201000229

34. Y. Zhao, C. Ding, J. Zhu, W. Qin, X. Tao, F. Fan, R. Li, C. Li (2020) A Hydrogen Farm Strategy for Scalable Solar Hydrogen Production with Particulate Photocatalysts. Angew. Chem. Int. Ed. 59 (24):9653-9658. doi:10.1002/anie.202001438

35. X. Wang, D. Liao, H. Yu, J. Yu (2018) Highly Efficient $BiVO_4$ Single-Crystal Photocatalyst with Selective Ag_2O-Ag Modification: Orientation Transport, Rapid Interfacial Transfer and Catalytic Reaction. Dalton Transactions 47 (18):6370-6377. doi:10.1039/C8DT00780B

36. M. Lee, J. Oh (2011) Synergistic Effect of Hydrogen Peroxide Production and Sonochemiluminescence under Dual Frequency Ultrasound Irradiation. Ultrason. Sonochem. 18 (3):781-788. doi:10.1016/j.ultsonch.2010.11.022

37. J. Yu, H. Guo, W. Feng, X. Guo, Y. Zhu, T. Thomas, C. Jiang, S. Liu, M. Yang (2022) Co_4N–WN_x Composite for Efficient Piezocatalytic Hydrogen Evolution. Dalton Transactions 51 (18):7127-7134. doi:10.1039/D2DT00381C

38. N. Kaynan, B. A. Berke, O. Hazut, R. Yerushalmi (2014) Sustainable Photocatalytic Production of Hydrogen Peroxide from Water and Molecular Oxygen. J. Mater. Chem. A 2 (34):13822-13826. doi:10.1039/C4TA03004D

39. C. Dong, S. Lu, S. Yao, R. Ge, Z. Wang, Z. Wang, P. An, Y. Liu, B. Yang, H. Zhang (2018) Colloidal Synthesis of Ultrathin Monoclinic $BiVO_4$ Nanosheets for Z-Scheme Overall Water Splitting under Visible Light. ACS Catal. 8 (9):8649-8658. doi:10.1021/acscatal.8b01645

40. X. Chen, L. Liu, P. Y. Yu, S. S. Mao (2011) Increasing Solar Absorption for Photocatalysis with Black Hydrogenated Titanium Dioxide Nanocrystals. Science 331 (6018):746-750. doi:10.1126/science.1200448

41. P. J. Boruah, R. R. Khanikar, H. Bailung (2020) Synthesis and Characterization of Oxygen Vacancy Induced Narrow Bandgap Tungsten Oxide (WO_{3-x}) Nanoparticles by Plasma Discharge in Liquid and Its Photocatalytic Activity. Plasma Chem. Plasma Process. 40 (4):1019-1036. doi:10.1007/s11090-020-10073-3

42. B. Wang, X. Wang, L. Lu, C. Zhou, Z. Xin, J. Wang, X.-k. Ke, G. Sheng, S. Yan, Z. Zou (2018) Oxygen-Vacancy-Activated CO_2 Splitting over Amorphous Oxide Semiconductor Photocatalyst. ACS Catal. 8 (1):516-525. doi:10.1021/acscatal.7b02952

43. H. Li, J. Li, Z. Ai, F. Jia, L. Zhang (2018) Oxygen Vacancy-Mediated Photocatalysis of BiOCl: Reactivity, Selectivity, and Perspectives. Angew. Chem. Int. Ed. 57 (1):122-138. doi:10.1002/anie.201705628

44. X. An, L. Zhang, B. Wen, Z. Gu, L.-M. Liu, J. Qu, H. Liu (2017) Boosting Photoelectrochemical Activities of Heterostructured Photoanodes through Interfacial

Modulation of Oxygen Vacancies. Nano Energy 35:290-298. doi:10.1016/j.nanoen.2017.04.002

45. C. Shi, X. Dong, J. Wang, X. Wang, H. Ma, X. Zhang (2017) Interfacial Defect Engineering over Fusiform Bismuth Vanadate Photocatalyst Enables to Excellent Solar-yo-Chemical Energy Coupling. RSC Adv. 7 (43):26717-26721. doi:10.1039/C7RA04328G

46. J. Wang, Z. Wang, B. Huang, Y. Ma, Y. Liu, X. Qin, X. Zhang, Y. Dai (2012) Oxygen Vacancy Induced Band-Gap Narrowing and Enhanced Visible Light Photocatalytic Activity of ZnO. ACS Appl. Mater. Interfaces 4 (8):4024-4030. doi:10.1021/am300835p

47. Y. Li, B. Yang, B. Liu (2021) Synthesis of $BiVO_4$ Nanoparticles with Tunable Oxygen Vacancy Level: The Phenomena and Mechanism for their Enhanced Photocatalytic Performance. Ceram. Int. 47 (7, Part A):9849-9855. doi:10.1016/j.ceramint.2020.12.126

48. S. Wang, P. Chen, J.-H. Yun, Y. Hu, L. Wang (2017) An Electrochemically Treated $BiVO_4$ Photoanode for Efficient Photoelectrochemical Water Splitting. Angew. Chem. Int. Ed. 56 (29):8500-8504. doi:10.1002/anie.201703491

49. J.-M. Wu, Y. Chen, L. Pan, P. Wang, Y. Cui, D. Kong, L. Wang, X. Zhang, J.-J. Zou (2018) Multi-Layer Monoclinic $BiVO_4$ with Oxygen Vacancies and V^{4+} Species for Highly Efficient Visible-Light Photoelectrochemical Applications. Appl. Catal. B 221:187-195. doi:10.1016/j.apcatb.2017.09.031

50. Y. Chen, M. Yang, J. Du, G. Ke, X. Zhong, Y. Zhou, F. Dong, L. Bian, H. He (2019) MoO_3/$BiVO_4$ Heterojunction Film with Oxygen Vacancies for Efficient and Stable Photoelectrochemical Water Oxidation. Journal of Materials Science 54 (1):671-682. doi:10.1007/s10853-018-2863-6

51. H. Wang, D. Yong, S. Chen, S. Jiang, X. Zhang, W. Shao, Q. Zhang, W. Yan, B. Pan, Y. Xie (2018) Oxygen-Vacancy-Mediated Exciton Dissociation in BiOBr for Boosting Charge-Carrier-Involved Molecular Oxygen Activation. J. Am. Chem. Soc. 140 (5):1760-1766. doi:10.1021/jacs.7b10997

52. Y. Zhao, J. Zhang, W. Wu, X. Guo, P. Xiong, H. Liu, G. Wang (2018) Cobalt-Doped MnO_2 Ultrathin Nanosheets with Abundant Oxygen Vacancies Supported on Functionalized Carbon Nanofibers for Efficient Oxygen Evolution. Nano Energy 54:129-137. doi:10.1016/j.nanoen.2018.10.008

53. Y. Zhu, W. Lu, H. Li, H. Wan (2007) Selective Modification of Surface and Bulk V^{5+}/V^{4+} Ratios and its Effects on the Catalytic Performance of Mo–V–Te–O Catalysts. J. Catal. 246 (2):382-389. doi:10.1016/j.jcat.2006.12.019

54. W. Wang, P. J. Strohbeen, D. Lee, C. Zhou, J. K. Kawasaki, K.-S. Choi, M. Liu, G. Galli (2020) The Role of Surface Oxygen Vacancies in $BiVO_4$. Chem. Mater. 32 (7):2899-2909. doi:10.1021/acs.chemmater.9b05047

55. J. Lee, W. Choi (2005) Photocatalytic Reactivity of Surface Platinized TiO_2: Substrate Specificity and the Effect of Pt Oxidation State. J. Phy. Chem. B 109 (15):7399-7406. doi:10.1021/jp044425+

56. S. A. C. Carabineiro, B. F. Machado, R. R. Bacsa, P. Serp, G. Dražić, J. L. Faria, J. L. Figueiredo (2010) Catalytic Performance of Au/ZnO Nanocatalysts for CO Oxidation. J. Catal. 273 (2):191-198. doi:10.1016/j.jcat.2010.05.011

57. H. Nakamatsu, T. Kawai, A. Koreeda, S. Kawai (1986) Electron-Microscopic Observation of Photodeposited Pt on TiO_2 Particles in Relation to Photocatalytic Activity. Journal of the Chemical Society, Faraday Transactions 1: Physical Chemistry in Condensed Phases 82 (2):527-531. doi:10.1039/F19868200527

58. V. R. Choudhary, C. Samanta, T. V. Choudhary (2006) Direct Oxidation of H_2 to H_2O_2 over Pd-based Catalysts: Influence of Oxidation State, Support and Metal Additives. Appl. Catal. A 308:128-133. doi:10.1016/j.apcata.2006.04.010

59. F. Wang, C. Xia, S. P. de Visser, Y. Wang (2019) How Does the Oxidation State of Palladium Surfaces Affect the Reactivity and Selectivity of Direct Synthesis of Hydrogen Peroxide from Hydrogen and Oxygen Gases? A Density Functional Study. J. Am. Chem. Soc. 141 (2):901-910. doi:10.1021/jacs.8b10281

60. Y. Wang, F. Chen, L. Zheng, J. Gao, Y. Liu (2022) Oxygen-Vacancy-Induced Structural Transition and Enhanced Magnetism in Sc, Fe-Codoped $SrTiO_3$: A Theoretical Study*. Chem. Phys. Lett. 805:139943. doi:10.1016/j.cplett.2022.139943

61. Z. Xie, H. L. Tan, H. Wu, R. Amal, J. Scott, Y. H. Ng (2022) Facet-Dependent Spatial Charge Separation with Rational Cocatalyst Deposition on $BiVO_4$. Materials Today Energy 26:100986. doi:10.1016/j.mtener.2022.100986

62. W. Ji, M.-H. Lee, L. Hao, X. Xu, S. Agathopoulos, D. Zheng, C. Fang (2015) Role of Oxygen Vacancy on the Photoluminescence of $BaMgSiO_4$:Eu Phosphors: Experimental and Theoretical Analysis. Inorg. Chem. 54 (4):1556-1562. doi:10.1021/ic502568s

63. C. Shi, X. Dong, J. Wang, X. Wang, H. Ma, X. Zhang (2017) Interfacial Defect Engineering over Fusiform Bismuth Vanadate Photocatalyst Enables to Excellent Solar-to-Chemical Energy Coupling. RSC Adv. 7 (43):26717-26721. doi:10.1039/C7RA04328G

64. X. Zhao, J. Hu, X. Yao, S. Chen, Z. Chen (2018) Clarifying the Roles of Oxygen Vacancy in W-Doped $BiVO_4$ for Solar Water Splitting. ACS Applied Energy Materials 1 (7):3410-3419. doi:10.1021/acsaem.8b00559

65. W. Qiu, S. Xiao, J. Ke, Z. Wang, S. Tang, K. Zhang, W. Qian, Y. Huang, D. Huang, Y. Tong, S. Yang (2019) Freeing the Polarons to Facilitate Charge Transport in $BiVO_4$ from Oxygen Vacancies with an Oxidative 2D Precursor. Angew. Chem. Int. Ed. 58 (52):19087-19095. doi:10.1002/anie.201912475

Chapter 5. Conclusions and Future Prospects

5.1. General Conclusions

In this thesis, the main objective is to rationally design some superior monoclinic $BiVO_4$ photocatalysts via structural engineering and surface modulation for highly efficient visible-light-driven photocatalysis. More importantly, this thesis emphasizes the great essence of controlling and exploiting the unique properties of monoclinic $BiVO_4$, which would enable a significant enhancement on the charge carrier dynamics and/or catalytic surface reaction kinetics, thus effectively satisfying the fundamental requirements for promoting more efficient photocatalysis process. The detailed study can be concluded in the following parts.

1. Lattice distortion engineering over ultrathin monoclinic $BiVO_4$ nanoflakes triggering AQE up to 69.4% in visible-light-driven water oxidation

In this part, simultaneous 2D structure tailoring and lattice distortion engineering over $BiVO_4$ photocatalyst were successfully performed through a facile template-directed strategy and simple introduction of Na^+ additive, respectively. In particular, the lattice distortion effect was characterized by the shrinking of V−O bonds and the elongation of Bi−O bonds. In-depth analysis unravels the cooperative contribution of the ultrathin 2D features and the lattice distortion effect to the modulation of charge carriers dynamics and catalytic surface features of the ultrathin 2D monoclinic $BiVO_4$ nanoflakes, yielding superior photocatalytic water oxidation performance with remarkable apparent quantum efficiencies up to 69.4%. The findings of this work prompt the functional exploitation of dimensional modification and lattice distortion engineering in order to design and fabricate superior monoclinic $BiVO_4$ photocatalyst for various photocatalytic applications.

2. New insights into water oxidation reaction over (010) facet of monoclinic $BiVO_4$: Unravelling the key role of lattice distortion

In summary, a combination of experimental and theoretical approaches was utilized to gain some new insights into water oxidation reaction over (010) facet of monoclinic $BiVO_4$, by which the key role of lattice distortion was unraveled and highlighted. By ATR-IR analysis, some water oxidation intermediates including the active Bi–OH and unique bridged Bi–O–O–V species were firstly identified, thus allowing the stipulation

of possible water oxidation mechanism. Correspondingly, the DFT calculations for Gibbs free energy indicate the favorable water oxidation process over the (010) surface of $BiVO_4$ slab model with greater degree of lattice distortion, thus elucidating the additional benefit of lattice distortion effect over the catalytic surface features of monoclinic $BiVO_4$ for driving more efficient OER. In addition, by employing the first-principal molecular dynamic simulations and the corresponding electronic structure calculations, the observed key intermediates (Bi–OH and Bi–O–O–V species) were found to possess high enough O 2p energy levels, thus enabling them to readily donate some electrons and be oxidized by the photogenerated holes. Lastly, some spontaneous dissociative adsorption process of water molecules over the unsaturated 6c-Bi sites was also demonstrated, by which hydroxyl ion (OH^-) would play a critical role in triggering the transformation of undissociatively adsorbed water molecules into the active –Bi–OH species. The findings of this study deepens the understanding of water oxidation reaction over monoclinic $BiVO_4$ and might provide some inspiration for the rational design of superior $BiVO_4$-based material for more efficient photocatalytic OER.

3. Oxygen vacancy-mediated size engineering of Pd cocatalyst over monoclinic $BiVO_4$ for visible-light-driven H_2O_2 synthesis

In summary, an effective oxygen vacancy-mediated size engineering strategy was successfully applied and demonstrated over the homogenously distributed palladium cocatalyst photodeposited on the (010) surface of monoclinic $BiVO_4$. The manipulation of oxygen vacancy level was accomplished by simply adjusting the pH of the hydrothermal solution for the fabrication of pure monoclinic $BiVO_4$ samples, by which higher pH would generate more oxygen vacancy. It is proposed that the oxygen vacancy would serve as surface charge redistributor and positively influence the electrostatic interaction between the (010) surface of monoclinic $BiVO_4$ and the negative $PdCl_4^{2-}$ precursor ions, thus yielding smaller size of Pd cocatalysts. An appropriate trade-off between the enhanced surface catalytic reaction kinetic as the result of downsized Pd cocatalyst and charge recombination by oxygen vacancy in the bulk material of monoclinic $BiVO_4$ bestowed the optimized sample with an outstanding visible-light-driven H_2O_2 evolution performance of 2.35 mM within 1 h illumination, corresponding to a high AQE of 19.2% at 420 nm. The findings in this study highlight and prompt the importance of surface modulation and optimization for fabricating superior monoclinic $BiVO_4$ photocatalysts for efficient solar-driven H_2O_2 synthesis via ORR.

5.2. Future Prospects

Although some achievements have been made in developing monoclinic $BiVO_4$ photocatalyst for efficient visible-light-driven photocatalytic reactions, there are many challenges towards the significant enhancement of photocatalytic performance and practicability, especially considering the demands which must be fulfilled in order for artificial photosynthesis technology to step further onto the industrial stage. Some issues listed below are worthy of special attention:

1. The fruitfulness of developing superior and stable noble metal-free semiconductors (light absorbers) and cocatalysts with satisfactory photocatalytic performance is one of the decisive factors in determining the viability of artificial photosynthesis technology. Especially for the cocatalyst cases, noble metals are still located at the peak of the summit and are yet to be easily replaced. Therefore, future research should be devoted to exploring and developing novel materials, such as metal-free (carbon-based) materials, transition metal-based catalysts, metal-organic frameworks (MOFs), covalent-organic frameworks (COFs), etc., to alleviate the dependency on noble metals. Furthermore, surface engineering by defect implanting or single-atom (metal) doping can also be a powerful option since it can regulate the reactions in a completely different way compared with traditional catalysis, while also modulating the intrinsic properties of the host photocatalysts.
2. Up until now, complete understanding of the detailed reaction pathways over the surface reactive sites has been one of the most difficult yet also important issues to address in order to realize the rational design of efficient photocatalyst materials. Intriguingly, investigating the cataytic reaction mechanism is like peeling the skins of an onion, whereby each discovery will lead to additional discoveries, hence requiring continuous in-depth investigations and also patience. For example, in these past recent years, a new reaction mechanism where lattice oxygen (derived from the catalyst) also participates in the oxygen evolution reaction has been proposed, which opens the door to many novel approaches for the development of superior (photo)catalysts and thus bypasses the design limitations of engineering materials under the conventional mechanism. In this regard, integrated *in-situ*/operando characterization techniques through X-ray absorption spectroscopy, infrared spectroscopy, and Raman spectroscopy are undoubtedly necessary to locally and accurately identify the key intermediate species and structural variations, as well as unravel the nature of reactive

centers. The practice of theoretical study, especially density-functional-theory calculation, is also of equal importance to gain more comprehensive clues for the ultrafast surface reaction process and structural transformation. In addition, some new insights into the excited state of semiconductor-adsorbate systems under light irradiation might also be worthy of investigation to complement the understanding of what truly happens during photocatalytic reactions.

3. Although many photocatalytic systems have been successfully demonstrated at the laboratory scale, there are still some important scientific challenges which must be overcome to allow the practical use of large-scale artificial photosynthesis in our future society. With that being the case, scalable photocatalyst will be the key to further advancement of photocatalysis technology into industrial application. Accordingly, the conversion of particle suspension systems to immobilized particulate systems (printed photocatalyst panel), which are more readily scaled up, has exhibited great potential to solve the above issues. In addition, the reactor design must also be considered carefully and systematically in order to facilitate efficient solar light absorption and regulate effective interaction between the reactants and photocatalyst surface while still allowing the delicate extraction of the targeted product(s).

Acknowledgement

First, I want to praise and glorify God for His undying love, grace, and faithfulness in my life. He picked me up when I was nothing but trash and made me His beloved child despite my weakness and sins. He didn't cast me away when I was devastated, but He stands right by me through all of my troubles as my father, best friend, and defender. He gives me strength and enough courage so that I can rise and fight through the challenges in life. Through His wonderful plan, He sent me an amazing, brilliant, and very kind supervisor, Prof. Jinhua Ye, who has given me a golden opportunity to carry out my doctoral study under her supervision. Words cannot express my gratitude and feelings for everything she has done for me. If it's not because of her invaluable guidance and instructions, kind support, and constant encouragement throughout all these years of my doctoral study, I wouldn't be able to come this far. I would also like to highly appreciate the academic freedom and great research platform that Prof. Ye offered. I feel so lucky and blessed to meet such a great supervisor.

I am also grateful to my sub-supervisors, Prof. Taro Nagahama and Prof. Naoto Shirahata, as well as my defense committee, Prof. Kei Murakoshi and Prof. Hidenori Noguchi. Thank you for all your constructive advice and suggestion to further improve the quality of my Ph. D. thesis. Additionally, this endeavor would not have been possible without the generous support from The Indonesia Endowment Funds for Education (LPDP), which provided the financial support for my Ph.D. study and research.

Many thanks to Dr. Fumihiko Ichihara, Dr. Huiwen Lin, and Dr. Shunqin Luo, who gave me a lot of advice and support for the completion of my Ph.D. study. I would also like to express my thanks to Dr. Tetsuya Kako, Dr. Mitsutake Oshikiri, Dr. Hong Pang, Dr. Hui Song, Dr. Yunxiang Li, Dr. Xiaohui Ren, Dr. Qi Wang, Dr. Bowen Deng, Dr. Sijie Li, Dr. Hamza El-Hosaeny, Dr. Hao Huang, Dr. Xusheng Wang, Dr. Yao Xie, Dr. Yu He, Dr. Shuang Song, Prof. Kun Chang, Ms. Haruna Kurokawa, and Ms. Kanae Hasegawa, and all the members in the Photocatalytic Materials Group, NIMS for their kind helps in both experiments and daily life.

Last but not least, I want to take this good chance to extend my sincere thanks to my spouse (Destiny Marisa Simarmata), son (Daiki Timothy Philo), parents, parents-in-law, other family members, and friends for their constant support during this very long process. Especially, I would like to express my deepest appreciation to my wife who has never

stopped believing in me, even when I started doubting myself. She provides the home for me to rest and feel secure and she comforts me whenever I'm troubled and weary. She has been the guiding light when life threw me in the darkest of corners. Her presence and love in my life are the very reason that I can finally complete this Ph.D. study.